Deployment and evaluation of an aerosol time-of-flight mass spectrometer

Evelyn J. Freney

Ph.D Thesis

University of Edinburgh

2006

To

Mum, Dad,

Declan & Laura

The work presented in this thesis is the original work of the author, except where specific reference is made to other sources. It has not been submitted in part, or in whole, for any other degrees.

Evelyn Freney

February 2006

Acknowledgements

First and foremost, I would like to thank my two supervisors, Dr. Mathew Heal and Professor Robert Donovan for enduring the endless proof-reads that have to be done whenever I type anything. Without their help and persistence this work would not have been possible. I would also like to thank Professor Peter Harland (University of Canterbury, New Zealand) for all his enthusiasm and advice during his visit in October 2004.

I would like to thank Professor Dick Derwent and Dr. Mark Harrison from the Met. Office for supplying NAME back plots to the NAMBLEX consortium and to the CAPs study, respectively. To Dr. Nick Millls and Paul Fokkens for their help during the CAPs study. I would also like to thank Dr. David Beddows who spent a month at Mace Head acquiring the ATOFMS data during NAMBLEX and also for acquiring and analysing the MOUDI data and to the rest of Professor Harrison's group at Birmingham University especially Dr. Manuel Dall'Osto, Wayne Smith, Dr. Mark Crampton and Dr. Marie-Jo Schofield who were always very helpful during my visits to Brimingham to use the ATOFMS instrument. I would also like to thank Dr. Dave Prime and Tony New from GSK for their help in acquiring the pharmaceutical data.

Finally, thanks to Pierre-Emmanuel who has always been there throughout my PhD. To all my friends and family for being so patient and understanding especially my mum and dad for their endless support.

Abstract

Aerosol particles play a significant role in the pollution of the Earth's atmosphere as well as contributing to climate change and having strong influences on health. Understanding aerosol particle physical and chemical properties is important in assessing their effects. A number of instruments have been developed that allow the real time analysis of single particles. This thesis presents research using a commercial aerosol time-of-flight mass spectrometer (ATOFMS TSI 3800), which was deployed in the laboratory to determine fundamental aspects of ion formation as well as to develop scaling factors to improve the number and chemical quantification of the ATOFMS instrument and to characterise pharmaceutical drug products. Additionally, data from field campaigns both in Ireland and Scotland were evaluated.

The ATOFMS uses pulsed UV Laser Desorption Ionisation (LDI) at 266 nm to ablate, desorb and ionise the particle material. Little work has been carried out to investigate the mechanisms for formation of negative ions in single particle LDI instruments. In this thesis, the ATOFMS was applied to micron-sized aerosols consisting of alkali halides, nitrates and sulphates as models for atmospherically-relevant particles. Processes that can lead to negative ion formation and removal are considered in some detail and it is concluded that their formation is dependent on collisional processes and the thermodynamics of reactions in the post-irradiation ablation plume rather than the result of direct ejection from the lattice.

Data from the deployment of the ATOFMS instrument at Mace Head, Galway, Ireland were used to determine the size and chemical composition of individual particles in the atmosphere as part of the North Atlantic Marine Boundary Layer Experiment (NAMBLEX) during August 2002. A total of 191,504 particles were detected. Rapid changes in number density, size and chemical composition of the atmospheric aerosol were observed. These data were analysed using a combination of statistical clustering procedures and manual classification, yielding three broad categories of particles; sea salt, dust and carbon-containing.

During the NAMBLEX campaign, aerosol size and composition was also characterised using an impactor and an aerodynamic particle sizer alongside the ATOFMS. Comparative analyses were undertaken in order to elucidate factors determining the particle detection efficiency of the ATOFMS, according to the efficiency of the inlet system and the hit-rate of particles (as a function of particle composition). An elemental/molecular relative sensitivity factor was determined from the measured ion signals. The results show the existence of a matrix effect dependent on chemical composition of the aerosol sampled, as well as a strong inverse power-law dependence of inlet transmission efficiency on particle diameter. The observation of an inverse cubic dependence of ion signal on particle diameter indicates that a constant mass of material is ionised from each particle.

A field evaluation of a Mobile Ambient Particle Concentrator Enrichment Laboratory (MAPCEL) was carried out during February and March 2002. The MAPCEL was coupled with the ATOFMS in order to determine the size, chemical composition and concentration enrichment of single particles with diameters < 2.5 μm. During the 9 days of sampling most of the particles detected were mixtures of sea salt with occasional short episodes of carbonaceous material. Comparison of the pre- and post-concentrated particle composition suggests that the MAPCEL did not induce significant changes in particle composition during the concentration process.

Finally, in separate work, the ATOFMS instrument has been used to assess the level of co-association of individual drug components present in different pharmaceutical products. Different efficiencies for different aerosolised pharmaceutical asthma drug products are reported.

Full title	Abbreviation
Active Pharmaceutical Ingredient	API
Aerodynamic Particle Sizer	APS
Aerosol Mass Spectrometer	AMS
Aerosol Time-of-Flight Mass Spectrometer	ATOFMS
Air Quality Expert Group	AQEG
Air Quality Network	LAQN
Artic regions	AR
Artificial Resonance Theory	ART
Atlantic regions	AT
Atmosphere/Ocean Chemistry Experiment	AEROCE
Automatic Urban and Rural Network	AURN
Background Maritime contribution to Atmospheric Pollution in Europe	BMCAPE
Cavity Ring Down Spectroscopy	CRDS
Cloud Condensation Nuclei	CCN
Committee on the Medical Effects of Air Pollutants	COMEAP
Concentrated Ambient Particles	CAP
Concentration factors	CF
Continuous wave	CW
Department for Environment, Food and Rural Affairs	DEFRA
Differential Mobility Analyser	DMA
Differential Optical Absorption Spectroscopy	DOAS
Dimethylsufide	DMS
Downstream sampling	DS
Electron Impact	EI
Environmental Scanning Electron Microscope	ESEM
European Aerosol Conference	EAC
European Centre for Medium-Range Weather Forecasts	ECMWF
GlaxoSmithKline	GSK

Full name	Abbreviation
Harvard Ambient Particle Concentrator	HAPC
Heart Rate Variability	HRV
High Efficiency Particle Air Filter	HEPA
High Performance Liquid Chromatography	HPLC
Hydroxymethanesulphonate	HMS
Laser Ablation Mass Spectrometry	LAMMS
Laser Desorption Ionisation	LDI
Marine Boundary Layer	MBL
Matrix Assisted Laser Desorption Ionisation	MALDI
Metered Dose Inhalers	MDI
Methyl Sulphonate acid	MSA
Micro Orifice Uniform Deposit Impactor	MOUDI
Microchannel plate	MCP
Mobile Ambient Particle Concentrator Laboratory	MAPCEL
Mutual deliquescence relative humidity	MDRH
Neodyium:Yttrium Aluminium Garnet	Nd:YAG
North Atlantic Marine Boundary Layer Experiment	NAMBLEX
Numerical Atmospheric-dispersion Modelling Environment	NAME
Optical Particle Counters	OPC
Organic Carbon/Black Carbon ratio	OC/BC
Particulate matter	PM
Particulate matter < 0.1 μm in diameter	$PM_{0.1}$
Particulate matter < 1 μm in diameter	PM_1
Particulate matter < 2.5 μm in diameter	$PM_{2.5}$
Peroxy Radical Chain Amplification	PERCA
Photomultiplier tubes	PMT
PolyStyrene latex spheres	PSL
Powdered Dose Inhalers	PDI
Rapid Particle Mass Spectrometer	RSMS

Full name	Abbreviation
Readily Accessed Memory	RAM
Relative Humidity	RH
Scanning Electron Microscopy	SEM
Scanning Mobility Particle Sizer	SMPS
Secondary Ion Mass Spectrometry	SIMS
Single Particle Analysis and Sizing System	SPASS
Single Particle Laser Ablation Time-of-Flight Mass Spectrometer	SPLAT
Single-Particle Raman Spectrometer	SPaRS
Tapered Element Oscillating Microbalance	TEOM
Time-of-Flight Mass Spectrometer	TOF-MS
Transmission Electron Microscopy	TEM
Ultraviolet	UV
Unified Model	UM
United States Environmental Protection Agency	USEPA
Upstream sampling	US
Versatile Aerosol Concentration Enrichment System	VACES

Chapter 1

Introduction

Chapter 1 Introduction

1.1. Aerosol research

An aerosol by definition is a suspension of solid or liquid particles in a gas. The term aerosol includes both the particles and the suspending gas. The aerosol size distribution can range from 0.002 – 100 μm (Hinds, 1999).

Aerosol science is involved in a number of important scientific research fields. Examples are air pollution (urban and regional smog formation, acid deposition and stratospheric ozone depletion), global warming, medicine problems and treatment (airborne microbes, respirable aerosols), combustion processes (soot and soot precursor formation), materials synthesis, processing (nano-particles, coatings, mining operations) and clean-room technology (particle contamination).

Aerosols can be divided into two broad categories; 'healthy' aerosols such as those that are used to deliver drugs, 'unhealthy' aerosols such as those that result in air pollution and global warming. Both of these categories are considered in the work to be presented in this thesis.

1.1.1. Health impacts

There is evidence that anthropogenic particles directly effect human health (Pope, 1999). Epidemiological studies have correlated elevated levels of particulate matter (PM) with decreased pulmonary function, respiratory disease and increased mortality. Whilst epidemiological studies have consistently demonstrated adverse effects of PM exposure on human health, the mechanism of the effect is currently unclear (Donaldson *et al*, 2004). One of the major issues is whether the toxicity of the particles resides in some particular fraction of the particles as defined by chemical composition or size. Anderson *et al.* (1992) exposed volunteers to carbon particles coated with sulphuric acid to simulate exposures to carbonaceous/acid particle mixtures. Although these studies have made an attempt to simulate particle exposures, their approach does not fully achieve a "real world" simulation. Chapter 6

assesses a technique that exposes volunteers to 'real world' concentrated ambient aerosols.

Controls on the total amount of annual pollution and magnitude of pollution episodes have been put in place by authorities in an attempt to reduce the health burden of atmospheric particulate pollution. Traditionally monitoring of particles with diameters less than 10 μm in size have been used as these particles are more likely to pass the throat when inhaled. Recently much research has illustrated that exposure to fine (< 2.5μm) and ultrafine (< 0.1 μm) particles can affect respiratory and cardiovascular function (Seaton *et al*, 1995; Harrison & Yin, 2000). These smaller particles tend to be more dangerous and more reactive than larger particles due to their larger surface-to-volume ratio. This has led to the use of the $PM_{2.5}$ standard in the United States, where the total mass of particulate matter less than 2.5 μm is regulated (United States Environmental Protection Agency (USEPA)).

The UK Department of Health's Committee on the Medical Effects of Air Pollutants estimated that in Great Britain, in 1996, PM_{10} pollution was associated with around 8,100 deaths brought forward and 10,500 hospital admissions that were either brought forward or would not otherwise have happened (COMEAP, 1998). This was due to short-term (acute) exposure. It is likely that the health impacts of long-term (chronic) exposure on the population were even greater. COMEAP have estimated that over the lifetime of the current population of England and Wales, the health gain that would result from a reduction of 1 μg m^{-3} of $PM_{2.5}$ could lead to a gain of 0.2 – 0.5 million life years (COMEAP, 1998).

1.1.2. Pharmaceutical applications

As particles with diameters < 2.5 μm are efficient at entering and depositing in the respiratory system many medical companies have employed the use of respiratory devices to deliver drugs, in the form of small particles, to combat a number of illnesses. It is also known that particles can work most efficiently through the use of respiratory drug delivery devices as they can enter into the blood stream in a very

short time compared to other means of drug delivery. Chapter 7 characterises drug products from a range of commercially available asthma inhalers.

1.1.3. Global warming

PM in the atmosphere arises from natural sources and from anthropogenic activities, such as combustion of fuels. Consequently atmospheric aerosols consist of natural and anthropogenic PM. Natural aerosols are important because they provide a base level to aerosol impact, and there is no effective control on them, unlike anthropogenic aerosols where regulations can govern their emissions. On a global scale the mass abundance of natural aerosols is several times greater than that of the major anthropogenic aerosols. The major natural aerosols are sea-salt, soil dust, natural sulphates, volcanic aerosols, and those generated by natural forest fires. Major anthropogenic aerosol species in the atmosphere include sulphate, nitrate, black carbon and organic carbon. Many of the natural and anthropogenic gases and particulate matter that are traditionally associated with air quality also interact with solar or terrestrial radiation and therefore exert a significant radiative forcing resulting in climate change (Penner *et al*, 2001). Radiative forcing applies to the increased or decreased trapping of radiation relative to some past time point, to provide a simple quantitative measure of a potential mechanism of change in the climate (Wayne, 2000). The radiative forcing is the change in the net vertical irradiance (expressed in Watts per square metre: Wm^{-2}) at the tropopause due to an internal change or a change in the external forcing of the climate system, such as, for example, a change in the concentration of carbon dioxide or the output of the sun. Usually radiative forcing is computed after allowing for stratospheric temperatures to readjust to radiative equilibrium, but with all tropospheric properties held fixed at their unperturbed values (IPCC, 2001).

Aerosol particles have both direct and indirect effects on radiative forcing and therefore potentially also on the Earth's climate. The direct effect of aerosols arises from increases in aerosol concentration. Direct effects of aerosols are difficult to calculate as aerosols can contain chemicals that will both absorb and scatter solar radiation. Determining the amount of black carbon internally mixed in the particle is

used to determine the single scattering albedo (fraction of radiation reflected by a surface) of particles. The specific absorption of aerosol particles is roughly twice that when it is internally mixed with elemental carbon than when it is externally mixed (Jacobson, 2000).

Knowing the amount of vapour that condenses on the aerosol is another important factor to consider when determining direct effects. For example at high relative humidity sulphate aerosols can absorb water vapour. This moves sulphate particles into a size class that causes a large increase in the amount of light scattering.

Indirectly particles can act as Cloud Condensation Nuclei (CCN). Changes in liquid clouds at low altitudes tend to mainly change the amount of scattered solar radiation. Radiative effects of changes in ice clouds at high altitudes are dominated by the change in outgoing thermal radiation.

There are two different types of indirect effects. First is the Twomey effect which states that at constant liquid water content, increases in aerosols will tend to increase the number of cloud droplets and decrease their size. Increases in the number concentration of cloud droplets at low-altitude leads to an increase in the scattering of solar radiation. This increase in scattering leads to a cooling effect. The second effect is that changes in aerosol causes changes in droplet concentration which subsequently alters the precipitation effects of clouds (Penner *et al*, 2001). Figure 1.1 shows the effects of different particle types on the Earth's radiative balance.

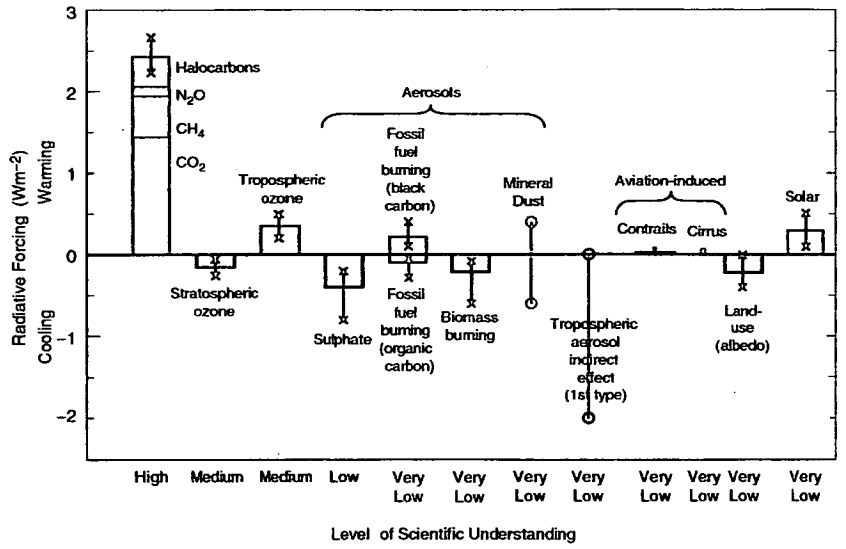

Figure 1.1. Estimates of radiative forcing of different particle composition on the Earth's climate and the level of scientific understanding (IPCC, 2001)

1.2. Aerosol properties

1.2.1. Aerosol size and mass distributions

Airborne PM includes a wide range of particle sizes and many different chemical constituents. Aerosol particles can have "diameters" anywhere between 2 nm and 100 μm. There are a number of properties such as number concentration, size, shape and chemical composition that are important for their role in atmospheric processes. The size of an individual particle is an important parameter as it can be related to effects on health, visibility, and climate as well as giving information on the source of particles.

Airborne particles are frequently not spherical and the diameter used to describe the size of an individual particle depends to a large extent on the instrumentation used to measure it. The equivalent diameter refers to the diameter of a sphere having the same value of a specific physical property as the irregularly shaped particle that is being measured. When a particle is reported by a technique, the measurement usually corresponds to a specific physical property. Figure 1.2 shows different particle size definitions that depend on observations of particle behaviour. Aerodynamic diameter,

D_a, is the most common type of diameter that is measured and is defined as the diameter of a sphere of unit density that has the same terminal falling speed in air as the particle under consideration.

Airborne particles are usually considered as belonging to three ambient particle size modes (Figure 1.3). Particles with diameters < 0.1 μm belong to the nucleation mode and consist mainly of particles created from gas to particle conversion processes (Figure 1.4) (Raes *et al*, 2000). Highest number concentrations exist in this size mode. Particles with diameters between 0.1-2.5 μm are considered to be part of the accumulation mode representing the region of particle growth mainly due to coagulation and condensation. The accumulation mode has the greatest surface area distribution (Figure 1.3).

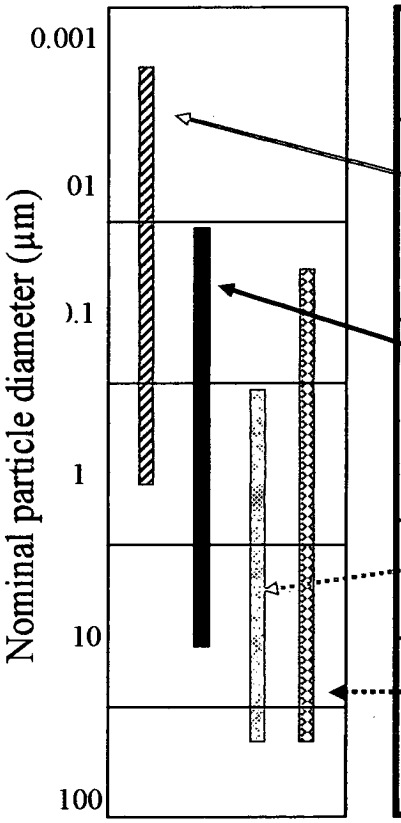

Instrumental technique	Operational principles	Size property measured
Scanning mobility particle sizer (SMPS) (with condensation particle	Charge added to particle and drift mobility in an electrical field measured	Mobility diameter
Electrostatic low pressure impactor (ELPI)	Cascade impactor, but charge added to each particle and current flow to each size stage is converted to particle number	Inertial/ aerodynamic diameter
Aerodynamic particle sizer	Measure time-of-flight of particle between two laser beams	Aerodynamic diameter
Optical scattering	Scattered light pulse as particle passes through a single laser beam is converted to particle size	Optical diameter a function of shape and optical scattering properties of particle

Figure 1. 2. Summary of size ranges covered by various analytical techniques for the analysis of atmospheric aerosols. TEM, transmission electron microscopy; SEM, scanning electron microscope, CPC Condensation particle counters.

Larger, coarse mode particles (> 2.5 μm in diameter) are generally mechanically generated; examples include natural sea-salt particles off the ocean or dust particles and anthropogenic particles from quarrying, construction work and industrial machining. Highest mass distributions are found in the accumulation and coarse mode particles (Figure 1.3). The atmospheric lifetimes of the nucleation mode particles are relatively short due to particle coagulation or dry deposition by Brownian motion. Similar lifetimes exist for coarse mode particles due to gravitational settling. The accumulation mode particles however do not experience efficient deposition processes and therefore have long atmospheric lifetimes from days to weeks. It is possible for these particles to become scavenged by fogs or precipitation.

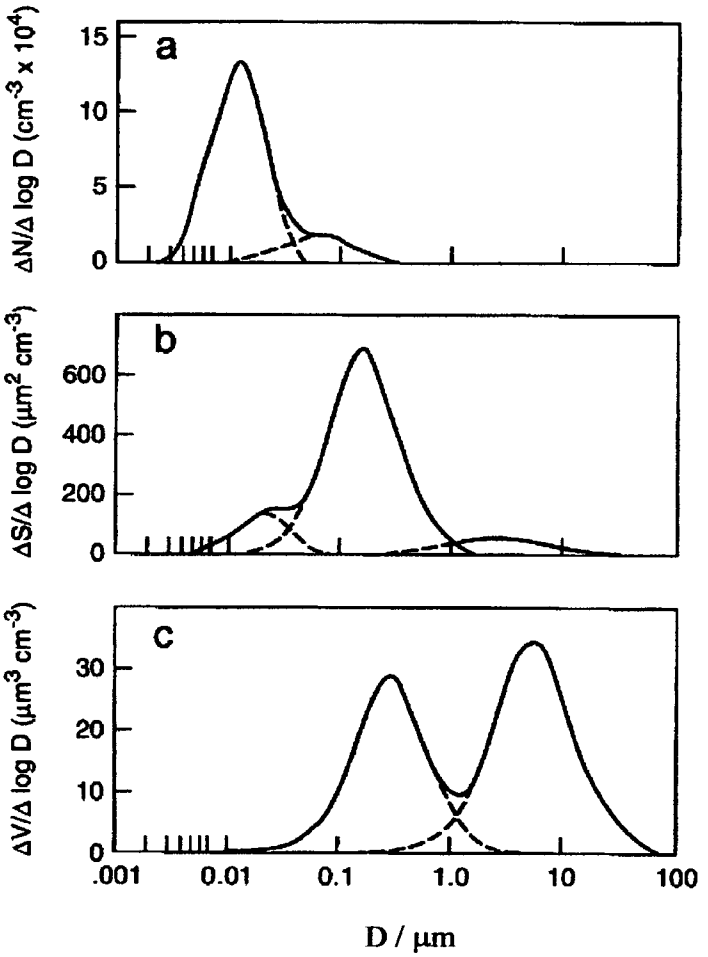

Figure 1.3. Number (a), surface (b) and volume (c) distributions for a typical urban model aerosol (Finlayson-Pitts & Pitts, 1999b).

Figure 1.4 shows the microphysical processes that influence the size distribution and chemical composition of the atmospheric aerosol, highlighting the large range of sizes that are involved in the formation and evolution of aerosol particles. For observational reasons aerosol particles have traditionally been divided into two size classes; coarse (D_a > 2.5 μm) and fine (including accumulation and fine mode particles) (D_a < 2.5 μm). Recent research has suggested that aerosol size distribution is more appropriately described using a 1 μm size cut. This is supported diagrammatically in Figure 1.4 where a minimum in the distribution is reached near 1 μm. (Guazzotti *et al*, 2003; AQEG, 2005).

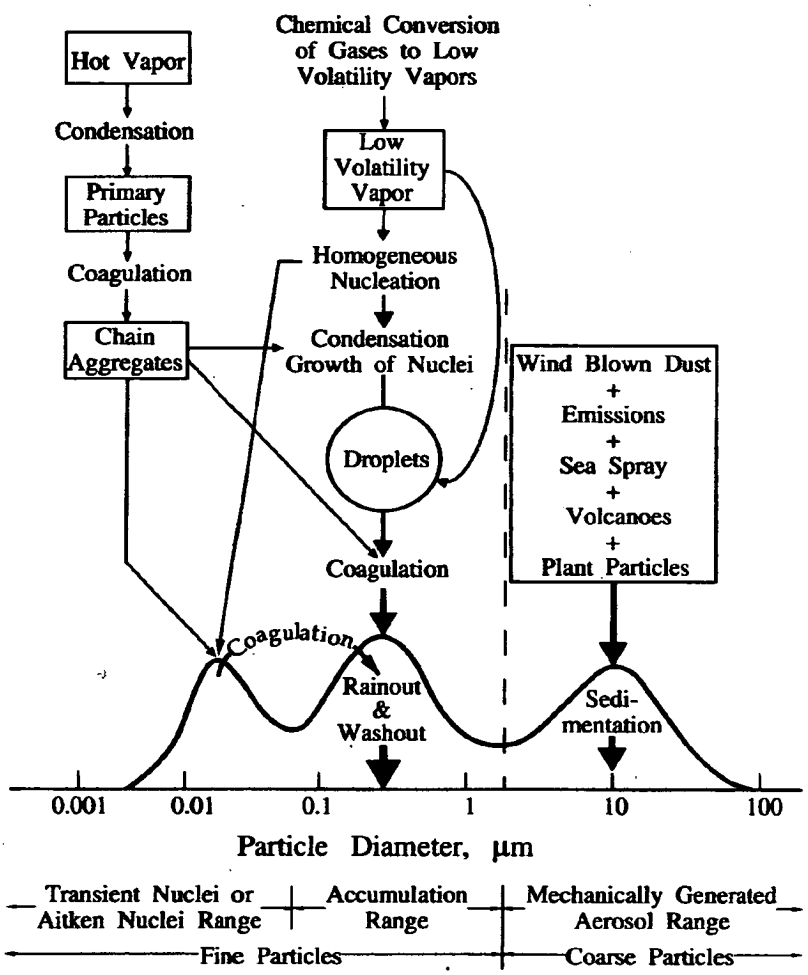

Figure 1.4. Idealised schematic of the distribution of surface area of an atmospheric aerosol (Whitby and Cantrell, 1976). Principal modes, sources, and particle formation and removal mechanisms are indicated.

Aerosol particles can be considered as belonging to a primary or secondary source, primary particles are those that have not undergone reaction in the atmosphere and are formed through natural processes. Secondary aerosols, such as 2-methyltetrols, are those particles that have undergone reaction with volatile organic carbon (VOC) species, such as isoprene and monoterpenes, or other particles and can be termed as anthropogenic or natural processes.

Those primary particles that are derived from natural processes include the break-up and suspension of bulk material by the wind, such as sea-salt, soil dust, and biological material and have most of their mass associated with super-micron modes (Figure 1.4). Particles that are formed mechanically tend to be strongly dependent on wind speed and the number concentration increases non-linearly with increasing wind speed (O'Dowd, 2002). Important types of anthropogenic primary particles are soot particles formed in combustion. High concentrations of particles with diameters ranging from 5-20 nm are formed during combustion processes. Coagulation into fractal-like aggregates occurs very rapidly which eventually collapse to more compact structures of increased size (Raes *et al*, 2000). The main sources of anthropogenic primary PM are road transport (combustion by-products, brake and tyre wear and re-entrainment of dust from road surfaces); stationary combustion (mainly domestic coal burning) and industrial processes (production of metals, cement, lime, coke and chemicals, bulk handling of dusty materials, construction, mining and quarrying) (AQEG, 2005).

Secondary aerosol mass is formed by transformation of gaseous compounds to the liquid or solid phase. Secondary particles are not emitted directly from sources instead they are formed in the atmosphere as a result of chemical reactions forming low volatile gaseous substances which can then condense into solid or liquid phase to become particulate matter, this process is referred to as nucleation. Such particles generally result from atmospheric oxidation processes and the substances oxidised may be either natural or anthropogenic in origin.

There are two types of nucleation processes (AQEG, 2005). Heterogeneous nucleation is when newly formed substances condense onto existing particles

whereas homogenous nucleation is when newly formed molecules condense onto one another and form a new particle. An example of homogeneous nucleation occurs when sulphuric acid is formed from the atmospheric oxidation of SO_2 (AQEG, 2005). This H_2SO_4 can nucleate with water vapour (binary nucleation) or, more readily, with water vapour and ammonia (ternary nucleation) to form droplets of sulphate which can grow rapidly to 10 nm in size (Covert *et al*, 1992).

1.2.2. Chemical composition

Aerosol particles consist of a wide range of different chemical compositions that are consistently changing due to transportation of air masses as well as heterogeneous chemical reactions in the atmosphere. As mentioned in Section 1.2.1, the size distribution of particles is very important in understanding the sources and therefore the types of ambient PM. Chemical composition of aerosol particles is strongly associated with particulate diameter. Carbonaceous aerosols emitted from combustion processes normally exist in the ultrafine to fine mode whereas NaCl particles produced from wave breaking and bubble bursting are generally formed with super-micron diameters. Due to coagulation and nucleation processes outlined in Figure 1.4, it is common to find particles that are made up of two or more components. These particle types are referred to as being internally mixed. Examples of internally mixed particles are those containing NaCl as well as sulphate or nitrate materials.

The major chemical constituents of airborne particles include sulphate, both natural and anthropogenic, nitrate, ammonium, sodium, chloride, elemental carbon, organic carbon, mineral components and water. Minor components present in the atmosphere consist of trace metals such as lead, cadmium, mercury as well as trace organic compounds.

Identifying the source of airborne particles is essential to their control, if the source is anthropogenic and is crucial to understanding natural environmental processes, if the source is biogenic. Research and development in this area require analytical methods that can monitor changes in aerosol particles as they grow or are transformed by

condensation, evaporation, or chemical reaction. This can be challenging because the particle size of greatest interest ranges from 2 nm to 100 μm and the concentrations of minor components in particles are often of considerable interest (Johnston & Wexler, 1995). The first measurements of aerosol number concentration in the atmosphere were performed by Aitken (1888) who used an expansion chamber to condense water vapour on to particles and made them grow to visible droplets.

1.3. Aerosol instrumentation

Atmospheric aerosol particles range in size over more than four orders of magnitude, from freshly nucleated clusters containing a few molecules to cloud droplets and crustal dust particles up to tens of microns in size. Average particle compositions vary with size, time and location, reflecting the particles diverse origins and atmospheric processing (McMurry, 2000). McMurry *et al.* (2000) illustrated the different types of aerosol sampling instruments available and subdivided them into two broad groups; those instruments that provide measurements on size-resolved aerosol physical properties and those that provide size-resolved chemical properties. In this chapter different methods of instrumentation are discussed starting with instruments that provide information on the physical properties of particles followed by those instruments that supply size-resolved information on chemical properties. More detail of these instruments can be found in McMurry *et al.* (2000) and Finlayson-Pitts and Pitts (1999a).

Atmospheric aerosols typically include hundreds of organic and inorganic compounds, and only a small fraction of these can be identified by state-of-the-art analytical methodologies. Figure 1.2 illustrates the size range covered by different instruments that are used to obtain both physical and chemical information from ambient particles.

1.3.1. Mass measurements

Impactors are common instruments used to provide size and mass measurments of particles present in both ambient and laboratory environments. Impactors are based on the principle that particles in an air stream will tend to continue in a straight line

due to their inertia when the flow of air bends sharply; particles then adhere to the surface of an impaction plate. Particles of a specific aerodynamic/inertial diameter impact on a corresponding plate where they are collected for analysis. Occasionally it is necessary to coat the impaction plate with a substrate that will cause the particle to adhere strongly to the impaction plate. This reduces particle 'bounce/re-entrainment', where particles hit the impaction surface and bounce back into the air stream.

A variety of sampling artefacts can affect the measured composition of the collected particles deposited relative to what was actually in the atmosphere. Volatilisation of semi-volatile compounds (compounds that are found in both the vapour and particulate phases) is known to be a significant source of error for species like ammonium nitrate and many organics in impactor instruments. Volatilisation can occur because of a pressure drop in the sampler, which upsets the equilibrium between the deposited particles and the vapour or due to changes in temperature, relative humidity or composition of the incoming aerosol during sampling. Artefacts associated with sampling transport and storage have also been reported (Chow, 1995). Evaporative losses of particulate nitrates have been investigated in laboratory and field experiments with filters and impactors (Wang and John, 1988).

The impaction efficiency (η) for particles depends on the particle aerodynamic diameter (D_a), the flow velocity of the air (V) and the particle density (ρ); it varies inversely with the gas viscosity (μ) and a parameter dependent on particle diameter (D_b) e.g. for impactors in which particles pass through a slit or opening and are captured by a plate-typed collector D_b is the slit width (McKetta, 1997).

$$\eta = D_a^2 V\rho / 18\mu D_b \qquad \textbf{(1.1)}$$

Cascade and virtual impactors are widely used impactors. Cascade impactors consist of a series of consecutive stages connected in parallel. The diameters of the nozzles or slits above each impactor plate become increasingly smaller as the air moves through the impactor so that the air moves increasingly faster through these orifices and smaller and smaller particles impact on the plates. Impactors can fractionate aerosol particles from 0.05 - 30μm.

The Anderson impactor is a cascade impactor that is commonly used to investigate those fractions of aerosol particles that interact with the lung. The different stages of the impactor can be related to different stages of the human respiratory system. Because lung deposition and dry deposition of particles larger than 0.5 μm depend on aerodynamic size, data from these instruments provides direct information on such aerosol effects (McMurry, 2000).

A Micro Orifice Uniform Deposit Impactor (MOUDI) collects particles down to 0.056 μm and gives a uniform particle deposition on each plate. Uniform deposition is achieved using a number of nozzles above each stage and rotating the plates beneath the nozzles.

The virtual impactor is a modified type of impactor where the sampled airstream impacts against a mass of still air rather than against a plate. The inertia of the particles carries them into a still air mass, which is slowly drawn through a filter to collect the particles.

A Tapering Element Oscillating Microbalance (TEOM) and a Beta-particle attenuator are automated methods for measuring collected particles. They provide an alternative method to gravimetric techniques. The TEOM operates by measuring the frequency of mechanical oscillation of an element such as a tapered glass tube. The frequency of oscillation is directly proportional to the mass of the tube. A beta-particle attenuator measures the reduction in intensity of beta particles passing through a filter containing particles. A change in attenuation reflects the concentration of the sampled particles. For some particles the attenuation of beta particles is directly dependent on the mass of particles deposited. Both instruments are operated downstream of a size selective inlet e.g. PM_{10} or $PM_{2.5}$ inlet.

1.3.2. Number concentration

There are several instruments available that measure the number concentration of atmospheric aerosols. Some of these instruments measure the number of particles present that can act as CCN. CCN are dependent on the particle physical properties

such as size and composition. CCN particle counters operate through saturating particles with butanol or, more recently, with water causing them to grow in diameter. These particles are then counted by measuring the pulses of scattered light by a single droplet as it passes through the viewing volume. Important design features of CCN counters include a range of saturation ratios for which information can be achieved. This is the method used for determining the relationship between CCN concentrations and saturation ratio, and the particle growth time. CCN measurements are of central importance in determining the influence of anthropogenic particles on the atmosphere. For example, a significant fraction of the sulphate aerosol production in the atmosphere occurs in cloud droplets (Schwartz, 1988), and particulate pollution may increase cloud albedo, thereby decreasing the Earth's net incoming radiative energy (Twomey, 1991; 1984) . In order to develop valid models for such phenomena, it is necessary to understand the relationship between atmospheric aerosol properties and the number and size of cloud droplets that can be produced from them.

An Optical Particle Counter (OPC) is an instrument used to count and size particles of larger diameters and operates by detecting the scattered light from individual particles and relating the scattered light signal to the particle diameter. An example of an optical particle counter is a GRIMM (series 1.100) instrument. The principle of these instruments is to illuminate the particles with a light source such as a monochromatic laser, and measure the light scattered at a particular angle. It should be noted that the size quantity measured by these instruments, the optical diameter (D_o) is dependent on a particle's refractive index, geometry and internal structure, in addition to its physical size. This technique can provide accurate number concentrations with a very high time resolution and a degree of size information that is calculated from the peak scattering intensities. These instruments are normally calibrated by measuring fabricated particles of known sizes but scattering intensities of spheres can be predicted based on Mie Theory. The OPC is best suited to measuring particles of spherical shape because irregular particle shapes can generate unpredictable results, although some instruments can derive extra data on particle shape by simultaneously measuring the scattering intensities at multiple angles (Kaye *et al*, 2000).

Other techniques available for sizing particles include those that measure the particle size based on the mobility of charged particles in an electric field. These instruments are known as electrical mobility analysers. A widely used electrical mobility analyser is a Differential Mobility Analyser (DMA).

An Aerodynamic Particle Sizer (APS) is an instrument used to measure the aerodynamic diameter of single particles. The time-of-flight of single particles passing through the instrument is measured as they scatter radiation from two continuous wave lasers set a known distance apart. The time-of-flight of each single particle is used to calculate its aerodynamic diameter. These instruments are capable of sizing particles from 0:5 μm up to 20 μm.

Recently, instrumentation has been developed to allow freshly nucleated particles from 1 nm in diameter to be sized. The instrument consists of an atmospheric inlet attached to a time-of-flight mass spectrometer that allows the size selection of charged particles from atoms and nano-particles to particles of almost unlimited size (Von-Issendorff & Palmer, 1999; Leung *et al*, 2005).

Scanning Electron Microscopy (SEM) and Transmission Electron Microscopy (TEM) are microscopic methods that can provide information on single particles in the atmosphere. Through the use of these methods it has been discovered, amongst other things, that remote marine particles contain internal mixtures of silicates and sea-salt due to cloud coalescence (Andreae *et al*, 1986). More recently improvements of these microscopic techniques have allowed simulations of atmospheric reactions with particles in real-time using an Environmental Scanning Electron Microscope (ESEM). This instrument is ideal for studying the morphological changes in the aerosol particle during reaction. This instrument is operated at atmospheric pressure and allows 5 nm resolution imaging of systems like crystals dissolving in water, living biological surfaces and vapour-deposited growth of particles (Laskin *et al*, 2003).

1.4. Aerosol Mass Spectrometry

A lot of research has been carried out using impactor or filter based measurements. These methods provide information on both particle size and chemical composition but the information are based on bulk analysis techniques and can often lead to misinterpretation of the sampled aerosols. The need to provide single particle information has led to the development of a number of techniques that allow the size and chemical composition of individual particles to be analysed.

Aerosol mass spectrometry is a growing area with a large number of different instruments available for exploring the physical and chemical properties of aerosol particles. All aerosol mass spectrometers can be classified under four headings; sample introduction, particle detection and sizing techniques, ionisation techniques and mass spectrometry types.

1.4.1. Inlets

Particles are drawn through an inlet into an aerosol mass spectrometer from atmospheric pressure. The inlet controls the size range of particles that will eventually be focused into a particle beam. The inlet plays an important role in the detection and analysis of ambient aerosols and for this reason needs to be carefully considered when designing aerosol instrumentation.

Inlets can be described using the theory of particle motion in a gas which is based on the continuum approximation. The Knudsen number gives a measure of the validity of the continuum approximation,

$$Kn = \frac{2\lambda}{d_p} = \frac{2}{d_p}\left[\lambda_r\left(\frac{760}{P}\right)\left(\frac{T}{298}\right)\left(\frac{1+110/298}{1+110/T}\right)\right] \qquad \textbf{(1.2)}$$

where λ is the mean free path of the surrounding gas (air), d_p is the particle diameter, λ_r is the mean free path of air at standard temperature and pressure, *P(Torr)* is the pressure of the surrounding gas and *T(K)* is the temperature of the surrounding gas. If the mean free path is much smaller than the particle diameter, then $Kn << 1$ and the continuum approximation is valid. In the slip flow regime, the mean free path is of

the order of the particle diameter ($Kn \approx 1$) and significant changes in particle flow properties are observed (Baron & Willeke, 2001).

Whether particles follow gas streamlines or depart from them is determined by the Stokes number (St). If $St << 1$, then particles follow the gas streamlines. If $St >> 1$, then particles may depart from the gas streamlines and maintain their trajectories. If $St = 1$, then particles are tightly focused along the centreline of a gas stream as it expands through an orifice. For an aerosol flowing through an orifice, the Stokes number is,

$$St = \frac{\rho_p d_p^2 U C_C}{9\eta D_0} \tag{1.3}$$

where ρ_p is the density of the particle, d_p is the particle diameter, U is the gas velocity at the orifice, C_c is the Cunningham correction factor which takes into account non-continuum effects when the particle size approaches the mean free path, η is the gas viscosity and D_o is the diameter of the orifice (Baron & Willeke, 2001). A good approximation of the Cunningham correction factor for all values of Kn is given by, (Mallina *et al*, 2000).

$$C_c \approx 1 + 1.66Kn \tag{1.4}$$

Several different inlet designs are available for use in aerosol mass spectrometers. These inlets may focus particles of only one diameter or a range of diameters.

An orifice inlet is the simplest type of inlet and only allows particles with diameters where $St = 1$ to be focused along the centreline of the instrument. Different particle sizes can be selected in some orifices by controlling the gas pressure upstream of the orifice (dynamic orifice inlet).

A capillary inlet is described using two Stokes numbers, one at the inlet and one at the outlet. For this reason capillary inlets are capable of efficiently transmitting a broader range of particle sizes than orifices. At the capillary entrance particles with $St << 1$ follow gas streamlines into the capillary whereas particles having $St >> 1$ either do not enter the capillary or become deposited on the walls of the capillary. At the exit only particles having $St >> 1$ continue along their trajectories and enter the mass spectrometer region. A pressure drop along the capillary causes the C_c and St to

increase. As a result particles of a range of diameters may be focused as they simultaneously achieve St <<1 at the capillary entrance and St >>1 at the exit (McMurry, 2000).

A third type of inlet available for use in aerosol mass spectrometers is an aerodynamic lens. These are circular apertures that operate under the same principle as an orifice except that the pressure drop across the lens is negligible. Figure 1.5 illustrates how the apertures become successively smaller in diameter and eventually terminate in a capillary. Since all of the lenses operate at approximately the same pressure the Stokes number of a given particle diameter varies according to the aperture diameter. A flow-limiting orifice at the entrance of the lens system sets the pressure to an optimum value for the size range to be focused.

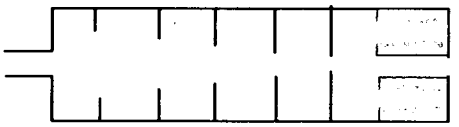

Figure 1.5. Schematic diagram of an aerodynamic lens

Rapidly changing environments of both temperature and pressure are encountered by particles as they pass through an inlet. In aerosol mass spectrometers, condensation of semi volatile species present on particles is usually induced by gas expansion from the inlet. The temperature decrease generated by expansion and the short transit time to analysis (< 1 ms) inhibits evaporative losses. It is thought that aqueous droplets become super-cooled or freeze. Water vapour provides the greatest opportunity for condensation since it is present in such a large amount in the atmosphere (Mallina *et al*, 1997).

Density and particle morphology also play a large role in aerosol mass spectrometry. Density (ρ_p) can greatly affect the aerodynamic diameter of particles. Particles with the same geometric diameter (d_p) have significantly different aerodynamic diameters (d_a) as illustrated in Equation 1.5.

$$d_a = \sqrt{\rho_p d_p} \qquad \textbf{(1.5)}$$

All calculations describing how particles are focused by the inlet assume that all particles are spherical. Particles with irregular shapes often have reduced efficiency of aerodynamic focusing relative to spherical particles (Liu *et al*, 1995a; 1995b).

1.4.2. Particle detection

The size of ambient particles is crucial as many chemical and physical properties as well as particle behaviour depend on size. Also, in combination with chemical composition, the size of particles can provide information of their source characteristics and on any secondary reactions the aerosol may have undergone. With regard to health effects, the size of particles determines how the respiratory tract will be affected with smaller particles penetrating deeper than coarser particles.

Many if not all aerosol mass spectrometers are capable of sizing each individual particle or size selecting individual particles before chemical analysis takes place. In aerosol mass spectrometers that employ laser desorption ionisation (LDI) to produce ions for analysis, it is required that there is some method of detection in order to trigger the laser to fire unless it is already chosen to free fire the laser.

Many aerosol mass spectrometers use the size determination as a method of detecting particles in the instrument. Two broad categories of mass spectrometers exist, those that use pulsed laser ablation to determine chemical composition and those that vaporise particles that impact on a filament.

Instruments that collect particles on a filament before vaporising them use time-of-flight measurements of the particle travelling from a beam chopper to a particle detector to carry out the size analysis. The detection process is sufficiently sensitive to be able to detect single particles as small as 50 nm, so that the number of particles can be determined as a function of particle size (Jayne *et al*, 2000).

For those instruments that acquire chemical information through the use of a pulsed LDI, coordinating the particle arrival into the ablation region with the triggering of the pulsed laser can be difficult (McMurry, 2000). In the LDI instruments that are

currently available a number of different arrangements are used. These are illustrated in Figure 1.6.

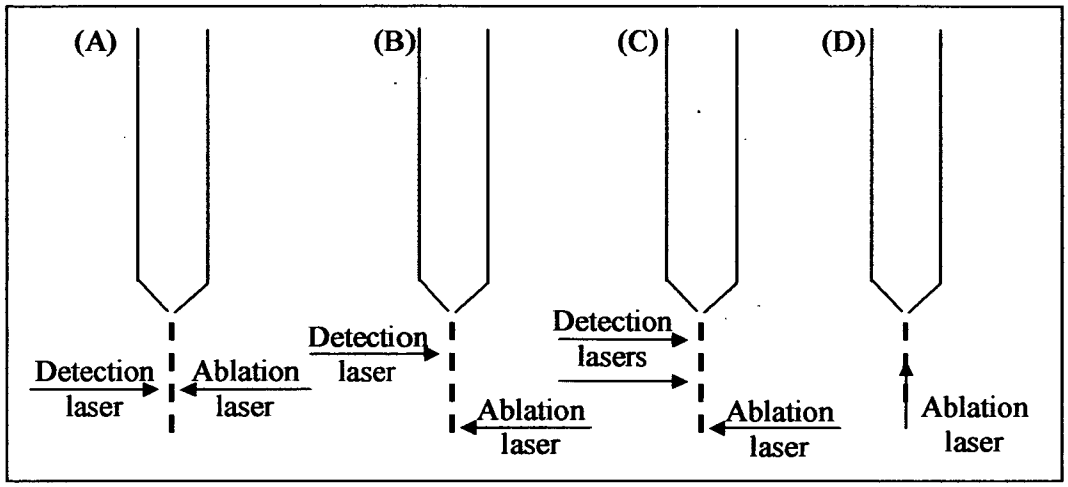

Figure 1.6. Configurations for detecting and ablating particles in a mass spectrometer (McMurry, 2000).

Figure 1.6 (A) explains the method that is used for an aerosol mass spectrometer that has been employed in both field and aircraft measurements (Mckeown *et al*, 1991). This setup requires that particles travel though the centre of the instrument and intersect a continuous laser beam. The resulting scattered signal is used to determine the optical diameter of the particle and at the same time it triggers an excimer laser to fire and ablate the particle. The time between the light scattering signal and the triggering of the excimer laser is less than 1 μs which ensures that the particle does not move too much. This technique allows the detection of particles of all different diameters and because a continuous laser beam in the red region is used it ensures that particles with diameters as small as 200-300 nm can be analysed. The disadvantage to this instrument is that it acquires information on the optical diameter of particles which is strongly dependent on particle morphology and chemical composition.

The second type of detection set up is illustrated in Figure 1.6 (B). This set up incorporates velocity measurements to size and ablate the particle and therefore measures the aerodynamic diameter of the particle. A particle is detected by the detection laser and a set time later the ablation laser is fired and ablates the particle.

The time required for the laser to fire is user defined and is pre-selected for particles with a certain diameter. This instrument has a compact design but can only measure one particle diameter at a time. A similar set up is shown in Figure 1.6 (C) but this time two detection lasers are used (Yang *et al*, 1996; Salt *et al*, 1996). This setup has proven accurate in sizing a range of particle diameters using two detection lasers. The velocity of the particles travelling through these two lasers is relayed to the ablation laser which is triggered at a certain time related to the velocity of each particle. The disadvantage to this set up is that it is a larger and more complex design. The aerosol mass spectrometer described in this thesis has a set up similar to that shown in Figure 1.6 (C).

The final type of setup allows the analysis of all particles that are transmitted by the inlet. As there is no method built into the instrument to size the particles a DMA is used prior to the instruments inlet and is used to preselect the particle diameter to be sampled. This setup is good because it has a compact design and is not limited to particle sizes that scatter light so particles with diameters as small as 10 nm can be analysed. A disadvantage associated with this setup is similar to the one for instruments with a setup similar to that in Figure 1.6 (B) in that only a subset of particles is examined at any one time.

1.4.3. Ionisation methods and different instruments

A number of ionisation techniques have been applied to aerosol mass spectrometry. These include Laser Ablation Microbe Mass Spectrometry (LAMMS), Secondary Ion Mass Spectrometry (SIMS), surface or thermal, Electron Impact (EI) and Laser Desorption Ionisation (LDI).

1.4.3.1. Laser Ablation Microbe Mass Spectrometry (LAMMS)

LAMMS provides information on single particles. Particles are collected on a filter or substrate and subsequently irradiated with a tightly focused (0.5 μm) high-powered pulsed laser. The ejected ions are then analysed by mass spectrometry. Detection limits of a LAMMS instrument are at ppt levels. It is capable of speciating inorganic compounds including nitrates and sulphates and can also detect trace

organic species. A disadvantage to LAMMS is that it is offline which occasionally leads to a considerable delay between sampling and analysis. It is also a technique that exposes particles to a vacuum which results in significant evaporative losses and alteration of particle composition by chemical reactions occurring prior to analysis

1.4.3.2. Secondary Ion Mass Spectroscopy (SIMS)

SIMS uses an ionisation process in combination with a microscope such as a SEM (Christie *et al*, 1981) to obtain detailed surface analysis. The instrument is made up of two mass spectrometers. One spectrometer focuses a mass-analysed primary ion beam (Ar^+, N_2^+,Cs^+ or O_2^+) onto the sample surface which forms secondary ions by various sputtering processes. The sputtered ions are collected by an extraction electrode and directed by an electrostatic lens into a mass spectrometer (Christie *et al*, 1981). SIMS has also been used as a surface analysis tool for depth profiling measurements, with depth resolution between 50-100 Å achieved (Wittmaack, 1995).

LAMMS and SIMS provided a great deal of information on ambient single particles but they still required particles to be collected on a filter and taken to a laboratory. The development of mass spectrometry instrumentation that could size and determine the chemical composition of individual particles using high time-resolved techniques allowed more studies of anthropogenic and natural aerosols to be carried out over longer time periods. Due to the mobility of many of these instruments, studies investigating PM in the upper troposphere as well as PM over the ocean could be studied in near real-time. Some of the most widely used instruments are discussed below under two categories depending on the method of characterising particles (thermal ionisation or laser ablation).

1.4.3.3. Surface/Thermal ionisation mass spectroscopy

Surface/Thermal ionisation mass spectroscopy was first described by Davis (1973) using a surface ionisation magnetic sector mass spectrometer. The technique involves a heated metal surface to produces ions.

Significant improvements and advances have been made since Davies (1973) first introduced the instrument. A full account of these can be found in Suess and Prather (1999). A commonly used instrument that applies surface ionisation is the Aerodyne Aerosol Mass Spectrometer (AMS) described by Jayne *et al.* (2000). The instrument is capable of providing quantitative particle size and composition measurements.

The AMS consists of three major parts: a particle beam generation inlet system, an aerodynamic sizing chamber, and a particle composition detection section. Particles are sampled through an aerodynamic inlet that provides a narrow beam of particles. As the air containing the particle beam expands into the vacuum at the end of the inlet, the particles are accelerated, with smaller particles attaining higher speeds and vice versa. The beam of particles entering the sizing chamber is chopped to provide a time-of-flight measurement for the time taken for a particle to reach the detector, from which the particle size can be determined. The particle then collides with a heated surface that flash vaporises volatile and semi-volatile components. The vaporised species are subsequently ionised by electron impact and a quadrupole mass spectrometer records mass spectral signals. The quadrupole mass spectrometer is only capable of collecting one mass value for a single particle or scanning the full mass spectral range for an ensemble of particles. More recently a time-of-flight mass spectrometer has replaced the quadrupole mass spectrometer and allows the full mass spectral pattern to be recorded. This instrument is capable of providing quantitative information on important volatile and semi-volatile species present in the atmosphere such as ammonium sulphates and nitrates. Aerosol Mass Spectrometers (AMS) have most commonly been operated using a quadrupole mass spectrometer.

The Aerodyne AMS has been used in a large number of rural (Longley *et al*, 2003; Alfarra *et al*, 2004), urban (Topping *et al*, 2004) and aircraft (Bahreini *et al*, 2003) studies. To date, all of these studies have been focused on providing quantitative information on the non-refractory component of the atmosphere. As the AMS is not limited to light scattering techniques it is capable of investigating particle sizes as small as 50 nm. Several studies have investigated new particle formation or nucleation events using the AMS (McFiggans *et al*, 2004). Recently laboratory

studies have been carried out using the AMS in conjunction with smog chambers and other instrumentation to investigate secondary organic aerosol formation (SOA) (Baltensperger *et al*, 2005).

Improvement in instrument characteristics has been the focus of recent research and several research papers were presented at the European Aerosol Conference (EAC 2005). Using a quadrupole mass spectrometer does not allow the full mass range of each particle to be recorded. Changing the quadrupole mass spectrometer to a time-of-flight mass spectrometer will allow the AMS to obtain quantitative single particle analysis. DeCarlo *et al.* (2005) presented a high time resolution time-of-flight AMS with mass resolution up to 5000 a.m.u. Recently this instrument has been deployed in the field (Drewnick *et al*, 2005). Methods are also being developed using softer ionisation techniques within the AMS instrument as electron impact causes substantial fragmentation and makes identifying certain organic chemical species difficult. Northway *et al.* (2005) described how vacuum ultraviolet photo-ionisation and Li^+ ion attachment were employed in the AMS. Less fragmentation of organic species were reported but at the expense of sensitivity. An AMS instrument has also being developed incorporating an ion trap into the instrument (Kurten *et al*, 2005). An advantage to this is that reactions of gaseous species with single particles can be investigated.

A similar approach to the measurement of a continuous beam of volatile and semi-volatile particles with diameters as small as 20 nm is an aerosol particle mass spectrometer. In this instrument particles are sized using a DMA prior to the aerodynamic lens (Tobias *et al*, 2000). This instrument has also been deployed in ambient studies (Kulmala *et al*, 2004) and has been used in a number of studies to investigate diesel exhaust characteristics (Smith *et al*, 2004).

1.4.3.4. Laser Desorption Ionisation (LDI)

LDI coupled with mass spectrometry was first described by Sinha (1984). In this instrument a quadrupole mass spectrometer was used. Significant development has occurred since then. Suess and Prather (1999) give a detailed review of the

progression of LDI since it began in 1984. The most pronounced improvement on early techniques was coupling the LDI with time-of-flight mass spectrometry to allow the entire mass range of each particle to be analysed (Mckeown *et al*, 1991). The first deployment of a LDI-TOF-MS for ambient measurements was described by Hinz *et al.* (1994). Since then several new generation instruments have been developed by different research groups (Carson *et al*, 1995; Nordmeyer & Prather, 1994; Murphy & Thomson, 1995). The layout of each instrument differs slightly depending on its intended application but they all remain fundamentally the same and consist of three basic components; aerosol inlet, particle detection and sizing region and a mass spectrometer. The aerosol inlet and particle detection regions and how they differ for different instrument set-ups have already been explained in Section 1.4.1 and 1.4.2.

The instruments can be separated into two broad categories. One type relies on pre-selecting a narrow size distribution of particles for analysis and randomly firing a laser (Reents *et al*, 1995) and the second type uses light scattering to measure the particle size to generate a trigger to fire the interrogating laser synchronously with the particles arrival in the mass spectrometer (Gard *et al*, 1997; Zelenyuk & Imre, 2005).

An example of a mass spectrometer that uses a randomly firing laser is the Real time Size Mass Spectrometer (RSMS). It is a transportable field instrument that allows the detection of particles down to 10 nm. The RSMS instruments perform single particle analysis on-line. Particles are drawn into a nozzle, which aerodynamically focuses them to the centreline and removes the gas. The RSMS instrument aligns an excimer laser and the particle beam collinearly and free-fires the excimer laser so that particles are hit randomly. The TOF mass spectrometer is designed to analyze ions from a 4 cm source region so that the probability of hitting particles is about 2%. A DMA instrument is often operated with this instrument to determine particle size prior to analyzing particle composition. This instrument has been used in a large number of field campaigns (Tolocka *et al*, 2004).

The instrument used for the work described in this thesis uses particle velocity to size each individual particle and also to trigger the LDI laser to fire. The instrument is a commercial version of the original Aerosol Time-Of-Flight Mass Spectrometer (ATOFMS) described by Gard *et al.* (1997) and was purchased from TSI Inc. A detailed description of the instrument and how it works can be found in Chapter 2. An overview of the instrument is presented here.

Air is sampled from the atmosphere through a differentially pumped aerodynamic nozzle to produce a collimated beam containing the particles which then passes two orthogonal laser beams separated by a known distance (~ 6 cm). Scattered light from a particle actuates a timing circuit and the transit time yields an aerodynamic diameter of the particle. The particles pass through a mass spectrometer section where they are ablated and ionised in the focus of a pulsed UV laser at 266 nm. The LDI is triggered by the same timing circuit used to size the particles. The mass to charge (*m/z*) ratios of both positive and negative ions produced are determined simultaneously in two time-of-flight reflectron mass spectrometers.

The ATOFMS instrument has been deployed in field campaigns all over the world (Guazzotti *et al*, 2003; Liu *et al*, 2003; Beddows *et al*, 2004; Dall'Osto *et al*, 2004) and continues to be widely used to investigate the composition of single particulate matter. Results from a field campaign in which the ATOFMS was deployed at Mace Head, Ireland are presented in Chapter 4 of this thesis. Recently a number of research experiments have been carried out using the ATOFMS in an attempt to characterise and determine specific fingerprints for different vehicle emissions (Sodeman *et al*, 2005; Gross *et al*, 2000b). Results have shown that although the ATOFMS is capable of producing fingerprints from heavy duty vehicles and other means of transport these fingerprints can be strongly influenced by weather conditions (Gross *et al*, 2005).

Heterogeneous gas/particle chemistry can be monitored in near real-time using the ATOFMS instrument. Gard *et al.* (1998) monitored heterogeneous chemical reactions between sea-salt and gas phase nitric acid leading to sodium nitrate

production in the particulate phase. Laboratory measurements investigating heterogeneous aging of natural particles have recently been studied using a flow tube with an ATOFMS. Sea-salt and mineral dust were reacted with nitric acid and it was possible to distinguish which particle type accumulates the most nitric acid (Sullivan *et al*, 2005).

The commercial ATOFMS (TSI 3800) is capable of accurately sizing particles between 0.3 and 3 μm, although 100% transmission efficiency is not achieved over this region and correction factors need to be applied to the raw ATOFMS data in order to correct for this. A scaling factor correcting for the ATOFMS transmission efficiency has been developed using conventional sizing instrumentation using raw data acquired during a rural sampling campaign and is explained in Chapter 5.

More recently improved detection efficiency of the ATOFMS instrument has been achieved using a aerodynamic lens (Su *et al*, 2004). The aerodynamic lens attachment allows the ATOFMS instrument to detect particles as small as 30 nm. As the particles focused by the aerodynamic lens are too small to scatter light at the wavelength employed by the two CW lasers (532 nm) it is not possible to use light scattering to aerodynamically size the particles as the particles diameters are less than the wavelength of the two sizing lasers (532 nm). Therefore the LDI is free-fired and particle sizes are pre-selected using a DMA/ or other particle sizing instrumentation prior to the aerodynamic inlet. More recently other groups have developed their own aerosol time-of-flight mass spectrometer (Erdmann *et al*, 2005). These instruments are based on the original ATOFMS design, differing only in the wavelengths of the lasers used, and are known as the Single Particle Analysis and Sizing System (SPASS).

The laser desorption ionisation technique gives rise to a considerable variation in mass spectral signatures even for nominally identical particles. This is mainly due to the pulse-to-pulse variations in the laser pulse. Also the laser pulse used in the ATOFMS instrument has a Gaussian profile so it is possible that different particles will interact with different regions of the laser and therefore absorb different

quantities of laser energy. Modifications have been made to the ATOFMS instrument to enable it to produce more reproducible spectra. Wenzel & Prather (2004) and more recently Steele *et al,* (2005) have demonstrated that flat top laser profiles can be achieved through the use of either optic fibres or extra-cavity optics.

This pulse-to-pulse variation in laser energy makes quantification of ions formed using LDI difficult. Several attempts of quantification of ATOFMS data have been attempted using data from mass impactor measurements (Bhave *et al*, 2002; Fergenson *et al*, 2001). A similar procedure is described in Chapter 5 where quantitative scaling factors are developed for Na^+, K^+ and Cl^-.

Alternatively Morrical *et al.* (1998) used a two-step LDI process with the ATOFMS. Their results showed that reproducible mass spectra could be obtained as well as obtaining more detailed molecular information from each particle. Woods *et al.* (2001) also employed two-step LDI and reported that quantitative information could be achieved using laser-based systems. More recently Zelenyuk and Imre (2005) describe a new aerosol time-of-flight mass spectrometer, the Single Particle Laser Ablation Time-of-Flight Mass Spectrometer (SPLAT). This instrument is slightly different to the SPASS and ATOFMS in that it employs two lasers to vaporise and then ionise each particle. By decoupling desorption from ionisation, the two laser method provides added flexibility of allowing both the laser power and wavelength to be optimised independently.

Moffet and Prather (2005) showed that by measuring the scattered light signals obtained by the ATOFMS sizing lasers in the particle detection and sizing regions it was possible to obtain density and refractive index information on each particle. This information could eventually be used to test assumptions in current global climate models regarding how particle mixing state impacts aerosol optical properties. It is also hoped that the density and morphology information will facilitate the transformation of particle number concentration to mass concentration.

Other research groups have modified the ATOFMS instrument to allow for the detection of single bio-aerosols. Van Wuijckhuijse *et al.* (2005) described a new ATOFMS instrument that combines laser-induced fluorescence selection and Matrix Assisted Laser Desorption Ionisation (MALDI) to detect and analyse single bio-aerosols in real-time. The detection and analysis of bio-aerosols may help prevent potentially large-scale disease (Gard *et al*, 2005). Other research groups have used LDI mass spectrometry to study bio-aerosols. In one study an ion trap mass spectrometer was used to record positive and negative ion mass spectra from bacteria (Gieray *et al*, 1997).

LDI has been used in MALDI for a long time to characterise proteins. Although the technique is well established the method by which positive and negative ions form after interacting with the laser beam is less well understood (Kruger & Karas, 2003; Knochenmuss & Zenobi, 2003). Laser ablation of alkali salts is explained in Chapter 3 and several mechanisms for the formation of ions with an emphasis on negative ion formation are suggested.

1.4.3.5. Other single particle analysis techniques

Another interesting technique for determining the chemical composition of atmospheric particles is a Single-Particle Raman Spectrometer (SPaRS) for the non-destructive chemical characterisation of aerosols. This is a new system that is designed for the analysis of single levitated micron sized particles. Raman scattering can give information on light scattering which can be used to determine particle size, shape, and physical structure. This system is still being developed although it has demonstrated its use in laboratory experiments (Greenaway *et al*, 2005).

The aim of this thesis was to evaluate the capabilities of a commercial ATOFMS instrument in a number of areas within aerosol research. This thesis covers the deployment of the ATOFMS instrument for environmental sampling campaigns which examines both anthropogenic and natural aerosols (Chapter 4 + 6). The interaction between aerosolised drug particles and how it affects the efficiency of respiratory drugs was examined using the ATOFMS in Chapter 7. Fundamental interactions between laser light and single particles that resulted in the formation of

positive and negative ions were investigated for alkali salt particles (Chapter 3). Also included are methods that correct for the ATOFMS transmission bias as well as scaling efficiencies to obtain high time resolved quantitative information (Chapter 5).

Chapter 2

Experimental

Chapter 2 Experimental

2.0. Introduction

The data for the experiments described in this thesis have been acquired through the use of an ATOFMS. This chapter explains the design and operation of a commercial ATOFMS. Explanation of how aerosol particles were formed in laboratory experiments have also been detailed along with a brief discussion of the data handling of single particle mass spectra.

2.1. The Aerosol Time-of-Flight Mass Spectrometer (ATOFMS)

The ATOFMS instrument can be roughly divided into 2 main sections, the instrument and its controls. The instrument section can be further divided into 3 regions, (a) an interface region (particle sampling), (b) a particle sizing region and (c) a mass spectrometry region, which are described in Section 2.1.2-2.1.4.

2.1.1. General Design Features.

Figure 2.1 is a photograph of the field transportable commercial ATOFMS instrument purchased from TSI. The ATOFMS instrument is 170 cm x 74 cm x 130 cm (length x width x height) and weighs approximately 345 kg. The frame is composed of extruded aluminium beams that are bolted together. This frame is designed to support the weight of the instrument as well as pumps, electronics, and laser systems. The frame was constructed to act as a buffer from bumps during transport. As can be seen in Figure 2.1, the roughing pumps are mounted below the main body of the frame in order to lower the centre of gravity and make the instrument more stable. These pumps, along with the flight tube, are mounted on rubber shock absorbers to minimise the effects of vibration during transport and from the roughing pumps themselves. Mounted above the electronics is the main body of the instrument which includes the time-of-flight mass spectrometer, light scattering region, and particle interface. The computer controlling the instrument is located at

the bottom left hand side of the frame. The computer is linked to the instrument control box. MS-Control software (TSI) manages the electronic relays inside the control box to switch the instrument on and off.

The instrument was designed to be able to fit through normal doorways, thereby increasing the number of locations that can be easily accessed. It was fitted with 15 cm diameter pneumatic tyres for increased mobility and improved shock resistance. The tyres can be inflated completely to minimise rolling resistance when pushing the instrument onto a truck or into a building, and then partially deflated to increase the shock absorbing capabilities once put into the desired position. In addition the frame is strong enough that the entire instrument can be lifted, if necessary, by the frame.

Figure 2.1. A photograph of the ATOFMS (TSI 3800)

2.1.2. Interface region

The interface region consists of a capillary air inlet and nozzle, together with two regions of differential pumping through which the particles enter the ATOFMS system (Figure 2.2). Air and particles are drawn in through the air inlet at a rate of 0.9 l/min. The inlet nozzle is a convergent nozzle with a channel diameter of 340 μm and a length of 400 μm. It is responsible for the initial pressure drop from

atmospheric pressure to about 2 Torr* in the first vacuum stage of the particle sampling region. This initial pressure drop contributes to the formation of the particle beam to be analysed.

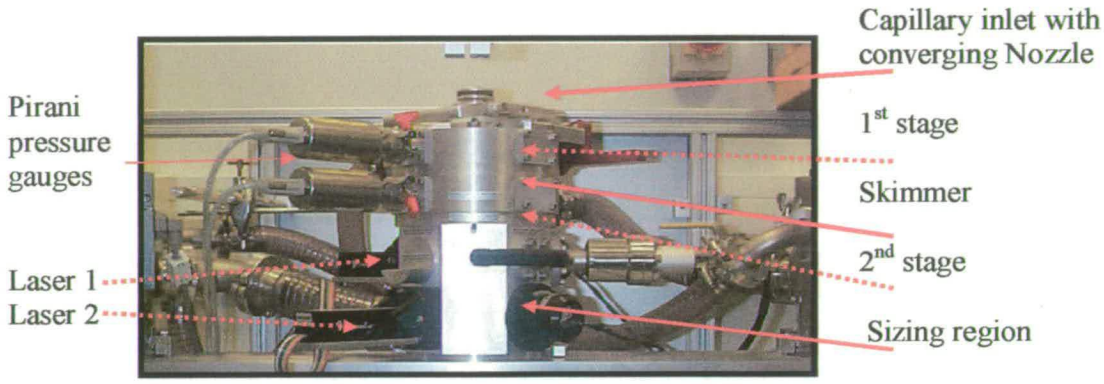

Figure 2.2. A photograph of the ATOFMS particle sampling and sizing region.

The region between the inlet nozzle and the first skimmer (first stage) is held at approximately 2 Torr by a mechanical rotary (roughing) pump. The first stage of the interface region is important for generating the velocity difference between particles of different aerodynamic diameter. The first skimmer effectively separates the first and second stage and is responsible for the pressure reduction between the two stages. The second stage is located between the first stage and the particle sizing region. This stage also provides a pumping port and a port for a Pirani pressure gauge. A second skimmer, located between the second stage and the particle sizing region, is used to maintain the pressure at about 10^{-4} Torr in the particle sizing region and to collimate the particle beam.

Pirani pressure gauges are used to measure the pressure on the first and second vacuum stages. The pressure is displayed on the pressure gauge controller and on the desktop of the MS-Control (TSI Inc.) computer screen.

The inlet nozzle of the ATOFMS can get blocked over time, particularly when high particle concentrations are being sampled and frequent cleaning is then required. Keeping the nozzle clean ensures that optimal particle expansion is occurring

* 1 Torr = 133 Nm^{-2}

through the interface. In order to facilitate cleaning of the inlet, a ball valve is incorporated into the interface. This allows the air inlet nozzle to be removed without having to vent the whole instrument to the atmosphere. A special lifting tool allows the air inlet nozzle to be removed more easily, and ensures that the nozzle barrel is not damaged, thus preventing misalignment or accidental reinsertion while the ball value is closed. It also has a built-in stop to ensure the nozzle cannot be withdrawn too far as this would break the vacuum seal before the ball valve was closed.

2.1.3. Particle Sizing Region

The particle sizing region (Figure 2.3) is located between the particle sampling region and the mass spectrometry region. It consists of two Continuous Wave (CW) lasers; two photomultiplier tubes (PMTs) and a timing circuit.

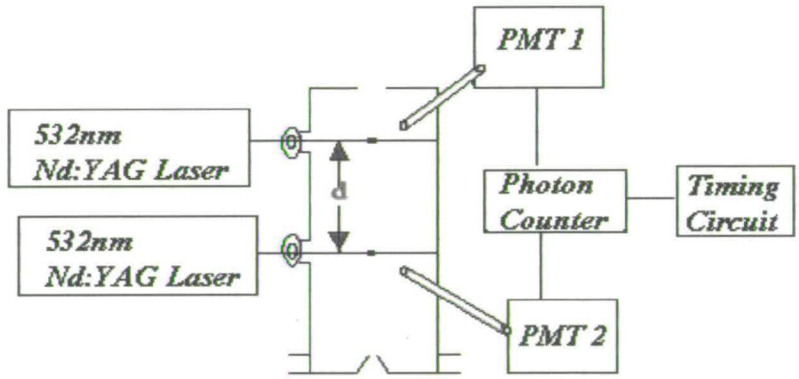

Figure 2.3. Schematic diagram of the ATOFMS particle sizing region

Once the particles pass through the second skimmer they enter the light scattering region where the particle velocity (calculated from the time it takes a particle to travel from one CW laser beam to the next) is used to determine the aerodynamic diameter of each particle using an internal calibration curve.

The particles are detected by scattering light from two CW diode pumped solid state Neodyium:Yttrium Aluminium Garnet (Nd:YAG) lasers. Each laser emits 50 mW of green laser light (532 nm). The light is introduced into the sizing region through beam probes. The beams are located orthogonal to one another so that only particles

travelling through the centre of the system will be measured. Particles passing through both scattering laser beams are therefore likely to make it to the ablation region.

The scattered light signal resulting from the interaction of individual particles with the CW lasers is focused on to the PMTs using ellipsoidal mirrors. The signal from the PMTs is sent to a timing circuit. The timing circuit starts a count up sequence when a single particle scatters light from the first CW laser. The count up sequence is stopped when the particle scatters light from the second CW laser beam. The time taken for the particle to travel from one CW laser beam to the next is used to calculate the particles velocity using an internal calibration. This velocity is then translated into an aerodynamic diameter. The particle's velocity is also used to determine the time that it will take for the particle to reach the centre of the source (ablation) region of the ATOFMS. The timing circuit signals the desorption/ionisation (DI) laser to fire ablating the particle and generating ions that are analysed by the dual-ion time-of-flight mass spectrometer.

The ultimate verification for the size of a given particle with the ATOFMS system is the acquisition of a mass spectrum. The mass spectrum can only be acquired if the time recorded by the timing circuit was not due to a coincidence error. A coincidence error occurs when a particle passes through the first laser, starting the count up sequence, and a different particle, either one moving faster and overtaking the initial particle, or a particle that is ahead of the initial particle but did not pass through the first laser, passes through the second laser. This type of error results in a recorded time that is shorter than the true time-of-flight of the particle that started the timing circuit count up. When a coincidence error occurs it causes the DI laser to fire either too early or too late, depending on which type of error occurs. Another type of error occurs when a particle passes through the first laser but does not pass through the second laser. Typically, another particle will pass through the second laser to stop the count but this will result in a time that is too long for the particle that started the count up sequence. This type of error is related to the divergent inlet nozzle of the ATOFMS.

The aerodynamic sizing region of the ATOFMS makes it possible to monitor rapid changes in particle size distributions in real-time. The ATOFMS aerodynamic sizing region has proven to be accurate in sizing particles in the range from 0.3 μm to 3 μm. This broad size range enables the ATOFMS system to cover a range of particle sizes found in the ambient atmosphere.

Size calibrations were preformed using PolyStyrene Latex spheres (PSL) in various sizes, ranging from 0.2 to 7 μm in diameter. These size calibrations were used to test the performance of the light scattering region and to generate a calibration curve. It was important to carry out size calibrations often in order to obtain correct size values for the sampled aerosols. Ideally size calibrations should be performed at least every two months or whenever the instrument is moved to a different sampling location.

A particle size calibration is performed by running a number of particles of known aerodynamic size through the instrument and recording their transit time between the two sizing lasers. The resulting set of data points is then fitted to a third-order polynomial function (aerodynamic diameter D_a versus transit time) and the resulting function is used to calculate the size of sampled particles. A third order function is used because it describes the actual size velocity relationship in the chosen size range very well (Figure 2.4).

Full details of how the two continueous szing lasers are aligned are outlined in the TSI user manual which can be found at http://www.tsi.com/documents/1930036A-3800.pdf on page 38 of Chapter 7.

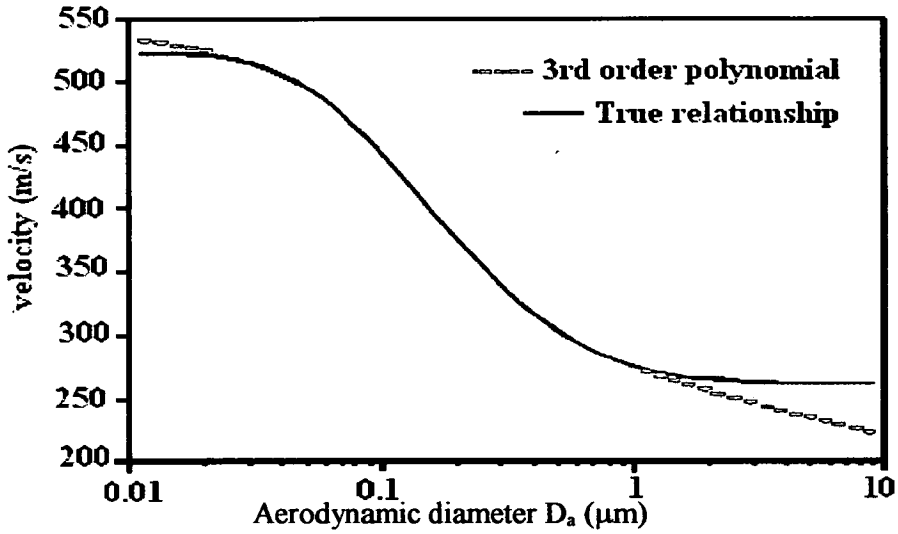

Figure 2.4 Shows an example of a size calibration. This Figure does not represent real data and has been taken from the TSI user manuel.

2.1.4. Time-Of-Flight Mass Spectrometer region

The mass spectrometry region is the largest part of the instrument. It provides information about the chemical composition of the single particles analysed. A schematic diagram of the mass spectrometry region is shown in Figure 2.4.

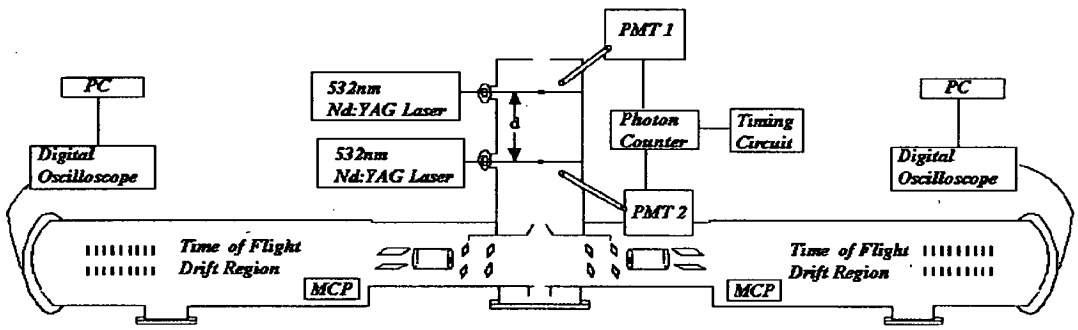

Figure 2.4. Schematic diagram of the ATOFMS mass spectrometer region with particle sizing region.

As the particle exits the light scattering region it passes through a conductance limiting tube. This tube serves two purposes; one is to act as a pumping conductance limit, in order to isolate the interface vacuum system and the time-of-flight mass spectrometer, while the other is to act as a charge shield for particles entering the

source. It was determined that excessive charge on a particle could cause sufficient deflection for the Nd:YAG laser to miss the particle (Morrical, 1999). Therefore, the conductance limiting tube shields the particle until it reaches the ion source.

Upon reaching the ion source, the particle is ablated and ionised by a Q-switched Nd: YAG laser operating at 266 nm. The laser light is directed into the ablation region by the UV laser optics. The laser head of the DI laser is mounted on the side of the mass spectrometer housing.

The Nd:YAG laser with a maximum output of 1 mJ/pulse and a pulse length of 5 ns is used for ablation and ionisation. The UV laser optics consists of two mirrors and a lens. The two mirrors can be adjusted to position the laser beam in the centre of the UV window. Two types of feedthroughs are used to provide the necessary potentials to the relevant parts of the mass spectrometer. Two turbo molecular pumps are used to pump the mass spectrometer region to ~ 10^{-7} torr. These pumps are specially manufactured to allow them to run upside down.

There is a UV laser energy probe mounted on the back side of the mass spectrometer housing. It measures the DI laser energy and also acts as a beam stop. The laser energy is measured for each shot and displayed on the laser energy meter. If a mass spectrum is detected, this value is displayed on the MS-Control desktop and saved with the mass spectral data.

The mass spectrometer system consists of an ion source, two microchannel plate (MCP) detectors, and two flight tubes with reflectron ion optics. This allows the detection of both positive and negative ions at the same time. The use of a non-scanning method and the simultaneous detection of ions of both polarities are important features application since particles are unique and you only get one shot at each particle.

Once the particle has been hit by the DI laser the positive and negative ions formed are extracted from the ion source and accelerated in opposite directions. Each side

has its own flight tube (reflectron and detector). The MCP detectors consist of two plates with small channels going through them. The diameter of the channels is about 25 μm. A potential of ~ 1800V is applied across the detector plates. When an ion hits the wall of one of the channels it releases a number of electrons. These travel further down the channel and hit the wall again, releasing a number of electrons again, and so on. This cascade of electrons finally exits the back of the detector and is accelerated towards a metal anode. When the electrons hit the anode, they create a pulse that is recorded by the data acquisition system.

During the DI event, ions can get additional kinetic energy from the rapid ablation process. Some ions travel in the direction that they are accelerated in and some ions travel in the opposite direction. This leads to a spread in ion energy. As a result of this, ions of the same *m/z* end up with different velocities which then lead to peak broadening, due to different arrival times at the detector. In order to correct for this a reflectron has been included in the instrument design. The reflectron consists of a number of parallel concentric electrodes to which a potential ramp is applied. When ions enter into the reflectron, they slow down, stop, turn around, and are accelerated out of the reflectron again. This reduces the spread in kinetic energy and leads to sharper peaks

2.2. Data analysis and manipulation

The ATOFMS instrument records and stores mass spectral information for each particle sampled. This information is stored on line using MS-Control software (TSI Inc.). For the experiments presented in this thesis mass spectra were usually collected in blocks, dependent on the number of particles sampled by the instrument. These data blocks varied from 1 hour to 6 hours for atmospheric measurements and up to one hour for laboratory experiments, depending on the total sampling time as well as the particle hit rate. The datasets were kept relatively small as large sets of data are difficult to analyse and the analysis is limited by the computer used (i.e. RAM, processor speed etc.). For all experiments and campaigns the data were analysed after collection using MS-Analyze software (TSI version 3.4.2). This acts as a front

end or graphical interface to Microsoft Access and has been specially developed to analyse and display results from the ATOFMS. MS-Analyze is important in the first stages of analysis and for calibrating the spectral data, as it allows one to become familiar with the total dataset. It displays a statistical summary of the data including hit rate, sampling time and the total number of particles sampled. It also displays the number of hit and missed particles as a function of aerodynamic diameter and as a function of time. Furthermore it has a built in search function which allows the user to search through the entire dataset for ion signals corresponding to certain chemical species.

Mass spectral calibration is accomplished by running a well characterised sample such as a solution containing a number of known inorganic ion salts of varying *m/z*. Alternatively, brake dust, where strong metal, carbon and inorganic peaks are observed over a wide range of *m/z* values can be used. A typical calibration would use the maximum number of peaks allowed by the software (~12) selected from a number of spectra. It is necessary to run a calibration file before sampling takes place as well as at regular intervals during sampling and again after sampling. This ensures that if mass spectral shift occurs in the dataset it will be identified by the different calibration files. This is especially important when sampling pharmaceutical datasets or other particle types with a high organic content which normally result in a high number of positive and negative ions as a result of extensive fragmentation.

Once the calibration is in place and checked against the whole dataset it is often necessary to further adjust the calibration to reduce small mass spectral shifts. A typical calibration curve is shown in Figure 2.5. The curve is described by the following equation (Equation 2.1):

$$m/z = (aT_f + b)^2 \qquad \textbf{(2.1)}$$

where T_f is the time-of-flight (2 ns/unit and 'a' and 'b' are constants. Using this equation the time-of-flight recorded by the mass spectrometer for a specific ion can be converted into an *m/z* ratio. The mass resolution of the TOF flight region is ± 0.5

m/z units which is not as high as some other commercially available instruments. This resolution becomes poorer as higher masses are analysed.

This is because of the relationship between m/z and Time-of-Flight (TOF) which is $m/z = K*t^2$, where K is a constant. When doing error analysis it is seen that $\Delta(m/z) = 2*K*t\ \Delta(t)$. If it is assumed that the error in the time measurements (Δ (t)) giving small m/z values is the same as that for large m/z values then from this relationship we see that the error in the m/z value, $\Delta(m/z)$ is proportional to t. What this means is that as larger m/z values are measured the error in the measurement goes up.

To improve the mass resolution at higher masses you can increase the length of the TOF tubes or/and decrease the velocity of the ions at the source in order to reduce the value of K which is given by $K = ((2*Vs*e)/(d^2))$.

In order to reduce the amount of error in the mass calibration it is necessary to ensure that the values used to calibrate the mass spectra are outside the range of values that need to be measured, i.e. make sure you interpolate and not exterpolate. Exterpolation on a second order polynomial can be quite erroneous (Beddows, D.C.S, personal communication).

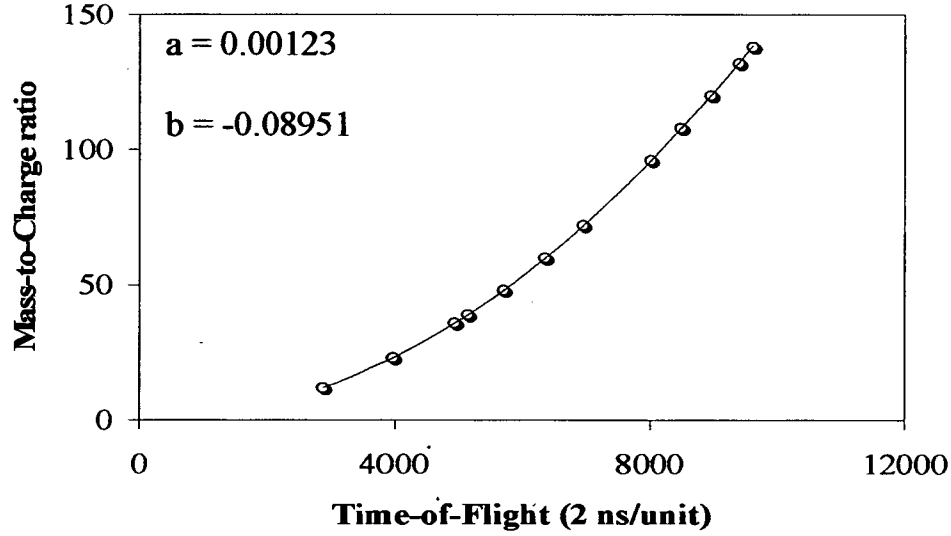

Figure 2.5. Positive calibration curve for converting time-of-flight values into mass-to-charge ratios.

Before establishing the major chemical components in the dataset it is necessary to select peak parameters that will differentiate the peak signals from background noise. This is important in order to make sensible classifications at a later date. Typical parameters used to define the peak baseline in this analysis were, 20 units above the baseline, 20 square units of area and greater than 0.002 as a fraction of the total area. These values were varied in order to obtain the optimum information from each dataset, particularly for the lab based studies. Once the calibration was in place and peak parameters were set, all particle spectral information was recorded into a Microsoft Access 2000 database. Once all the mass spectral information was recorded in MS-Access, MS-Analyze was used to confirm search criteria and results obtained from MS-Access. MS-Access was then used in conjunction with Microsoft Excel by designing queries to produce particle hit rates, compositional classification and temporal trends.

In some datasets where large numbers of particles were acquired it was necessary to incorporate statistical analysis techniques in order to provide an unbiased analysis of the data. Clustering techniques are the most commonly employed in single particle mass spectrometry and in this thesis a K-means clustering algorithm is used. Further explanation of the K-means clustering algorithm is provided in Chapter 4.0.

2.3. Aerosol Generation

During laboratory studies aerosols were generated using commercial air jet nebulisers (RESPIRGARD-II®). Air jet nebulisers employ the Bernoulli Effect to draw solution from a reservoir through a capillary to a region of low pressure induced by a high airflow. Figure 2.6 illustrates a common arrangement of an air jet nebuliser.

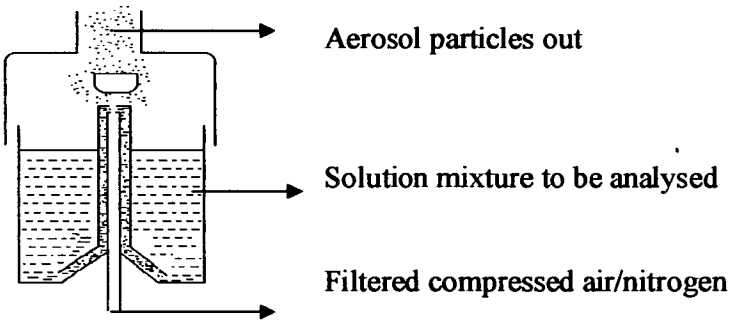

Figure 2.6. Schematic diagram of an air jet nebuliser.

Liquid aerosols are typically droplets of spherical shape. The air jet nebuliser operates to produce a thin film of liquid that breaks up into droplets. The air enters the nebuliser at a flow rate which depends on the diameter of the orifice and the pressure drop across it. The air expands and passes the mouth of the liquid inlet tube at high speed. A drop in pressure brings about the flow of liquid into the airstream. Acceleration of the droplets causes large ones to impinge on the walls of the nebuliser and return to the bulk solution with a decrease in the temperature of the solution. Water evaporation causes a continuous increase in the concentration of the solute in the liquid remaining in the nebuliser. The small droplets can evaporate to form a small particle of solute which is entrained in the airstream. These particles can be sized and an estimate of the initial droplet size (d_D) can be obtained from the relationship between the initial droplet size and the final particle size ($d\rho$) if the density of the droplet (ρ_D) and particle (ρ_p) and solution concentration (C, mass fraction) are known according to equations 2.2 and 2.3. The size distribution sized by the ATOFMS sizing lasers gave a distribution of 0.7 μm ± 0.2 μm sd.

$$\frac{1}{6}\pi d_p^3 \rho_p = C(\frac{1}{6}\pi d_D^3 \rho_D) \quad (2.2)$$

$$d_p = d_D (C\rho_D / \rho_p)^{1/3} \quad (2.3)$$

2.4. Aerosol drying

Drying of aerosol droplets was achieved using a laboratory made silica-gel dryer (Figure 2.7). Two concentric cylinders, formed by an inner wire screen cylinder and

a glass outer cylinder, contained the silica-gel. As wet aerosol flows through the inner cylinder, water vapour diffuses through the wire screen and is absorbed by the silica-gel. As the particles do not come into contact with the silica-gel, particle loss is minimised. In order to regenerate the silica gel it was placed overnight in an oven at 120°C.

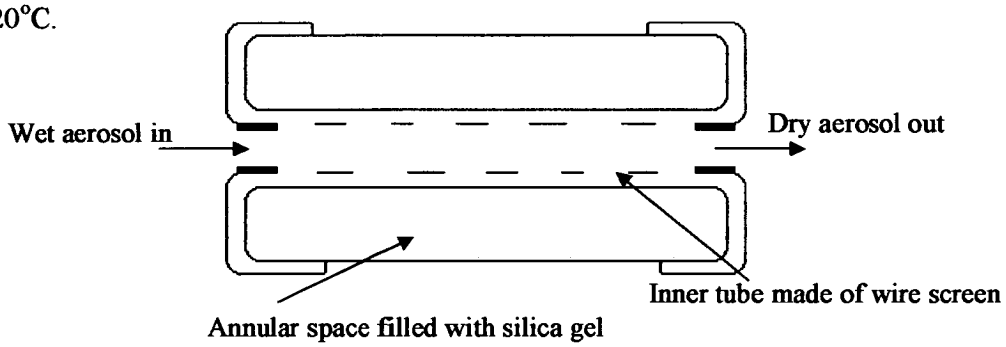

Figure 2.7. Schematic diagram of the cross section of the silica gel dryer

Chapter 3

Investigation of ion formation by UV laser irradiation of alkali aerosols using the ATOFMS

Chapter 3 Investigation of ion formation by UV laser irradiation of alkali aerosols using the ATOFMS

3.1. Introduction

Aerosol mass spectrometers enabling near real-time, size and chemical analysis of atmospheric particles have been developed by a number of different research groups (Sullivan & Prather, 2005). These instruments all require desorption and ionisation of some or all of the particle material (Chapter 1). In many instruments this is achieved by pulsed LDI using ultraviolet laser radiation (McMurry, 2000). To relate resultant mass spectral data both qualitatively and quantitatively to particle composition, a comprehensive understanding of the ion-formation processes is required. Although aerosol mass spectrometers are now extensively deployed to analyse ambient particles, almost no work has been done to interpret the main processes of negative ion formation in LDI systems.

LDI requires mechanisms for transfer of laser energy to the particle and for the disintegration and ionisation of the constituent material. In the late 1970's experimental investigations on particle disintegration were carried out on a 20 μm water droplet using a 10.6 μm laser (Kafalas & Ferdinand, 1973). Ablation and expansion of the front side of the particle followed by spallation of the backside of the particle was evident in the photographs. More recently Garrison and co-workers (Schoolcraft *et al*, 2000; 2001; Zhigilei & Garrison, 1998) have applied molecular dynamics simulations to particle disintegration following resonant absorption of ultraviolet light and showed that the particles undergo a rapid temperature rise with the formation of molecular and larger fragments in a number of picoseconds after irradiation. However, in both of these examples, the coupling of radiation to the particle was resonant.

Even in MALDI, a widely-deployed and closely-related experimental technique, the ion formation process(es) remains unclear. In a recent review Krüger and Karas (2003) stated there is clear evidence that typical MALDI analytes are already incorporated pre-charged, as defined by the solution pH, in the matrix crystal, i.e. that ions are preformed and an active ionisation step by charge transfer to neutral species is not required. These studies were carried out using organic indicator dyes to compare the original sample state in solution with the sample state in the matrix. It was reported that the sample stays in the charged state in which it would be found in solution and therefore there are ions preformed in the lattice which could be blown out. On the other hand, Knockenmuss and co-workers (2003) have proposed that secondary reactions in the MALDI plume are the dominant determinant of the final detected mass spectrum.

In real-world atmospheric measurements, the particles to be analysed differ widely in chemical composition so, in general, there will not be resonant energy coupling between the laser radiation and the matrix/analyte as is the case for the above experiments. As a model system for investigation in this work, particles composed of mixtures of halide, sulphate and nitrate salts of alkali metals were used. Particles containing such salts constitute a large fraction of atmospheric aerosol, particularly in environments with marine influence. Sea-salt aerosols are formed from mechanical or abrasive processes such as wind-blown sea spray and bubble bursting (Finlayson-Pitts & Hemminger, 2000). Gaseous atmospheric species such as sulphuric or nitric acids condense onto the surface of these (and other) particles and lead to reactive displacement of chloride ions to form mixtures of NaCl, $NaNO_3$ and Na_2SO_4 salts within the particle. Oxidation of natural and anthropogenic sulphur compounds emitted to the atmosphere also leads directly to homogeneous nucleation of sulphate-containing aerosol with consequent effects on health, visibility and climate radiative forcing (Kane & Johnston, 2001). Furthermore, because of the low ionisation potentials of the alkali metals and high electron affinities of the halides, sulphates and nitrates, such particles are particularly amenable to detection by LDI aerosol mass spectrometers making it additionally relevant to try and understand the mechanisms leading to the observed mass spectra from these types of particles.

Negative ion detection is particularly useful for some species, such as sulphate, where detection in the positive ion mode by laser ablation mass spectrometry is difficult (Kane *et al*, 2002).

Alkali salt aerosols have been studied previously using an ATOFMS (Gross *et al*, 2000a) to determine relative sensitivity factors for the alkali metal cations in the positive ion mass spectra. Increased sensitivity with cation atomic mass, consistent with the periodic trends of both alkali metal ionisation potential and lattice energy of the corresponding salt, was reported. The response factors obtained for Na^+ and K^+ were used to accurately determine the relative amounts of Na^+ and K^+ in sea-salt particles. Negative ion formation processes were not investigated. Using a different type of LDI aerosol mass spectrometer, with irradiation at 193 nm, Kane *et al.* (2002) suggested that negative ions formed in the ablation of oleic acid, ammonium nitrate and sodium chloride particles arose via capture by vaporised molecules and fragments of free electrons produced during laser ablation. The study of negative ion mechanisms in LDI systems is thus extremely limited. Hence an overall objective of this work was to elucidate the possible mechanisms by which negative ions are formed in the 266 nm UV LDI of micron-sized alkali halide, nitrate and sulphate particles by analysing statistically-relevant ensembles of similar particles as a function of LDI fluence. All alkali salt systems examined are insulators with a wide band gap that ranges from 6 eV for iodides to 10-14 eV for fluorides making them transparent to UV radiation. The band gap refers to the energy difference between the conductance band and valence band and is illustrated in more detail in Figure 3.2.

3.2. Experimental

Aerosols were produced with an air jet nebuliser (RESPIRGARD-II®). Primary droplets were generated from equimolar solutions (ranging from 0.01M – 0.1M) of MCl/MX and where M = Na^+, K^+, Li^+ and Cs^+ and X= Br, I, F, SO_4, NO_3) in a 50/50 (v/v) mixture of methanol and water. The primary droplets were dried using a 17 cm silica gel dryer (fabricated in-house) to remove the methanol and water. The size distributions of the salt droplets were monitored by the ATOFMS sizing lasers giving a distribution of 0.6 ± 0.2 μm. Using Equations 2.2 and 2.3 outlined in Chapter 2 it

was possible to roughly calculate that the initial droplet diameter before drying was approximately 2.6 μm for a 0.7 μm particle sized by the ATOFMS.

In addition to the intrinsic pulse-to-pulse variation in laser energy, other uncontrollable causes of particle-to-particle variation in mass spectra for nominally identical particle/ablation conditions include inhomogeneity in the cross-section of the laser beam and variation in the exact intersection of the particle with the laser beam. At least 250 repetitive mass spectra were acquired for each experimental combination of particle composition and LDI fluence in order to provide reasonably robust ensemble statistics. Negative ions and positive ions ejected by the ablation event were accelerated into the reflectron Time-of-Flight mass analysers where they were detected with dual MCP detectors.

All chemicals were used without further purification: NaCl (Fisher), NaI (Fisons), NaBr (Fisher), methanol (HPLC grade, Fisher). The distilled water was taken from a water filtration system (ELGA LA613). Solutions investigated were made up to 0.01M, 0.05M and 0.1M concentrations.

3.3. Results and Discussion

3.3.1. Particle composition and laser-to-particle energy transfer

Aerosol particles were formed through nebulising an equimolar solution of the alkali salt mixture through a 17 cm silica gel dryer. The particles experience rapid solvent evaporation and freezing as they pass through the silica gel dryer into the low pressure regions of the ATOFMS (Mallina *et al*, 2000). Cohen *et al.* (1987) reported that particles were spatially heterogeneous in the dry state and water was possibly trapped between crystalline regions within the particle. As water has a high enough vapour pressure, partial evaporation and flash freezing of any remaining water may occur during the time between sampling and analysis, therefore, particle-to-particle variations in morphology may affect the ion formation (Mansoori *et al*, 1994). For this reason particles that entered the ATOFMS system are likely to have contained a

number of defects, and be irregular in shape. The exact nature of the spatial distribution of the co-crystallisation of the two salts in the particle is not known although some possible schematics are illustrated in Figure 3.1.

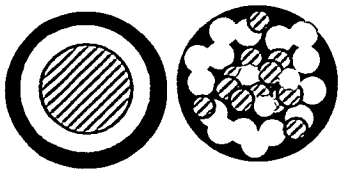

Figure 3.1. Two general schematics of possible structures for binary alkali salt particles. The darkest shade represents water that may still be associated with the particle even after drying. The light grey and the hatched areas represent, respectively, the most soluble and the least soluble of the two salts used to prepare the particle.

For the alkali salt mixtures that have been investigated one component of the mixture is far less soluble than the other. Recent work published by Hoffman *et al.* (2004) suggests that for a solution of mixed salts the least soluble component of a mixture will crystallise out of the droplet first followed by the second more soluble component. Further evaporation of water is expected to give a particle that consists of the least soluble component encapsulated in a mixed salt coating with the eutonic composition. For multi-component aqueous aerosols, the crystallisation behaviour depends on the temperature, relative humidity, and chemical composition, namely, the relative mole fraction of the electrolytes. Consider two salts in solution, as the relative humidity is lowered, one of the salts eventually becomes saturated and its crystalline phase forms. As the relative humidity is continually lowered, more of this salt crystallises and simultaneously the solution becomes more concentrated in the other salt. Eventually the other salt reaches its saturation point. At a certain relative humidity, the two salts precipitate together and a mixture of solid phases forms. This relative humidity point is called the mutual deliquescence relative humidity (MDRH), and the corresponding aqueous phase composition is called the eutonic composition.

It is likely that the crystalline phase of the particles contains a very large number of defects. Even nominally pure solids usually have defect concentrations, such as

vacancies, interstitials, non-equilibrium charge states or isotopic centres, in the parts per million range. Since all the alkali halides, sulphates and nitrates examined in this work are transparent to UV radiation (band gaps ranging from 6 eV for iodides to 10-14 eV for fluorides) it is the defects present in the solid structure that lead to radiation absorption (Cramer *et al*, 2002).

If $h\nu$ is less than the band gap E_g, the optical properties of these materials are controlled by the lower energy intraband electronic transitions and by excitation of vibrational modes within the lattice. In addition, laser radiation may induce one-photon transitions between defect states and the conduction band, absorption by impurities, excitonic resonances or multiphoton transitions between valence and conduction bands (Figure 3.2).

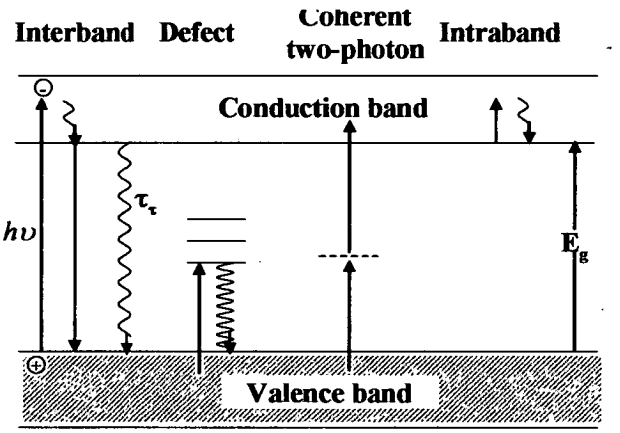

Figure 3.2. Schematic of different types of electronic excitations in a solid. Straight lines indicate absorption or emission of photons with different energies, *hν*. Oscillating lines indicated non-radiative processes (adapted from (Bauerle, 2000)). E_g is the energy required by an electron in the highest energy valence state, to cross the gap up to the lowest level in the conduction band.

In general terms, irradiation of alkali halides with energetic electrons or photons results in the creation of hot electron–hole pairs (free excitons) in the solid which subsequently could cause defect production and diffusion, as well as particle emission from surfaces. It has been demonstrated that hot carrier formation and

transport processes, occurring prior to lattice trapping and localisation, are responsible for the so-called non-thermal desorption of atomic halogen in several alkali halides (Szymonski *et al*, 2001). Figure 3.3 shows a number of different types of defects that maybe present in the lattice after the irradiation with a UV-laser.

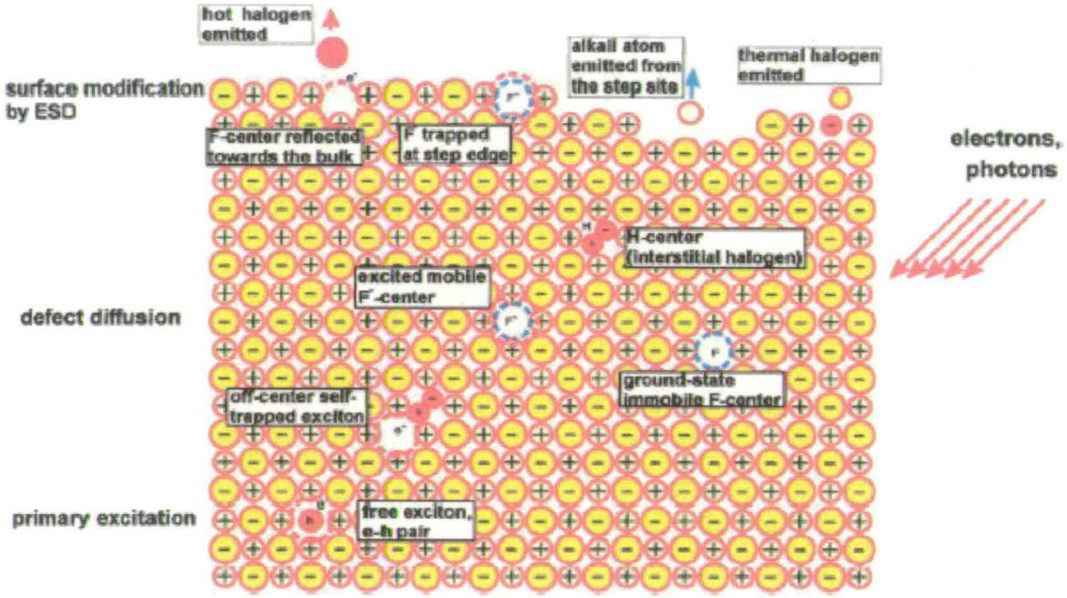

Figure 3. 3. Defects in NaCl lattice, F-centres arise when an electron gets trapped at an anion vacancy. A H-centre occurs when two halogen atoms occupy one lattice site (Szymonski *et al*, 2001).

Laser radiation is absorbed either by exciting free electrons, or electronic or vibrational transitions in atoms, ions, or molecules (Figure 3.3). Various electronic excitations can occur (interband and intraband transitions, excitons, plasmons (a quasiparticle resulting from the quantisation of plasma oscillations), etc), as well as excitations of phonons (vibrations occurring within the crystal lattice), polaritons (a polariton is the result of the mixing of a photon with an excitation of a material), magnons (A collective excitation of the electrons' spin structure in a crystal lattice), etc. Electronic or vibrational states may be localised or non-localised, and may be related to the solid surface itself but also to defects and impurities.

In particular, F-centre defects (an anion vacancy with a trapped electron) absorb strongly in the UV region (Pedraza, 1998) and are likely to be responsible for coupling the ATOFMS DI laser energy (4.66 eV) to the particle. The defect electrons become photo-detached and are either ejected from the surface and contribute directly to plasma formation or heat the lattice through electron-phonon collisional energy transfer and heat conduction. These transfer processes occur within a few 10 ps, well within the LDI pulse duration of 5 ns. Within a few ns, the rapid heating leads to melting and rapidly expanding vaporisation of the plasma plume containing electrons, charged and neutral atoms, clusters and larger fragments. It will take many μs for the plume to expand to collision-free densities in a field free region (ions will be quickly removed in the presence of high voltage accelerator plates whereas neutrals will continue to expand). Thus whilst both creative or destructive photo-processes can only occur during the 5 ns of laser radiation, reactions between electrons, ions and neutrals can continue as long as there are collisions. If the number and energies of these collisions are sufficiently high, thermodynamically-favourable processes will proceed to equilibrium. Chapter 5 discusses work on the analysis of ambient data which has shown that within the ATOFMS instrument the laser ablates a constant amount of material regardless of particle size, i.e. that for particles in the size range analysed by the ATOFMS, not all the particle is ablated. As a consequence, observed ion spectra more strongly reflect the outer composition than the core of the particle being analysed. Similar results were reported by Carson *et al.* (1997) and Ge *et al.* (1998).

In the ATOFMS each particle will be irradiated for a period of 5 ns, by a 266 nm laser (4.66 eV), in which time disintegration into a large number of neutral and charged fragments will occur. The laser pulse typically lasts 5 ns but the time required for expansion to collision-free densities is much longer. For a one micron particle to expand to a 10 μm diameter will take approximately 13 ns by this time the acceleration plates will have caused many of the electrons, and other charged particles to be accelerated down their respective flight tube. The primary ions will be generated during the laser pulse. For micron sized particles, the ablation event

creates a gaseous plume dense enough that electrons are efficiently captured by molecules and atoms to form negative ions (Lake *et al*, 2004).

Laser ablation is defined as a sputtering process leading to the ejection of atoms, ions, molecules, and even clusters from a surface as a result from the conversion of an initial electronic or vibrational photo excitation into kinetic energy of nuclear motion.

Figure 3.4 shows an illustration of the different processes occurring during laser ablation. The initial laser-material interaction may create excited electrons in the solid, leading to the ejection of electrons by photoelectric or thermionic emission, and eventually forming a plasma above the sample surface in a pico-second time scale. In the solid the excited electrons undergo electron-phonon relaxation and the energy is transferred to the lattice. Through lattice vibrations, the transferred energy is dissipated from the irradiated zone to the bulk in the form of heat. Heat conduction occurs on a time scale of several tens of picoseconds, which is slightly longer than the electron-phonon relaxation time. Heating of the material leads to melting and vaporisation. The particles leaving the liquid during evaporation establish an equilibrium distribution of velocity in a small region above the surface called the Knudsen layer. Above the Knudsen layer the vapour plume will expand rapidly, compressing the ambient gas and forming a shock wave front. In addition, the expanding plume can interact with the laser pulse effectively shielding the sample surface from the laser energy. The high temperature plume can also heat the sample surface via radiative heating. The vaporisation of the sample and the subsequent gas dynamic processes in the expanding plume take place on a time scale of nanoseconds. Other material removal processes such as exfoliation or liquid ejection may occur on a substantially longer time scale (Mendes, 2002).

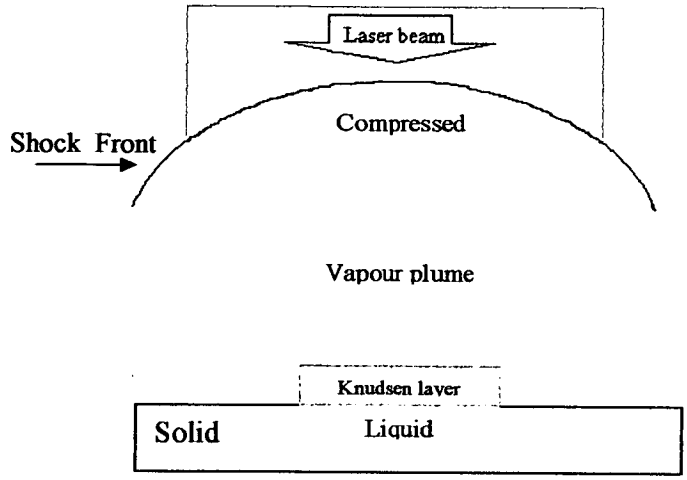

Figure 3.4. Scheme of relevant processes during pulse laser ablation, namely laser-induced vaporisation, surface melting and shock wave formation (Mendes, 2002).

3.3.2. Alkali Halide aerosols

Sampled data included mixtures of alkali halides of MCl/MX, where M = Na^+, K^+, Li^+ and Cs^+ and X = I^-, Br^-, Cl^-, SO_4^- and NO_3^-. Only the anion (X) varied in each sampled mixture. Several consecutive mixtures were run where each of the alkali metal cations was changed. The results showed the same trends for all mixtures of MCl/MX so only results from NaCl/NaX and KCl/KX will be referred to.

As with all alkali salt mixtures the time required to collect equal numbers of mass spectra increased with decreasing laser energy suggesting that at lower laser energies there was not sufficient energy available to ablate the particle. The intensities of the negative ion mass spectra were considerably weaker (x3) than the positive ion mass spectra at all laser energies. This is because it is necessary for the electrons created in the ablation process to react to form negative ions (Kane *et al*, 2002) and also because the excess electron in negative ions is weakly bound and is easily photo- or collisionally detached. The total number of ions (positive and negative) produced per particle (quantified as the average total ion area per spectrum) increased with LDI fluence, for all compositions and concentrations of salt mixture analysed. This confirms that particles in the μm size range are not fully ablated at the LDI fluences

used in the ATOFMS, consistent with the semi-quantitative interpretation of ATOFMS mass spectra of ambient particles presented in Chapter 5.

Ions identified in the positive and negative mass spectra from mixed alkali halide particles (NaCl/NaX) included the monatomic ions Na^+, Cl^-, I^-, Br^- as well as cluster ions ($NaCl^{(-/+)}$, $NaI^{(-/+)}$, $NaBr^{(-/+)}$, $(NaCl)Cl^{(-/+-)}$, $(NaBr)Br^{(-/+)}$, $(NaI)I^{(-/+)}$ & $(NaCl)I^{(-/+)}$) and electrons. Example spectra from LDI at a laser fluence of 0.2 J cm^{-2} of a single particle produced from a 0.01 M mixture of NaI/NaCl are shown in Figure 3.5. It is the analysis of the relative abundance of different ions as a function of particle composition and laser energy that provides information on the formation processes that are likely to be dominant.

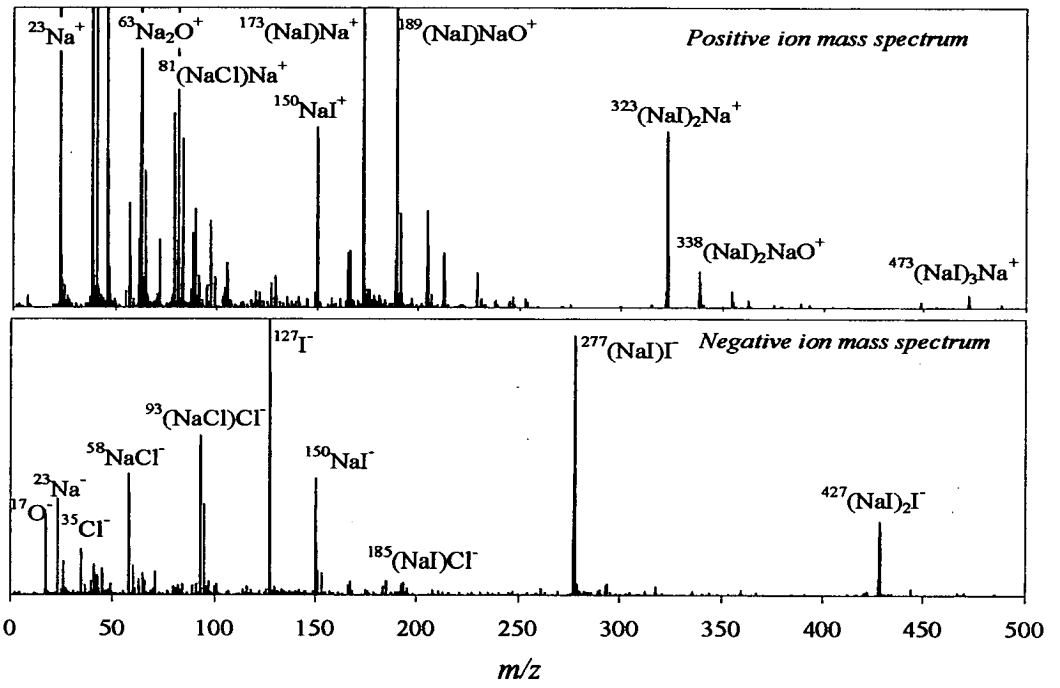

Figure 3. 5. Positive and negative ion mass spectra from an individual particle (0.54 μm) derived from a mixture of 0.01 M NaI/NaCl (LDI fluence = 0.2 J cm^{-2})

The relative peak area of OH^- in the negative ion mass spectra declined as the concentration of the salt solution from which the particles were derived increased from 0.01 M to 0.1 M. At the same time, the number and intensity of peaks due to n = 3 and 4 cluster species in the spectra increased with salt concentration. Both these

observations are consistent with a greater proportion of water being incorporated into the solid matrix at lower salt concentrations and a consequent dilution of collisions between salt ions in the desorbing plume by water.

3.3.2.1. Formation of X^- ions

Despite considerable particle-to-particle variability in mass spectra, statistics from the ensembles of spectra corresponding to different combinations of the halide salts showed that the relative formation abundance of the halide ions decreased in the order $I^- >> Br^- > Cl^-$. Figure 3.6 illustrates the relative ion intensity comparison for I^- and Cl^-. Two additional important observations were: (i) the ratios I^-/Cl^- and Br^-/Cl^- both decreased with increasing LDI fluence. (For example, Figure 3.6 shows that the I^- ion intensity levels off at highest LDI fluences whilst the Cl^- ion intensity increases with LDI fluence) (ii) the ratios in average peak areas of halide ions, I^-/Cl^- (Figure 3.6) increased with increasing salt concentration used to form the particles. Figure 3.7 illustrates how Br^- is the strongest ion detected in the 0.01M NaBr/NaCl mixture at laser energies from 0.1 to 0.4 J / cm^{-2} but at the highest energy the mass spectra are dominated by $(NaCl)Cl^-$ clusters.

Whilst these observations undoubtedly reflect the relative energetics of halide ion formation (Table 3.1), the observations are also consistent with the picture that the particles are not homogeneous in chemical composition but have a core composed relatively more of the lower solubility NaCl salt with relatively more of the higher solubility NaI or NaBr salts in the outer layers (Table 3.1). Higher LDI fluences are capable of ablating more of the internal chloride-containing particle material, and since the higher concentration salt solution particles are slightly larger proportionally less of the core is sampled for a given laser fluence.

	NaCl	*NaBr*	*NaI*	*KCl*
Electron affinity /eV	0.73	0.79	0.87	0.58
Dipole moment, μ /D	9.21	9.6	10	
Solubility /g (100g H_2O)$^{-1}$	36	98	170	53
Lattice Energy[†] /eV	7.97	7.58	7.07	7.26

Table 3.1. Physical properties of some alkali halides

[†] Energy required to break the solid form of a molecule into oppositely charged ions in the gas phase.

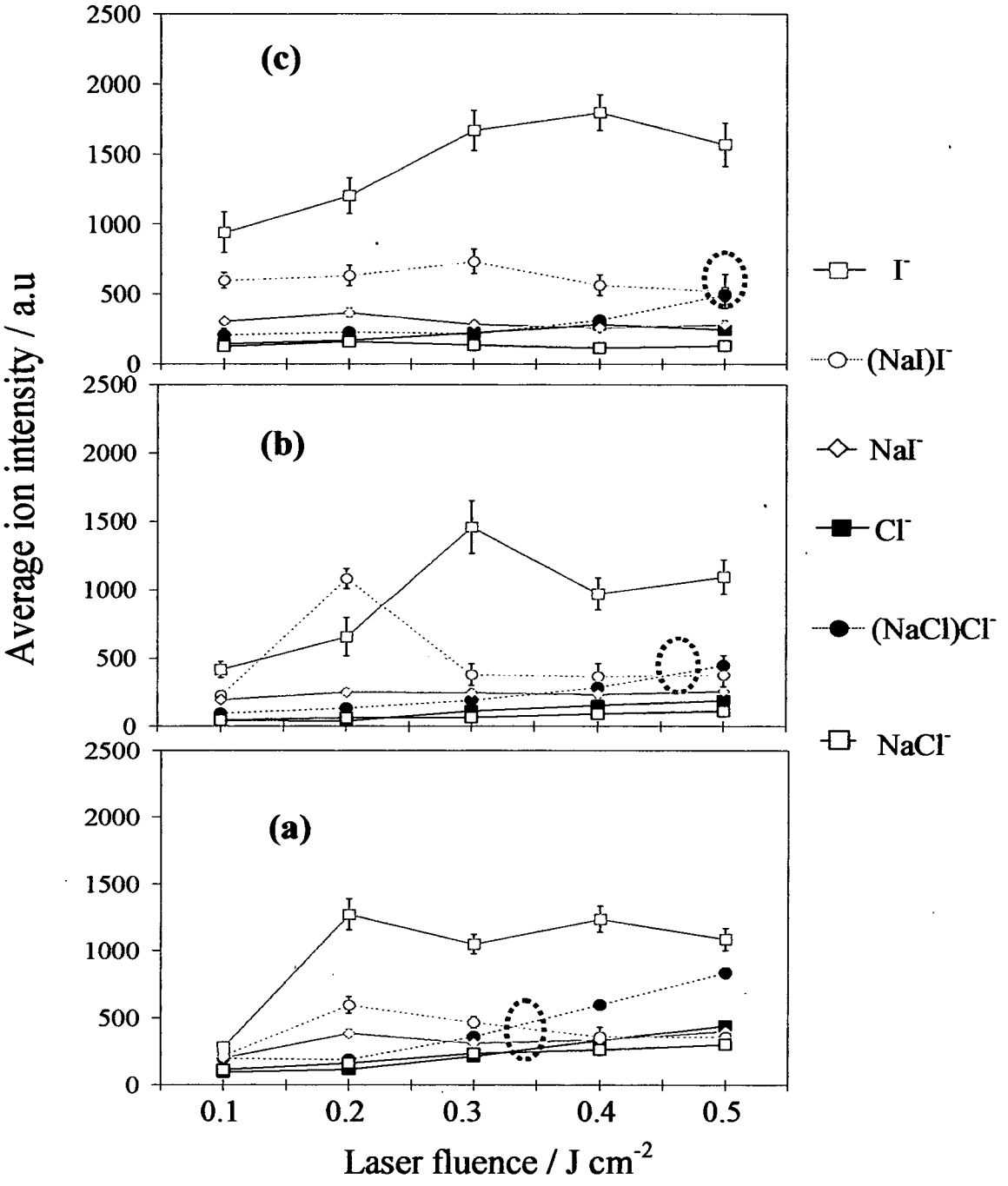

Figure 3.6. The relative intensity as a function of LDI fluence of the most intense ions formed from particles derived from an equimolar solution of (a) 0.01 (b) 0.05 and (c) 0.1 M NaCl/NaI. The dotted circle highlights the fluence at which the $(NaCl)Cl^-$ average ion signal intensity equals that of the $(NaI)I^-$ ion. Error bars are 95% confidence intervals.

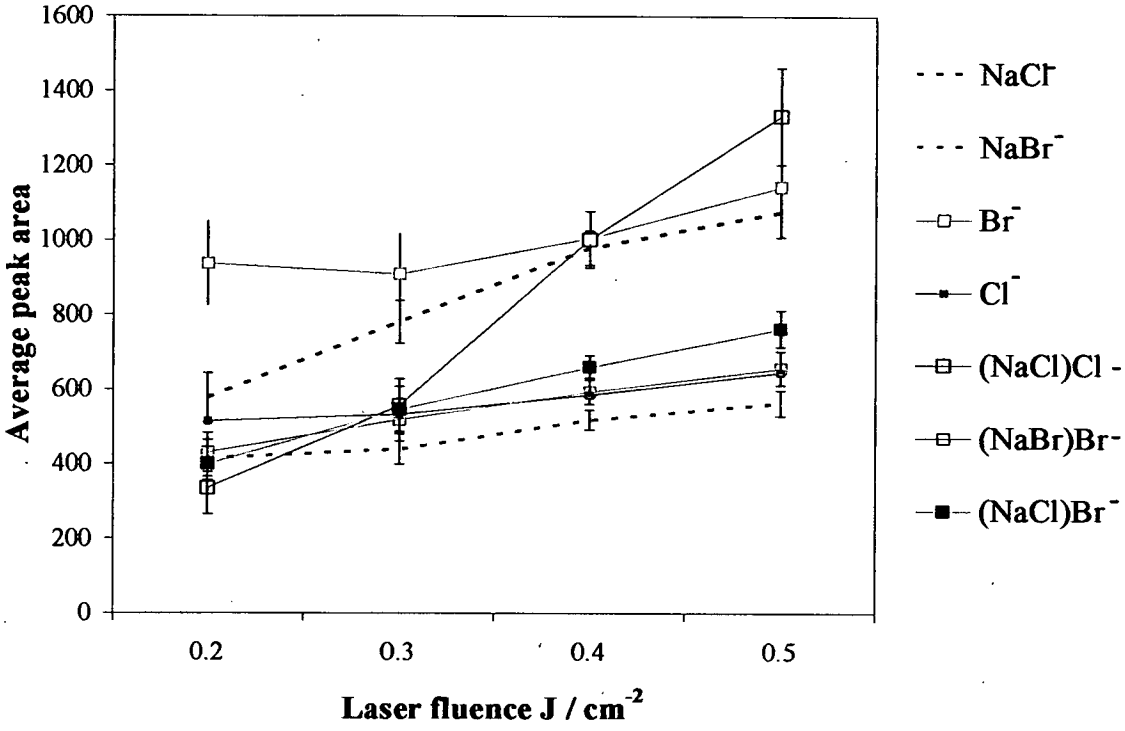

Figure 3.7. The relative intensity as a function of LDI fluence of the most intense ions formed from particles derived from an equimolar solution of 0.01 M NaCl/NaBr. Error bars are 95% confidence intervals.

Furthermore, since the laser photon energy exceeds the electron affinities of each of I$^-$, Br$^-$ and Cl$^-$ (Table 3.2), photo-detachment of an electron is likely to be a major loss route for any halide ions formed during the laser pulse. Therefore the majority of these ions must be formed through in-plume processes after the cessation of the laser irradiation rather than by direct ejection from the lattice. The energetics for the ion-pair and dissociative attachment routes of halide ion formation, Equations 3.1 and 3.2, respectively are given in Table 3.2.

$$e^- + NaX \rightarrow Na^+ + X^- + e^- \quad \textbf{(3.1)}$$

$$e^- + NaX \rightarrow X^- + Na \quad \textbf{(3.2)}$$

X^-		Cl^-	Br^-	I^-
Electron affinity (EA)	/eV	3.04	3.59	3.34
Ion pair formation	/eV	5.78	5.54	5.12
Dissociative attachment	/eV	0.64	0.40	-0.020

Table 3.2. Energies required for ion-pair formation and dissociative attachment

In both cases, the energetics favour halide formation in the same order as observed (I^- > Br^- > Cl^-), but the much higher energies required for ion-pair formation compared with dissociative attachment make this process unfavourable given the likely distribution of photo-detached electron energies (a further justification for post-irradiation processes is noted from the multiphoton requirement for photo-initiation of ion-pair reactions). On the other hand, the energetics of dissociative attachment closely parallels the observed trend.

3.3.2.2. Formation of NaX^- ions

NaI^-, $NaBr^-$ and $NaCl^-$ were also identified in the mass spectra (Figure 3.6 and 3.7). At lower LDI fluence, ion intensities followed the order NaI^- > $NaCl^-$ and $NaBr^-$ ~ $NaCl^-$, but at the highest LDI fluence $NaCl^-$ intensity exceeded NaI^- intensity. A similar trend was observed in the NaBr/NaCl mixture only that NaCl was always more intense at all laser energies (Figure 3.7). As with X^- ion formation, the relative intensities are a consequence of both the energetics of ion formation reactions and the morphology of the particle. A likely route to the formation of these anions is electron capture by neutral fragments volatilised from the lattice followed by collisional stabilisation (Equation 3.3). The very large dipole moment of the alkali halide molecules will lead to large electron capture cross-sections:

$$\begin{aligned} NaX\,(lattice) + \Delta H_{cr\text{-}g} &\longrightarrow NaX\,(g) + ... \\ NaX\,(g) + e^-\,(low\ energy) &\longrightarrow NaX^-{}^*(g) ... \\ NaX^-{}^*(g) + M &\longrightarrow NaX^-(g) + ... \end{aligned} \qquad \textbf{(3.3)}$$

Collisional stabilisation will be most effective in the early stage of the desorption plume development where number density is high. The electron capture process depends on both the dipole moment and electron affinity of the neutral which both favour NaX^- formation in the order $NaI^- > NaBr^- > NaCl^-$.

Neutral fragments may be released directly from the lattice. These neutral fragments capture low energy electrons. If NaX^- is produced by low energy electron capture of gas phase NaX it will be metastable until collisionally stabilised. Since the particle density close to the surface will be high, stabilisation could be efficient. If collision with the surrounding material is energetic then NaX^- may dissociate to X^-. This process is less endothermic for $NaI^- >> I^-$ (82 kJ mol^{-1}) than for $NaBr^- >> Br^-$ (114 kJ mol^{-1}) and for $NaCl^- >> Cl^-$ (127 kJ mol^{-1}). NaI and NaBr could be more readily dissociated by collision than $NaCl^-$ so depleting $NaI^-/NaBr^-$ relative to NaCl and enhancing I^-/Br^- relative to Cl^-.

Electron capture depends on the dipole moment and electron affinity of the neutral which do not vary enormously from NaCl → NaI (Table 3.1). At lower laser energies $NaI^- > NaCl^-$ as there is less NaCl being ablated (due to being situated in the core of the particle). At higher laser energies the peak area of $NaCl^-$ are greater than $NaI^-/NaBr^-$. The electron affinity of NaBr is comparable to NaCl but it is expected that there is less $NaBr^-$ and NaI^- present at higher laser energies as these ions more readily dissociate through ion-pair formation, dissociative attachment or collision.

Variability between spectra precludes the assignment of an absolute value to the intensities. For example, the ratio $NaI^-/NaCl^-$ for a sequence of 17 spectra chosen at random has the range from 0.02 to 9.6 with a mean and standard deviation of 1.64 ± 2.76. If the two higher values for the ratio, 9.6 and 3.1, are excluded and the lowest value of 0.022 is excluded (justified by Q-test) then the range is from 0.24 to 1.00 yielding a mean and standard deviation for the ratio of 0.76 ± 0.29. Wenzel and Prather (2004) have recently employed fibre optics to improve the output of the Nd:YAG laser reducing pulse to pulse variability, although differences in particle morphology will still affect the ions formed.

From Figure 3.6 it can be observed that the average areas for $(NaCl)Cl^-$ and $(NaI)I^-$ are higher than for $NaCl^-$ and NaI^- (Table 3.1). This coupled with the ablation of only outer layers of the particle which are relatively depleted in lower-solubility NaCl lead to the relative intensities observed for NaX^- ions. At high LDI fluences, however, relatively more of the NaCl-rich particle core is ablated, plus the more highly extended plume means the influence of competing collisional reactions becomes relatively more important. Thus, as LDI fluence increases, the ablation plume will be relatively depleted in NaI, or NaBr, relative to NaCl because the former more readily undergo ion-pair formation and dissociative attachment to form I^-, or Br^-, than does NaCl, as discussed above. In addition, once formed, NaX^- ions may undergo photo- or collisional induced dissociation to form X^- (Equation 3.4).

$$NaX^- + M \rightarrow Na + X^- + M \qquad \textbf{(3.4)}$$

The lower endothermicity for dissociation of NaI^- (82 kJ mol^{-1}) compared with $NaCl^-$ (127 kJ mol^{-1}) could contribute to the more rapid depletion of the former. All of these loss processes are relatively enhanced at the higher plume densities arising from higher LDI fluences leading to the observed relative enhancement of $NaCl^-$ under these conditions. A possible alternative process for formation of NaX^- is dissociative attachment to $(NaX)_n$ clusters, Equation 3.5,

$$(NaX)_n + e^- \rightarrow Na^+ + Cl^- + (NaX)_{n-1} \qquad \textbf{(3.5)}$$

but it has not been possible to find reliable thermodynamic data for such processes and their involvement therefore remains speculative.

3.3.2.3. Formation of $(NaX)X^-$ ions

Figure 3.6 shows that average ion intensities for the $n = 1$ mono-cluster ions $(NaCl)Cl^-$ and $(NaI)I^-$ exceed those of $NaCl^-$ and NaI^-, respectively. This broadly suggests that electron capture and collisional stabilisation of NaX^- does not compete particularly effectively with collisional dissociation of NaX^- or collisional association to form $(NaX)X^-$. More detailed inspection of the relative ion intensities reveals a relative abundance in favour of the halide ion, X^-, for the iodine and bromine systems, but in favour of the cluster ion, $(NaX)X^-$, for the chlorine system. Although direct ejection of $(NaX)X^-$ from the lattice is possible, as proposed by Krüger and Karas (2003), termolecular association in the gas plume, Equation 3.6, will have very

large cross-sections, due to ion-dipole attraction (leading to orbiting collisions), and is more likely.

$$X^- + NaX + M \rightarrow (NaX)X^- + M \qquad (3.6)$$

The rapid fall-off in efficiency of association reactions with decreasing number density in the expanding plume explains why clusters only up to $n = 3$ were observed.

For particles derived from a 0.01 M mixture of NaI and NaCl, ablation at laser fluences ≥ 0.3 J cm^{-2} yielded relatively more $(NaCl)Cl^-$ than $(NaI)I^-$ (Figure 3.6). The trend was the same for 0.01 M NaBr/NaCl mixed particles. For particles derived from more concentrated salt solutions, the LDI fluence at which relative intensity of $(NaCl)Cl^-$ exceeded $(NaI)I^-$ increased to 0.5 J cm^{-2}. This is again consistent with the proposal that the less soluble chloride salt forms the core of the particle so that chlorine-containing material is relatively less abundant in the ablation plume at lower LDI fluences. At the lowest LDI fluence used (0.2 J cm^{-2}), the iodine- or bromine-containing ions dominate the chlorine-containing ions. A similar trend was apparent for $(NaX)_nNa^+$ species in the positive ion mass spectra.

Ion signals for mixed cluster species, such as $(NaI)Cl^-$, are also evident in the ion mass spectra. Ion-molecule collisions occurring in the dense plume are the most likely routes to the formation of these mixed clusters as it is unlikely that mixed fragments would be ejected directly from the crystal lattice in significant quantities. The presence of these ions further supports the proposal that the ions detected in the negative ion mass spectra are mainly a result of reactions occurring in the plume.

3.3.3. Alkali nitrate aerosol

$NaNO_3$ is a common particle type present in continental air masses where gaseous HNO_3 has reacted with NaCl, causing the displacement of Cl in the form of HCl, and nitrate ions are retained in the particle as $NaNO_3$ (Harrison, 2001; Harrison & Pio, 1983). $NaNO_3$ like the alkali halides is a wide band gap material with a band gap of 10 eV. Strong absorptions centred at 6 eV due to a $\pi^* \leftarrow \pi$ transition in the NO_3^-

anion have been observed (Cramer *et al*, 2002). Mass spectra were obtained from particles derived from mixtures of sodium (and potassium) halides and nitrate. These mixtures are typical of partially processed sea-salt particles and, as already reported the formation of unusual metastable, amorphous solid phases of $NaNO_3$ and mixtures of NaCl and $NaNO_3$ play a significant role in both the chemistry and radiative properties of salt particles in the marine boundary layer (Hoffman *et al*, 2004). Sodium nitrate also does not absorb a LDI photon energy of 4.66 eV, so coupling of laser energy into the lattice must again occur via lattice defects. Solubility, lattice energy and electron affinity for some of the alkali salts and nitrates used in this experiment are shown in Table 3.3.

Compound	*Solubility /g(100g H_2O)$^{-1}$*	*Lattice energy /eV*	*Electron affinity /eV*
KCl	53	7.2	0.58
KNO_3	281	7.1	
NaCl	35	7.9	0.73
$NaNO_3$	92	7.8	
NO_3			3.94
NO_2			2.27

Table 3.3. Physical properties of some of the more intense ions present in the negative ion mass spectra.

A plot of the variation in intensity of the most abundant negative ions observed in the LDI of mixed NaCl/$NaNO_3$ particles is shown in Figure 3.8 as a function of LDI fluence. For particles derived from the lowest concentration mixture (0.01M), NO_3^- and NO_2^- ions were the predominant negative ions, particularly for LDI fluences $\leq$ 0.3 J cm^{-2}. The next most abundant ion was $(NaCl)Cl^-$ which, like NO_3^-, increased markedly with LDI fluence, whereas NO_2^- declined in abundance at higher LDI fluence. An example of single-particle positive and negative ion mass spectra is shown in Figure 3.9, and illustrates that Cl^- and mixed $NO_3^-.NO_2^-$ clusters were formed.

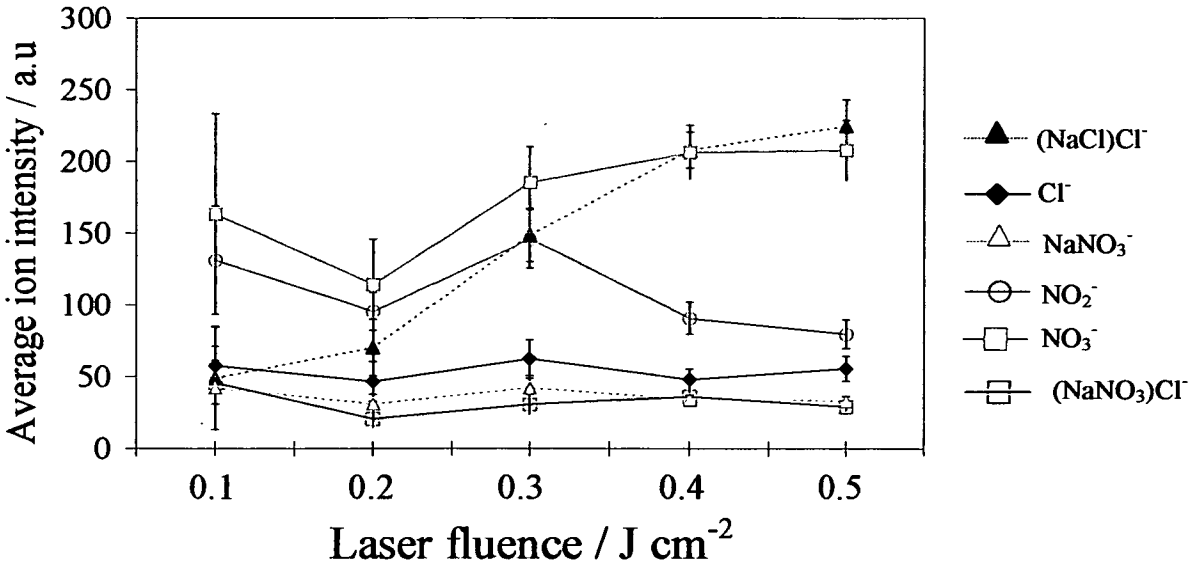

Figure 3.8. Average response of different ion signals against laser energy for $NaNO_3$/NaCl Mixture at 0.01 M.

Error bars are calculated 95% confidence intervals.

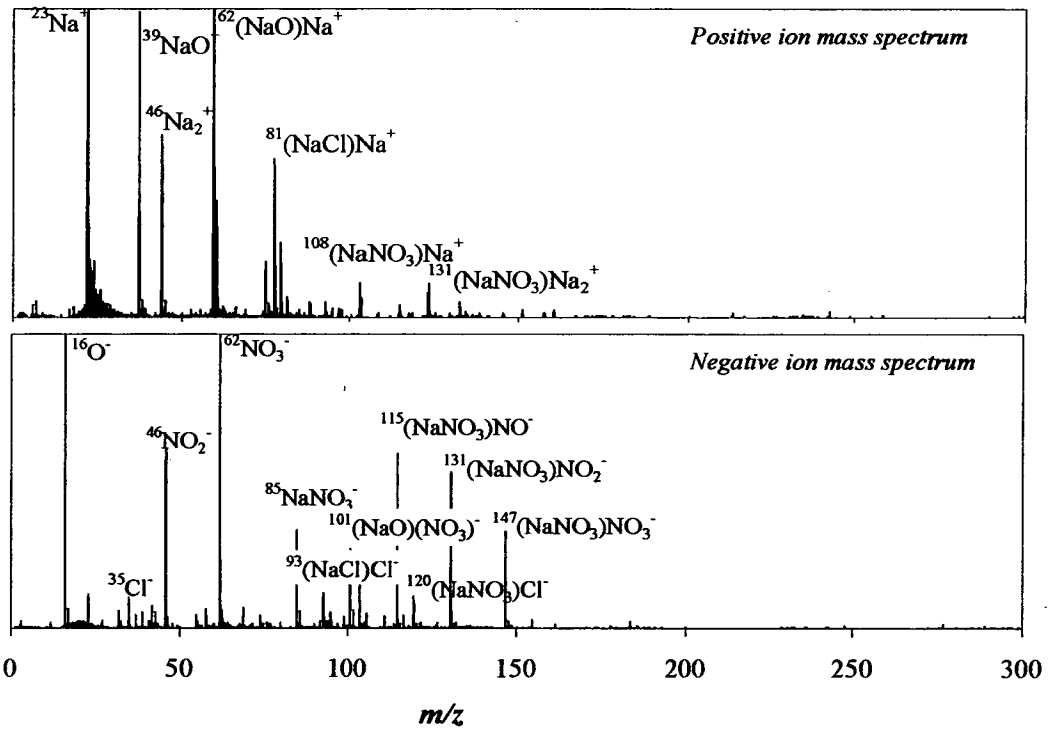

Figure 3.9. Example positive and negative ion mass spectra from an individual particle (0.53μm) derived from a mixture of 0.01 M $NaNO_3$/NaCl (LDI fluence = 0.2 J cm^{-2}).

The analogous plot to Figure 3.8, for the variation in most abundant negative ion intensity produced by LDI of mixed KCl/KNO_3 particles, is shown in Figure 3.10. As in Figure 3.8, NO_3^- is the predominant negative ion formed and the relative abundance of the $(KCl)Cl^-$ ion increases rapidly with LDI fluence. As discussed in Section 3.3.2.3, the $(NaCl)Cl^-$ and $(KCl)Cl^-$ cluster ions are most likely to be formed through termolecular association reactions in the ablation plume.

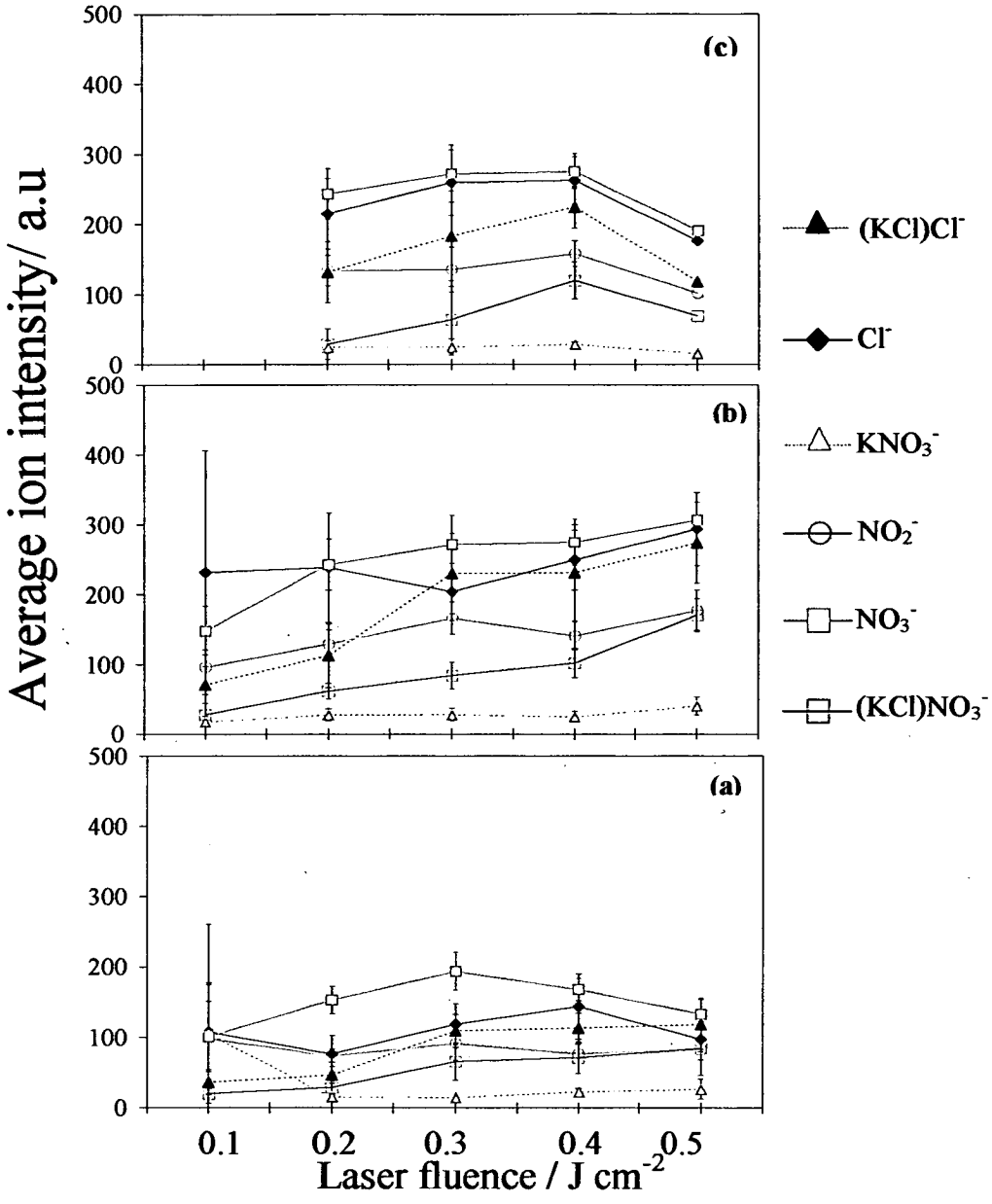

Figure 3.10. The relative intensity as a function of LDI fluence of the most intense ions formed from particles derived from an equimolar solution of (a) 0.01 (b) 0.05 and (c) 0.1 M KNO_3/KCl. Error bars are 95% confidence intervals.

The relative increase in chloride-containing ions at highest LDI fluences is, as before, rationalised in terms of the likely particle structure. Sodium and potassium nitrates are much more soluble than their corresponding chlorides (Table 3.3) so the

former will dominate the outer layers of each particle. As LDI fluence increases, proportionally more chloride material is ablated.

The NO_3 radical has a high electron affinity (3.94 eV, Table 3.3). However, electron capture by NO_3 would result in an energy-rich ion that would almost immediately auto-detach or undergo dissociation to $NO_2^- + O$. Since direct ejection of NO_3^- from the lattice is unlikely, the most likely source of the high abundance of NO_3^- ion is dissociative attachment of gas phase $NaNO_3$ or $(NaNO_3)_n$. The NO_2^- ion can then be formed by dissociative attachment of NO_3 or possibly photodissociation of NO_3^-, as shown in the reactions in Table 3.4. These processes have relatively low enthalpy which accounts for the relatively high abundance of NO_2^- also. However, subsequent photodissociation of NO_2^- to NO^- is very much less favourable since it is a two-photon process (Table 3.4). Furthermore, although NO_2 can undergo dissociative attachment to form NO^-, this ion has a very low electron affinity and is therefore likely to autodetach, explaining the absence of NO^- in the spectra. Again, as with the halide salts, ions of mixed cluster species, such as $(NaNO_3)Cl^-$, are observed (Figure 3.9), supporting the view that post-irradiation reactions in the expanding plume are important.

	/eV
Dissociative attachment	
a) $e^- + NaCl \rightarrow Na + Cl^-$	0.64
b) $e^- + KCl \rightarrow Cl^- + K$	0.79
c) $e^- + NO_3 \rightarrow NO_2^- + O$	-0.085
d) $e^- + NO_2 \rightarrow NO^- + O$	3.15
Ion-pair formation	
a) $NO_3 \rightarrow NO_2^- + O^+$	13.53
b) $NO_2 \rightarrow NO^- + O^+$	16.76
c) $NaCl \rightarrow Na^+ + Cl^-$	5.78
Dissociation reactions	
a) $h\nu + NO_3^- \rightarrow NO_2^- + O$	3.82
b) $h\nu + NO_2^- \rightarrow NO^- + O$	5.39

Table 3.4. Dissociative attachment and dissociation reactions for NO_3,NO_2 & NO species

3.3.4. Alkali sulphate aerosol

Although sulphate is an important component of atmospheric aerosols the sensitivity of laser ablation mass spectrometry to sulphate is very low in the positive ion mode making negative ion detection methods very useful for the detection of sulphate (Kane *et al*, 2002). It is well known from laboratory studies that sulphate is detected almost exclusively in negative ion mass spectra (Lake *et al*, 2004). Sulphur aerosols are important contributors to acid rain, visibility degradation, adverse health effects, and cloud condensation nuclei. Sulphur is emitted to the atmosphere both naturally as dimethylsufide (DMS) from marine organisms and anthropogenically as sulphur dioxide from combustion processes (Kane & Johnston, 2001; Whiteaker & Prather, 2003).

In contrast to the other binary mixtures studied, the chloride salt is more soluble than the sulphate salt, and has considerably lower lattice energy (Table 3.5), so the sulphate will form the least ablatable core of each particle. An example of observed positive and negative ion mass spectra is shown in Figure 3.11.

	Lattice Energy /eV	*Solubility /g(100g H_2O)$^{-1}$*
NaCl	7.9	35
Na_2SO_4	18.8	4.76

Table 3.5. Lattice energy and solubility of NaCl and Na_2SO_4

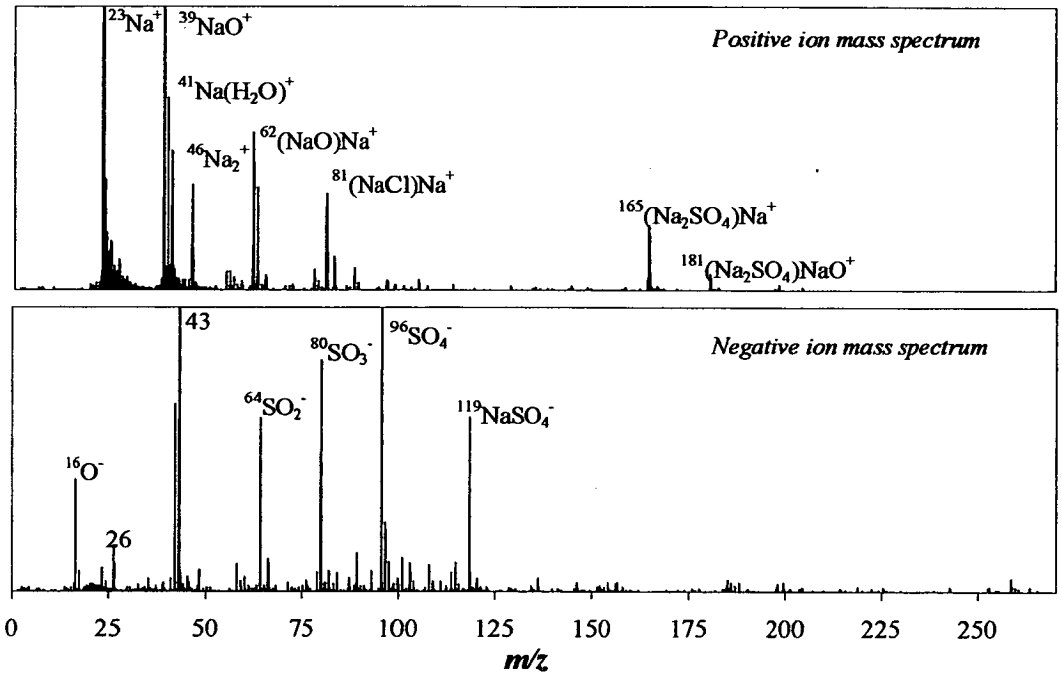

Figure 3.11. Positive and negative ion mass spectra from an individual particle (0.57μm) derived from a mixture of 0.01 M NaCl/Na_2SO_4 (LDI fluence = 0.2 J cm^{-2}).

Despite the mixed salt composition of the particle, and the expectation that chloride will predominate in the outer regions of the particle, the negative ion mass spectra predominantly contained only oxysulphur anions and or only chloride anion but rarely contained mixed ions. Lake *et al.* (2004), using LDI at 193 nm, also observed that very few particles yielded multiple-species negative ions, even if the particle produced positive ions indicating the presence of other components such as nitrate and carbon. Together, the two studies suggest that there is negative ion suppression in the ablation plume in the presence of sulphate species. The total ion signal from LDI of Na_2SO_4/NaCl particles was considerably lower than from NaX/NaCl particles so a possible explanation of the lack of chloride-containing ions in the former is efficient electron transfer from initially dominant Cl^- from the particle outer layer to a smaller flux of SO_4 (high electron affinity of 5.10 eV Table 3.6) from deeper in the particle.

Although sulphate could possibly be ejected directly from the particle as the doubly-charged anion, it would immediately lose an electron to form SO_4^-, via auto-detachment. Any SO_4 neutral formed will rapidly undergo electron attachment due to its very high electron affinity. Similarly, SO_4^- will not undergo photodetachment because the EA exceeds the photon energy of the LDI laser. In contrast, the low electron affinities of SO, SO_2 and SO_3 (Table 3.6) suggest that these ions are more likely formed through dissociation of SO_4^- (Table 3.7) than by electron capture by the corresponding neutral.

Group	*Bond energies /eV*	*Dipole,μ/D*	*EA /eV*
SO	5.38		1.12
SO_2		1.6	1.11
SO_3			1.90
SO_4			5.10

Table 3.6. Physical properties of the groups studied in the Na_2SO_4/NaCl mixture

Table 3.7 shows that the dissociation energies of SO_4^- to SO_3^- and of SO_3^- to SO_2^- are both one-photon (LDI energy is 4.66 eV), while further dissociation of SO_2^- to SO^- is multiphoton. This explains the lack of SO^- ion in the observed the mass spectra (Figure 3.11). Similarly, the formation of SO_4^-, SO_3 & SO_2 ions by dissociative attachment reactions is very much less favourable for formation of SO^- than for higher $SO_{4/3}^-$ species (Table 3.7).

	eV
Dissociative attachment	
a) $e^- + SO_4 \rightarrow SO_3^- + O$	0.88
b) $e^- + SO_3 \rightarrow SO_2^- + O$	2.50
c) $e^- + SO_2 \rightarrow SO^- + O$	4.59
Dissociation reactions	
a) $SO_4^- \rightarrow SO_3^- + O$	4.19
b) $SO_3^- \rightarrow SO_2^- + O$	4.37
c) $SO_2^- \rightarrow SO^- + O$	5.66

Table 3.7. Dissociation reactions of SO_x^-

3.4. Conclusions

Detection of negative ions in single particle LDI techniques provides information complementary to the positive ion mass spectra for the analysis of many chemical species in the atmosphere, particularly sulphates. The solubility of different species during particle growth affects the particle composition as a function of depth. As a consequence, the distribution of ions is strongly affected by the LDI pulse fluence. The consequence is that altering the LDI fluence reveals information on the chemical heterogeneity of the particles in the ensemble.

Formation of negative ions appears to be mainly dependent on collisional processes and the thermodynamics of reactions in the post-irradiation ablation plume, rather than the result of direct ejection from the lattice. There was a general tendency for negative ion abundance to be biased towards those species with greatest electron affinity, with collisions in the ablation plume providing the stabilisation, as also reported by Kane *et al.* (2002).

Although relative sensitivities for various negative ions can be determined by statistical averaging of particle ensembles, this work demonstrates again that particle-to-particle variability limits the determination of fully-quantitative ion sensitivities.

Chapter 4

Chemical and physical analysis of ambient particles detected during the North Atlantic Marine Boundary Layer Experiment

Chapter 4 Chemical and physical analysis of ambient particles detected during the North Atlantic Marine Boundary Layer Experiment

4.1. Introduction

The marine boundary layer (MBL) is an important part of the atmosphere as about 70% of the earth's surface is covered by water. At the MBL particulate matter originates from land-based sources as well as from sources over the open ocean. Patriculate matter from the ocean consist of two major types; sea-salt particles that are created mechanically at the surface of the ocean due to wave action and bubble bursting and non sea-salt (nss) particles which are predominantly sulphate-based particles created from gas to particle conversion. The sea-salt particles tend to have larger particle diameters than the nss variety and therefore tend to dominate the mass of particulate matter detected in maritime air. The nss particles tend to be in the fine size range and often undergo gas to particle condensation (Raes *et al*, 2000).

Marine aerosols affect the climate directly through scattering of radiation and indirectly as they can act as CCN. The global mass emission of sea-salt particles is more than 20 times the combined emissions of organics, black carbon, sulphate, nitrate and ammonia in the atmosphere (Raes *et al*, 2000).

Mace Head, (Galway, Ireland) is a marine boundary site that experiences air masses mainly arriving from a clean sector between 180°- 300°. Continuous background measurements are sampled at this site giving long-term physical and chemical information on air masses. However, air masses arriving both inside and outside the clean sector can be influenced by continental sources, i.e. North America and Europe as well as local land sources.

A multidisiplinary study, the North Atlantic Marine Boundary Layer Experiment (NAMBLEX), took place at Mace Head, during the 1st-21st of August 2002. Mace

Head is situated on the shore of a headland in a remote part of the west Irish coastline at 53.33°N, 9.90°W as illustrated in Figure 4.1. The aims of this study were to investigate the oxidation processes, atmospheric chemistry and composition of a number of species primarily in the MBL.

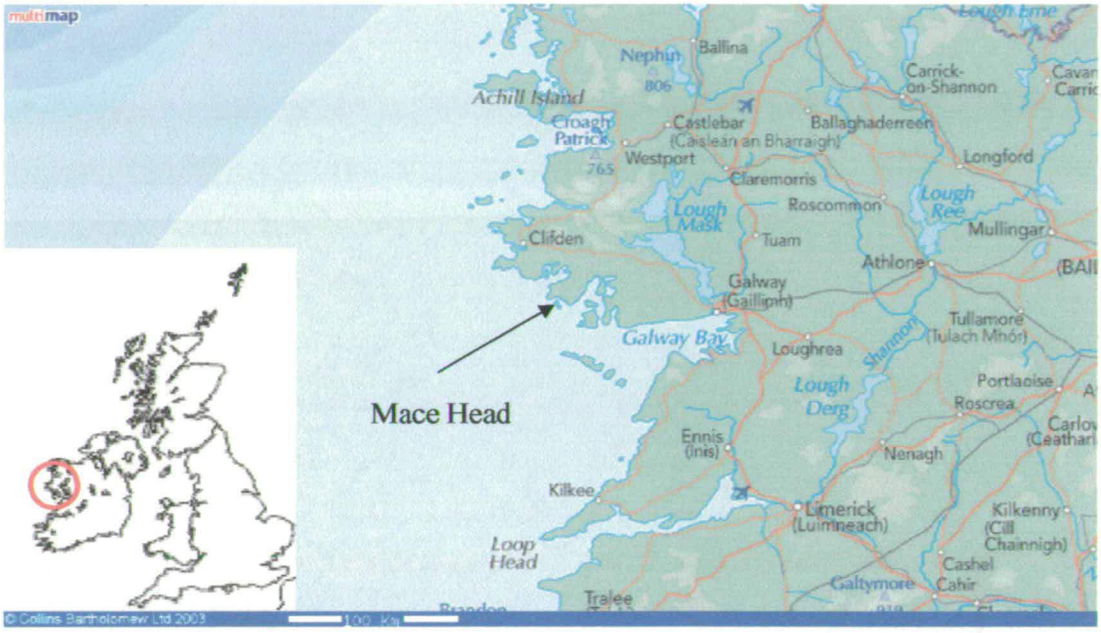

Figure 4.1. Location of the sampling site during NAMBLEX

4.1.1. Overview of studies carried out on the marine boundary layer

There have been many field experiments focused on the characterisation of tropospheric aerosols to improve estimates of aerosol direct radiative forcing on the climate, to gain better knowledge of the chemical and physical properties of aerosol particles and to understand long and short range transport of aerosols over land and ocean (Quinn & Bates, 2005). Many of these experiments have been carried out near or at a MBL site. By understanding the chemical composition of background marine air the impacts from anthropogenic sources as well as natural sources can be assessed and quantified. Examining clean maritime air masses allows basic chemical and microphysical properties to be monitored without the effect of secondary continental air masses.

Measurements of sub micrometer atmospheric aerosol particles, together with black carbon and radon, were reported by O'Dowd *et al.* (1993) during a cruise in the North Atlantic (63°N, 8°W) from October to November 1989. Measured soot carbon mass showed excellent correlation with accumulation mode number concentration demonstrating its usefulness as an air mass tracer and as an indicator of anthropogenic pollutant transport. By comparison, radon, which is often used for this purpose, exhibited a significantly poorer correlation for this region. Approximately 9% of the total accumulation mode mass was accounted for by soot, regardless of air mass origin, suggesting that early winter marine aerosol in the remote North Atlantic is primarily of anthropogenic origin (Odowd *et al*, 1993).

Aerosol properties were measured during two ship transects across the North Atlantic between Halifax and the Moroccan coast in a latitude band between 32°N and 44°N, by Van Dingenen *et al.* (1995). Measurements of the chemical composition of the total aerosol, the black carbon concentration and the number size distributions with particle diameters in the range 16 nm < D_p < 1 μm were made. The non sea-salt (nss) fraction of the sulphate concentrations encountered during this campaign spans 3 orders of magnitude (0.02 μm / m^3 to 19 μg / m^3) and shows a high correlation with black carbon (Van Dingenen *et al*, 1995).

A European Commission sponsored project entitled "Background Maritime contribution to Atmospheric Pollution in Europe" of BMCAPE, coordinated by University College Galway was carried out from January 1993 - December 1994 with the objective of determining the chemical and microphysical properties of predominantly maritime air masses at a range of coastal field stations (Jennings *et al*, 1997).

Other boundary layer studies include the first and second Aerosol Characterization Experiments (ACE 1 and ACE 2), a cruise across the Atlantic (Aerosols99), the Indian Ocean Experiment (INDOEX), the Asian Aerosol Characterization Experiment (ACE Asia), the Tropospheric Aerosol Radiative Forcing Observational Experiment (TARFOX), and the New England Air Quality Study (NEAQS). These experiments were focused either on the remote marine atmosphere (ACE 1) or areas

downwind of continental aerosol source regions including western Europe, North America, Africa, India, and Asia (Quinn & Bates, 2005). Quinn and Bates (2005) compared the results of all these studies and reported that nss SO_4^{2-} makes up only 16 to 46% of the submicron aerosol mass, indicating that there is a large fraction of the aerosol that is not sulfate and that particulate organic matter makes up 1 to 51% of the submicron mass.

4.1.2. Importance of Mace Head as a research station

Mace Head has a present status as one of the most important sites for atmospheric research in the northern hemisphere. Strategically located with open exposure to the North Atlantic Ocean, Mace Head occupies an ideal position for studying changes in the global atmosphere. Its location facilitates the investigation of both natural and man made trace constituents in marine and continental air masses. Long-term measurements of such substances can reveal trends in background concentrations, which may influence weather and climate.

Research activities at Mace Head have been mainly concerned with measurements of northern hemisphere background levels of trace substances in air from the Atlantic Ocean. Sources and sinks of these substances and the complex biogeochemical processes which they undergo in the atmosphere have been investigated.

The Atmosphere/Ocean Chemistry Experiment (AEROCE) was carried out to investigate aerosol sources at a number of research sites which included Mace Head, Barbados, Bermuda and Izana. It was reported that Mace Head had dust concentrations an order of magnitude lower than the other sites but had the highest sea-salt concentrations (Arimoto *et al*, 1995). This was due to the storminess of the region and its location far north of the main transport pathways for Saharan dust.

Huang *et al.* (2001) studied aerosols at Mace Head and, through the use of positive matrix factorization, classified the Mace Head aerosols into a number of chemical classes such as mineral dust, sea-salt, general pollution, a secondary SO_4-Se signal, ferrous industries and a second (possibly biogenic) marine source. It was reported that the marine signal is particularly strong in winter. The main pollution transport

from Europe to Mace head is during May, but the influence of continental Europe is observed throughout the year. Mineral aerosol follows a transport pathway similar to that of pollution aerosol, i.e., recirculation via the westerlies brings pollutants mixed with dust to the site from nearby land, i.e., Ireland, the United Kingdom and the Belgium, Netherlands and Luxemburg (Benelux) region, with some inputs from Scandinavia, Western Europe, Eastern Europe, and even the Mediterranean region. Compared with Bermuda, the aerosol at Mace Head has stronger marine sources (especially marine-derived secondary SO_4^{2-} and Se) but weaker dust and pollution sources.

Derwent *et al.* (2002) presented a 5-yr record of continuous high-frequency carbon dioxide (CO_2) observations during the 1995–1999 period for the Mace Head Atmospheric Research Station. During the winter months, it was observed that an additional CO_2 source, over and above fossil fuel combustion, was required to support the observed concentrations of CO_2 in European regionally polluted air masses. During the summer months, an additional CO_2 sink is required.

More recently, Simmonds *et al.* (2005) compared annual growth rates of CO_2 compared with those measured from an observatory site in Hawaii. It was reported that the temporal variations in the annual increases in N_2O, at Mace Head, are not in phase with those of the other gases. As N_2O is recognised as a combustion product of biomass burning, it was suggested that the recent increase in the rate of accumulation of CO_2 is a hemispheric wide phenomenon related to large-scale biomass burning rather than a change in ocean exchange. This increase in biomass burning has also been reported to be responsible for the increase in O_3 concentrations measured at Mace Head (Simmonds *et al*, 2004).

Cavalli *et al.* (2004) presented results from a comprehensive size segregated analyses of clean marine aerosol samples collected at Mace Head during periods of phytoplankton bloom (spring and autumn), providing new evidence on the chemical composition of marine aerosol. It was reported that the fraction of water insoluble and water soluble organic carbon increased as particle diameter decreased. The

results from this study showed that these organic particles had a strong biogenic origin.

From the same campaign O'Dowd *et al.* (2004) reported that the sub-micron biogenic carbon detected at Mace Head were formed during plankton blooms. This organic material arising from the sea surface micro-layer, generated during bubble bursting, contributes 63% to the sub-micron aerosol mass (about 45% is water-insoluble and about 18% water-soluble). It was reported that externally mixed organic carbon can significantly alter the cloud droplet number in the atmosphere and thereby significantly affecting aerosol radiative properties. Organic matter from the ocean has not previously been included in climate models (Novakov and Penner 1993; Kleefeld et al. 2002; O'Dowd et al. 2004).

4.1.3. Aims and goals of NAMBLEX

The majority of air masses arriving at Mace Head Atmosphere Research station arrive from the nominal clean sector (Jennings *et al*, 1993), lying between 180° and 300°, which is dominated by south-westerly winds from the Atlantic Ocean. Most of these air masses are considered clean (not strongly influenced by anthropogenic activity) making Mace Head well suited for marine background experiments. Mace Head is often influenced by continental emissions from Europe. Therefore, by studying aerosols at Mace Head, information on marine sources, emissions from Europe, and long-range transport across the ocean can be obtained.

During August and September 2002 the North Atlantic Marine Boundary Layer Experiment (NAMBLEX) took place at Mace Head. As part of this campaign the ATOFMS was operated continuously for 21 days from 1st – 21st August 2002. The ATOFMS was deployed with the intention to characterise the physical and chemical properties of individual particles at this remote marine site.

NAMBLEX was an interdisciplinary project where a number of different research groups sampled different properties of the marine aerosol. The main objective of

NAMBLEX was to make detailed measurements of the chemical composition of aerosol particles and of gas phase species from predominantly clean air reaching the site from the Atlantic. These measurements are valuable for testing the predictions of models of atmospheric chemistry and understanding better the chemical mechanisms that control the concentrations of greenhouse gases, radiatively-active aerosols and gases responsible for the deterioration of air quality (e.g. ozone). An overview of the NAMBLEX campaign can be found in Heard *et al.* (2005).

4.2. Experimental

4.2.1 Instrument set-up

The research station is located on the west coast of Ireland (53.33°N, 9.90°W), about 90 km west of Galway city, on a peninsula, about 100 m from the shoreline. The sampling area is surrounded by coastline and tidal areas except for a small sector between 20° and 40°. The nominal clean sector, at Mace Head, is between 180° and 300° (Jennings *et al*, 1997). The nominal clean sector is also defined by measurements of black carbon (<75 ng m^{-3}) and particle number concentration. The prevailing wind direction is from this sector and as the air has often travelled over the Atlantic Ocean for five days before its arrival at Mace Head it can be considered representative of background conditions for the Northern Hemisphere.

Many of the instruments were operated inside shipping containers or permanent buildings. Figure 4.2 illustrates the set up of the different instruments operated during NAMBLEX. The ATOFMS instrument was housed inside a shipping container alongside an Aerodynamic Particle Sizer (APS). The inlet of the ATOFMS instrument was linked by a steel pipe (diameter and length 0.25 inch and 2 m, respectively) to a manifold that was connected to a 23 m sampling tower (Figure 4.2). The tower was 23 metres in height but had two inlets at 7m and 22 m. The sampling height was alternated each hour between 7 and 22 m by switching a valve in the pipe at 7 m height. Analysis has shown that the variation in height did not make any difference to particle composition (Coe *et al*, 2005). The sampling tower was equiped so that several instruments sampled from the same sampling port.

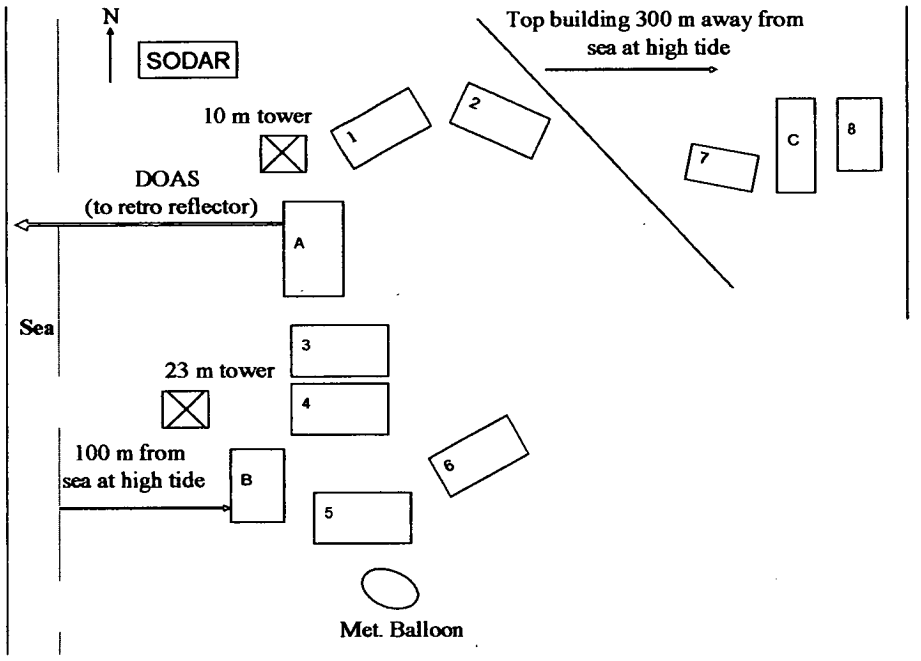

Figure 4. 2. A schematic diagram illustrating the position of each of the containers containing different instrumentation operated during NAMBLEX (Heard *et al*, 2005).

Laboratory detail	*Measurement technique and main species measured (inlet position)*
A. Building	NO_3, IO,OIO, BrO, I_2 (DOAS retro reflector positioned 4.2 km away on Island) Leeds H_2O_2 and ROOH (10 m Tower)
B. Building	O_3, CO, CH_4, H_2, (23 m tower), CN, Met. station (10 m tower)
1. Leeds FAGE container	OH, HO_2, NO, O_3, H_20, JO^1D and Met. station (roof at 5 m)
2. York HC container	VOC, and reactive halocarbons (23 m tower)
3. Site Office	-
4. UMIST container	Aerosol measurements (23 m tower, 2 inlets at 7 m, and 22 m). ATOFMS
5. UEA/Leicester container	HO_2 + ΣRO_2 (PERCA), j values, speciated peroxides, PAN, HCHO, NO_{xy}, Met. station (roof at 5 m)
6. Cambridge container	OIO, I_2 and NO_3 (CRDS)(roof at 5 m)
C. Building	Leeds HCHO, $>C_7$HC, alkyl nitrates (roof at 20 m)
7. Wind Profiler	Vertical wind-speed, wind-direction, velocity
8. Campaign Office	Modelling studies

Table 4. 1. Detailed information to accompany Figure 4.2. (Heard *et al*, 2005).

The ATOFMS instrument was operated from the 1st - 21st August 2002 but during this period there were two short periods when the instrument was not operating. The first of these was a 6 h period on the 10th August and the second a 12 h period on the 18th August when over-heating problems were encountered with the roughing pumps (Chapter 2).

The irradiance of the desorption/ionisation laser, of the ATOFMS, was maintained at a maximum value of 10^9 W cm^{-2}. This allowed the detection of the maximum number of different chemical species present in the ambient air. Since Mace Head is a marine site it was presumed that the majority of particles sampled would consist of inorganic alkali salt particles. As alkali salts particles are insulators they do not readily absorb ultraviolet radiation and will require higher energies in order for particle ablation to occur (Chapter 3).

4.2.2. Data analysis

The ATOFMS software has been previously explained in Chapter 2 where it was stated that for each dataset different mass spectral thresholds were set in order to qualify an ion signal at a specific *m/z* ratio as a peak. In this particular analysis, an ion signal had to be 20 units above the baseline, contain 20 units of area and represent at least 0.001 as a fraction of the total peak area of the mass spectrum in order to be included. A selected set of the different ions present in each positive and negative ion mass spectrum was used to identify the composition of each particle. The ATOFMS can analyse between 50 and 100 particles / min under typical atmospheric conditions. This significant volume of data requires efficient methods of data analysis.

Clustering analysis identifies and classifies samples on the basis of the similarity of the characteristics they possess. So in the case of single particle mass spectra, it groups the mass spectra containing similar sets of *m/z* values. In this thesis a K-means algorithm was employed in the analysis of the NAMBLEX data in order to aid in the characterisation of the particle ensemble. The K-means algorithm is a non-hierarchical clustering procedure and is a simple and easy way to classify a given dataset through a certain number of clusters defined by the user. The algorithm

chooses 'n' centroids, one for each cluster. Once all the centroids have been selected then each point/ particle mass spectrum in this case is taken and associated with its nearest cluster. The procedure is repeated until the distance of each data point from its centroid is minimised. The K-means algorithm aims at minimising the differences from each point of its cluster (Equation 4.1).

$$J = \sum_{J-1}^{k} \sum_{i-1}^{n} \left\| x_i^{(J)} - C_j \right\|^2 \tag{4.1}$$

Where $\left\| x_i^{(J)} - C_j \right\|$ is the distance measure between data points $x_i^{(j)}$ and the cluster centre C_j. The result of cluster analysis is a number of heterogeneous groups with homogenous contents (Adams, 1995).

Other types of clustering procedures have been employed with single particle mass spectrometry. The most commonly employed clustering procedure for single particle mass spectrometry is the Artificial Resonance Theory (ART-2a) neural network. It is popular because of its flexibility. ART has the ability to add a class should the data points fall outside of a preset proximity to all existing classes without disturbing the existing categories. The ART-2a requires the user to define a vigilance factor, learning rate and the number of iterations to be run. The vigilance factor is the maximum distance that a point can be from its cluster center while still remaining a member of that cluster. The learning rate is the rate at which the algorithm converges to a solution.

The ART-2a algorithm conducts multiple iterations of each dataset. Cluster assignments for each point are not retained through the course of the algorithm; the only information retained is the centroid themselves. At the end of the clustering procedure each point is assigned to its closest centroid so long as the distance to that centroid is less than or equal to the vigilance value. Any points at the end with no centroid within a distance less than or equal to the vigilance value are classified as outliers.

The purpose of the application of the ART-2a network, or indeed other clustering methods, is to identify the various classes of particles that exist, without any *a priori*

assumptions about their possible identities. There have been several reports (Song *et al*, 1999; Bhave *et al*, 2001) of work using neural networks to classify single particle data. Recently a software program employing the ART-2a algorithm for real-time analysis of ATOFMS data has been patented (Gard *et al*, 2005) and is available on line at www.YAADA.com.

The ART-2a clustering mechanism is a hierarchical clustering procedure so it adds a new particle cluster each time one is detected. The K-means algorithm is a non-hierarchical clustering procedure. It is based on one cluster seed at a time and membership in that cluster is fulfilled before another seed is selected, i.e. it runs through the whole dataset before updating each seed. The K-means algorithm was investigated for the analysis presented here in order to compare different clustering procedures, namely hierarchical and non-hierarchical.

Both ART-2a and K-means require the user to supply certain information in advance. The information that the K-means requires however is considerably easier for the user to handle. ART-2a is complicated by the fact that the error metric (average of the squares of the distances of all points to their nearest centroids, (Equation 4.1)) does not converge monotonically, i.e. it is not guaranteed to decrease at each iteration. In fact, it is easily seen that with a learning rate of 1 the centroids will continue to drift from point to point without ever stabilizing. Unlike many other clustering algorithms, it is not known at any given point whether the error in the next ART-2a iteration will get worse or better. Kmeans, on the other hand, is theoretically guaranteed to reduce its error metric at each iteration. Therefore, K-means will continue to improve at each iteration until the cluster centroids stop moving. This frees the practitioner from needing to worry about how many iterations to run, or from trying to estimate if the changes from iteration to iteration are "small enough" in order to stop. K-means has a clear stopping point. Finally, ART-2a does not scale well to datasets that are too large to fit into core memory. Each iteration of ART-2a requires a full scan over the dataset. K-means differs significantly here as there are a considerable number of algorithms that adapt it, or algorithms related to it, to perform well on massive data sets (Anderson *et al*, 2005). K-means is a more user-

friendly algorithm than ART-2a for the reasons presented above. When ease of use is desired, K-means should clearly be preferred over ART-2a.

In this thesis the non-hierarchical K-means clustering has been carried out, although Dall'Osto *et al.* (2005) have used ART-2a on the same dataset and the results of both are compared.

The raw ATOFMS data were exported from Microsoft Access 2000® into MINITAB (version 14.10). Each particle positive and negative ion mass spectrum was identified as a row, containing the name of that spectrum as well as the aerodynamic diameter of the particle. Absolute areas of the *m/z* values were listed in columns. These data were standardised prior to clustering as some elements, such as sodium or potassium, that have very low ionisation potentials tend to exhibit peaks with large absolute areas in the mass spectra. If the data are not standardised the clusters generated by the algorithm will be dominated by the variances in absolute areas rather than the variances in *m/z* patterns.

It is possible to separate the raw dataset into different size or time distributions before performing clustering analysis. However, in this chapter all the particles were grouped together. As mentioned above it was necessary to determine the numbers of clusters to be used to define the data set. In the case of all the data considered in this chapter, 20 clusters were always chosen as the pre-defined number. Increasing the number of clusters results in a smaller error function values but it also increases the risk of overfitting. Huang *et al.* (2001) explained the effect of choosing fixed numbers of clusters for positive matrix factorisation of atmospheric data collected using impactors. It was noted that when using a smaller number of factors (3-4) the resulting factors contained mixtures of different chemical species. When using > 8 factors the marine compositions were less certain. Optimum cluster numbers used were between 6 and 8. In this thesis it was decided to use 20 clusters. The ATOFMS produces more variables (i.e. positive and negative *m/z* values) and therefore there is more potential discrimination into separate clusters. Several iterations of the dataset

were carried out using 6, 10 and 20 clusters and it was concluded that using 20 clusters provided the optimum amount of information for our data set.

Since K-means judges class membership on the types of ions present particles can be separated into different classes if they contain different ions even though they may represent the same particle type. Zhao *et al.* (2005) reported on how the ART-2a broke a carbonaceous particle distribution with a wide range of ammonium nitrate content into two composition classes. This was mainly due to different ion intensities. For this reason it is necessary to examine the members of each cluster by manual inspection in order to present a true picture of the detected particle composition.

By using 20 clusters for the analysis, many of the clusters contributed less than 1% to the total number of particles. Examination for similar size distributions, temporal evolutions and *m/z* values in individual particles meant that it was often possible to combine a number of small clusters into one particle grouping.

A disadvantage to the K-means clustering algorithm compared with other clustering methods is that the K-means algorithm uses a 'hard' clustering method, assigning the particles to classes by a yes/no decision. This means that each particle is allocated to a cluster but no information is available on how much each particle belongs to a cluster. For this reason there were no unclassified particles when using the K-means algorithm. When using the ART-2a method, a 'soft' attribution of individual particles to classes is preformed, a membership/vigilance factor is predefined to determine how much each particle must belong to a cluster before it is counted. As a result close manual inspection of each cluster is required when using the K-means algorithm.

In this work characteristic peaks detected in the positive and negative ion mass spectra of individual particles were used to further refine the general classes to assess the degrees of association of different secondary species, including sulphates and nitrates. Investigating different combinations of peaks in particles allows a particle to

be assigned to a known source, assess the complexity of particle composition, or infer possible chemical transformations that may have occurred in or on the particles.

4.3. Results and discussion

4.3.1. Meteorology

As mentioned already, Mace Head is remotely situated on the Atlantic coast of Ireland. The site is often characterised by conditions of exceptionally clean air which has source regions extending as far south as the Azores and as far north as Greenland. Occasionally, identification of air originating in continental Europe and west/northwest America, has allowed investigation into long-range transport of anthropogenic precursors to pollutant species observed at the site (Derwent *et al*, 1998). When the air arrives form the clean sector (180° – 300°) it has often travelled over the Atlantic Ocean for five days before its arrival at Mace Head and is therefore considered representative of background conditions for the northern hemisphere.

Local wind direction and wind speed measurements were made by the National University of Ireland, Galway, the University of Leeds and the University of Leicester using standard meteorological stations. More details of these measurements can be found in Norton *et al.* (2005). During sampling 51% of the local wind arrived from the clean sector. The remaining 49% was divided up amongst the north-easterly wind (10%), south-easterly wind (16%) and north-westerly wind (23%).

The relative humidity was high at Mace Head during NAMBLEX (80-85%). This is consistent with the typical range of variability (75-85%) at Mace Head (Jennings *et al*, 1997) and temperature measurements of 15.2 ± 1.3 °C were consistent with the average temperature measurements made at Mace Head in August (http://macehead.physics.nuigalway.ie). Five main meteorological periods were identified during the NAMBLEX campaign (Norton *et al*, 2005). Each of these periods is described in Table 4.2.

Meteorological period	*Description*
1st- 5th August	Complex, Azores high extending over the Atlantic and a stagnant low pressure system over Ireland and the UK, with re-circulating fronts. Winds were very weak north-easterly.
6th - 11th August	The Azores high extended toward Ireland and therefore winds were generally westerly or north-westerly. The 8th was an exception when the centre of a depression crossed just south of Mace Head.
12th- 17th August	Azores high retreated south allowing a succession of depressions to cross Ireland from the west.
18th- 28th August	On the 18th the air stagnated as the pressure gradually built. Anti-cyclonic conditions prevailed between the 19th and 27th of August.
28th-31st August	Westerly winds and unsettled weather.

Table 4. 2. Summary of the five meteorological conditions identified during NAMBLEX (Norton *et al*, 2005)

In this chapter the results published by Norton *et al.* (2005) are related to the ambient particle measurements made by the ATOFMS. Air mass back plots were used in this study to identify the atmospheric transport pathways at Mace Head and to aid in the interpretation of temporal trends. Air masses were studied using the Numerical Atmospheric-dispersion Modelling Environment (NAME) model (Ryall & Maryon, 1998). The Met. Office NAME model uses meteorological data obtained form the Met. Office Unified Model (UM) to calculate time-integrated back-maps for arrival, over any requested time interval, at the receptor. The UM is the Met. Office's state of the art numerical weather prediction model and is therefore assumed to yield the most accurate gridded weather data. The NAME model is based on Lagrangian trajectory dispersion and includes probabilistic descriptions of turbulent dispersion. It produces probabilistic maps of air mass source, rather than a single line trajectory. The NAME model takes into account the past history of all air arriving at the receptor over any user specified time-interval, not just arrival of a single time. The output back-maps are 'time-integrated' so that the numerical value (colour)

associated with each grid square expresses the relative contribution that air passing over that grid square makes to the total air that arrives over the receptor location during the receptor time interval specified. This time-integrated nature of the back-maps explains why the colours are always strongest in the vicinity of the receptor because all air, regardless of its more distant history, must pass over near-field locations on its way to the receptor. The back plots shown here only show six hour periods for each day sampled and are calculated for a 10-day period.

During the first meteorological period (1-5th August 2002) the hourly wind direction was highly variable (Figure 4.3). Local wind was arriving from a north-westerly direction off the sea during the day and switching to a north-easterly direction during the early hours of the morning. The air was identified as being from the clean sector for 2.5% of the sampling time during this period.

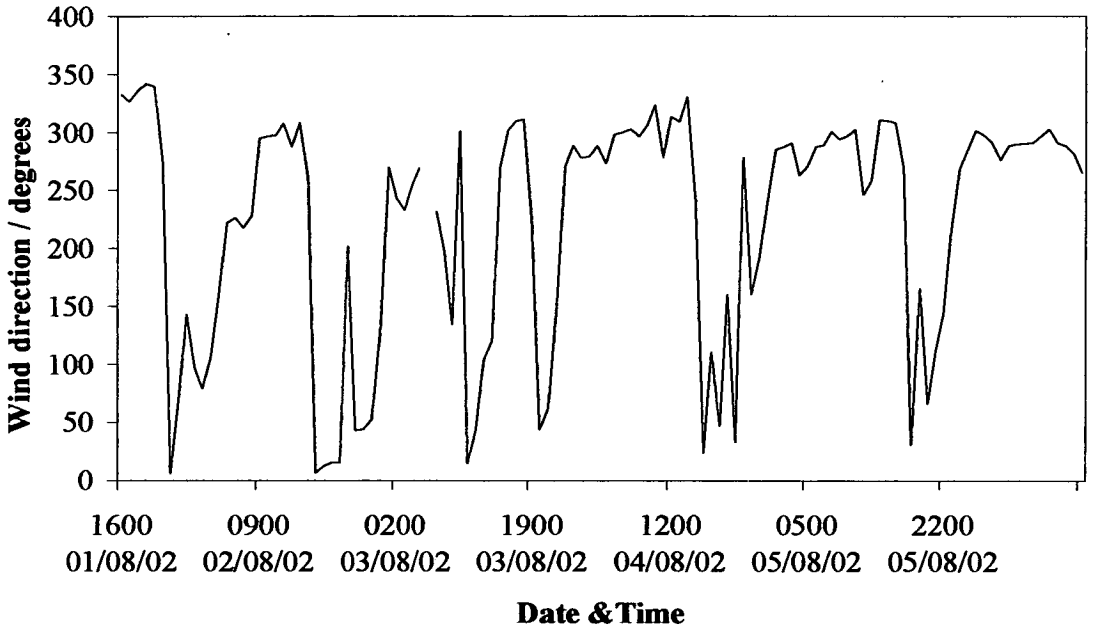

Figure 4.3. Hourly averages of wind direction for the first five days of sampling during NAMBLEX.

On examining the back plots it can be observed that although the air masses were arriving predominantly from over the continent there was still a possibility that a small fraction of the air masses were arriving from the Atlantic and Arctic regions (Figure 4.4). Norton *et al.* (2005) explain how lower level wind speeds were variable

on the 1st and 2nd August and settled into a sea breeze pattern with minimum speeds in early morning and maxima in late afternoon. Radar and the European Centre for Medium-Range Weather Forecasts (ECMWF) comparisons showed that period one was dominated by local flow introducing a high degree of error to trajectory calculations based on the ECMWF model. The NAME model used in this thesis to describe the air masses arriving at Mace Head use the UM data.

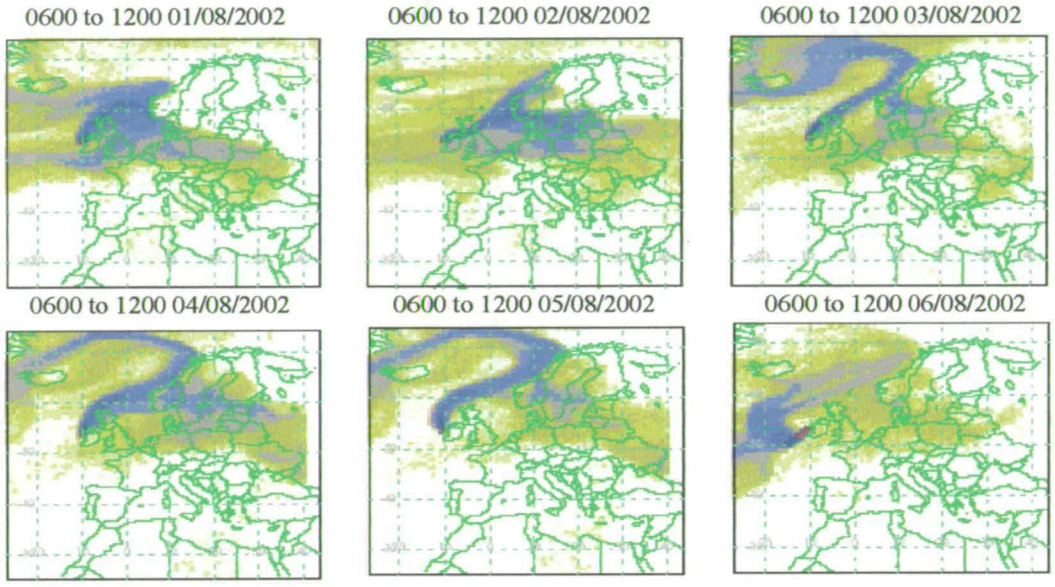

Figure 4.4. NAME back plots for the 1st-6th August 2002. Air masses are arriving predominantly from the north east.

Aerosol measurements made by the ATOFMS instrument during this period show the highest number concentrations compared with the whole of NAMBLEX as well as the highest carbonaceous number concentrations. More detailed discussion of the chemical composition will presented later in Section 4.3.3.

During the second period (6th-12th of August 2002) the wind direction was generally westerly to north-westerly. The 8th was an exception as the centre of a depression passed just south of Mace Head. During the time the wind direction went full circle from north-westerly to northerly. Another point to note is that on the eve of the 10th the wind speed dropped to < 2 m s^{-1} and therefore local circulation effects dominated. Air mass back plots for this period are illustrated in Figure 4.5.

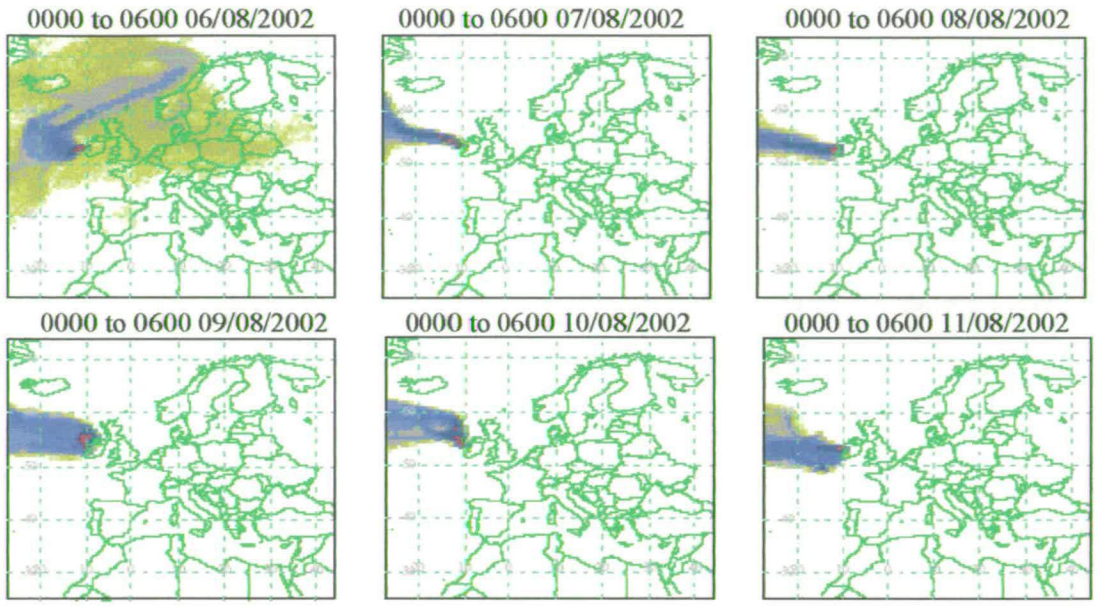

Figure 4.5. NAME back plots for the 6th-12th August 2002. Air masses were arriving generally from the west to north-west.

Hourly averages of wind speed for the 6th – 12th August are illustrated in Figure 4.6. The depression is clearly illustrated on the 8th when the wind direction changes from a strong westerly direction to a northerly direction. During this period increased numbers of calcium phosphate particles were detected. This particle type was also detected during the first meteorological period when air masses were arriving from the north indicating that the particle sampled on both days had a similar source (Figure 4.31). This particle type is discussed in more detail in Section 4.3.4.3. The wind direction also changed dramatically on the night of the 10th. Physical and chemical properties of the aerosol sampled during this period reflected particles that were arriving from the Atlantic with high numbers of coarse salt particles as well as occasional dust periods. Mace Head was exposed to the clean sector for 47% of the sampling time during the second meteorological period.

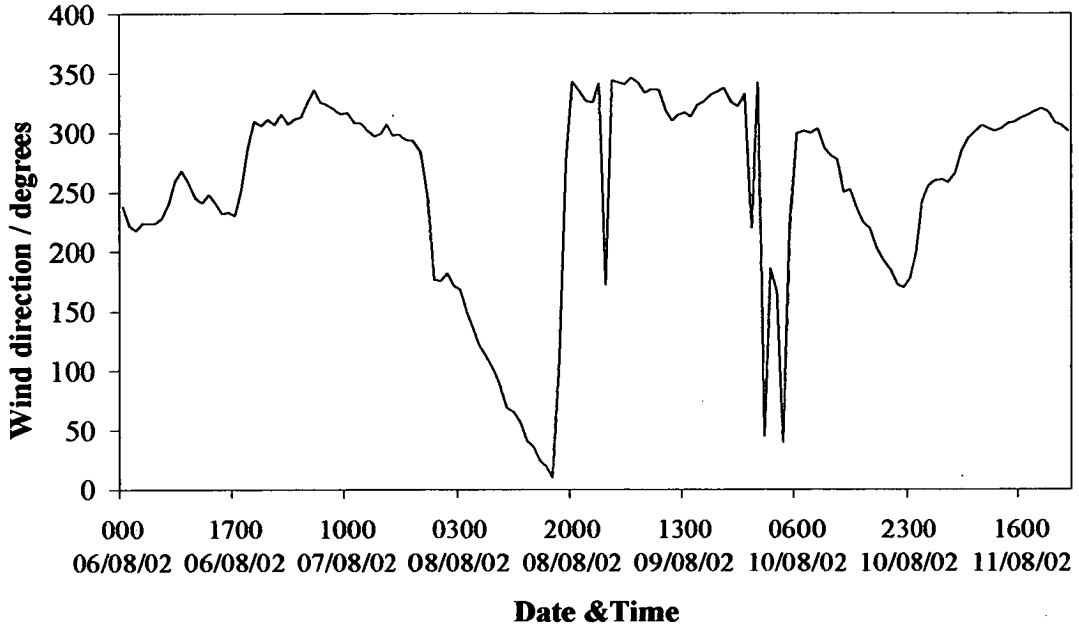

Figure 4. 6. Hourly averages of wind direction for 6th – 11th August during NAMBLEX.

Meteorological period three was characterised by another depression and occluded front passing over Mace Head and started on the 12th August and continued until 17th August. During this period three frontal systems passed over Mace Head, with the wind direction retaining a westerly component throughout (Figure 4.7).

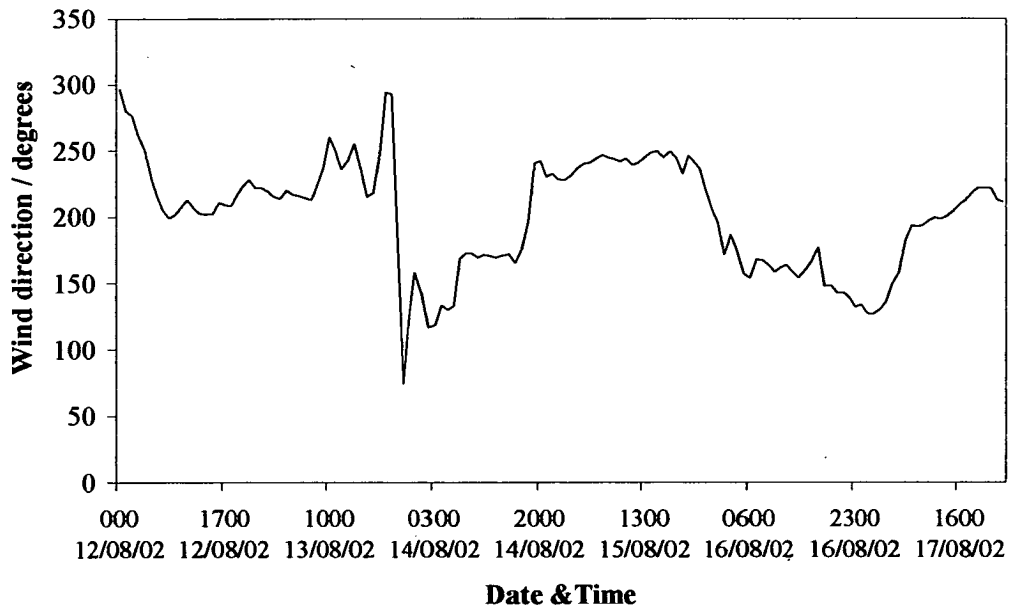

Figure 4.7. Hourly averages of wind direction for 12th – 17th August during NAMBLEX.

The particle composition observed during this period consisted of very pure and mixed sodium chloride as well as dust-type particles. Super-micron mode carbonaceous aerosols were also detected during this period and it is suspected that this carbonaceous type particle travelled over the Atlantic. This is discussed in more detail in Section 4.3.4.2. Back plots form the 12th – 17th August are shown in Figure 4.8. Higher wind speeds were experienced during this period, reaching a maximum of 20 m s^{-1} on the 17th of August and 15 m s^{-1} on both the 14th and 15th. Highest numbers of pure sea-salt were detected during these days. Clean air was observed 29% of the time

The only exception to the wind direction was observed during the night/morning of the 13th/14th, respectively, when the lower level wind vector rotated through the west to a south-easterly direction. This period was accompanied by very low wind speeds (< 2 m s^{-1}). During this period there was an increase in super-micron carbonaceous and aged/mixed sea-salt. Bursts of mixed and aged sea-salt are associated with periods of very slow moving air.

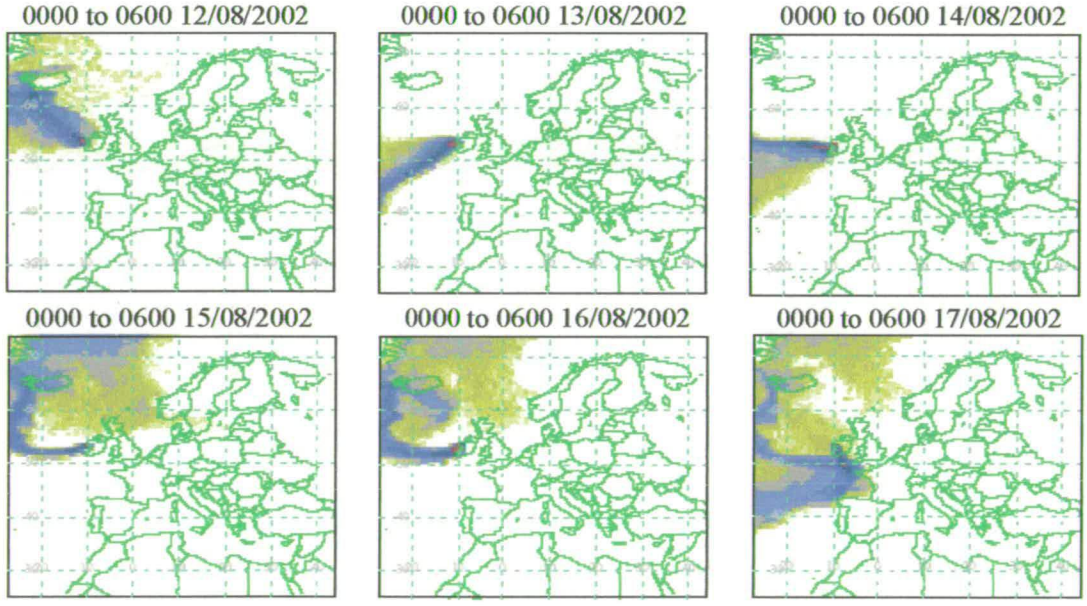

Figure 4.8. NAME back plots for the 12th -17th August 2002. Air masses were generally westerly throughout.

Period four started on the 18th and continued until the 28th of August; the ATOFMS only sampling until the 21st. The wind-speed dropped and anti-cyclonic conditions set in resulting in a stagnated air mass. The wind direction generally arrived from a westerly direction. The wind direction measurements show a weak representation of the sea breeze on the 18th to 20th (Figure 4.9), air mass back plots for the 18th -21st are illustrated in Figure 4.10. The particle composition during this period consisted of mixed and pure sea-salt as well as dust and carbonaceous species. Since the ATOFMS was not sampling during the fifth meteorological period it will not be discussed here but more information can be found in Norton *et al.* (2005).

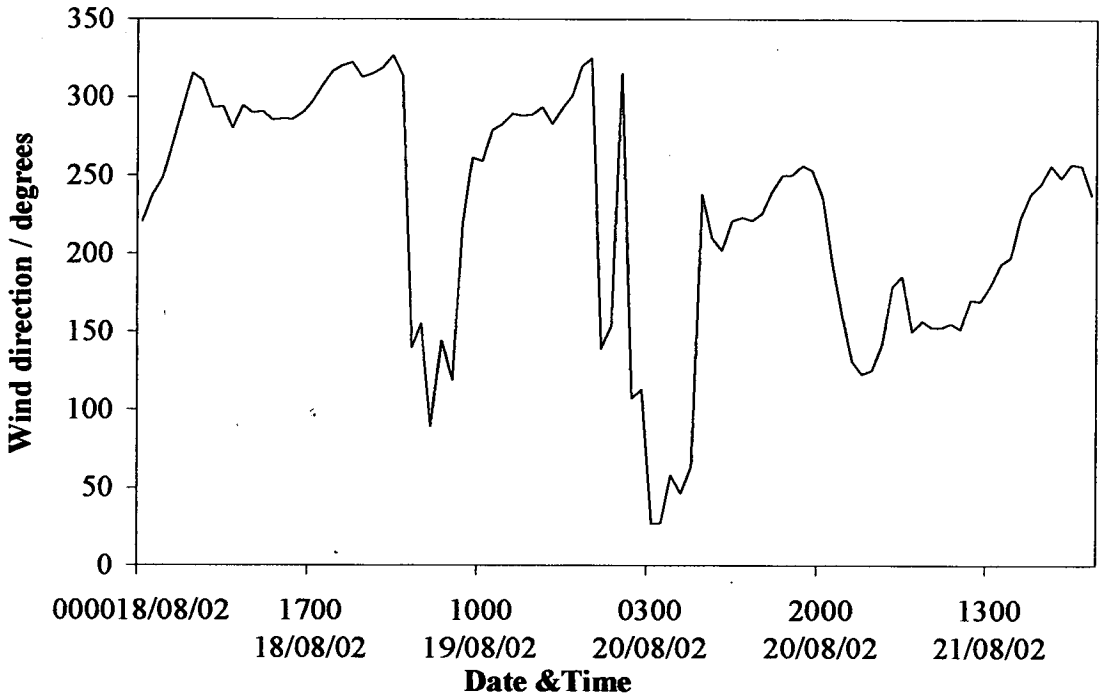

Figure 4.9. Hourly averages of wind direction for 18th – 21st August during NAMBLEX.

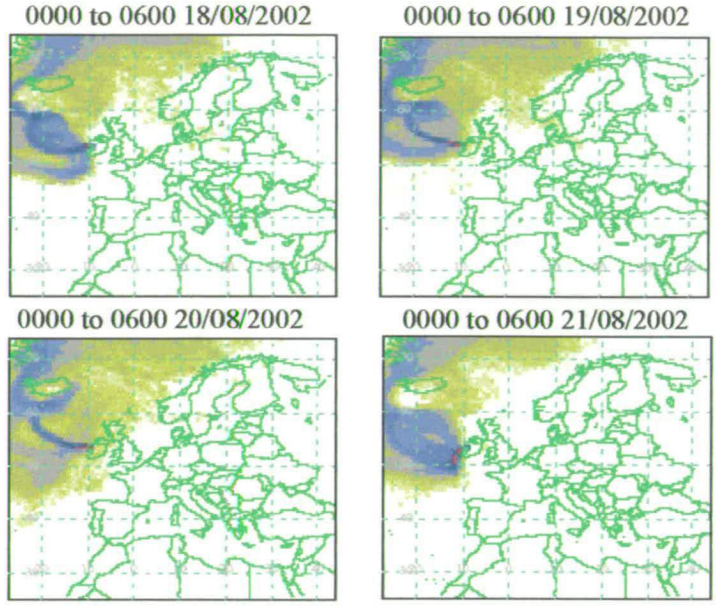

Figure 4.10. NAME back plots for the 18th -21st August 2002. Air masses were generally westerly throughout.

4.3.2. Hit rate

The number of particles that gave a mass spectrum was compared to the total number of particles that were sized by the two CW lasers in the particle sizing region. This is referred to as the hit rate and is shown as a function of time and meteorological period in Figure 4.11. As explained in Chapter 2.0 the ATOFMS can size particles using the two low powered Nd:YAG lasers but if a particle does not absorb the energy of the ablation laser it will not produce a mass spectrum and will be recorded as a missed particle. Certain chemical compounds absorb more strongly at the laser wavelength (266 nm) than others, for example the absorption coefficient of polyaromatic hydrocarbons at 266 nm is 10^3-10^5 mol cm^{-2} whereas pure alkali salts do not absorb at 266 nm due to their large band gap (Chapter 3). Using this information it is possible to broadly predict particle composition from the hit rate e.g. pure sea-salt particles will give a lower hit rate than carbonaceous species. From Figure 4.11 it is observed that the highest continuous hit rate was recorded from the 1st-5th August 2002 during the first meteorological period. As already mentioned this period was characterised by air masses arriving from over the continent containing

high numbers of carbonaceous particles. During the 15th and 17th of August lower hit rates were recorded, higher numbers of pure sea-salt was sampled on these days.

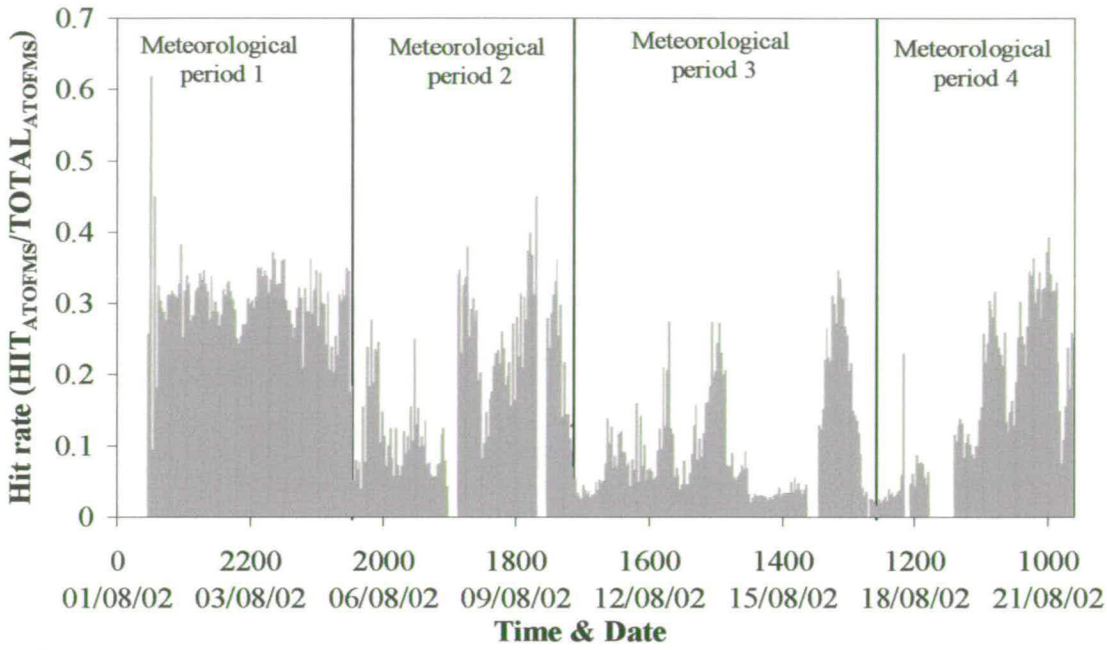

Figure 4.11. Hourly hit rate for the NAMBLEX sampling period.

4.3.3. ATOFMS inlet correction

The ATOFMS has been designed to detect particles with diameters between 0.3 and 3 μm although the inlet focuses particles with diameters between 0.5 and 1.6 μm with the highest efficiency. In order to obtain a true number concentration output from the ATOFMS instrument, raw ATOFMS data were compared with more conventional particle sizing instrumentation in order to develop a scaling factor which can be applied to the raw ATOFMS data to give a true atmospheric number concentration (Chapter 5). The size distribution data plotted in this chapter will show the scaled and unscaled ATOFMS number concentration using the scaling factor developed in Chapter 5.

4.3.4. Classification of particulate matter detected during NAMBLEX

Rapid changes in the size distribution, number density, and chemical composition of aerosols reaching a remote site such as Mace Head are caused by the arrival of different air masses. During NAMBLEX two different air masses arrived at Mace Head, the first was a continental air mass and arrived at Mace Head from the 1^{st}-5^{th} of August and contained high numbers of carbonaceous species. The second type of air mass arrived from the 6^{th} to the 21^{st} of August from the Atlantic bringing clean marine air.

The mass spectra of 191,504 individual particles were obtained over the entire NAMBLEX sampling period. Using the K-means algorithm, particles in the size range from 0.1 to 5 μm were divided into 20 different chemical classes. After manual inspection of each of the clusters the number of clusters were reduced to 4 large classes; Sea-salt, Dust, Carbonaceous and Other. Classes were only combined if their size distribution, temporal trends and mass spectral patterns were similar. Two other classes were identified by manual inspection of the data-set that were not previously identified as separate clusters by the K-Means algorithm. All particle types detected by the ATOFMS instrument are shown in Table 4.3. Each of the large particle classes were a combination of three or more clusters. Each of the particle types will be discussed in the following sections with regard to ion signals and temporal trends.

Particle type	*Typical ion signals and example m/z values*	*%*
K-means algorithm		
Sea-Salt		**77.4**
- Pure sea-salt	Na^+ (*m/z* 23), $(NaCl)_xNa^+$ (*m/z* 81), Cl- (*m/z* -35) & $(NaCl)xCl^-$ (*m/z* -93)	16.8
- Mixed sea-salt	Pure sea-salt + NO_2^- (*m/z* - 46), NO_3^- (*m/z* - 62)	43.4
- Aged sea-salt	Na^+, NO_2^-, NO_3^-, $(NaNO_3)xNa^+$ (*m/z* 108), $(NaNO_X)NO_Y^-$ (*m/z* - 131)	5.56
- Sea-salt w/o negative ion spectra	Na^+ (*m/z* 23), NaO^+/K^+ (m/z 39) $(NaCl)_xNa^+$ (*m/z* 81)	11.6
Carbonaceous		**16.4**
-Elemental carbon (EC)	C^+ (*m/z* 12) and C_3^+ (*m/z* 36)	6.54
- Secondary EC	EC + NO_2^- (*m/z* - 46) and SO_3^- (*m/z* - 80)	8.53
- EC with K^+ and SO_4^-	EC + K^+ (*m/z* 39) and SO_4^- (*m/z* -96)	1.31
Dust		**5.94**
- Al/Ti/Silicates	Al^+ (*m/z* 27), AlO^- (*m/z* -43), SiO_2^- (*m/z* -60), PO_2^- (*m/z* -63)	0.27
- Calcium	Ca^+ (*m/z* 40) and CaO^+ (*m/z* 56)	5.67
Other		**0.26**
- *Amines*	$C_3H_8N^+$ (*m/z* 58), $H_2NCH_{10}^+$ (*m/z* 74) and $NC_3H_{12}^+$ (*m/z* 86)	0.14
- KCl	K^+ (*m/z* 39) and $(KCl)K^+$ (*m/z* 113)	0.08
- Vanadium	V^+ (*m/z* 51) and VO^+ (*m/z* 67)	0.04
Manual classification		
Na-EC	Na^+ (*m/z* 23), $(NaCl)Na^+$ (*m/z* 81) & EC	2.64
Mixed Organic carbon/EC	EC & CH_3^+ (*m/z* 15), $C_2H_3^+$ (*m/z* 27), $C_2H_3O^+$ (*m/z* 43)	6.03
HMS	HSO_3^- (m/z 81), HSO_4^- (m/z -97) & $HOCH_2SO_3^-$ (m/z -111)	0.09

Table 4.3. Particle types resulting from the K-means algorithm/manual classification detected by the ATOFMS during NAMBLEX.

4.3.4.1. Sea-salt

Sea-salt particles play a significant role in both the chemistry and radiative transfer occurring in the lower troposphere. Due to their large surface area and typically low acidity, sea-salt particles are significant, if not dominant, removal sites for sulphur species and other gaseous compounds in the MBL. Marine aerosols affect climate directly through scattering and absorption of radiation and indirectly as CCN. In addition marine aerosol particles play an important role in the cycling of various elements through the atmosphere (Raes *et al*, 2000). Sea-salt particles are produced at the ocean surface by the bubble bursting resulting from the entrainment of air induced by wind stress. On bursting, these bubbles produce film and jet drops. These bubbles are most concentrated in whitecaps associated with the breaking waves which commences at wind speed of approximately 3-4 m s^{-1} (O'Dowd et al, 1997). The meteorological conditions along with the sampling location ensured that marine sea-salt would be the dominant particle type expected.

Sea-salt type particles contributed 77% to the total particle number detected. Four different types of sea-salt particles were identified during NAMBLEX, these were classified according to the degree of displacement of Cl^- peaks, with all Cl^- peaks present the particle was classified as being pure sea-salt (16.8%), mixed sea-salt (43.4%) contained ion signals for both Cl^- and NO_x[‡] and aged sea-salt (5.56%) particles were defined as those with all of the Cl^- being replaced with NO_x species. The fourth sea-salt class contained little or no negative ion mass spectra but positive ion signals for sea-salt. Similar spectra are reported again in Chapter 6. It is thought that this particle type may have be due to instrumental problems rather than a different particle type (Moffet *et al*, 2004). Figure 4.12 shows a timeline of mixed, aged and pure sea-salt particles detected during NAMBLEX. Considerably more particles have been assigned to the mixed sea-salt class when using the K-means algorithm (43.4%) than when using the ART-2a (14.5%) (Dall'Osto *et al*, 2005). On examination of the other classes detected by the ART-2a and spectra present in the mixed sea-salt class it appears that the other particle types were agglomerated by the

[‡] NOx refers to oxides of nitrogen

K-means algorithm. The K-means clustering algorithm did not identify any Mg-rich particle class in the NAMBLEX data set.

Mixed sea-salt particles were most prominent during the first meteorological period (1-5/8/02) and then again during the third meteorological period (12-17/8/02) when air masses were arriving from the west. The highest number of pure salt particles were detected between the 12/08/02 – 17/08/02. During this period clean air was observed 29% of the time also wind speeds on the 14th, 15th and 17th August were in-excess of 15 m s^{-1}. A size distribution showing both raw and scaled ATOFMS sea-salt number counts is shown in Figure 4.13.

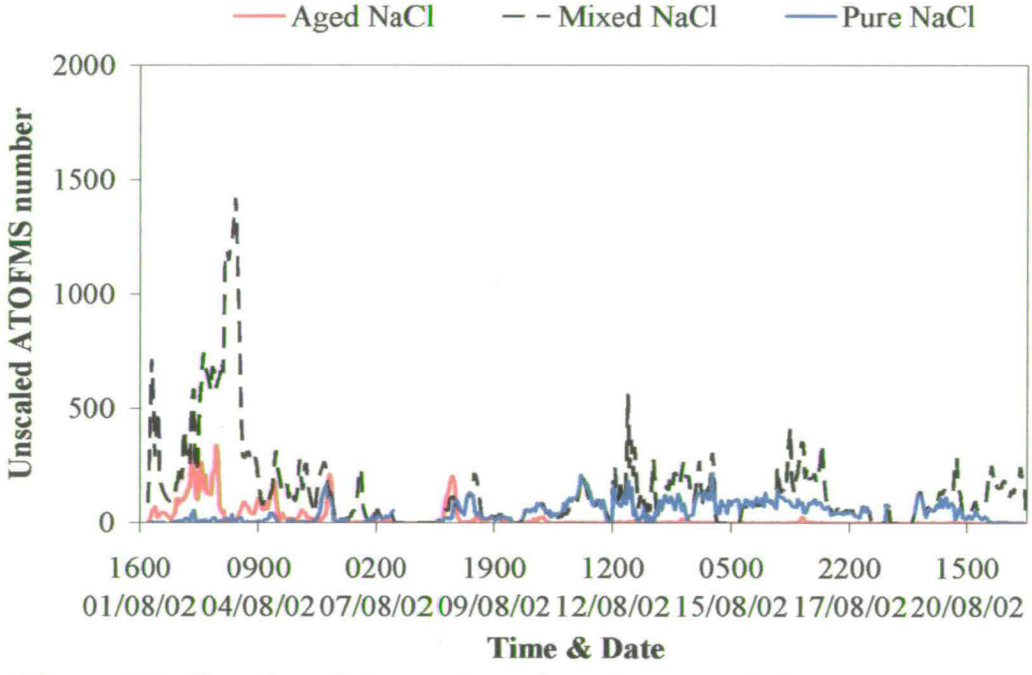

Figure 4.12. Time line of the numbers of particles containing ion signals for Aged, mixed and pure NaCl detected during NAMBLEX

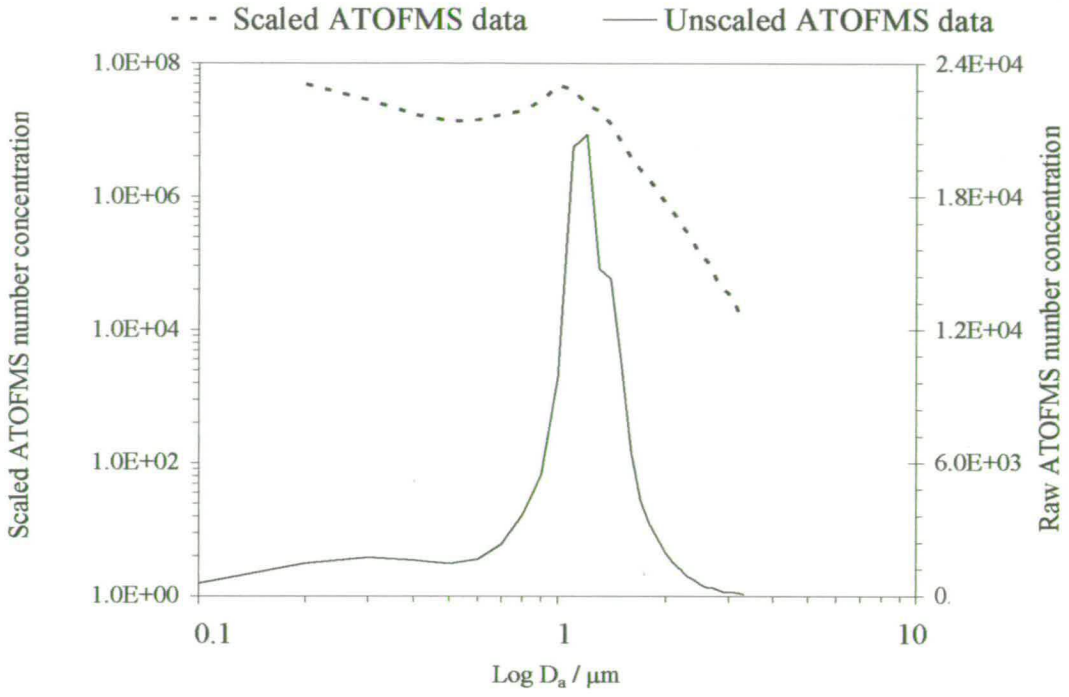

Figure 4.13. Size distribution of unscaled (solid line) and scaled (dotted line) ATOFMS counts for the total NaCl particles detected during NAMBLEX

During this study, sea-salt particles were identified by the presence of peaks for Na^+ (*m/z* 23), NaO/K^+ (*m/z* 39) and $(NaCl)_xNa^+$ (*m/z* 81, 139, 197). In the negative ion mass spectrum peaks are present for OH^- (*m/z* 17), Na^- (*m/z* 23), Cl^- (*m/z* 35), $NaCl^-$ (*m/z* 58), $(NaCl)_xCl^-$ (*m/z* 93, 151, 209) and $(NaCl)Cl(H_2O)_n^-$ (*m/z* 111, 129). Liu *et al.* (2003) reported mass spectra where sodium was detected with water cluster ion signals. The presence of peaks for $Na(H_2O)^+$ (*m/z* 41) and $Na(H_2O)_2^+$ (*m/z* 59) were observed in several mass spectra along with some negative sodium chloride cluster peaks for $(NaCl)Cl(H_2O)^-$ (*m/z* -111) and ($(NaCl)Cl(H_2O)_2^-$) (*m/z* -129) as well as the presence of peaks due to O^- (*m/z* -16) and OH^- (*m/z* -17). These peaks were detected in both the mixed and pure salt. Additional ion signals for nitrate, NO_2^- (*m/z* -46), NO_3^- (*m/z* -62), $(NaCl)NO_2^-$ (*m/z* -104) and $(NaCl)NO_3^-$ (*m/z* –120) were present in the negative ion mass spectra of those particles classified as mixed salt. Mixed and aged sea-salt aerosols were formed when sea-salt particles reacted with HNO_3 to form nitrate and release hydrogen chloride to the gas phase (Equation 4.2) (Harrison *et al*, 1999; Harrison & Pio, 1983; Pakkanen, 1996).

$$NaCl + HNO_3 \rightarrow NaNO_3 + HCl \qquad \textbf{(4. 2)}$$

Typical positive and negative ion mass spectra from a mixed, pure and aged sea-salt particle are shown in Figures 4.14 - 4.16.

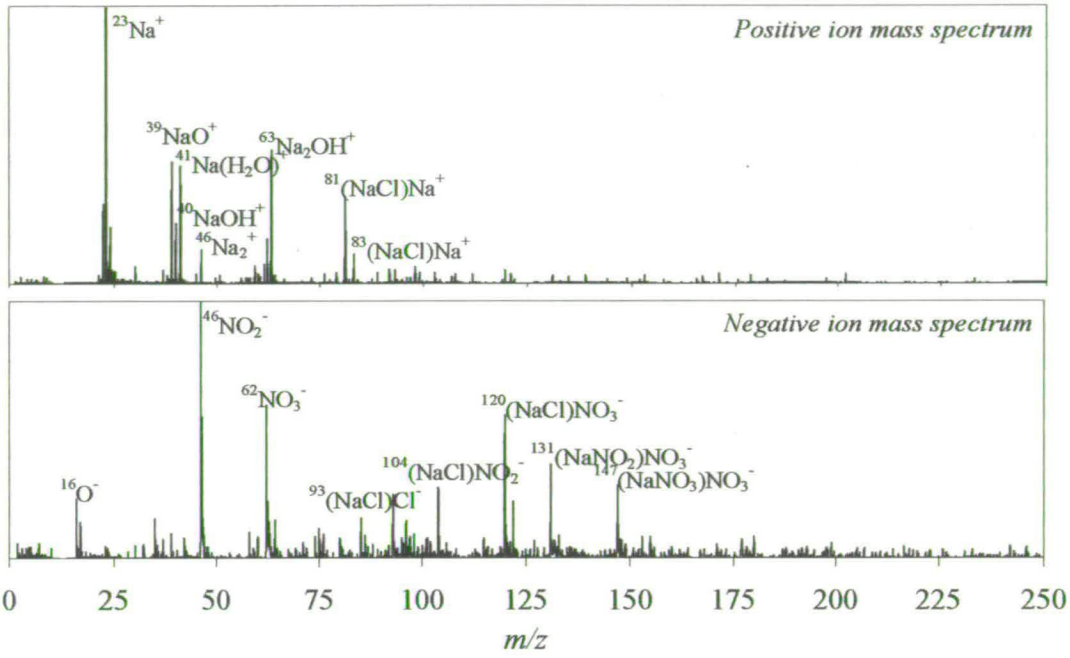

Figure 4.14. Positive and negative ion mass spectra from a single mixed sea-salt (2.15μm) particle sampled during NAMBLEX.

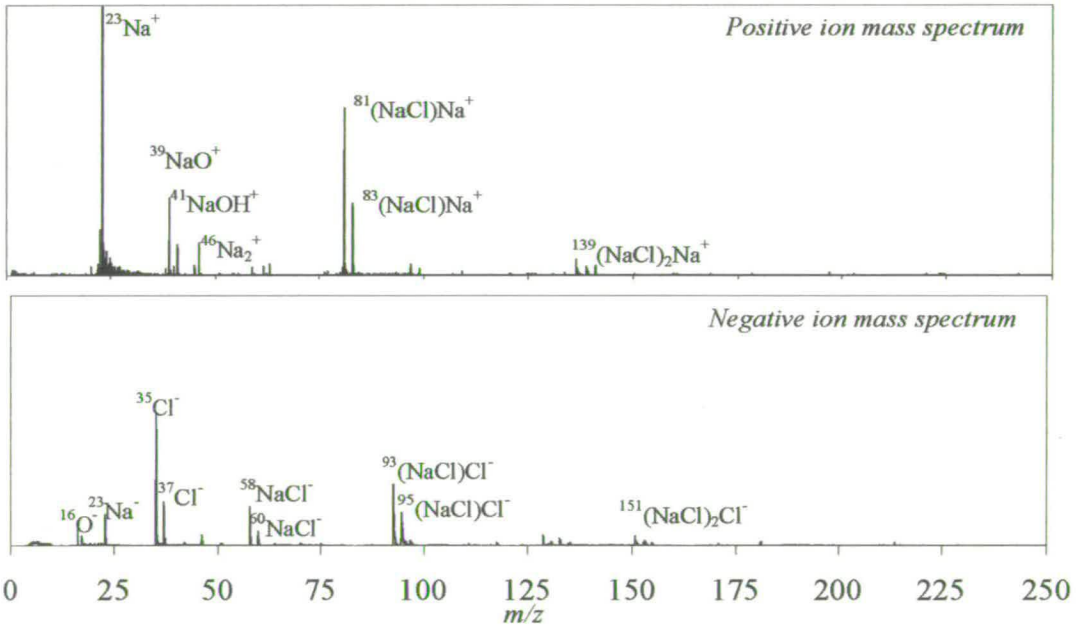

Figure 4.15. Positive and negative ion mass spectra from a single pure sea-salt particle (1.43 μm) particle sampled during NAMBLEX.

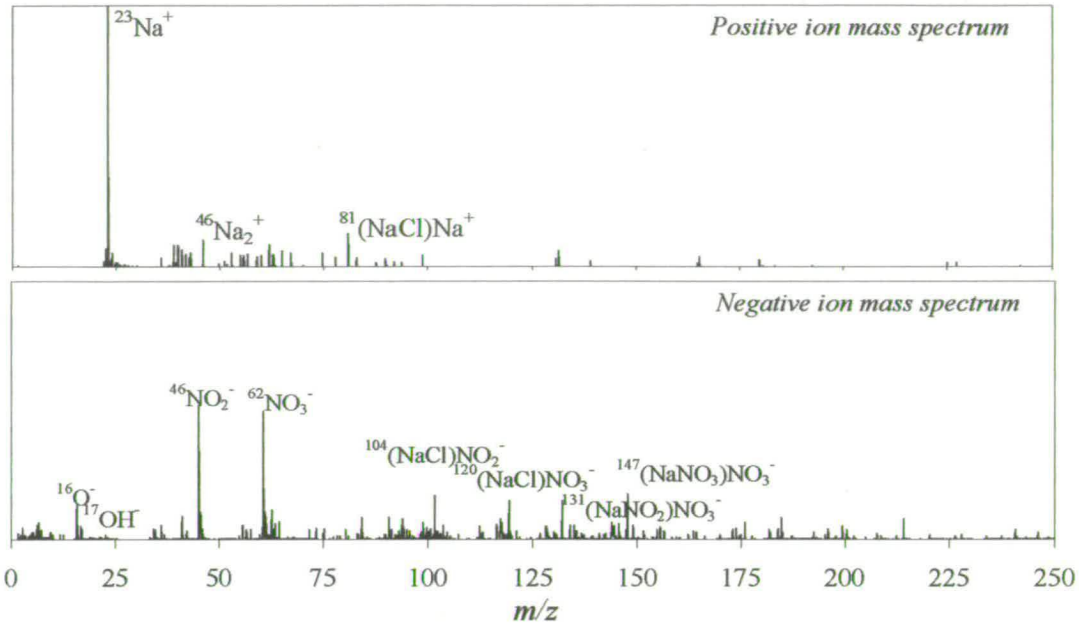

Figure 4.16. Positive and negative ion mass spectra for a single aged sea-salt particle (1.32 μm) particle sampled during NAMBLEX.

Heterogeneous atmospheric chemistry

Relative humidity (RH) plays an important part in the reactions of NaCl with nitric acid (Equation 4.2). If the RH is above 75%, the deliquescence point of NaCl, the particle becomes an aqueous droplet and with sufficient nitric acid the reaction can proceed to completion (Carson *et al*, 1995). But if the RH is low the particle will be solid and the reaction will be limited by diffusion in the solid (Langer *et al*, 1997). 60.6 % of the sea-salt detected during NAMBLEX was mixed or aged sea-salt and the relative humidity was always above 75%.

The ratio of the number of super-micron particles containing nitrate anions to the number of super-micron particles containing chloride anions was plotted against sampling time in Figure 4.17. The ratio was greater than unity for an air mass that has travelled over the continent, providing evidence for chloride displacement by acidic gases. Figure 4.17 indicates that, for particles detected during the period when NAMBLEX was impacted by continental air, the chloride originally present in the particle had been exchanged via the reaction shown in Equation 4.2.

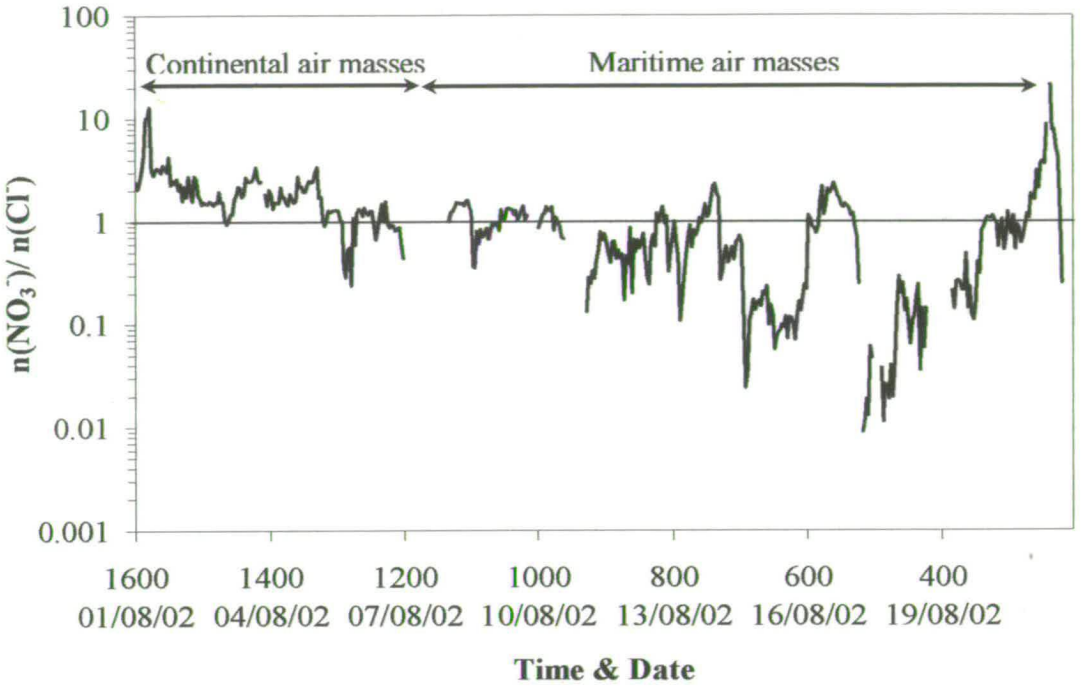

Figure 4.17. The temporal trend in the ratio $n(NO_3^-)/n(Cl^-)$ of the number of super-micron particles per hour containing nitrate and chloride. The ratio is greater than unity during the dirty period and less than unity during the clean period.

Some of the detected mixed or aged sea-salt particles show a peak at *m/z* 108 in their positive ion mass spectra; this is identified as $(NaNO_3)Na^+$. This peak has been used in previous experiments as an indicator of the reaction of NO_x species leading to the formation of sodium nitrate with displacement of chloride from the sea-salt particles (Gard *et al*, 1998). This heterogeneous reaction plays an important role in atmospheric chemistry because it is a permanent sink for gas-phase nitrogen oxide species. During NAMBLEX the signal at *m/z* 108 was not very strong but was sufficiently strong during the first period of the campaign to be used as a marker for heterogeneous reactions. On the 02/8/04 when the air mass was arriving from the continent carrying high number concentrations of secondary polluted particles it is possible to see a short diurnal trend in the data, shown in Figure 4.18.

The sea-salt particles detected during NAMBLEX were grouped into 1-hour time bins, and the relative peak area of the chloride and nitrate marker ions, $(NaCl)Na^+$ and $(NaNO_3)Na^+$, respectively, was determined in each single-particle mass

spectrum. The average relative area for both $(NaCl)Na^+$ and $(NaNO_3)Na^+$ was then determined for all sea-salt particles in each 1-hour time bin and plotted versus time. A diurnal trend in chloride replacement by nitrate on sea-salt particles is observed in Figure 4.18 starting at 000 02/08/02. The black squares indicated the relative area intensity of $(NaNO_3)Na^+$ particles and the yellow circles show the relative area intensity of the particles containing $(NaCl)Na^+$. The diurnal trend is only observed during this short period when air masses contained high numbers of secondary aged particles and gaseous species. Gard *et al.* (1998) illustrated a strong diurnal trend occurring in particles analysed by the ATOFMS over a 2-day period. Strong pollution episodes from the Los Angeles basin were sampled during this study. Sullivan *et al.* (2005) have recently demonstrated the ability of the ATOFMS instrument to measure in real-time the kinetic uptake of nitric acid on single mineral dust and sea-salt particles.

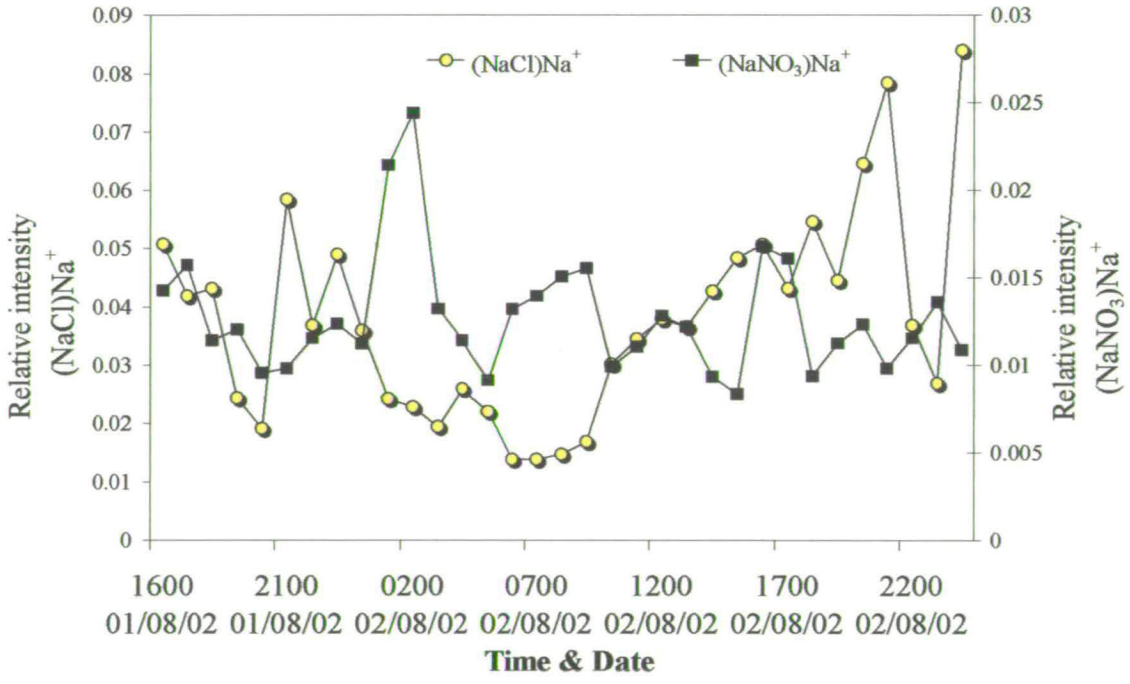

Figure 4.18. Possible evidence of heterogeneous chemistry during NAMBLEX 2004

Two things that seem to influence most of the observed chloride losses are the air transport time over continental areas and the concentration of sea-salt particles in the air. Chloride depletion is higher for air masses with longer continental transport times (1^{st}-5^{th} of August) and lower for air masses having larger sea-salt particle

loadings (6^{th}-21^{st} of August). The depletion of chloride from sea-salt particles is caused by the accumulation of strong acid anions, such as sulphate, nitrate, methyl sulphonic acid (MSA), and various dicarboxylic acid anions, into these particles (Kerminen *et al*, 1998).

It is important to note that these heterogeneous processes will only occur when sea salt loadings are high and are fresh. Due to the location of Mace Head, fresh sea salt particles will be produced in high quantities especially when wind speeds are high. During the period when this diurnal variation in $NaCl/NaNO_3$ was observed the wind speeds were 4 ms^{-1}. Sea-salt production increases with wind speeds and at wind speeds in excess of 7-11 m^{s-1}, the tearing of wave crests results in the injection into the marine boundary layer of ultra-large spume sea-salt particles.

If sea salt has been in the atmosphere for some time it will not have a diurnal signature. Furthermore the HNO_3 produced at night should exceed that produced in the day by NO_2 + OH. In studies carried out by Gard *et al.*(1998), model calculations were carried out to follow the air mass trajectories and calculate the relative mole concentrations of HNO_3 and NaCl. During the NAMBLEX study these calculations were not available. Therefore, although ion-exchange reactions between NaCl and HNO_3 are possible, without addition information on the mole fractions or formation rates of the HNO_3 and NaCl it is not possible to say with confidence that this is the process being observed in Figure 4.18.

4.3.4.2. Carbonaceous particles.

On manual classification of the sea-salt clusters, it was found that almost 3% of sea-salt particles also contained ion signals for carbon. These particles were detected in the highest number concentrations when the air masses were arriving from the east. These particles have also been detected in air masses arriving over the Atlantic. Mixed NaCl and carbon particles suggest that there is in-cloud processing occurring and also that carbonaceous particle are being transported over the Atlantic Ocean before arriving at Mace Head. This particle type was not identified as a separate cluster by the K-means algorithm.

Carbonaceous aerosol contributed 16% to the total number of particles detected during NAMBLEX. 79% of the particles identified as containing ion signals for carbon were detected during the first meteorological period when the air masses were arriving from the continent. Figure 4.19 shows all the carbonaceous particles sampled during NAMBLEX subdivided into sub and super-micron mode particles.

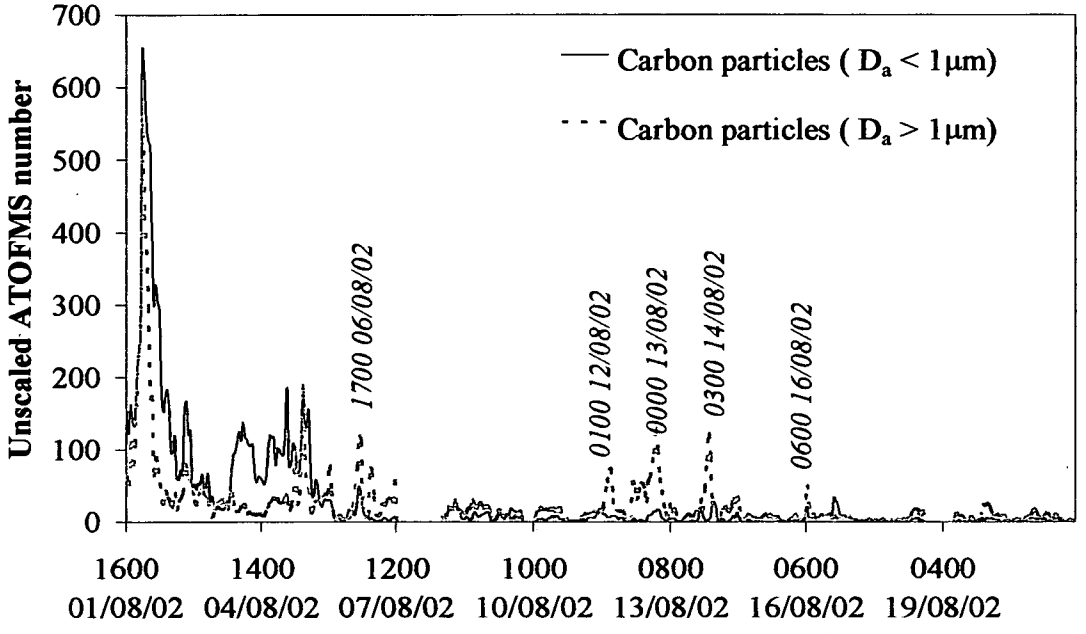

Figure 4.19. Time line of sub and super-micron carbonaceous particles sampled during NAMBLEX

The carbonaceous episodes occurring during NAMBLEX correlate with increased hit rate shown in Figure 4.11. Carbonaceous particles were present predominantly in the sub-micron size distribution. A size distribution, illustrating the scaled and unscaled particle number, is shown in Figure 4.20.

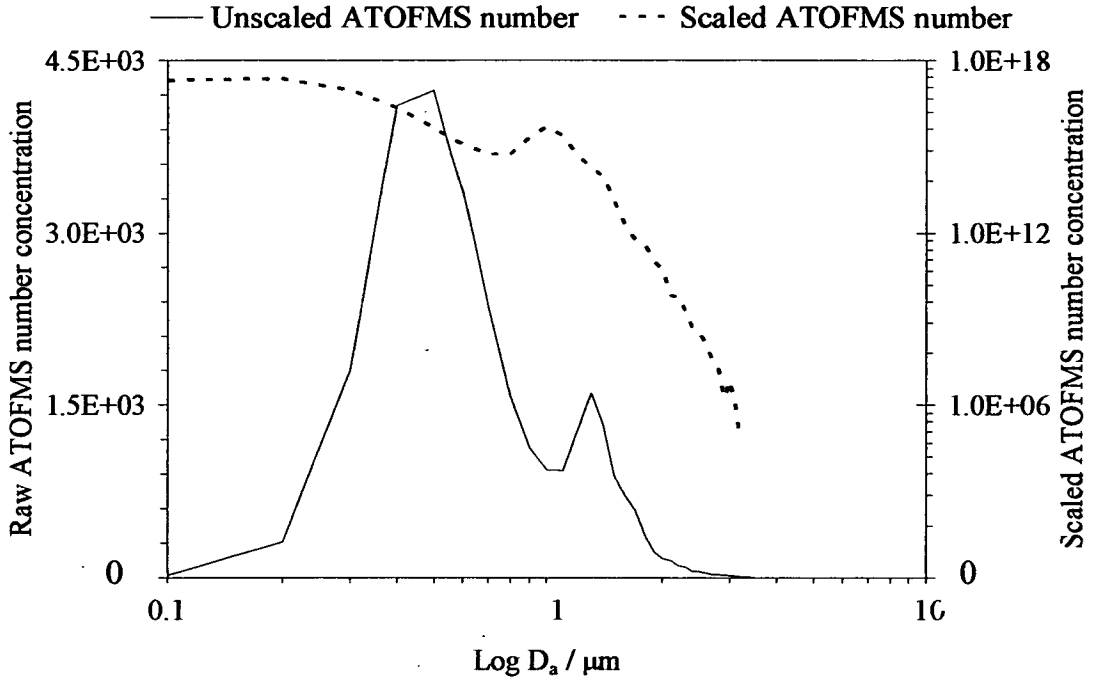

Figure 4.20. Size distribution of unscaled (solid line) and scaled (dotted line) ATOFMS counts for carbon particles detected during NAMBLEX

The presence of super-micron carbon episodes on the 13th, 14th and 16th August 2002 (Figure 4.19) are correlated with bursts of mixed sea-salt detected during this period (Figure 4.12). Back trajectory analysis reveals that air masses were arriving at Mace Head from the west, suggesting polluted air masses from North America/Canada. Carbonaceous particles associated with sodium suggest that anthropogenic combustion products are being transported across the north Atlantic to Mace Head. It is important to note that dirty air masses coming from USA/Canada bring carbon-containing particles associated with sodium that are distributed predominantly in the coarse mode, suggesting secondary formation on existing particles.

During the same period Dall'Osto *et al* (2005) identified a magnesium rich particle with ion signatures for carbon. It is suggested that this particle class is thought to be of biogenic origin. Recent publications by Cavalli *et al* (2004) and O'Dowd *et al* (2004) have shown increasing carbonaceous content in particles present in the marine environment as the particle size decreases. It is possible that the carbonaceous episodes shown in Figure 4.20 are from a biogenic origin but it is also necessary to consider the possiblility that these particles have been transported over the Atlantic,

especially since all the particles are present in the supermicron mode contrary to the findings reported by O'Dowd and Cavalli.

The carbon particle type was subdivided into four different carbon type particles. These were elemental carbon (EC), carbon with ion signals for K^+, secondary carbon and mixed organic carbon/EC. The elemental/black carbon particles gave ion signals for C^+ (*m/z* 12) and C_3^+ (*m/z* 36). Occasionally longer chained elemental carbon was present with higher mass ions for $C_4^{+/-}$, $C_5^{+/-}$, $C_6^{+/-}$ but as high laser irradiances were used to sample the ambient particles a lot of fragmentation was observed in the mass spectra. Elemental or black carbon is considered to be a good marker for biomass burning and fossil fuel combustion. This elemental particle type did not contain any other ion signals species. Figure 4.21 shows a single particle mass spectrum for short chained elemental carbon.

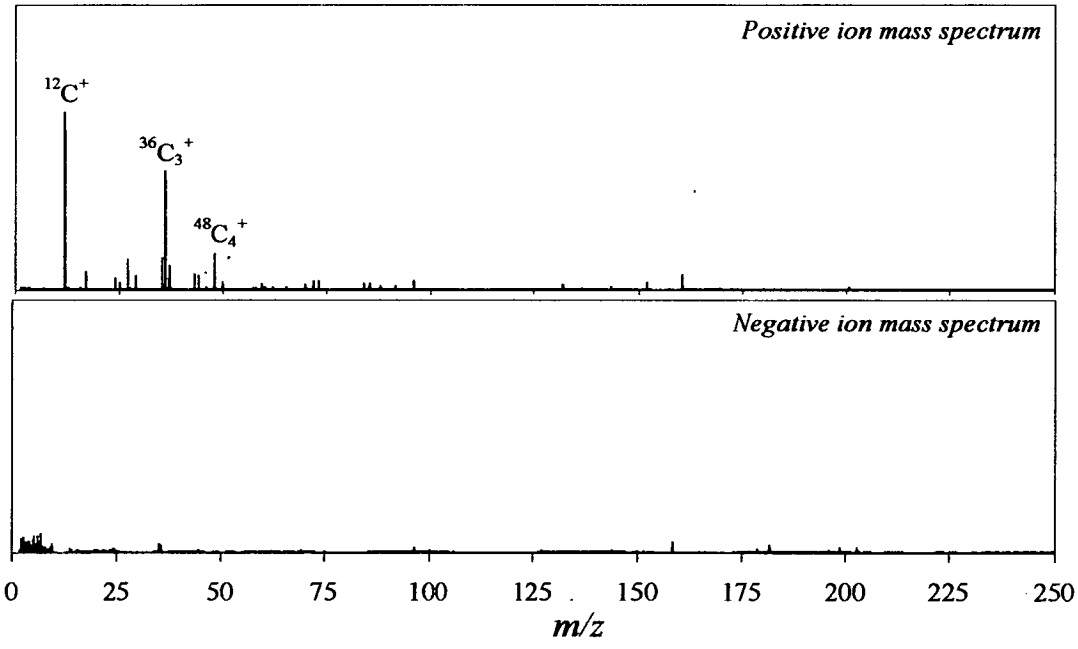

Figure 4.21. A positive and negative ion mass spectrum for a single short chained elemental carbon particle with an aerodynamic diameter of 0.61 μm

It was common to find ion signals for $^{39}K^+$ in the positive ion mass spectra of carbon containing particles. K^+ is a strong indicator of combustion sources including biomass burning (Silva *et al*, 1999) and coal combustion. This particle type correlated well with ion signals for sulphate. 53% of the sub-micron carbon particles

contained ion signals for K^+. Studies have shown that diesel exhaust engine does not produce detectable amounts of potassium (Gaudichet *et al*, 1995). Positive and negative ion mass spectra representative of a typical carbon-containing particle with K^+ are shown in Figure 4.22.

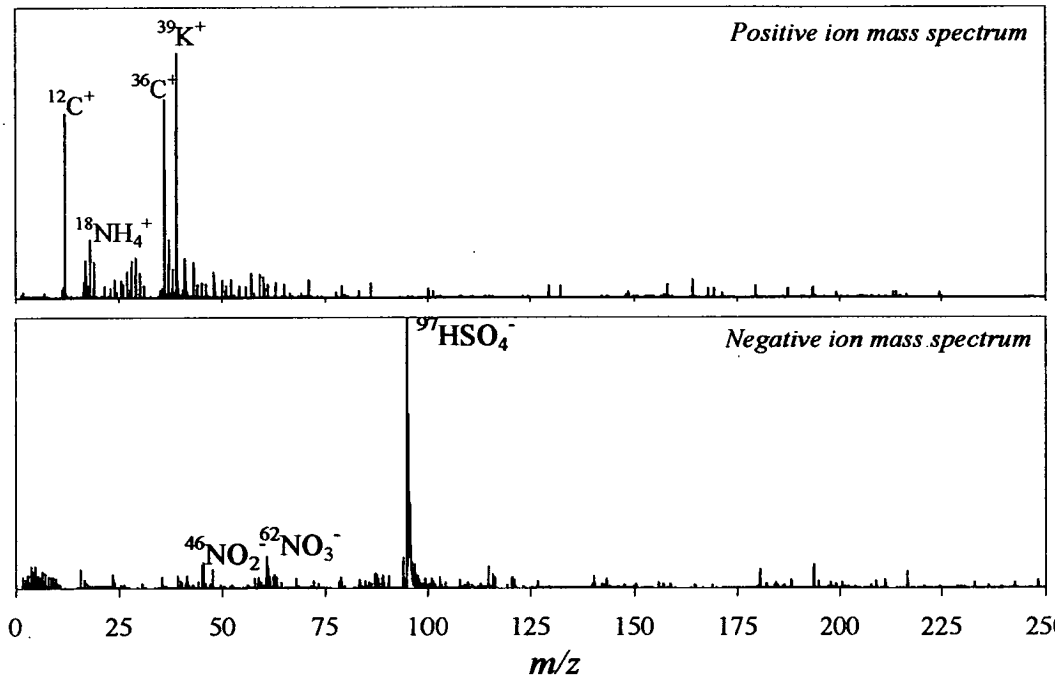

Figure 4.22. Positive and negative ion mass spectra from a secondary elemental carbon with K^+ as well as both sulphate and nitrate species (0.64 μm).

In the positive ion mass spectrum ion signals for C^+ (*m/z* 12), NH_4^+ (*m/z* 18), C_3^+ (*m/z* 36), K^+ (*m/z* 39), and in the negative ion mass spectrum signals for NO_2^- (*m/z* -46), NO_3^- (*m/z* 62) and HSO_4^- (*m/z* -97) were detected. The presence of sulphate in carbonaceous particles can result from direct emission by combustion sources, coagulation, cloud processing, and/or condensation and reaction of sulphur oxides on particles. Average sulphate associations for particles with aerodynamic diameters between 0.3 and 1 μm were determined to be 31% for carbon particles with K^+. Other studies have reported averages of 75% of sulphate associations with carbon particles containing K^+ (Guazzotti *et al*, 2003). In the particles sampled during NAMBLEX there appears to be higher sulphate associations with super-micron carbonaceous particles containing K^+ (59%) suggesting that the aerosol may be more aged than the aerosol detected in previous studies. The presence of chloride and/or

sulphate in combustion related particles depends on the temperature of formation of the particles as well as their aging processes (Ruellan *et al*, 1999a). In the case of particles produced from biomass burning, Gaudichet *et al.* (1999b) have indicated that near the emission source more chloride occurs in the observed soot particles than those collected further downwind from the sources, indicating the evolution from KCl to K_2SO_4.

During NAMBLEX the presence of chloride and sulphate signals associated with biomass burning particles were investigated. Between the 1-5/08/02, when the air masses were arriving over the continent, the biomass aerosols contained strong chloride signals indicating that the source may be local. A significant increase in the number of carbonaceous particles containing K^+ with sulphate was observed on 05/08/02. This suggests that the air masses containing this particle type may be associated with long range transport. The carbon particles sampled during this day also had a bimodal distribution with more particles detected in the super-micron mode than those sampled on previous days.

Carbon-containing particle with K^+ and Li^+

Using manual classification methods it is possible to determine the sources of certain particle types by investigating other elemental signals associated with them. In the case of carbon-containing particles with potassium, the presence of other species can be used as an indication of the original source of the detected particles.

Lithium, when present in carbonaceous particles has been reported to be an indicator for coal combustion. Guazzoti *et al.* (2003) reported that Li^+ was almost never present in the single particle mass spectra of particles produced from biomass/biofuel burning but it was commonly associated in particles produced by coal combustion processes. The presence of Li^+ in K^+ containing particles detected during NAMBLEX was investigated but only very low levels of particles containing Li^+ and carbon were detected. These results suggest that most of the carbon-containing particles with K^+ are likely to result from biomass or biofuel burning. An example of a sub-micron K^+ containing carbonaceous particle with Li^+ is shown in Figure 4.23.

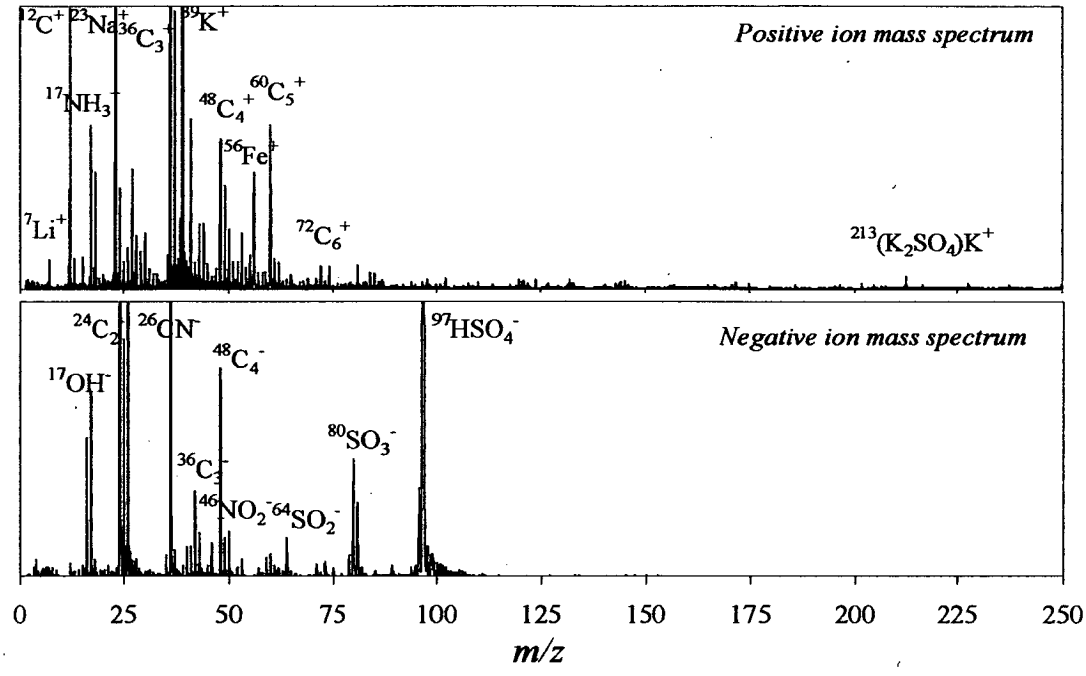

Figure 4.23. Positive and negative ion mass spectra for a secondary elemental carbon with K^+ and Li^+ (0.56 μm).

Studies have also shown that carbon-containing particles containing no ion signals for K^+ are likely to have arisen from the combustion of fossil fuels with little or no potassium, such as diesel. 47% of the total number carbon particles contained no detectable potassium signal. This indicates that there is a considerable fraction of carbonaceous material from the combustion of fossil fuels, such as diesel. The highest numbers of these particles were detected on 2nd, 4th & 5th of August 2002. Local or long range transport could have contributed to the presence of these particles.

Secondary Carbonaceous species

Carbonaceous species were also associated with nitrate such as NO_2^- (*m/z* 46) and NO_3^- (*m/z* 62) and sulphate such as HSO_4^- (*m/z* 97) and SO_3^- (*m/z* 80) and were classified as secondary EC. The presence of these peaks in the mass spectra serve as indicators that these carbon-containing particles have undergone reaction with NO_x and SO_x[§] species. The hydrolysis reaction of N_2O_5 in aerosol particles or cloud droplets to form nitric acid is a potentially important contributor to night time

[§] SOx refer to oxides of sulphur.

heterogeneous reactions in the atmosphere since it represents a principal sink of NO_x species. Rapid conversion of nitric acid to NO_x has been postulated to take place in aerosols as well (Chatfield, 1994). Figure 4.24 shows that sulphate and nitrate often co-exist in the same particle.

A number of secondary carbon particles also give signals for ammonium and nitrate together. The presence of ammonium nitrate in particles may result from the reaction of ammonia and nitric acid (Wexler & Seinfeld, 1990). Significant anthropogenic sources of ammonia are nitrogen based fertilisers, industrial emissions, and animal waste.

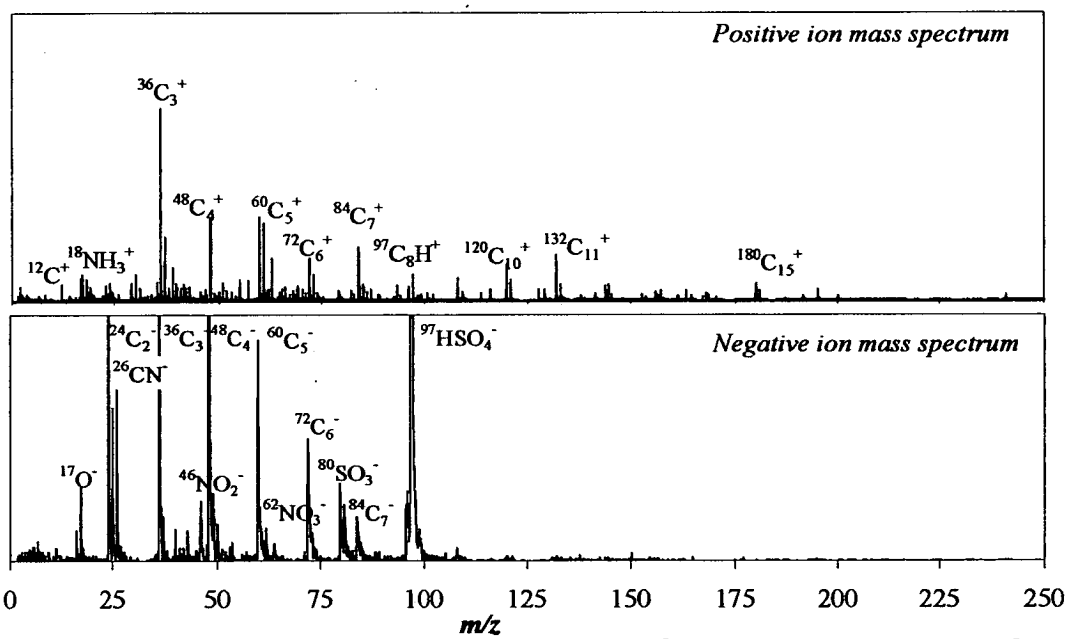

Figure 4.24. Positive and negative ion mass spectra from a secondary elemental carbon with both sulphate and nitrate species (0.80 μm).

Figure 4.25 shows the time-line for both primary and secondary elemental carbon. Elemental or unreacted carbon is present mainly at diameters less than 1 μm where as the secondary carbon appears to be evenly distributed between the sub and super-micron modes (Figure 4.26).

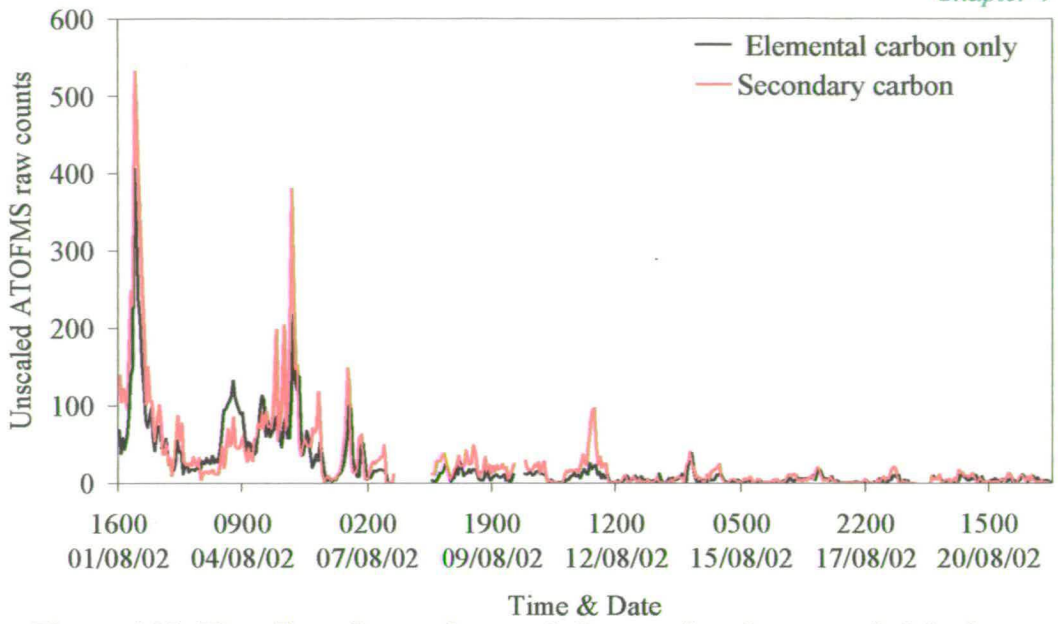

Figure 4.25. Time-line of secondary and elemental carbon sampled during NAMBLEX.

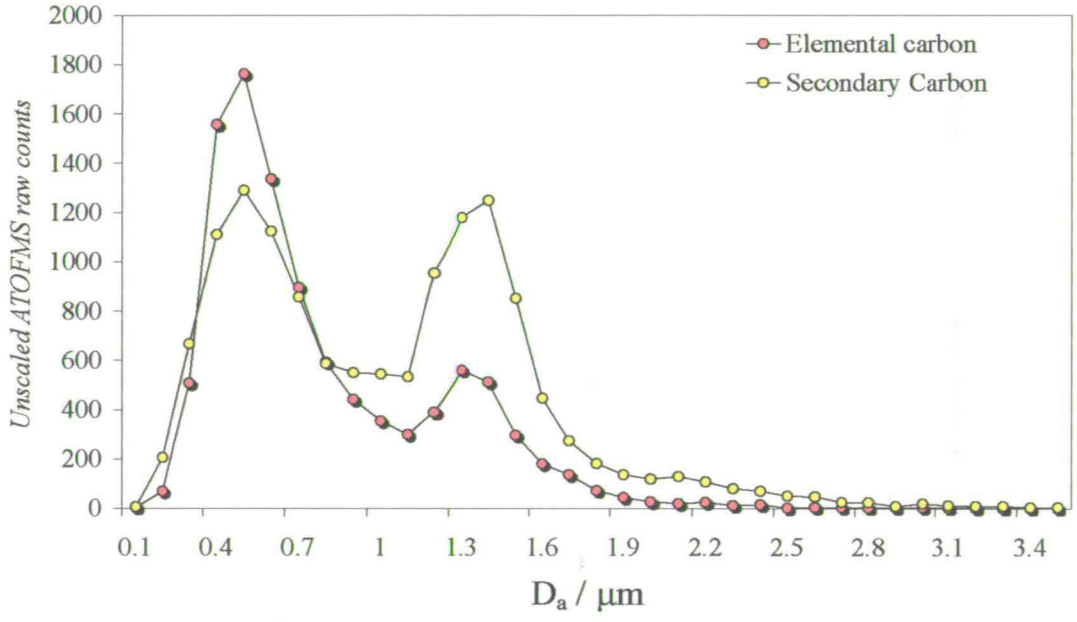

Figure 4.26. Size distribution for elemental and secondary carbon

Organic carbon particles

Castro *et al.* (1999) reported low carbonaceous particle concentration at Mace Head compared with urban areas. In their study a high value of 10.8 for the ratio of organic carbon (OC)/black carbon (BC) suggested that in the summer there is increased formation of secondary organic carbon, due to the more favourable conditions for

gas-to-particle conversion. OC was identified through manual inspection of the K-means cluster classes. The OC particles identified were mixed with signals for EC. In these particles ion signals for C^+ (*m/z* 12), CH_3^+ (*m/z* 15), $C_2H_3^+$ (*m/z* 27), C_x^+ (*m/z* 36) and $C_2H_3O^+$ (*m/z* 43) were present. These particles were mainly detected during the 1st-5th August 2002 but two other episodes occurred during the night of 12th & 13th August 2002. The size distribution of these particles was mainly in the sub-micron fraction. The size distribution of the organic carbon particles detected on the 12th & 13th had a broader distribution with a larger number of particles in the super-micron fraction. O'Dowd *et al.* (2004) recently described how sub-micron organic carbon detected at Mace Head was due to a biogenic origin. It was suggested that sea-salt generated through bubble bursting when a surfactant layer is present can lead to sub-micron particles with a high organic content and little sea-salt. This is a very significant finding as organic matter can significantly affect the cloud droplet number concentration and it has not previously been included in global climate models.

Organic carbon particles have both primary and secondary sources. Particulate organic carbon has a secondary origin from physical or chemical adsorption of gaseous species on the surface of aerosol particles, a process that can happen under sub-saturation conditions (Pandis *et al*, 1992). These particles are normally found in the sub-micron fraction. Super-micron organic carbon particles are produced mainly by mechanical processes, associated with the emission of plant spores and pollen, vegetation debris, tyre rubber, and soil organic matter.

Amine containing particles

A small sub class of the carbon type particles was identified as containing ion signals for amines. This particle class contributed less than 0.2% to the total number of detected aerosol particles. The amine class was labelled as such based on the presence of major ion peaks for $C_3H_8N^+$ (*m/z* 58), $C_3H_9N^+$ (*m/z* 59), $H_2NC_4H_{10}$ (*m/z* 74), NC_3H_{12} (*m/z* 86) and minor unidentified peaks at *m/z* 154 and 184 (Figure 4.27). Low molecular weight aliphatic amines are emitted by a variety of anthropogenic and biogenic sources, constituting an important class of environmental pollutants due to their toxic and odorous properties. A number of short chained alkyl-amines have

been detected in industrial emissions and car exhausts as well as air samples from cattle farms, waste incinerators, and sewage treatment plants (Angelino *et al*, 2001).

The amines in this study were only present in the super-micron mode and are usually coupled with a large potassium signal. The negative ion mass spectra of these compounds had a number of ions for nitrate and sulphate species. It has been reported that reaction with HNO_3 may occur in polluted urban areas. Very few particles were classified in this group making it difficult to examine correlations with RH or temperature which might have revealed whether this particle class underwent gas-to-particle partitioning.

As these compounds were only detected with diameters > 1μm and contain negative ion signals for nitrate and sulphate it is likely that these particles are a result of long range transport from polluted regions. This is further supported by the strong correlation of the number of amine particles with wind direction arriving from the south/north-east. Many of the spectra identified have a peak at *m/z* 104. A similar particle type was detected by Moffet *et al.* (2004) and it was reported that there were no correlations with temperature or RH. It was suggested that likely sources of this particle type included swine or poultry farms, combustion activities, synthetic or natural fertilisers, sea spray and reactions of NO_x with biogenic compounds (Moffet *et al*, 2004). It should be noted that on the west coast of Ireland there are both animal and agricultural farms as well as an abundant supply of sea-salt.

Reactions with atmospheric oxidants such as OH and O_3 are the major removal processes for these organic nitrogen compounds (Equation 4.3),

$$NH_3 + OH \xrightarrow{K_{OH}} NH_2 + H_2O \qquad \textbf{(4.3)}$$

where k_{OH} is the reaction rate constant (1.5×10^{-13} cm^3 s^{-1}). The reaction rates reported for amines are 150-400 times faster than the reaction rate with OH and NH_3 therefore oxidation by OH is a more important removal process for amines than for

NH_3, where the reaction with OH is probably not the dominant removal process (Van Neste *et al*, 1987).

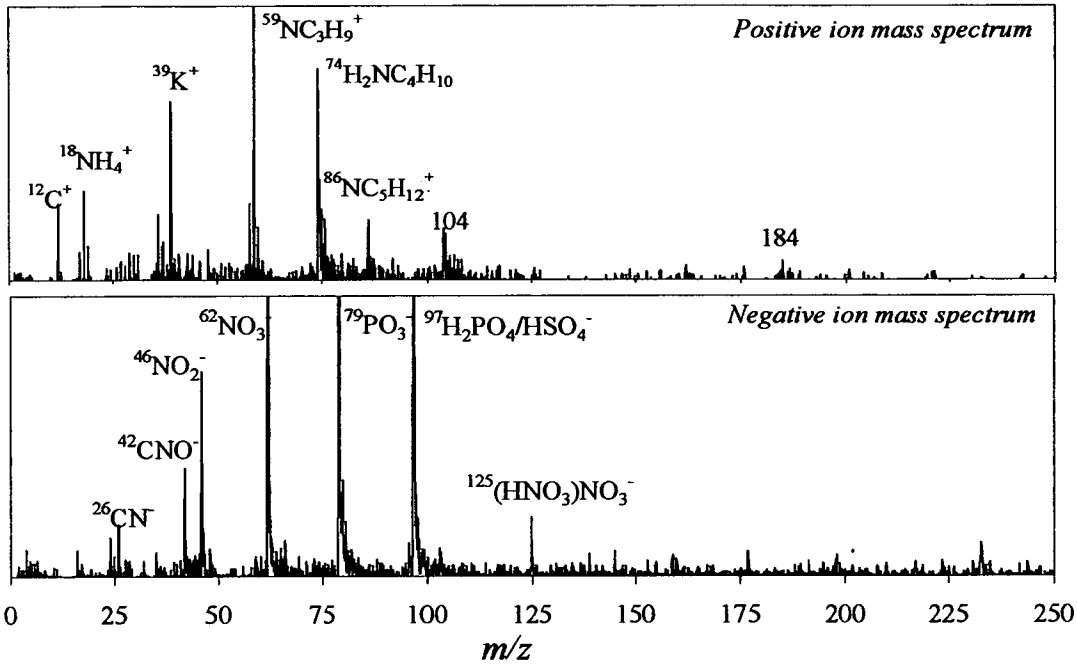

Figure 4.27. Positive and negative ion mass spectra sampled from a 1.78 μm size amine particle

Dall'Osto *et al*, (2005) used an ART-2a to classify the NAMBLEX data, an amine particle class was also detected but only during two distinct periods. The particle class detected here in this thesis occurred more frequently and correlated well with easterly wind directions.

Hydroxymethansulphonate (HMS)

During NAMBLEX a prominent marker for fog/cloud processing, Hydroxymethansulphonate (HMS) was observed in a small number of single particle mass spectra (<0.1%). HMS is identified in the negative ion mass spectra of individual particles sampled at *m/z* -111 ($HOCH_2SO_3^-$). Whiteaker and Prather (2003) assigned the peak at *m/z* -111 as HMS and confirmed this by analysing HMS particles using a controlled laboratory studies. HMS is an important component in atmospheric fog and cloud chemistry and is the product of the aqueous-phase reaction between formaldehyde and the bisulphite ion (Whiteaker & Prather, 2003)

The ion signal for HMS at *m/z* -111 overlaps with that of $(NaCl\text{-}H_2O)Cl^-$ but both can be distinguished by the use of isotope ratios as well as investigating other ions present in the positive and negative ion mass spectra. Particles containing the HMS also contained ion signals indicating the presence of sulphur species, such as SO_3^- (*m/z* 80), HSO_3^- (*m/z* -81), HSO_4^- (*m/z* -97).

In the mass spectra of this particle type there was no/little Na^+ present but strong signals for NH_4^+ are detected. Whiteaker and Prather (2003) showed, through laboratory studies, that no peak at m/z -111 was present for the pure salt NaHMS but when ammonium sulphate was added a peak at m/z -111 was produced. This was attributed to the matrix effect in the DI process. This is significant as ambient particles sampled at Mace Head contain a large amount of sodium relative to ammonium which explains why only small amounts of HMS are detected by the ATOFMS. An example of positive and negative ion mass spectra containing HMS are shown in Figure 4.28.

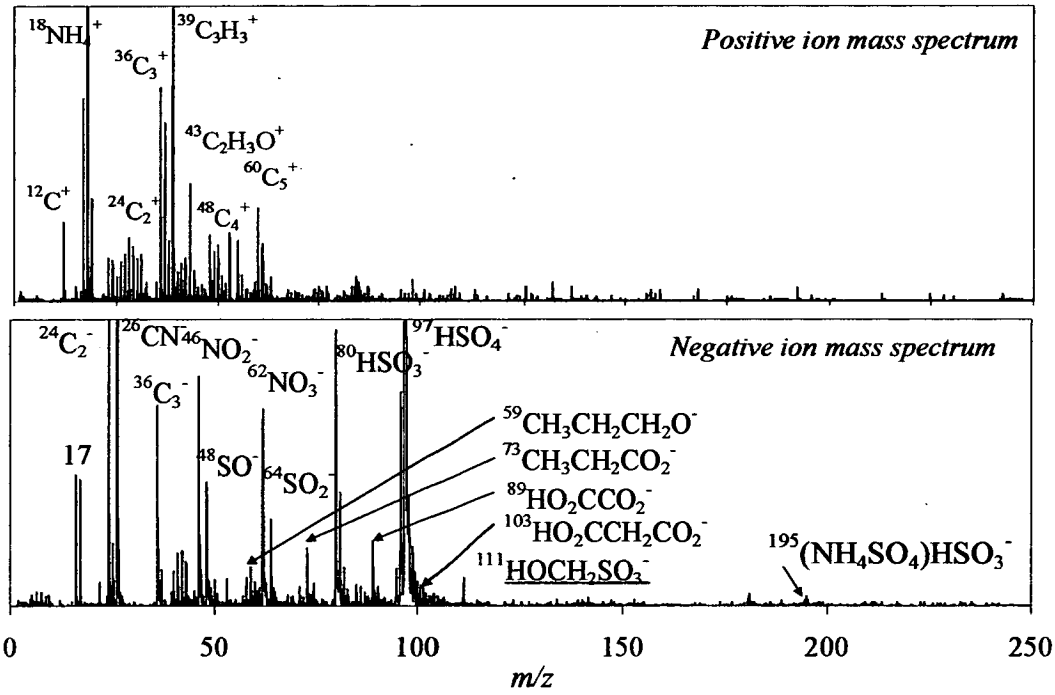

Figure 4.28. Positive and negative ion mass spectra from a particle containing ion signals for HMS

The use of the ATOFMS for measuring the presence of HMS in particles can provide important information in regions where fogs and clouds play a role in the

transformation of the aerosol. All of the HMS-containing particles sampled contain carbonaceous components and secondary aerosol species such as ammonium, nitrate and sulphate. A time-line of these particles is shown in Figure 4.29.

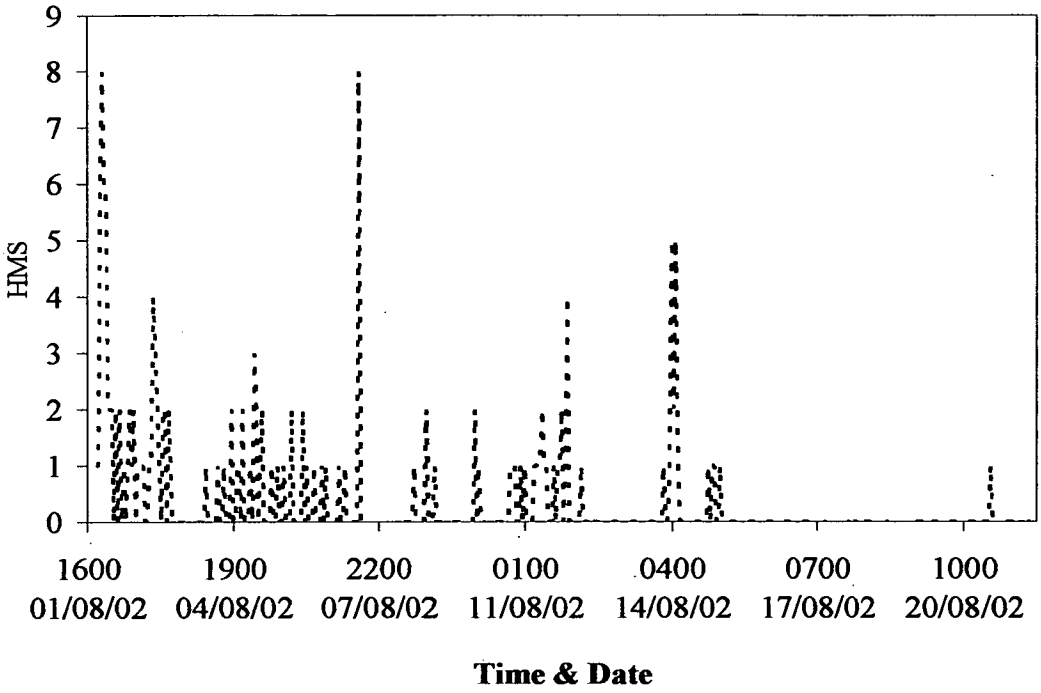

Figure 4.29. Temporal trend of the number of particles classified as HMS

Some mass spectra (~34%) containing HMS had peaks for oxidised organics (Figure 4.28) such as malonate ($HO_2CCH_2CO_2^-$ (m/z 103)), oxalate ($CHO_2CCO_2^-$ (m/z 89)), propionate ($CH_3CH_2CO_2^-$ (m/z 73)) and acetate ($CH_3CO_2^-$ (m/z 59)). The co-existence of HMS with oxidised organic peaks in the same particle suggests that some of the oxidised organics were formed by aqueous phase reactions. The HMS particles detected during NAMBLEX were mainly found in super-micron particles (78%). The abundance of oxidised organics in larger particles is consistent with aqueous reactions (Blando & Turpin, 2000). Similar size distributions were reported by Whiteaker and Prather (2003).

The formation and stability of HMS has been shown to be highly dependent on the pH of the particle or droplet, as well as the concentrations of formaldehyde, bisulphite ions, and oxidants present. The most relevant chemical equilibria involve

the dissolving of SO_2 in water, hydration, and complexation with aqueous formaldehyde. Equations 4.4-4.8 show some of the important reactions in the formation of sulphate species in the atmosphere.

$$SO_{2(G)} + H_2O \rightarrow SO_2.H_2O \quad (4.4)$$

$$SO_2.H_2O \rightarrow H^+ + HSO_3^- \quad (4.5)$$

$$HSO_3^- \rightarrow H^+ + SO_3^{2-} \quad (4.6)$$

$$HCHO_{(AQ)} + H_2O \rightarrow CH_2(OH)_2 \quad (4.7)$$

$$HCHO_{(AQ)} + HSO_3^- \rightarrow HOCH_2SO_3^- \quad (4.8)$$

Lee *et al.*(2003) reported that the RH dependence of oxidised organics suggests that gas particle partitioning also controls the abundance of the oxidised organics in aerosols. Lee *et al.*(Lee *et al*, 2003) were able to correlate high number of HMS with RH and oxidised organics and suggest that aqueous reactions, gas particle partitioning and photochemistry all contribute to the oxidised organics formation. As RH was always greater than 75% during NAMBLEX and only low numbers of HMS particles were detected it was not possible to investigate the role of RH in the formation of HMS particles detected during NAMBLEX.

Besides being HMS, the negative ion signal at *m/z* -111 could also be another organo sulphur compound, $CH_3OSO_3^-$, methylsulphate. However the correlation of the mass spectra found during NAMBLEX with that reported by other studies (Whiteaker & Prather, 2003; Lee *et al*, 2003; 2002) and the correlation of other ion signals suggests otherwise. No dimethylsulphite (m/z -126) was detected in these particles.

4.3.4.3. Dust containing particles

The third general particle type sampled during NAMBLEX was dust. A number of different sources of airborne dust particles have been identified (Hinds, 1999). Over a billion tons of mineral soil-derived dusts are transported annually from the African Sahara/Sahel over the Atlantic Ocean to the Americas and Caribbean and across the Mediterranean into Europe. The atmosphere is a global bridge connecting the continents. For this reason dust is an important contributor to radiative forcing as well as transporting micro organisms and organic chemical pollutants around the

globe. The radiative effect of dust particles on the earth as well as the effect on heterogeneous processes in the atmosphere is relatively unknown (Figure 1.1). Dust particles contribute more Tg yr^{-1} to the total estimated particles emitted to the atmosphere than organic carbon, black carbon, sulphate and nitrate. Among natural sources the two most significant are windblown soil or sand and volcanic eruptions. Anthropogenic sources of dust particles include metallurgical and farming processes, transportation (brake pad dust and road dust, (Schofield, 2003)) waste incineration and power plants. The majority of the dust particles detected during NAMBLEX had aerodynamic diameters > 1 μm. A size distribution showing both scaled and unscaled ATOFMS counts for dust is displayed in Figure 4.30.

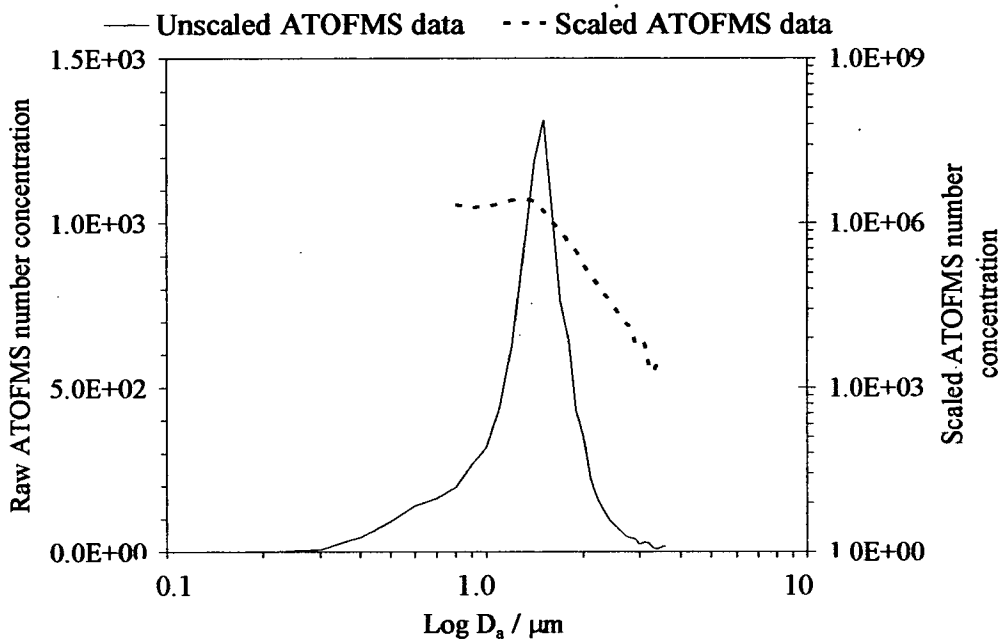

Figure 4.30. Scaled (dotted line) and unscaled (solid line) size distributions for all particles classified as dust.

Only 6% of all the particles detected during NAMBLEX were classified as dust. A number of different dust particles were observed during NAMBLEX. Some commonly detected ions in dust particles include calcium, iron, aluminium, magnesium, potassium, sodium, and titanium. The most commonly observed type of dust particle was identified by the presence of peaks in the positive ion mass spectra for Na^+ (*m/z* 23), Ca^+ (*m/z* 40) and CaO^+ (*m/z* 56). The second most abundant aerosol

type identified during NAMBLEX was dust particles containing ion signals for Al^+ (*m/z* 27) as well as Na^+ and negative ion mass spectra containing O^- (*m/z* -16) and AlO^- (*m/z* -43). A number of silicate (SiO_2^- (*m/z* -60) and SiO_2^-(*m/z* -76)), phosphate (PO_2^- (*m/z* -63) and PO_3^- (*m/z* 79)). Nitrate and sulphate ions were also identified as well as a percentage of carbonaceous ions. The common occurrence of many of these peaks (nitrate, sulphate and carbon) demonstrates how transformed the dust particles are, even at a rural marine site.

Calcium-type dust particle

The calcium particles were detected throughout the campaign and contributed 5.67% to all the detected particles. This particle type was detected at higher concentrations between the 2^{nd}-3^{rd}, 8^{th} –11^{th} and also on the 20^{th} August. Since calcium dust particles were present throughout the campaign it is assumed that this particle is from a local source, possibly from wind blown soil/rock dust around the Mace Head area (Huang *et al*, 2001).

58% of the calcium particles contained ion signals for nitrate (NO_2^- (*m/z* -46) and NO_3^- (*m/z* -62)). Ammonium and sulphate ions were detected in 5% and 6% of the calcium particles, respectively. HNO_3, SO_2, or H_2SO_4 can react with carbonates such as $CaCO_3$ and $MgCO_3$ on wet soil particles to form coarse mode nitrate and sulphate (Zhuang *et al*, 1999). Non-sea-salt sulphate formed by the reaction of H_2SO_4 with soil particles has also been reported (Pakkanen, 1996; Yeatman *et al*, 2001). The ability to detect nitrate and sulphate in dust particles is an advantage of single particle analysis. Obtaining this information is important for assessing the radiative properties of the particles as well as determining the ability of mineral particles to become CCN. Dust particles can scatter and absorb solar radiation. The dominance of mineral dust in aerosol light scattering has been discussed previously, indicating that mineral dust could be an important climate-forcing agent over regions where dust concentrations are high (Raes *et al*, 2000).

Phosphate (17%) and silicate (4%) ions were also present in calcium particles. The calcium-type particles containing phosphate ions were detected at high levels during

the 1st-5th and again on the 8-9th August (Figure 4.31). The air masses on the 8-9th appear to be circulating over Ireland as shown in Figure 4.32. As explained in section 4.3.1, a strong depression passed over Mace Head on the 8th causing the wind direction to change from a westerly direction to a northerly direction, implying that this particle type originates from a northerly source.

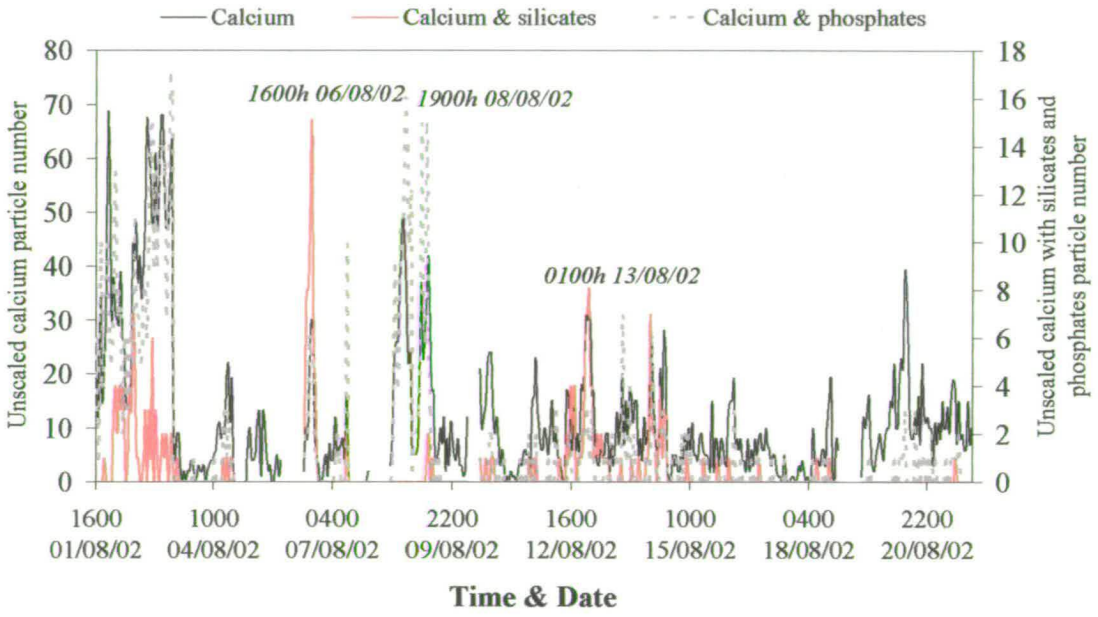

Figure 4.31. Time series showing the association between calcium silicates and phosphate.

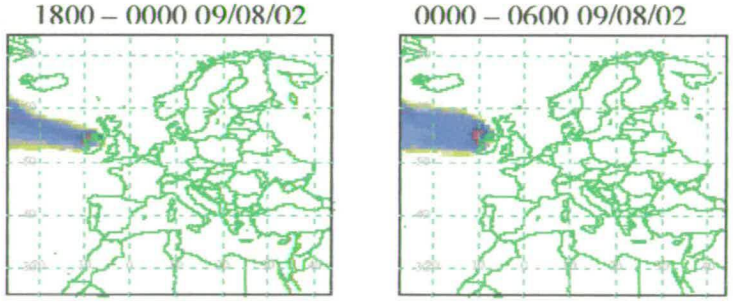

Figure 4.32. Air mass back plots for 8th & 9th of August 2002

The increase in calcium and silicate containing particles occur during two short periods on the 6th and 13th and correlate well with the aluminium type particle (Figure 4.34). Titanium ion signals were also associated with calcium particles.

These ion signals were mainly associated with calcium during first stage of the NAMBLEX and also during the 13th and 14th. The variation in air masses during these periods suggests that these particle types are not from the same source or that they are both a result of local emissions.

Aluminium-type dust particle

The second type of dust particle detected contained strong ion signals for aluminium and silicate material and contributed 0.3% to the total dust particles detected. This particle type was only detected during two short periods, one on 6th 18 h and the other 13th 03 h. Titanium ions were also associated with these particles and has been detected previously in single particle mass spectra from soil dust (Silva *et al*, 2000). Air mass back plots for 6th and 13th August 2002 (Figure 4.33) show that the air masses are predominantly approaching from the clean sector between 180 and 300°. Longer range back trajectory maps may provide more detailed description of these air masses. Suggestions have been made that this aluminium/silicate particle type could be the result of long ranged transport of soil dust from Saharan regions (Huang *et al*, 2001; Dall'Osto *et al*, 2004).

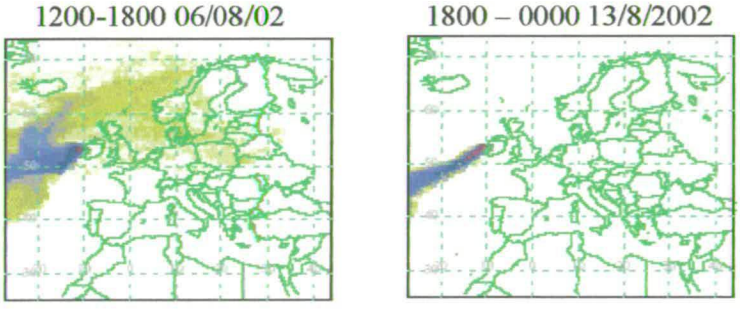

Figure 4.33. Air mass back plots for 6th & 13th August 2002

Aluminium particles were found to be associated with sulphate (35%), nitrate (40%) and phosphates (15%) ions. Aluminium particles associated with phosphate ions were detected during the 1st – 5th August whereas the silicate and aluminium particles were only detected during short periods on the 6th and 13th of August. This is clearly illustrated in Figure 4.34.

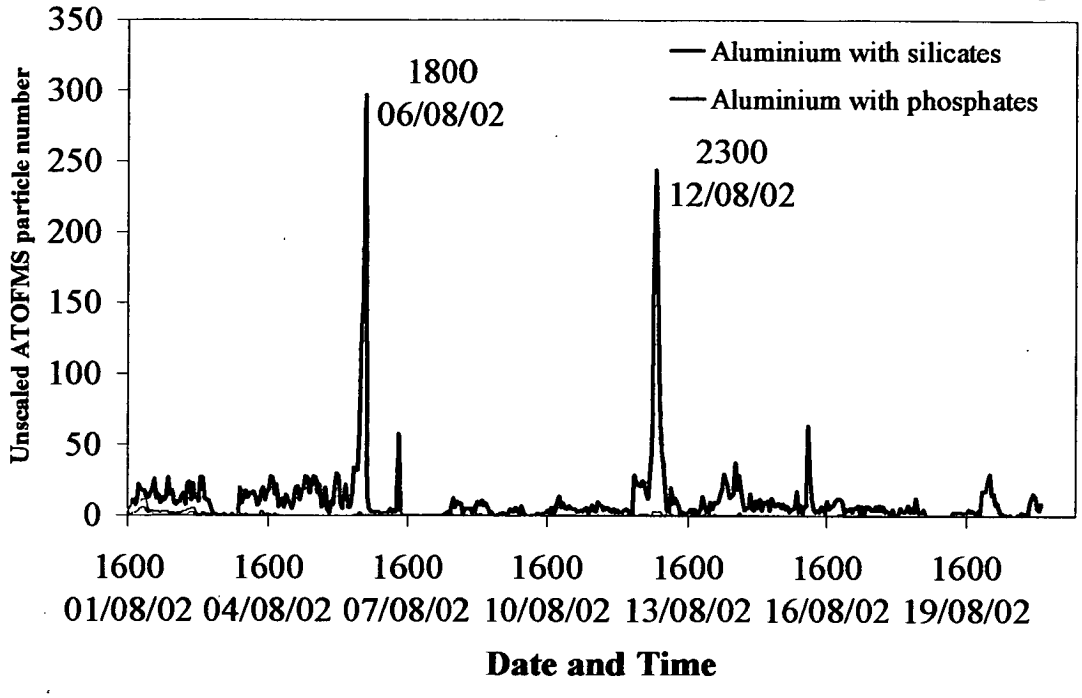

Figure 4. 34. Time series of aluminium particles with silicates and phosphates

During the field campaign, more complex particle types were also detected, including combinations of the general types discussed, such as dust, elemental carbon, sulphates and sea-salt particles with dust. Many of the dust particles sampled contained ion signals for carbonaceous species. This indicates that these particles are significantly aged and reacted with carbonaceous species. The majority of dust particles containing carbon were detected during the first five days of sampling when the air masses were arriving from the east. A representative spectrum is shown in Figure 4.35. These particular combinations indicate that agglomeration processes occurred. Dust particles associated with sea-salt have been observed previously in Beijing (China) and Nagasaki (Japan) as well as over remote oceans (Fan *et al*, 1996).

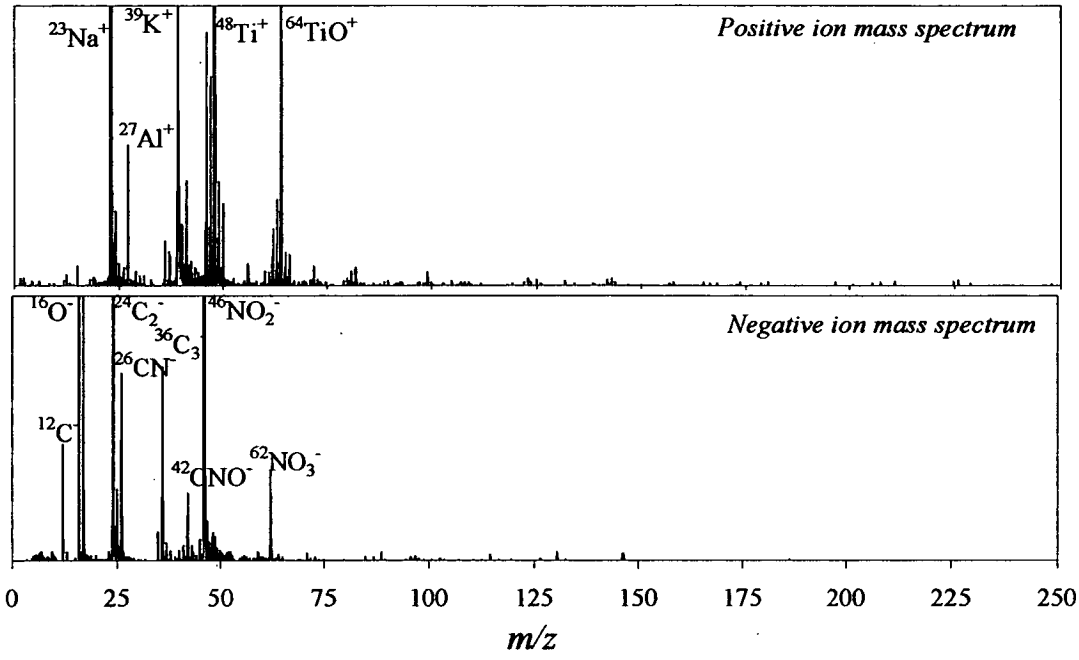

Figure 4. 35. Positive and negative ion mass spectra from an aluminium dust particle containing titanium and nitrates (1.52 μm)

Dust combined with sea-salt

Dust particles associated with sea-salt, particularly calcium containing dust particles were seen during the start of the NAMBLEX field campaign when air masses were arriving from the continent. Andreae *et al.* (1986) suggested that the presence of internal mixing of sea-salt and dust aerosols was due to in-cloud processing where (hydrophobic) dust particles become encased by droplets within the cloud and then act as a CCN. Since most cloud droplets do not fall as rain but evaporate, the solute from the original CCN is left behind as a residue on the surface of the mineral particle. The next time such a particle enters a cloud it will act as a CCN because of the soluble material on its surface (Andreae *et al*, 1986).

4.3.4.4. Other particles

Trace elements can be detected with the ATOFMS including V, Ti, Ba, Pb and Mn. The presence of these elements in different particle classes, alone or combined, provides information on the possible sources of such particles during NAMBLEX. For example, lead-containing particles were observed during NAMBLEX. The

presence of lead is indicated by the isotopic peaks at *m/z* 206, 207, 208 in the positive ion mass spectra of the particles. A number of particles containing lead were detected during the early hours of 5th August 2002. All of the particles containing lead during this period had aerodynamic diameters less than 1 μm and were internally mixed with carbon. These lead-containing particles most likely originate from combustion of leaded fuels. The number concentrations of these particles are generally low and they are usually associated with passing ship (Guazzotti *et al*, 2003). The wind direction from 0200 h to 0500 h on the 5th of August was arriving from a north-easterly/south-easterly direction. During 0000 h and 0100 h previous to the lead event the wind direction was arriving from a north-westerly direction. It is also possible that these lead containing particles may have come from an inland source. Figure 4.36 shows a dust particle containing strong positive ion signals for lead.

Several particles were classified as containing vanadium, but they represented less than 1% of the total particles classified (Figure 4.37). It is likely that the vanadium particles have a crude oil origin (Dall'Osto *et al*, 2004).

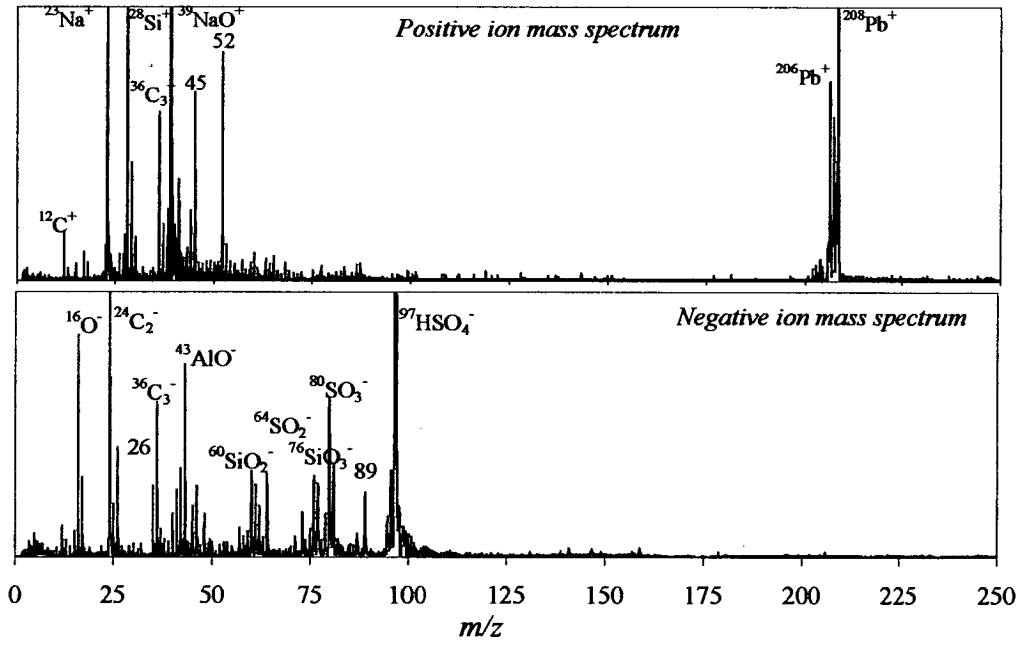

Figure 4. 36. Positive and negative ion mass spectra of a particle containing lead in association with silicates and carbon.

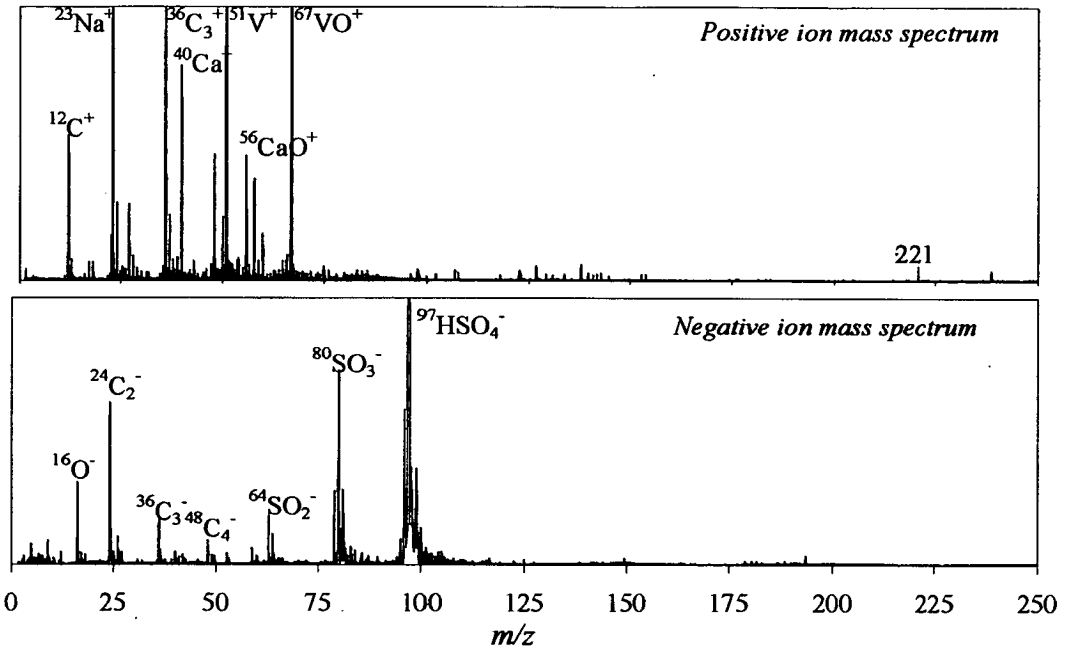

Figure 4. 37. Positive and negative ion mass spectra from a particle containing ion signals for vanadium (*0.26 μm*)

4.4. Comparison of clustering techniques

In this thesis a K-means algorithm was employed for the analysis of the ambient dataset obtained by the ATOFMS instrument. This technique employs a non-hierarchical clustering procedure whereby it selects clusters from the first 'n' different particle types. The number of different particle types or clusters needs to be defined by the user. For this reason this technique is slightly user biased. This bias may be overcome if a large number of clusters are predefined by the user.

Hinz *et al.* (2005) compared K-means and fuzzy clustering methods but reported that both methods gave similar pictures of the dataset with subtle differences in the number of particles allocated to each group.

The data presented in this chapter have been compared with classification using the ART-2a clustering algorithm. Figure 4.38 shows the influence of the clustering algorithm on class abundance. Little difference is observed in the large particle

groupings but a much larger difference is seen when investigating the small sub-particle types. For example Dall'Osto *et al.*(2005) reported on a Mg-rich particle type that was not detected by the K-means.

The K-means algorithm was capable of processing a very large amount of data (191,504) and provided a picture of the different types of particles present in the dataset. It is still necessary to examine individual particles and look at the associations of different chemical species with certain particle types or sizes in order to get a complete picture of the dataset. Although the K-means algorithm can pick up differences in particle composition it does not often see subtle changes within the particle type and the ART-2a appears to be more useful for examining single particle data.

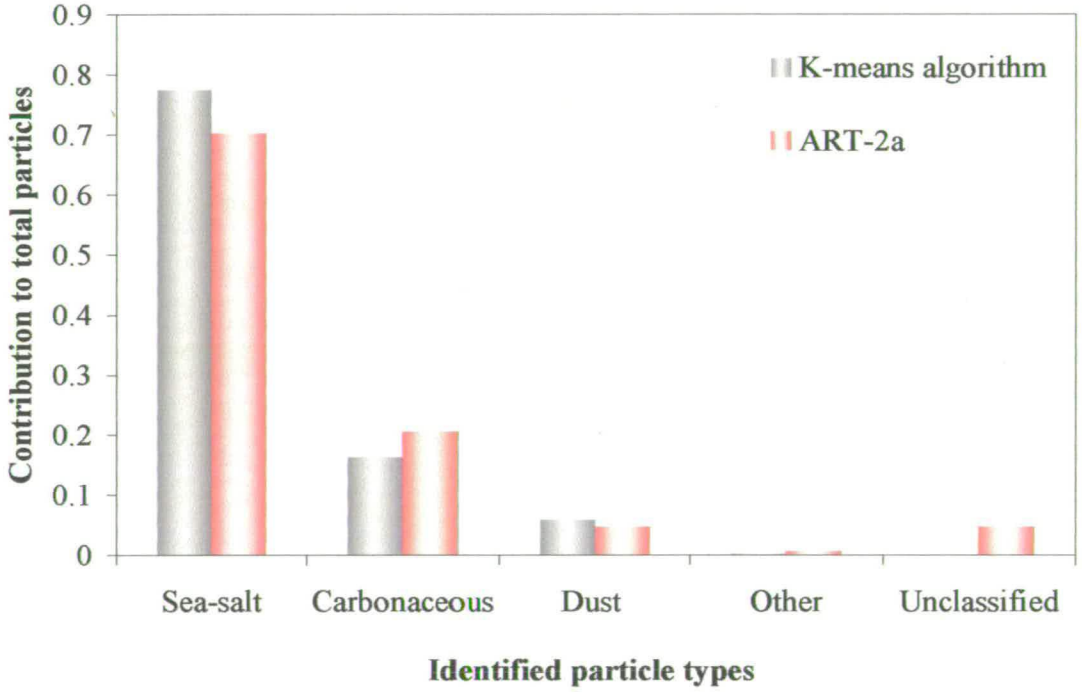

Figure 4. 38 Bar chart illustrating the influence of clustering algorithm on class abundance

Chapter 5

Single particle detection efficiencies of the ATOFMS instrument during NAMBLEX

Chapter 5 Single particle detection efficiencies of the ATOFMS instrument during NAMBLEX

5.1. Introduction

The ATOFMS instrument measures the size and composition of single particles in near real-time. However, the ATOFMS data do not provide direct quantitative information on aerosol composition. The analysis of ATOFMS data to determine quantitative aerosol composition presents some challenges. Firstly the inlet of the ATOFMS demonstrates bias towards particles in the size range 0.5 – 1.8 μm. This means that although the ATOFMS is capable of accurately sizing particles from 0.3 – 3 μm, it does not demonstrate 100% transmission efficiency over this size range. Secondly the DI laser demonstrates large fluctuations in laser energy from one laser pulse to the next which limits the ability to acquire reproducible spectra and hence the ability to deduce quantitative measurements.

Chemical quantification of single particles detected using single particle mass spectrometry has been an elusive goal for some time. The laser ablation/ionisation process used in the ATOFMS preferentially detects certain chemical species over others. The wavelength of the laser employed in the ATOFMS instrument is 266 nm. Certain chemical species absorb very strongly at the wavelength while others do not as already discussed in Chapter 3.

In the present work, the ATOFMS data are compared with aerosol mass concentration measurements taken with a MOUDI instrument and aerosol number concentration measurements made by an APS instrument. All instruments were sampling simultaneously during the NAMBLEX campaign at Mace Head (Chapter 4). The ATOFMS and APS were sampling continuously from the 1st -21st August 2002 whereas the MOUDI was only operating from the 12th -21st August 2002. Only comparisons in the overlapping sampling periods can be made. Full details of the NAMBLEX campaign can be found in Chapter 4. MOUDI and APS data are particularly useful for the calibration of ATOFMS response because both the

impactors and ATOFMS instruments segregate particles based on their aerodynamic diameters and operate over an overlapping aerodynamic size range, 0.32 – 3 μm (Chapter 1).

The ATOFMS instrument currently does not provide quantitative information on aerosol composition. Quantitative measurements are needed to better understand the sources, transformations, and fate of ambient particles, as well as the effects of particulate matter on global climate, human health, and regional visibility.

5.1.1. Related studies

Significant advances have been made towards characterising the transmission efficiencies and chemical sensitivities of the ATOFMS instrument. Allen *et al.* (2000) developed the first number scaling factor that could be applied to the ATOFMS instrument to obtain true atmospheric number concentrations. The ATOFMS instrument was operated along side an OPC and an inertial impactor. As the OPC measures particle size from light scattering intensity it was necessary to use an aerosol calibration to relate the scattering intensity to aerodynamic diameter (Hering & McMurry, 1991). Converting from one measure of size to another typically involves significant uncertainty (McMurry, 2000). Calibration functions were developed and applied to the ATOFMS data to yield continuous aerosol mass concentration as a function of particle size.

In another study, ATOFMS data were compared to size resolved particle counts with a laser particle counter (Wenzel *et al*, 2003). A scaling factor similar to the one reported in Allen *et al.* (2000) was described. It was noted that a strong chemical bias existed in the data. Previous scaling factors ignored any chemical bias present and made assumptions that particle losses were only due to transmission losses and optical detection. A second scaling factor was described where, through the use of semi-continuous particulate measurements, it was possible to account for a missed particle composition (Wenzel *et al*, 2003).

A study describing a scaling factor employing both APS and ATOFMS instruments has been described by Moffet *et al.* (2004). Hourly scaling factors were calculated for particles in the size range of 0.6 – 5 μm in diameter.

Determining instrument sensitivities to different chemical species has been difficult using LDI. To date, most efforts to determine instrument sensitivities to different chemical species have been based on particles generated in laboratory environments. These laboratory-generated particles are typically monodisperse, spherical, and have nominally identical chemical compositions. Mansoori *et al.* (1994) used LDI mass spectrometry to measure micrometer sized glycerol droplets containing dissolved inorganic salts (Fe^{3+}, Na^{+}, Cl^{-}, NO_3^{-} & SO_4^{2-}). The peak areas of ions in the mass spectra allowed cation and anion concentrations in solution to be delivered. Linear calibration plots over 2 orders of magnitude were reported (Mansoori *et al*, 1994). In another study LDI characteristics of single ultrafine multicomponent aerosols were investigated. A model quantifying the relationship between ion yield and particle composition using reference compounds was described. Gross *et al.* (2000a) investigated relative sensitivity factors for a series of alkali halide ions. Particles generated from solutions containing a mixture of two different alkali halides were delivered to the ATOFMS instrument. A series of relative sensitivity factors (RSF) were developed for each alkali cation. Although these RSF and other data from the previous studies have been used to better understand the relative quantities of different alkali species present in particles analysed by LDI it is not yet possible to apply these techniques in field experiments because atmospheric aerosols are far more complex than laboratory-generated aerosols.

Studies where ambient data have been correlated with reference samplers have been reported by Liu *et al.* (2000) and Fergenson *et al.* (2001). Liu *et al.* (2000) developed quantitative scaling factors for NH_3^{+} and NO_3^{+}. The number of nitrate containing particles detected by an ATOFMS instrument was compared with collocated NO_3^{-} mass concentration measurements taken by an automated nitrate monitor at 10 minute sampling intervals. It was reported that the number of nitrate-containing particles detected by ATOFMS exhibited a linear correlation with automated nitrate

monitor measurements throughout the 53 h sampling event at Riverside, CA, demonstrating the ability of an ATOFMS instrument to track atmospheric NO_3^- concentrations based on the presence of a specific chemical marker in the single particle mass spectra.

Fergenson *et al.* (2001) applied a multivariate calibration technique to compare ATOFMS data with collocated impactor measurements of 44 different aerosol-phase chemical species. The ATOFMS data were grouped into a large number of clusters which were compared with impactor mass measurements by a partial-least squares algorithm that related the cluster mass to atmospheric concentration. Agreement of 83% provides evidence that ATOFMS data can potentially yield quantitative measurements.

These studies demonstrated the potential for the ATOFMS instrument to yield quantitative measurements on ambient data but both compared bulk measurements of atmospheric aerosol. In another study ion signal intensity from single particles was compared with bulk quantitative measurements of atmospheric aerosol chemical composition (Bhave *et al*, 2002). The advantage of using ion signal intensities is that instrumental sensitivities can be deduced from atmospheric aerosol data.

In this work chemically speciated size-resolved aerosol composition data from impactor measurements were used to develop quantitative scaling methods using a MOUDI to obtain real-time mass measurements from the ATOFMS instrument.

5.1.2. Objectives

In the present work, a quantitative comparison of ATOFMS and reference sampler data was used to determine ATOFMS inlet transmission efficiencies as well as ATOFMS chemical sensitivities to Na^+, K^+ and Cl^- during NAMBLEX and possibly for other studies. The results obtained for the transmission efficiencies are based on 21 days of sampling and the chemical sensitivities are calculated for 1 h time intervals over 8 days.

5.2. Instruments used

5.2.1. ATOFMS

The ATOFMS instrument has been explained in detail in Chapter 2. The raw data used in this section were acquired by the ATOFMS instrument during NAMBLEX. The instrumental set-up along with the analysis of the detected particulate matter is explained in full in Chapter 4. The data for particles hit by the ablation laser and for those that were missed by the ablation laser were used to develop the scaling factor. The particle size information and mass spectral area measurements of the ion signals were used to develop the quantitative chemical scaling factor.

5.2.2. APS

The APS (Model 3320, TSI Inc. St. Paul, MN) measures particle size distributions from 0.5 μm to 20 μm (52 channels) by determining the time-of-flight of individual particles in an accelerating flow field. Significant counting efficiency problems in the Model 3320 have been reported (Stein *et al*, 2002; Armendariz *et al*, 2003). The newer model (3321) resolves issues identified with the earlier TSI APS (Armendariz *et al*, 2003; Stein *et al*, 2002). During this study corrected data from the model 3320 were used (Ceburnis *et al*, 2004b). APS number distribution were converted into a mass distribution and compared with a MOUDI deployed over the same period (1st-21st August 2002) in the same location (Mace Head) and a calibration curve was derived. The correction was < 30% for all particles of D_a > 0.8 μm. Figure 5.1 shows the scaling graph that was used to correct the APS data.

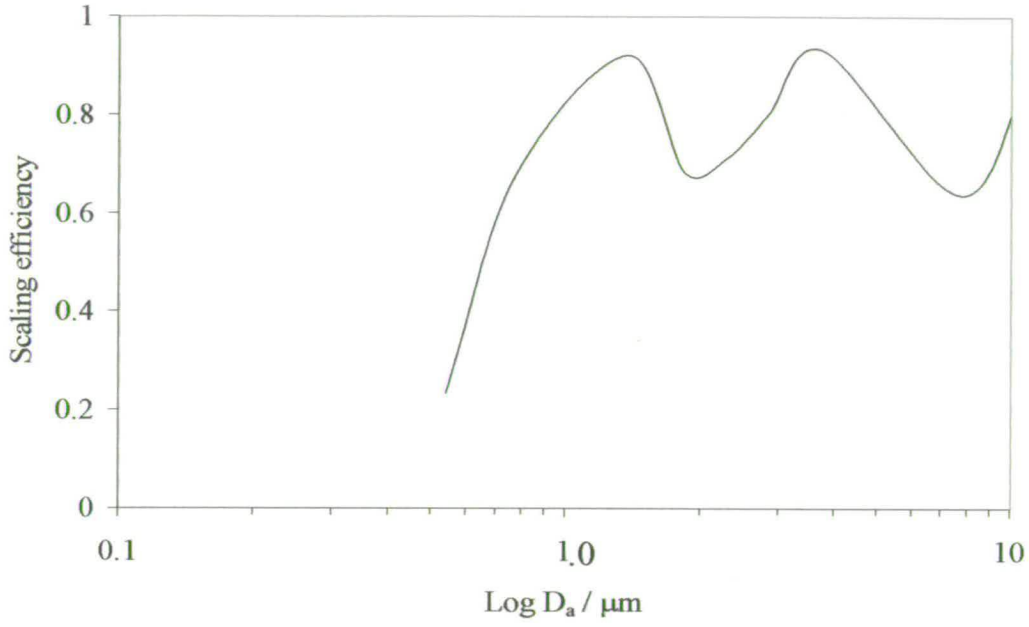

Figure 5. 1. Calculated scaling efficiencies for the APS 3320 instrument plotted as a function of particle diameter (Ceburnis *et al*, 2004b)

5.2.3. MOUDI

A type 110 MOUDI (MSP Corporation, Minneapolis, Minnesota, USA) was used to collect particles in ten size fractions. The 50% cut-points for the particle aerodynamic diameter (μm) are as follow: 18, 9.9, 6.2, 3.1, 1.8, 1.0, 0.55, 0.325, 0.175, 0.099, 0.054 (Marple *et al*, 1991). The pump used to supply the sampling flow rate (25.5 l min^{-1}) was a Gast twin piston pump. The 50% cut-off parameters were adjusted according to the actual flow rates employed. The fractionated particles at every MOUDI stage were collected on Teflon filters which were previously treated with silicone grease to avoid particle bounce.

The MOUDI was placed on the top of the tower at Mace Head (Chapter 4) and its inlet was positioned under a simple plastic shelter to protect it from rain while allowing free ventilation. The size-segregated particle ensembles of each impaction substrate were analysed by the same procedure described by Huang *et al.* (2004a) and Allen *et al.* (2000). Ion chromatography was performed for sodium (Na^+), potassium (K^+), calcium (Ca^{2+}), magnesium (Mg^+), chloride (Cl^-),

methanesulphonate ($CH_3SO_3^-$), sulphate (SO_4^{2-}) and nitrate (NO_3^-). Ammonium (NH_4^+) was analysed by using a flow injection fluorescence technique. Sampling time was 24 hours every day between 12-21/08/02.

5.3. Number and chemical scaling of the ATOFMS response.

5.3.1. Busy time

The ATOFMS instrument is unable to acquire new data while it is saving the data from a detected particle. The time required to save information on a particle is termed busy time and increases nonlinearly with ambient particle concentration.

Prior work has demonstrated the importance of ATOFMS instrument busy time (Bhave *et al*, 2002). During the time that the ATOFMS instrument processes and saves data on the size and composition of detected particles, the ATOFMS instrument electronic system is busy and cannot detect new particles. Instrument busy time alters ATOFMS instrument response so that changes in ambient particle concentration are not linearly propagated to the ATOFMS data.

Allen *et al.* (2000) discussed laboratory experiments that estimated the factors which affect ATOFMS busy time. In these experiments, hit and miss particle events were simulated electronically and the maximum rate of simulated event acquisition was measured. ATOFMS instrument busy times for missed particles were reported to be constant. Hit particle busy times were longer than missed particle busy times and these times increased with the number of mass spectra saved in a computer file directory. Busy time can be calculated using Equation 5.1;

$$\text{Busy time} = A\ \text{MissCount} + B\ \text{HitCount} + C\ \text{HitCount AvgFolderPos} \qquad \textbf{(5. 1)}$$

In the previous quantitative analysis of ATOFMS data (Allen *et al*, 2000; Bhave *et al*, 2002) the raw data were corrected for busy time. ATOFMS particle counts for each hour were multiplied by a scaling factor to account for sampling time lost to instrument busy time and off-line time.

Although busy time is an important factor it was not taken into account during this study. It was chosen not to correct for busy time as there was not an accurate measure of the time required to save hit and missed particles for the commercial ATOFMS instrument and scaling of the ATOFMS instrument with the APS would take into account all particles not detected by the ATOFMS instrument including those missed due to busy time.

5.3.2. Size detection efficiency of the ATOFMS instrument

Although the ATOFMS instrument is capable of transmitting and detecting particles in the range of 0.3 – 3 μm the inlet preferentially focuses particles with diameters between 0.5 μm and 1.8 μm with the highest efficiency.

The transmission efficiency of the particles through a supersonic expansion, defined as the fraction of the particles that is focused into the particle beam downstream of the expansion nozzle, has been both measured and modelled (Dahneke & Cheng, 1979). Maximum transmission efficiencies were observed for the particle sizes for which the nozzle has been designed and a sharp decrease in transmission efficiency for larger and smaller particles.

Nozzle transmission efficiency is only one of several factors that contribute to the probability that a particular atmospheric particle will be detected; other factors include the probability that the particle will be detected by the timing lasers that measure its velocity (hence size) and the probability that the particle will be successfully hit by the DI laser.

Accurate sizing is necessary in order to scale data into atmospherically representative concentrations. The ATOFMS obtains precise information on aerodynamic size using particle time-of-flight measurements. These precise size measurements allows the raw ATOFMS particle counts for different particle types detected to be scaled up to atmospherically relevant number concentrations using traditional particle sizing instruments.

In this section the data acquired by an APS instrument were compared to the raw ATOFMS particle counts, using 1 h temporal resolutions. The typical procedure involves dividing the ATOFMS particle counts occurring in each size and time bin by the APS counts into the corresponding size bins to produce the necessary scaling factors to match the raw ATOFMS counts to the APS data. In previous work where the transmission efficiency of an ATOFMS inlet was investigated assumptions were made when using the scaling procedure that all particle compositions are hit with equal efficiency, and that only instrumental bias are transmission losses and optical detection biases based on particle size. In this work two scaling factors were developed, the first was developed using the hit particles sampled by the ATOFMS and the assumption was made that all particle types were hit with the same efficiency. The second scaling factor was based on the total particles detected by the ATOFMS instrument (hit and miss). The second scaling factor was used to describe the inlet transmission efficiency and did not make any assumptions on particle composition. The effect of particle composition was later corrected for using the hit rate (Particles hit by the ATOFMS DI laser/Total particles sized by the ATOFMS CW sizing lasers).

Incorrectly-sized particles are occasionally recorded by the ATOFMS instrument. This is sometimes due to coincident particles in the sizing chamber. In this case one particle scatters light from the first timing laser, and a different particle, travelling faster, scatters light from the second timing laser. The measured velocity in this case is greater than the original particle's actual velocity. As a result, the DI laser is fired too early, and a mass spectrum is not acquired for the particle. Therefore, although many correctly sized particles are not hit, hit particles are very unlikely to have been incorrectly sized.

For all data used in this study, scaling factors were obtained using hourly APS mass concentration data. The APS data measured particle number concentration in 52 size bins (0.542 μm to 20 μm) in five minute integrals. The ATOFMS efficiency was calculated in the range 0.523 to 2.943 μm using corrected APS data. This involved merging the APS data into 8 size ranges from an initial 24 bins. The 8 size ranges were: 0.523 to 0.649 μm, 0.649 to 0.806 μm, 0.806 to 1.00 μm, 1.00 to 1.241 μm,

1.241 to 1.54 μm, 1.54 to 1.911 μm, 1.911 to 2.207 μm and 2.207 to 2.943 μm. The size bins were combined in order to obtain a statistically significant ATOFMS number count for each size bin. It was necessary that at least 10 particles be detected in each size bin / h in order to be recorded. Lower numbers caused spurious variations in the scaling factor. The values used here represent hourly average concentrations.

5.3.2.1. Scaling factor 1 (Hit particles)

Initially, in order to obtain atmospherically-representative ATOFMS number concentrations for the different particle types, the scaling factors for each of the 60-min periods were calculated using the assumption that the only sampling biases were due to transmission losses and optical detection. This is an important assumption because it does not allow for any potential particle composition bias.

The total number of particles for which a mass spectrum was obtained by the ATOFMS system was counted and subdivided into APS size bins in 60-min intervals (HIT_{ATOFMS}). The number of particle hits in each size bin during the 60-min interval was converted to particles / cm^3 (using the measured ATOFMS flow rate of 0.85 l / min) and compared directly with the corresponding APS value of particles / cm^3 (N_{APS}). A scaling factor (ϕ) (Equation 5.2) was obtained that allows the true ambient particle concentrations to be obtained when multiplied by the raw ATOFMS number count. The value ϕ can be thought of as the inverse of the ATOFMS transmission efficiency.

$$\phi = \frac{N_{APS}}{HIT_{ATOFMS}} \qquad \textbf{(5.2)}$$

The resulting scaling factors obtained by comparing the ATOFMS to the APS are shown in Figure 5.2 as a function of particle size and sampling time. Values for the scaling factor show a strong dependence on particle diameter; as particle size is reduced, a smaller fraction of the particles actually present in the atmosphere is detected. The scaling factors increase for particles with smaller diameters. Figure 5.2 shows the higher scaling factors required for particles in the smaller size bins than in the coarser size bins. Also of note are the different temporal variations of scaling

factors observed for each of the size bins. Scaling factors during the 1st-5th August 2002 were mainly concentrated in the sub-micron size fraction. This reflects the particle composition that was detected during this period. High number concentrations of fine sub-micron carbonaceous particles were detected (Chapter 4). After 5th August the air masses were arriving predominantly from the Atlantic and bringing with them high numbers of coarse mechanically-derived sea-salt and dust. For this reason scaling factors during this period only become significant in the coarser size ranges.

The average hit rate during NAMBLEX was 19% but varied from 13% to 62% during the sampling period of 21 days. Often differences of 3% to 42% were recorded over 4 h sampling periods. In previous studies an average hit rate for all particle sizes of ~ 25% is typical (Wenzel *et al*, 2003). The hit rate is strongly dependent on particle composition. Variations that were apparent in the hit rate observed during sampling are reflected in the scaling factors (Figure 5.3). Similarities are shown between the hit rate and the scaling factor. The fact that the ATOFMS still detects and sizes the "missed" particles by light scattering is critical to knowing when the chemical bias is present and being able to accurately account for it.

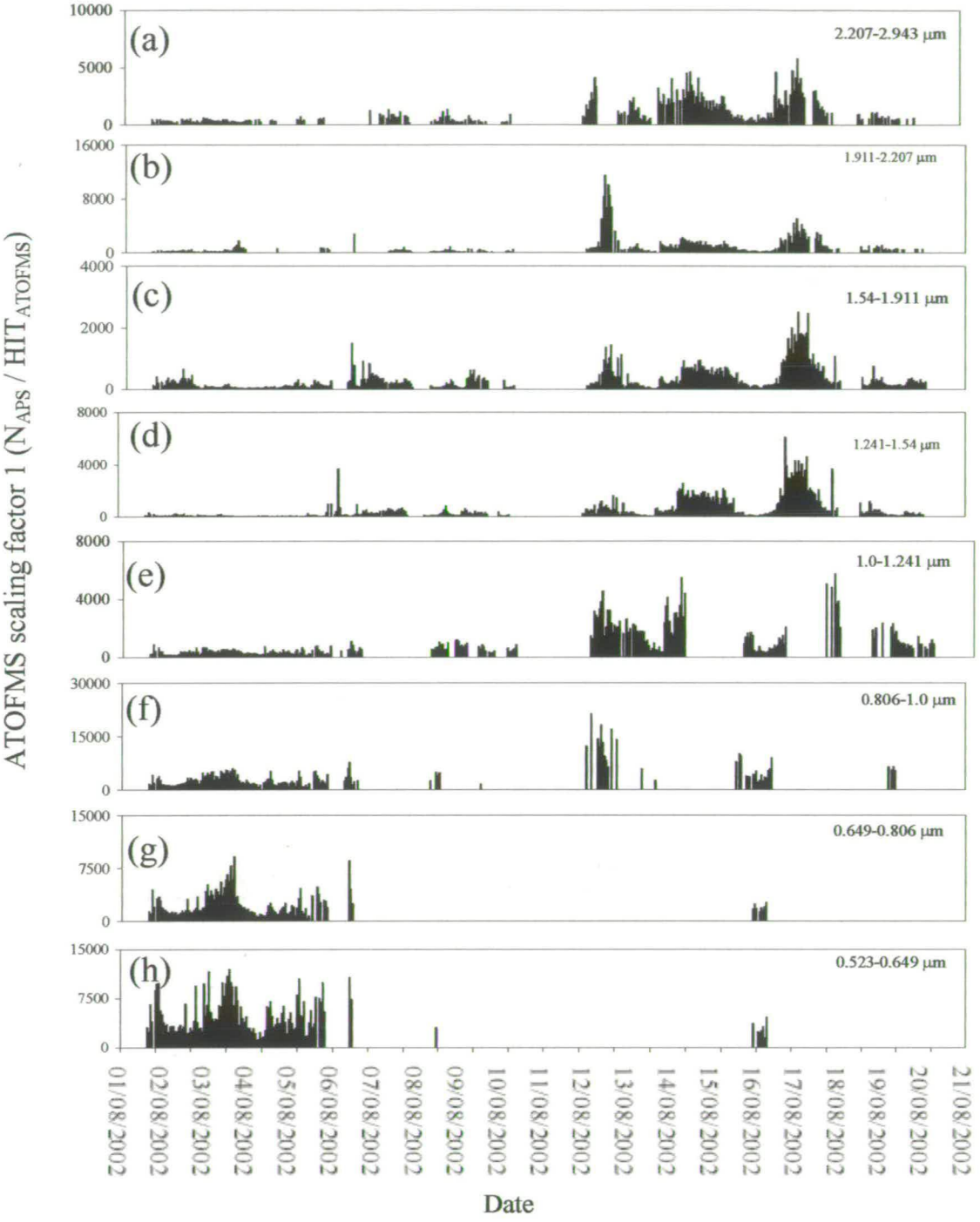

Figure 5.2. Scaling factors necessary to scale ATOFMS particle concentrations to APS number concentrations. Data shown span the entire NAMBLEX period of 21 days in one hour time bins subdivided to match APC size bins (a)-(h).

Increases in the scaling factor (and decreases in the hit rate) are observed on the 15/8/02 and 17/8/02. These periods were characterised by higher numbers of pure

NaCl particles. It is known from Chapter 3 that pure alkali salt particles do not absorb energy at 266 nm due there their large band gap.

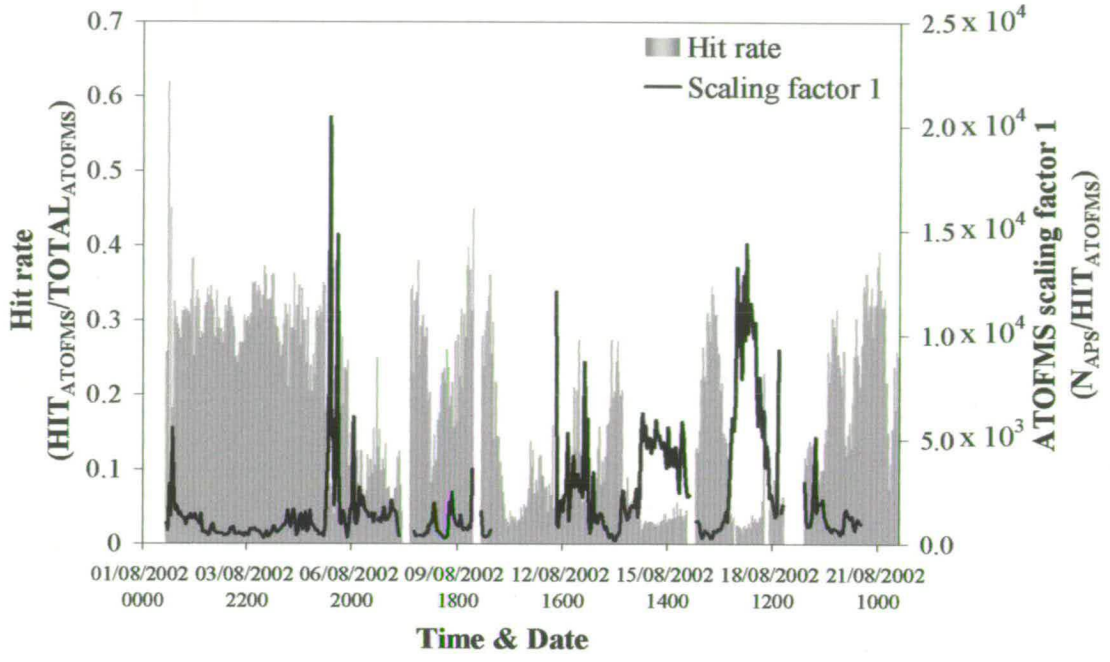

Figure 5.3. Hit rate for the ATOFMS sampling period 1st-21st August 2002 and the corresponding scaling factor calculated using collocated APS data.

Figure 5.4 (a) shows the scaling factor plotted against aerodynamic diameter. The plots of ϕ against D_a show that ϕ, in the size range of 0.3 to 3 μm is strongly dependent on particle diameter. Allen *et al.* (2000) plotted ϕ against D_a for diameters between 0.56 μm and 1.8 μm and showed that ϕ followed a power law relationship in D_a according to Equation 5.3,

$$\phi = \alpha D_a^{\beta} \tag{5.3}$$

where α and β are determined by nonlinear regression of APS number concentration data on ATOFMS particle data. In this size range (0.56 – 1.8 μm) ϕ obtained using the ATOFMS and APS data follow the same trend as reported by Allen *et al.* (2000) (Figure 5.4 (b)). Values quoted by Allen *et al.* (2000) for field experiments are compared to those from this work in Table 5.1. The α and β entities are the parameters in the power law fit. The value of α simply corresponds to the value of the scaling factor ϕ for a particle of D_a = 1 μm and is an indication of the fraction of

particles not detected by the ATOFMS. The value of β is a measure of the strength of the dependence of the scaling factor on particle diameter; the greater the magnitude of β the greater the variation of ϕ with D_a. (If the scaling factor was independent of particle diameter then β would be zero). The magnitude of β reported in this work (Table 5.1) is smaller than that reported by Allen *et al.*(2000). It therefore appears that the ATOFMS used in this work has less of a change in particle detection efficiency for particles over the size range of 0.56 – 1.8 μm than the ATOFMS employed by Allen *et al.* (2000) , i.e. the ATOFMS used in this work has a flatter spread in detection efficiencies. These differences can be attributed to the different instruments used in the two analyses, as well as may be the different particle composition sampled.

	α	β	***Applicable range of D_a / μm***
Allen *et al.* (2000)	2133 ± 501	-5.5 ± 0.86	0.56-1.8
This thesis	1364 ± 800	-2.45 ± 0.1	0.56-1.8

Table 5.1. Parameter values fit to the scaling function $\phi = \alpha D_a^{\beta}$

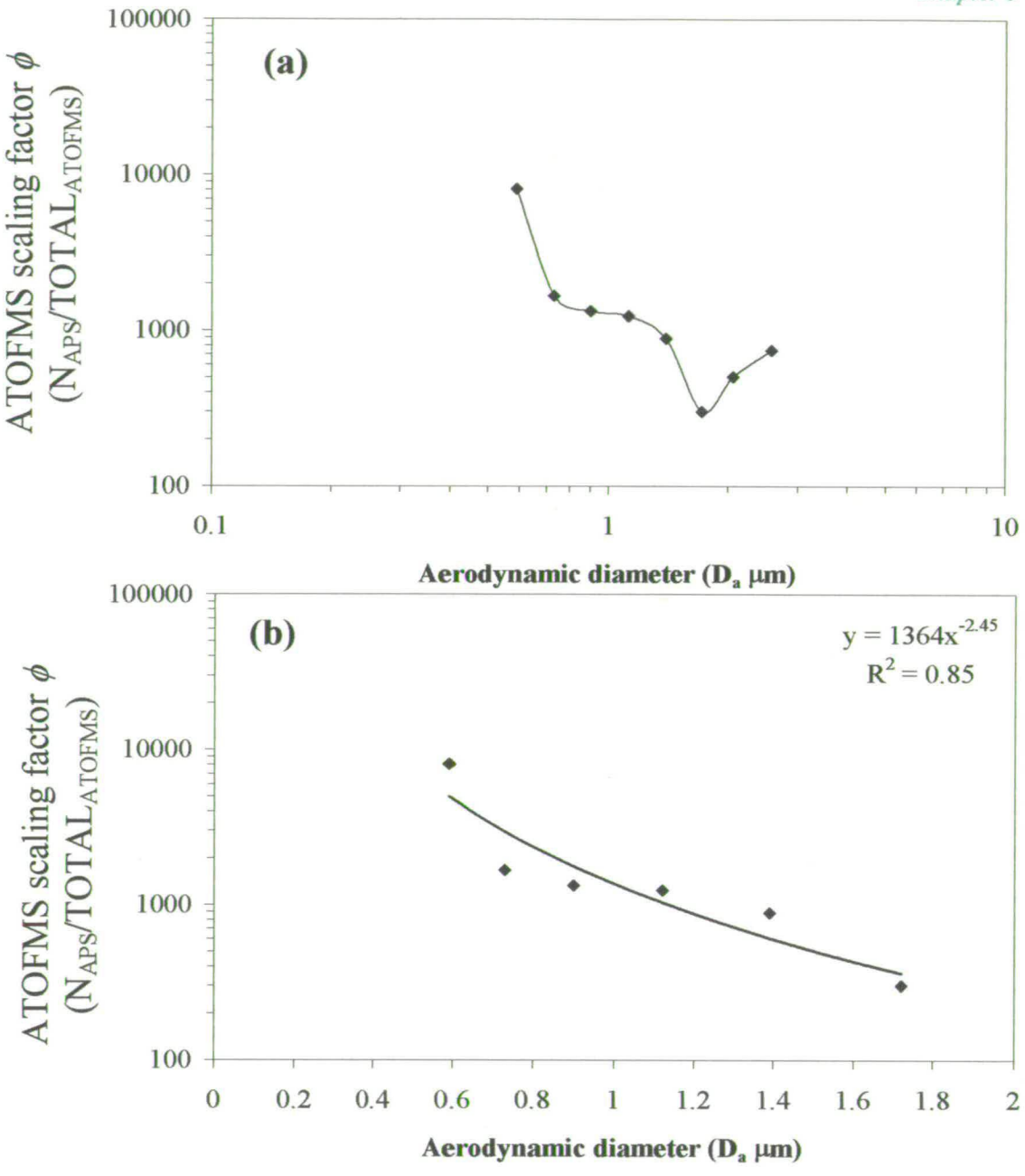

Figure 5. 4. (a) Inverse particle transmission efficiency (ϕ) versus aerodynamic diameter (D_a) for the TSI 3800 ATOFMS instrument sampling ambient aerosol at Mace Head in August 2002 during NAMBLEX. Size range is (a) 0.52-2.94 μm (non-linear scale) and (b) 0.52-1.91 μm (linear scale). Error bars are 95% confidence intervals on the average scaling factor.

The particle-phase chemical compositions of air parcels sampled during NAMBLEX changed according to their geographic origin. Using this information it is possible to

compare periods during NAMBLEX when a known air mass was arriving and compare this with the corresponding scaling factor. During 1st-5th August 2002 air masses were arriving from over the continent, the particle size distribution sampled during this period contained particles with diameters <1 μm. The single particle mass spectra indicated that these particles contained a high percentage of carbonaceous material (17%) and the average hit rate was 35%. The scaling factors for this period represent a scaling factor that maybe applied to carbonaceous material.

Later on during the campaign on 14th, 15th & 17th the air masses were arriving from the Atlantic carrying super-micron marine particles. The hit rate for these days was particularly low at 9% and the single particle mass spectra showed that the particles consisted of alkali salt species. A scaling factor plotted during this period represents that for sea-salt species.

The 6th and 13th was characterised by a period where a large number of particles were detected containing dust, this is explained in detail in Chapter 4. The size distribution of these particles is broad and monomodal ranging from 0.3 to 3 μm. The hit rate for this period was on average 12%. The scaling factors for dust, sea-salt and carbonaceous material are plotted in Figure 5.5. Values for α and β were not calculated for these distributions as Figure 5.5 clearly demonstrates that the scaling factor does not follow a power law relationship in diameter. It is possible to separate the scaling factor into two separate scaling factors above and below 1.6 μm.

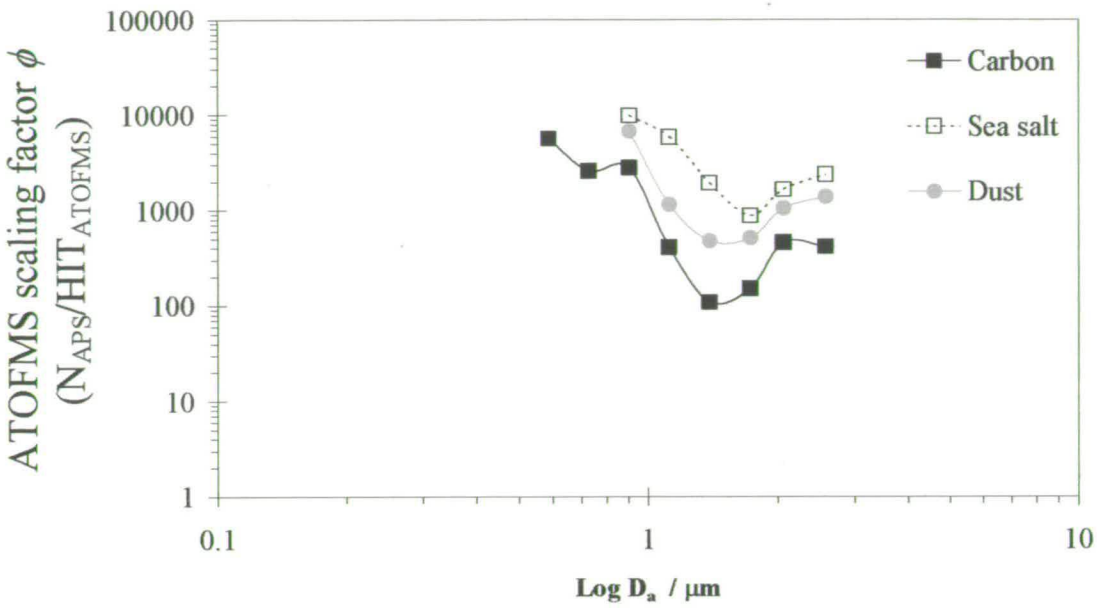

Figure 5.5. Inverse particle transmission efficiency (ϕ) versus aerodynamic diameter (D_a) for particles with ion signals for carbon, dust and sea-salt. Size range is 0.5-2.9 μm.

Although this scaling factor corrects for the inlet efficiency of all particles resulting in a mass spectrum it also demonstrates that there is a strong chemical dependence within the ATOFMS instrument and that all particles are not detected with the same efficiency at the laser wavelength used (Figure 5.5). Scaling factor 1 therefore describes the ATOFMS sensitivity to different species but does not provide true information on the transmission efficiency of the ATOFMS inlet as it is affected by the ability of the DI laser to produce a mass spectrum. In order to determine inlet transmission efficiencies a second scaling factor was developed using the total particles sampled

5.3.2.2. Scaling factor 2 (Total particles)

The number of hit particles and the number of missed particles in a given time and size bin were totalled ($TOTAL_{ATOFMS}$). The total particles sized by the ATOFMS instrument during a 60-minute interval was converted to particle concentration and compared with the corresponding APS value (N_{APS}) as explained in section 5.3.2.1. Scaling factor 2 (χ) was calculated through Equation 5.4.

$$\chi = \frac{N_{APS}}{TOTAL_{ATOFMS}} \qquad \textbf{(5. 4)}$$

Scaling factor 2 (χ) is plotted as a function of size and time for each size bin in Figure 5.6. Similar to Figure 5.2 the scaling factors are strongly dependent on particle diameter. This scaling factor calculated represents the inverse of the inlet transmission efficiency of the ATOFMS inlet as it scales up all particles which were detected by the ATOFMS instrument with no consideration of whether the particle absorbs the energy of the DI laser. Calculating the ATOFMS scaling factor using this method introduces some bias to the results as a lot of missed particles do not get sized accurately but a more correct measure of the inlet transmission efficiency for the ATOFMS instrument is obtained. Any chemical bias introduced by particles absorbing at the laser wavelength is then determined using the hit rate.

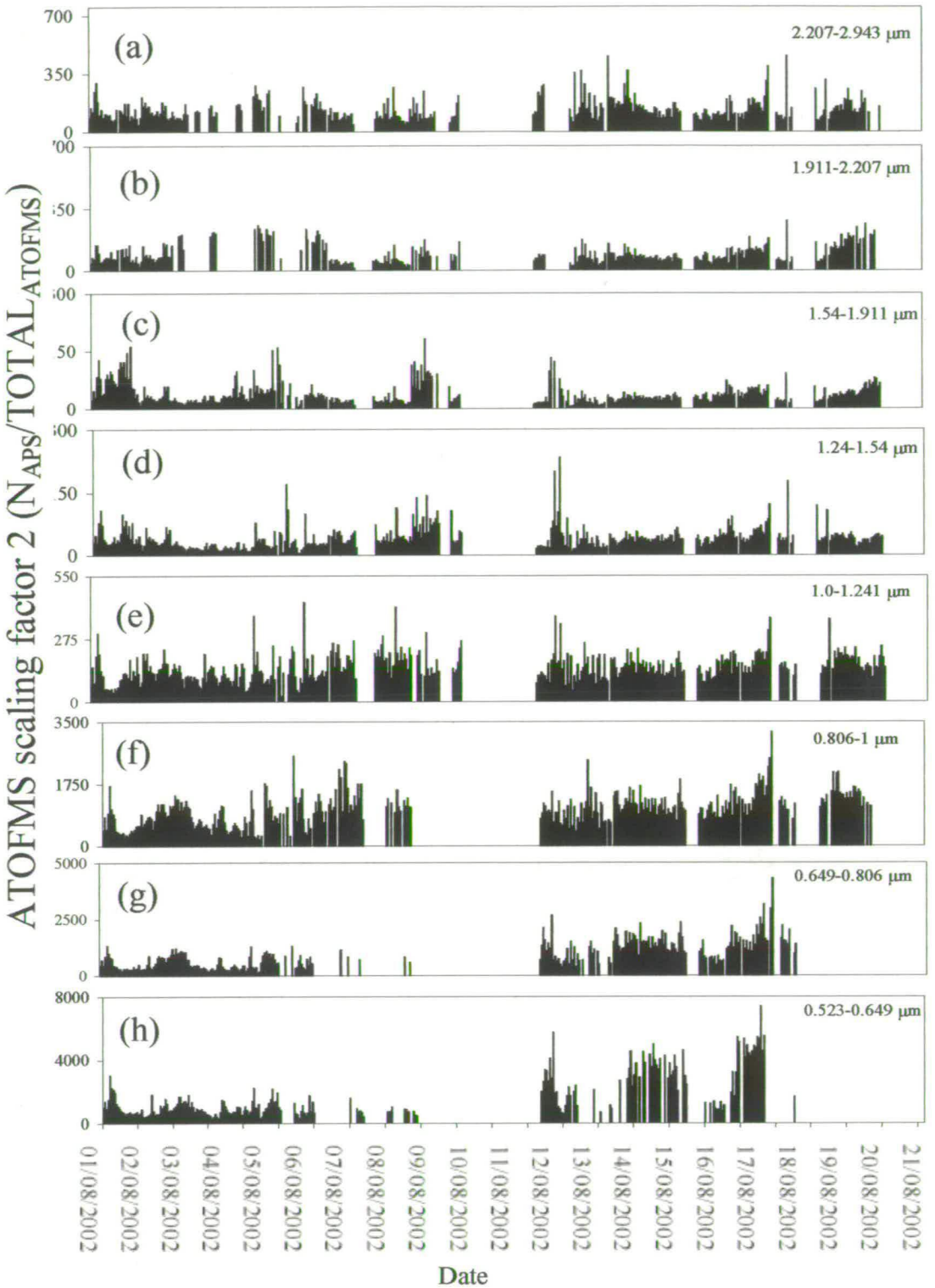

Figure 5.6. Scaling factors necessary to scale ATOFMS particle concentrations to APS number concentrations. Data shown span the entire NAMBLEX period of 21 days in one hour time bins subdivided to match APC size bins (a)-(h).

As shown previously in Figure 5.5 the scaling factor can be plotted for different particle compositions when calculated with the ATOFMS hit rate. Different scaling factors for different particle composition are not plotted using scaling factor 2 as it is only a measure of the inlet transmission efficiency and is not related to particle composition. Chapter 4 shows examples of scaled carbonaceous, sea-salt and dust size distributions. Figure 5.7 shows the scaling factor for particles with diameters in the range of 0.5 - 3 μm (a) and also for particles with diameters between 0.5 – 1.8 μm (b).

A comparison of the values for α and β for scaling factors 1 and 2 (SF1 and SF2) is shown in Table 5.2. The value of α is much smaller for SF2 than for SF1, whereas the magnitude of β is greater for SF2. The value for α is a general measure of the magnitude of the ability of the ATOFMS to transmit particles and since $TOTAL_{ATOFMS}$ (as used in SF2) is greater than HIT_{ATOFMS} (as used in SF1) the value required to scale the ATOFMS data to APS data is smaller. The higher value of β for SF2 (compared with its value for SF1) is similar to the value reported by Allen *et al.* (2000). The fact that β has a negative value is as expected because the ATOFMS inlet is designed to see the particles with coarser diameters. However, the increase in the β value for SF2 compared with SF1 demonstrates that the ATOFMS detects relatively less fine particles than coarse particles when considering all particles that are sized (but not necessarily ablated) (SF2) compared with the relative ability to detect fine and coarse particles when considering only those particles that are desorbed (SF1). In other words, the ATOFMS is less efficient at ablating coarse particles than fine particles. The reason for this is straightforward because, in general, the coarse particles were composed of alkali salts which do not absorb at the laser wavelength used. Therefore, it can be concluded that SF2 provides more information on the particles transmitted by the ATOFMS instrument and is not dependent on particle composition.

	α	β	Applicable range of D_a / μm
Scaling factor 1(ϕ)	1364 ± 800	-2.45 ± 0.1	0.56-1.8
Scaling factor 2(χ)	347 ± 100	-4.5 ± 0.1	0.56-1.8

Table 5.2. Parameter values fit to the scaling function 1 (ϕ) and 2 (χ) = αD_a^{β}

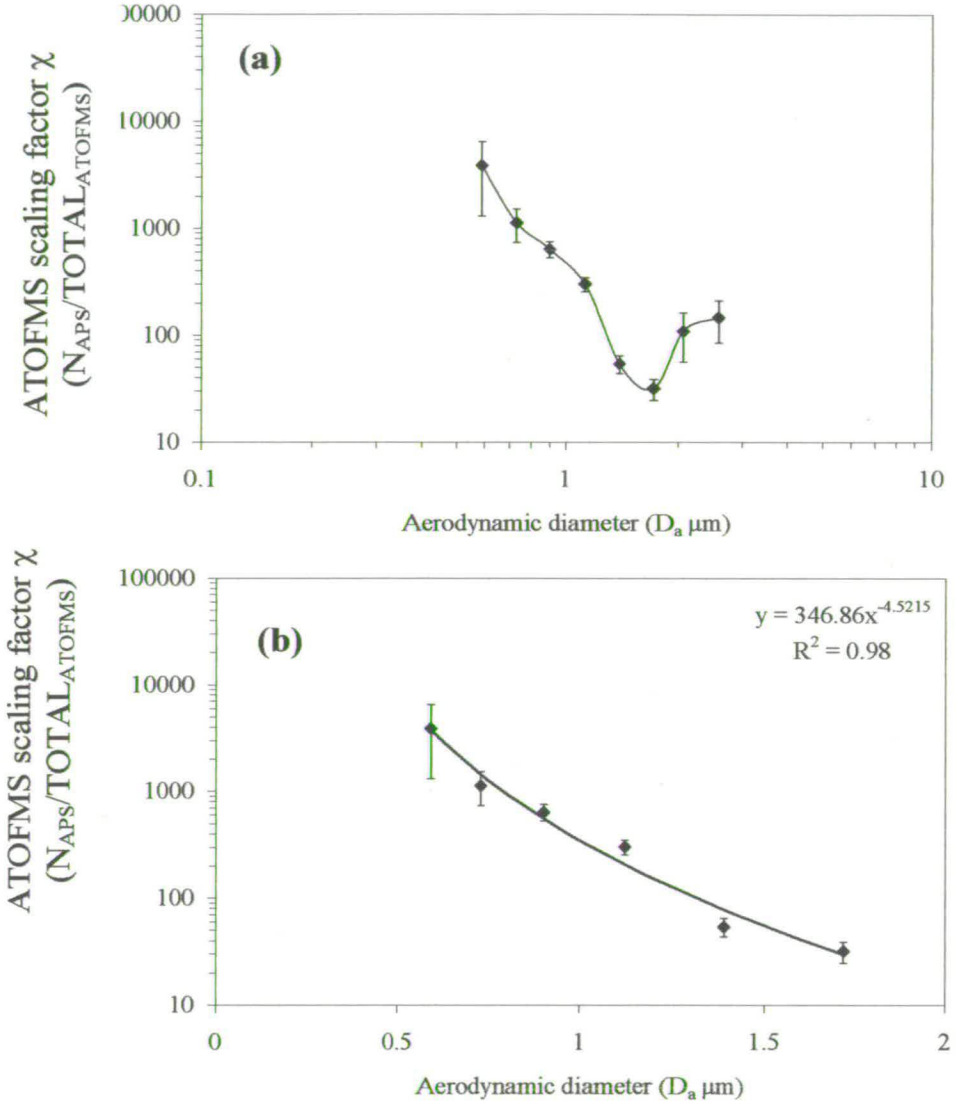

Figure 5.7. (a) Inverse particle transmission efficiency (χ) versus aerodynamic diameter (D_a) for the TSI 3800 ATOFMS instrument sampling ambient aerosol at Mace Head in August 2002 during NAMBLEX. Size range is (a) 0.52-2.94 μm (logarithmic scale) and (b) size range 0.52-1.91 μm (linear scale). Error bars are 95% confidence intervals in the average scaling factor).

Scaling factor 2 is plotted with the hit rate in Figure 5.8. Noticeable differences are observed between the scaling factor plotted in Figure 5.8 and that plotted in Figure

5.3. The scaling factor does not anti-correlate with the hit rate as it does in Figure 5.3 especially on the 15/08/02 and 17/08/02. Increases in the scaling factor are present in Figure 5.3 but it is now apparent that these episodes are due to a particle size/type that was not focused by the ATOFMS inlet rather than not ablated by the DI laser.

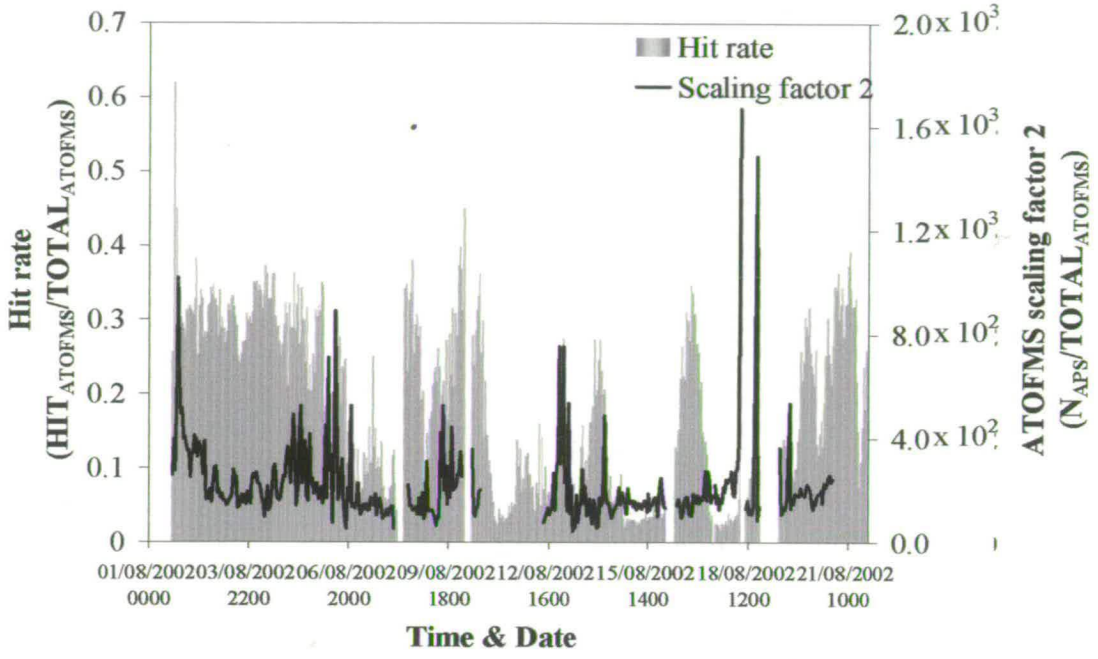

Figure 5.8. Hit rate for the ATOFMS sampling period 1st-21st August 2002 and the corresponding scaling factor calculated using collocated APS data.

5.3.3. Chemical quantification of ATOFMS single particle data

The Nd:YAG laser used in the ATOFMS instrument has a Gaussian profile. If particles always intercept the laser at the same place it is likely that they will absorb similar amounts of energy. As this can't be guaranteed it is likely that each particle hit by the ablation laser gets variable quantities of incident energy which affects the ions being formed.

A commonly cited limitation of the single-particle mass spectrometry instruments that employ LDI is that the chemical composition measurements are not quantitative. There are two main obstacles to quantitation. First, the ion signal intensities produced by the DI laser of nominally identical particles vary greatly from pulse-to-pulse primarily because of in-homogeneities in the DI laser beam. Pulse-to-pulse

variations in the laser energy and beam profile are substantial and inevitably cause large fluctuations in the ion yield. Secondly, instrument sensitivities to different aerosol-phase chemical species are largely unknown.

Pulse-to-pulse variations in the ion signal intensities can be mitigated by using very high laser irradiances but at the cost of molecular information. To retain molecular information, most single-particle mass spectrometry techniques use moderate laser irradiances (~ 10^7-10^8 W cm^{-2}). Quantifying chemical composition of an ensemble of single particles may be possible if the mass spectra from a collection of nominally identical particles are obtained and averaged. The quantification of aerosol chemical composition from an ensemble of single-particle mass spectra requires knowledge of instrument sensitivities to each chemical species in the particle ensemble. Due to chemical specific differences in ionisation efficiency instrument sensitivities can vary dramatically from one chemical species to the next.

Quantifying single particulate matter from field-based data relies entirely on atmospheric measurements. Instrument sensitivities determined from a field-based approach would be directly applicable to ambient aerosol data and could potentially elucidate the relative influences of particle size, particle composition and meteorology on instrument sensitivities under ambient sampling conditions.

ATOFMS chemical composition measurements are difficult to quantify, largely because the instrument sensitivities to different chemical species in mixed ambient aerosols are unknown. In this section a field based approach for determining instrument sensitivities to Na^+, K^+ and Cl^- using collocated ATOFMS and impactor sampling is developed. ATOFMS measurements are compared with collocated MOUDI measurements taken at Mace Head, Galway during 1st-21st August 2002 as part of the NAMBLEX campaign (Chapter 4).

A field-based approach to quantifying ATOFMS chemical composition is subject to three limitations. Firstly it is necessary that quantitative reference measurements of the chemical species of interest be taken in parallel with the single-particle

measurements. Secondly a field-based approach requires the collection of a much larger number of single particle mass spectra in order to have a statistically robust number of particles from the complex mixture of different particles in the atmosphere. The NAMBLEX campaign provided a good opportunity in that a very large number of particles were detected and there were only three main categories of chemical composition during the period that the impactor was operated. Thirdly, particle detection efficiencies of the single-particle instrument must be well characterised to ensure the success of a field-based approach. Unlike laboratory-generated particles, atmospheric aerosols are distributed by size, chemical composition, density and morphology, all of which can influence the particle detection efficiency of single-particle instruments.

5.3.3.1. Aerosol Measurements

The MOUDI impactor used in this study is described in Section 5.2.3. The MOUDI only operated from the 12th-20th of August 2002, so only ATOFMS data from this period could be used to develop chemical scaling factors. Although some nine ions were analysed in the MOUDI samples, due to the predominance of marine air masses during the period of impactor sampling (Chapter 4), only the concentrations of sodium, chloride and potassium were persistently high enough to provide a good comparison with the ATOFMS data (although the latter's concentrations were only sufficiently high in the coarser particle size ranges).

Stages 4 (0.61 to 1.1 μm), 5 (1.1 to 2.0 μm) and 6 (2.0 to 3.4 μm) were considered for the present analysis as particles collected on these three impactor stages span the overlapping aerodynamic size range of the ATOFMS instrument and the impactor. Data collected from the chemical analysis of 27 impaction substrates (9 days x 3 D_a ranges) are used in this work. It should be noted that the finest particle size range contained much less alkali halide aerosol than the two larger particle size ranges (Chapter 1 & 4) so there are less data for the comparison. (Stage 4 data were excluded altogether for the potassium comparison).

5.3.3.2. ATOFMS data treatment

The measurements which best represent ATOFMS instrument response to Na^+, K^+ and Cl^- must be selected before the ATOFMS and MOUDI measurements can be compared. The ATOFMS instrument must also be corrected for its inlet transmission bias as well as the different sensitivities of certain chemical species to the DI laser.

To compare ATOFMS data with quantitative measurements of Na^+, K^+ and Cl^-, a measure of the ATOFMS response must be precisely defined. Ion signals indicating the presence of Na^+, K^+ and Cl^- are most often detected at *m/z* of 23, 39 and -35 respectively. Ion signals for Cl^- at *m/z* -35 can also be attributed to other chemical compounds such as some organic clusters (Silva & Prather, 2000) but since the chemical composition of particles detected during this period is predominantly marine based it is unlikely that there should be interference at this *m/z* ratio.

There are several measures of ion signal available in the ATOFMS output data. Absolute and relative areas are the most appropriate for quantification of mass spectrometry data. Gross *et al.* (2000a) demonstrated how shot-to-shot variations caused the absolute areas of specific ion signals to vary by an average of 59% while the relative area of the same ion signals only varied by 16%. This would suggest that it is better to use relative area for quantification of ATOFMS data. However it has been shown that when sampling a polydisperse multicomponent aerosol, such as that found in an urban atmosphere, relative area measurements can be affected greatly by the presence of additional chemical species in the particle. For example, the relative area of an ion signal at *m/z* 18 produced from ablation/ionisation of a pure NH_4NO_3 particle will be larger than the relative area at *m/z* 18 measured from an identical particle that also contains a trace amount of potassium, because potassium is efficiently ionised and will therefore increase the total area of the mass spectrum. For this reason it was decided to use absolute area as a measure of the ATOFMS response to Na^+, K^+ and Cl^- as it is less affected by the total ion signal in the mass spectrum. The instrument response to Na^+, K^+ and Cl^- will be referred to as $Resp_{Na^+}$, $Resp_{K^+}$ and $Resp_{Cl^-}$.

A problem can arise from the high sensitivity of the ATOFMS to these chemical species resulting in an ion signal at the relevant diagnostic *m/z* value (23 ± 0.5, -35 ± 0.5 and 39 ± 0.5 Daltons for Na^+, Cl^- and K^+, respectively) exceeding the dynamic range of the data acquisition board. Only peak areas with peak height of less than 250 units were considered in order to avoid saturated signals and the peak clipping phenomenon. About 18% of the sodium containing particles used in the quantitative comparison to the MOUDI data exceeded the dynamic range of the data acquisition board, a greater proportion than in the work of Bhave *et al.* (2002). However, the correlation between the saturated and the non-saturated peaks was very high ($r^2 > 0.9$) and therefore it is considered likely that the integrated signal from the peaks of less than 250 units would be proportional to the total signal. The results therefore should not be regarded as absolute.

Correction for particle detection efficiencies was carried out using scaling factor 2 as described in Section 5.3.2.2. After the raw ATOFMS data had been scaled up to atmospherically relevant number concentrations, the scaled single particle data were multiplied by the ATOFMS response (Resp (absolute area)) to the chemical species (k) in each individual particle (j), $\chi_j Resp_{jk}$. The value for $\chi_j Resp_{jk}$ for each chemical species (k) was then normalised for hit rate (HR). Using this method it was possible to correct for both the inlet transmission efficiency as well as the chemical sensitivity of the laser.

5.3.3.3. ATOFMS-MOUDI data comparison

The main purpose of this comparison is to determine ATOFMS instrument sensitivities to Na^+, K^+ and Cl^- under ambient sampling conditions. Instrument sensitivity can be defined as the ion signal intensity per unit mass of a chemical species, averaged over a particle ensemble. In this section, large ensembles of single-particle ATOFMS data were compared with collocated MOUDI measurements of Na^+, K^+ and Cl^-. The ATOFMS spectra recorded were segregated into three aerodynamic diameter intervals, i; 0.61-1.1 μm, 1.1-2.0 μm and 2.0-3.4 μm. This size segregation yields 24 ensembles of ATOFMS spectra per chemical species which can

be compared with corresponding impactor measurements, m_i, for that chemical species, using a regression model of the form,

$$m_i = \frac{\sum_{j \subset i} \chi_j \mathrm{Resp}_j \psi_j}{V} + \varepsilon_i \qquad (5.5)$$

where V is the volumetric flow rate of the ATOFMS instrument which remained constant throughout the campaign, ε is the residual to be minimised in subsequent regression, and the ATOFMS inverse sensitivity function to each chemical species, ψ_j, is expressed in terms of aerodynamic diameter by Equation 5.7 (see later).

Figure 5.9 shows the average ion signal per hit particle for Na^+, binned by particle size range for days dominated by sea salt. The observation from the distribution of symbols is the same amount of material is ablated/ionized from the particles regardless of the particle size. This also means that no additional variation in ATOFMS ion signal was introduced by the LDI process for these particles.

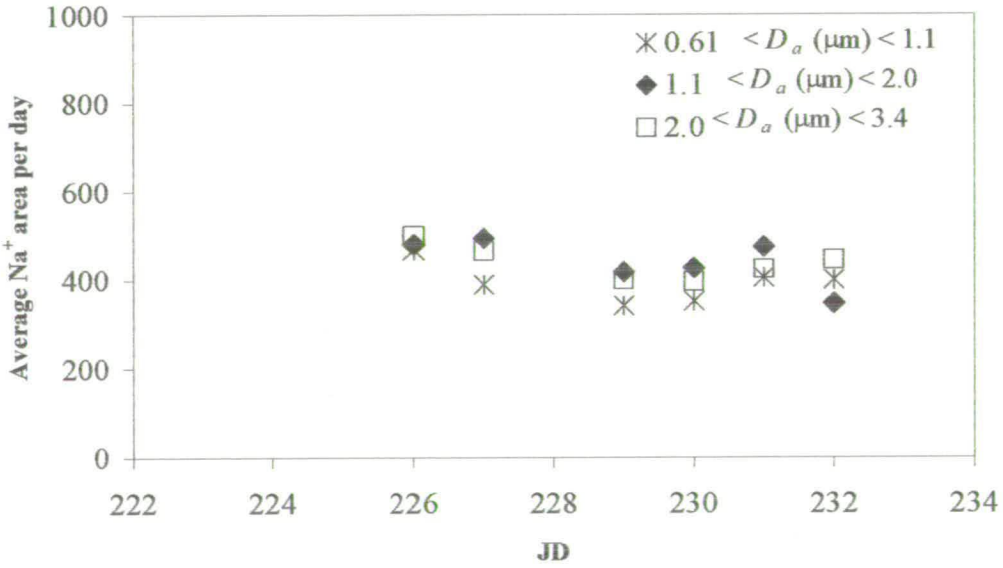

Figure 5.9. Average ATOFMS ion signal per hit particle per day in each size range, plotted against the MOUDI concentration (μg m^{-3}) for that size range and day for Na^+.

The invariance in average ion signal with particle size also implies that there is a particle size dependence in the quantitative relationship between ATOFMS signal

and chemical content of the particle. i.e., the ATOFMS ablates a larger fraction of a smaller particle than of a larger particle. Ge *et al.* (1998) reported on similar observations with LDI-MS of single particles. A constant mass of ablated material equates to an inverse cubic dependence of fraction ablated material on particle diameter. This is demonstrated more clearly in Figure 5.10 which shows the sum (corrected for the hit rate of each chemical species, (HR_k)), according to Equation 5.6, of the measured ATOFMS signals for Na^+, Cl^- and K^+ for all particles in each of the size ranges for each day, plotted against the MOUDI-derived concentration. Prior to the summation, each particle's ion signal, $Resp_j$, was scaled according to the particle detection efficiency, χ_j, described in Section 5.3.2.2.

$$\left(\frac{\sum_{j \subset i} \chi_j \mathrm{Resp}_j}{V}\right) HR_k \qquad \textbf{(5.6)}$$

(V is the volumetric flow rate of the ATOFMS instrument which remained constant throughout the campaign; the label i refers to an ensemble of particles comprising one day and one particle size range). Thus, this procedure differs from that developed by Bhave *et al.* (2002) in that the particle number scaling factor takes into account the variation in hit rate for particles of different composition. The data from each size range in Figure 5.10 each lie on approximately straight lines but of distinctly different gradients. This shows that the linear relationship between ion signal and concentration of chemical species is obtained when variation in particle hit rate with chemical composition is also included.

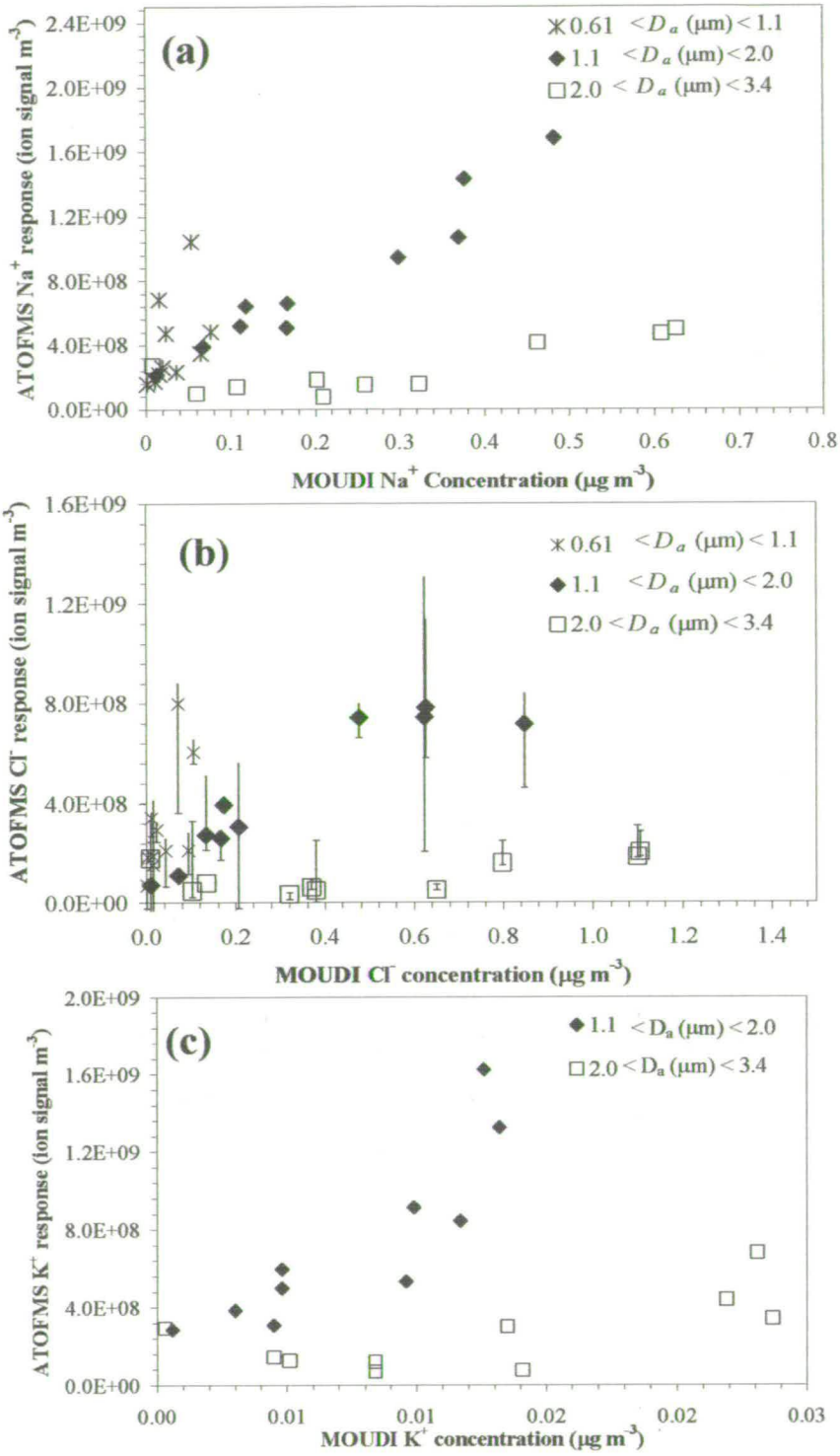

Figure 5.10. Total ATOFMS ion signal, scaled for inverse particle inlet efficiency and variation in hit rate with chemical composition, for all hit particles per day in each size range, plotted against the corresponding MOUDI concentration: (a) Na^+, (b) Cl^-, (c) K^+. Error bars carried through from the inverse transmission efficiency function are plotted on the Cl^- plot for illustration, and are similar for the other species. Uncertainties in MOUDI data are not shown.

By continuing the analogy with the work of Bhave *et al.* (2002) a function, ψ_j, was derived accounting for the dependence of ion signal on particle size by fitting Equation 5.5 simultaneously to all data per chemical species in Figure 5.10,

$$m_i = \frac{\sum_{j \subset i} \phi_j \mathrm{Resp}_j \psi_j}{V} + \varepsilon_i \qquad \textbf{(5.5)}$$

where m_i, is the impactor concentration for each ensemble of single particles, ε_i is the residual to be minimised in the regression, and the ATOFMS inverse sensitivity function to each chemical species, ψ_j, is expressed in terms of aerodynamic diameter by Equation 5.7 in which γ and δ are species-dependent constants.

$$\psi_j = \gamma_j D_a^{\delta_j} \qquad \textbf{(5.7)}$$

Figure 5.11 illustrates the best fits for (a) Na^+, (b) Cl^- and (c) K^+ according to Equation 5.5, where all the points lie as close to the solid line. If the points fall within the two dotted lines (2:1) the fit is said to be reasonably good. The regression for each chemical species yields the species-dependent parameters δ and γ. The γ parameter represents the inverse of the sensitivity of the ATOFMS to the mass of a particular chemical species. The γ values obtained here cannot be meaningfully compared with each other or to those of Bhave *et al.* (2002) because different sub-sets of particles were used for each species according to the extent of detector saturation ('peak clipping'). The δ parameter is, however, a physically-meaningful quantity which shows the relative dependence of ATOFMS response to a particular species in different sized particles. Best-fit values of δ and γ for Na^+, Cl^- and K^+ are given in Table 5.2, together with values for NH_4^+ and NO_3^- reported by Bhave *et al.* (2002).

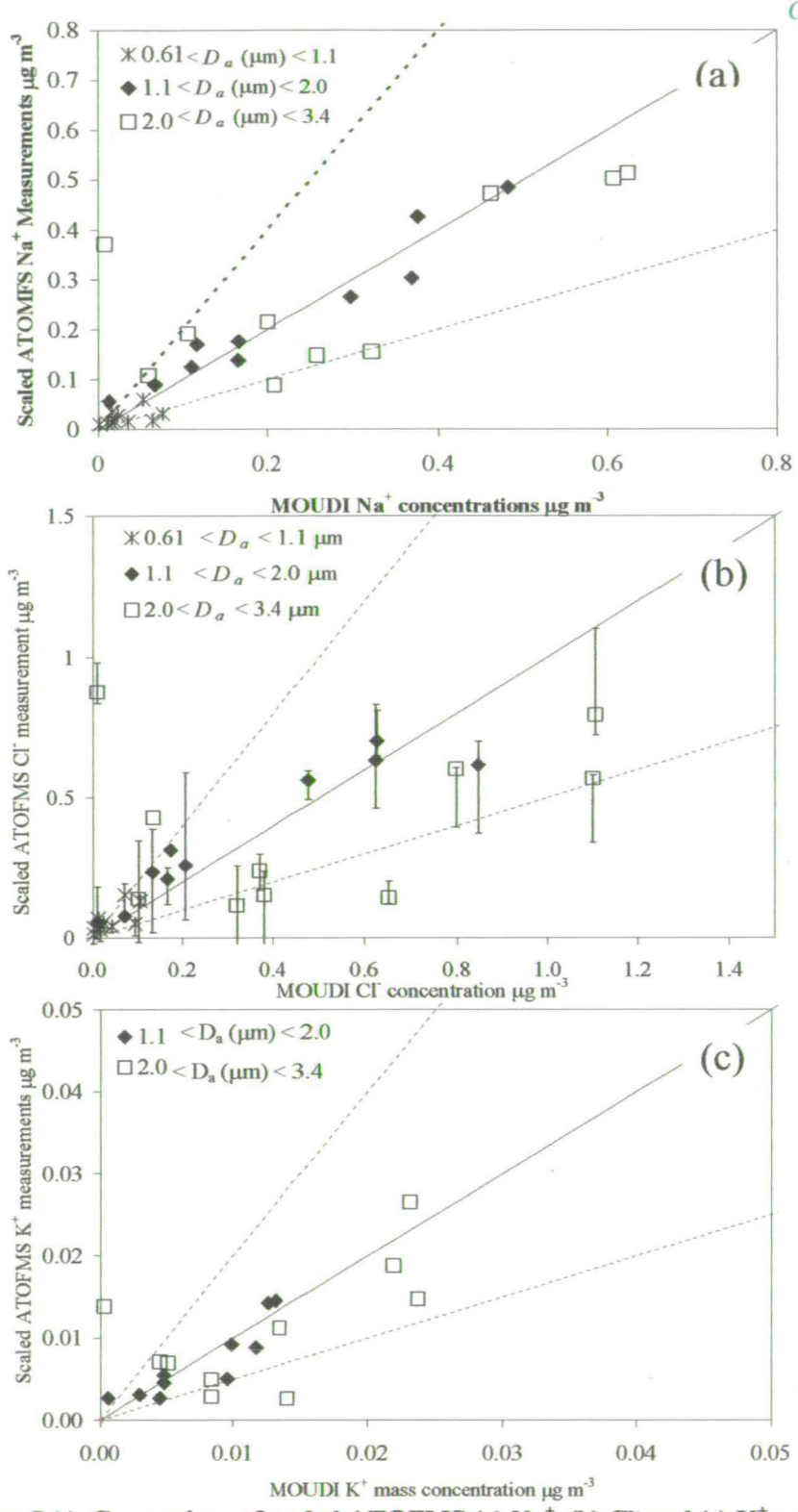

Figure 5.11. Comparison of scaled ATOFMS (a) Na^+, (b) Cl^- and (c) K^+ mass measurements with corresponding impactor measurements. Diagonal dashed lines represent the 1:2, 1:1 and 2:1 lines of correspondence. Vertical error bars are 95% confidence intervals of the scaled ATOFMS measurements.

Chemical species	δ	γ	No of particle ensembles in the regression
Sodium Na^+	2.7 ± 0.3	$9 \times 10^{-11} \pm 0.35 \times 10^{-11}$	30 (This study)
Chloride Cl^-	2.6 ± 0.3	$3.1 \times 10^{-10} \pm 0.25 \times 10^{-10}$	30 (This study)
Potassium K^+	2.7 ± 0.3	$3.2 \times 10^{-12} \pm 0.1 \times 10^{-12}$	20 (This study)
Ammonium NH_4^+	2.4 ± 0.4	$2.5 \times 10^{-10} \pm 0.40 \times 10^{-10}$	30 (Bhave *et al*, 2002)
Nitrate NO^+	2.4 ± 0.4	$4.7 \times 10^{-10} \pm 0.70 \times 10^{-10}$	33 (Bhave *et al*, 2002)

Table 5.3. Best-fit values of δ and γ in the ATOFMS inverse instrument sensitivity function ψ determined as described in the text.

The dependence of ψ on diameter approximately to the power three is consistent with the interpretation of a uniform signal per particle (Figure 5.9), as in a given aerosol mass particle number decreases with diameter to the power one third. The values of δ for Na^+, Cl^- and K^+ thus support the interpretation of Bhave *et al.* (2002) of uniform ablation of NH_4^+ and NO_3^-.

The values for γ are, in principle, a measure of the ionisation efficiency of each ion measured. Since, in this study, it was necessary to remove a number of saturated peaks which differed for each ion, the value cannot be used to represent a true value of the ions' ionisation efficiency. The values determined for Cl^-, K^+ and Na^+ can be used to determine the relative sensitivity of the ATOFMS instrument to each of the ions by using the following equation

$$\left(\frac{Na^+}{Cl^-}\right) = \frac{23}{35} \bullet \frac{\gamma Cl^-}{\gamma Na^+} \qquad \textbf{(5. 8)}$$

where 23 and 35 are the molar masses of Na^+ and Cl^- respectively. RSF are defined on a molar basis and are used to correct for differences between instrument sensitivities to two chemical species. Using Equation 5.8 and the best-fit γ values listed in Table 5.3, the RSF of Na^+ versus Cl^- under Mace Head sampling conditions is 2.3, and the RSF of Na^+ versus K^+ is 0.021. Gross *et al.* (2000a) reported relative sensitivity factors of K^+/Na^+ of 5.1:1 This implies that ATOFMS measurements of particles containing equal amounts of Cl^- and Na^+ should yield larger ion signals (x 2.3) at *m/z* 23 than at *m/z* -35 and that a particle containing equal amounts of K^+ and Na^+ should yield large ion signals (x 21) at *m/z* 39 than at *m/z* 23. While the results

for Na^+/Cl^- are plausible those for Na^+/K^+ are slightly larger than expected. This is most likely due to the large number of saturated peaks removed from the total number of Na^+ and K^+ particles present.

Illustrated in Figure 5.12 are three graphs containing scaled Na^+, Cl^- and K^+ and mass measurements plotted with high time and size resolution. Although the values presented here are not absolute it is possible to illustrate that with a combination of laboratory and field measurements, as well as measurements from other instrumentation it may be possible to develop scaling factors that will allow true quantitative data to be acquired using an ATOFMS.

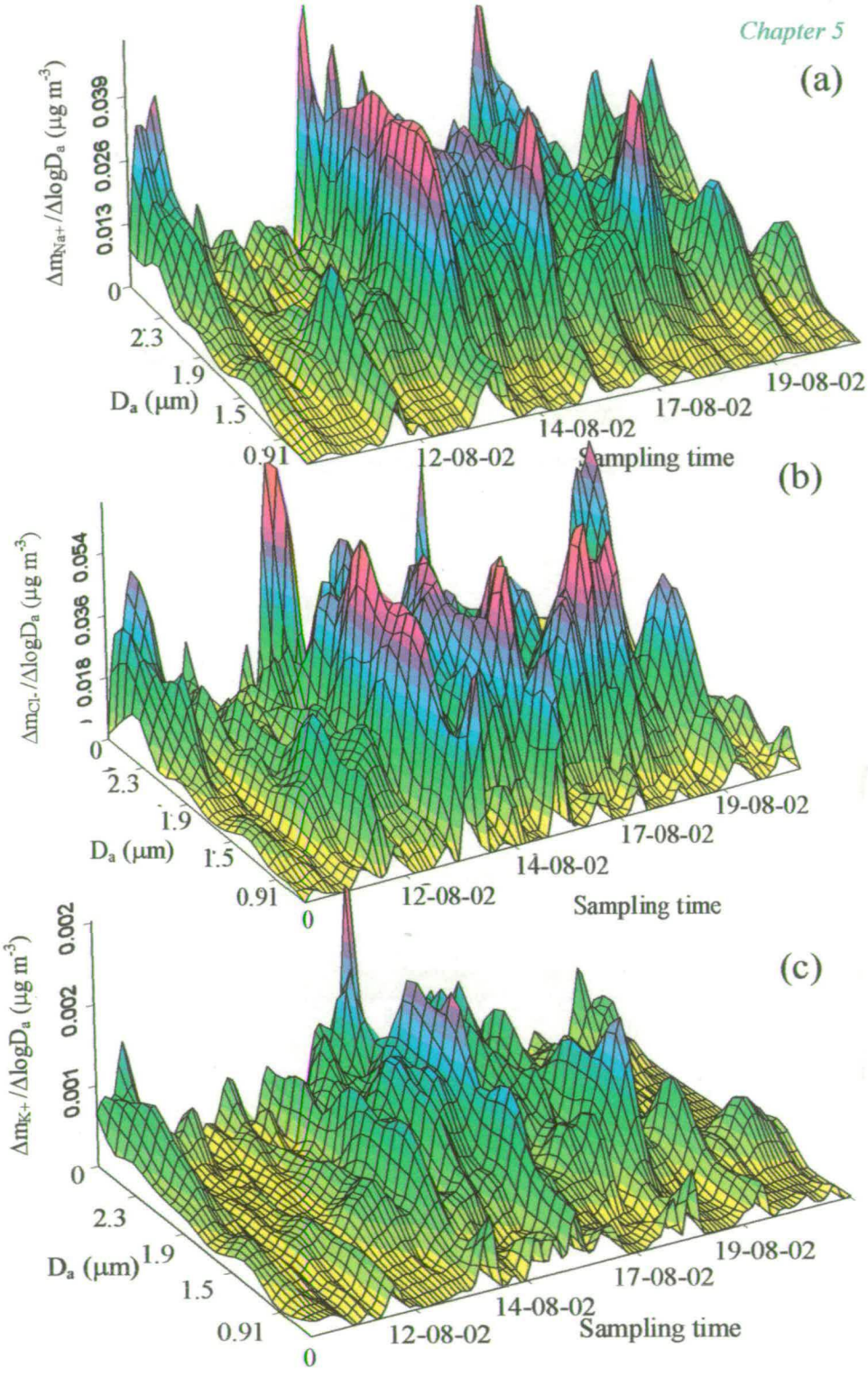

Figure 5. 12. Mass distributions during NAMBLEX. The time series is based on scaled ATOFMS measurements for 4-h intervals from August 12th-21st 2002 for (a) Na^+, (b) Cl^- and (c) K^+.

5.4. Conclusion

In conclusion, by analysing a dataset of single particles consisting of distinct episodes of different particle composition type, it has been shown here that there is a strong particle compositional-effect for the particle hit rate efficiency but no significant additional composition-effect for the ablation and ionisation process once the desorption-ionisation energy couples to the individual particle. Ideally, the instrument sensitivities deduced from a field-based approach may be verified and further tested in laboratory experiments.

The instrument sensitivity factors derived from tandem ATOFMS-impactor sampling can be used to reconstruct continuous ATOFMS measurements of size-segregated Na^+, K^+ and Cl^- concentrations during NAMBLEX 2002. It has been demonstrated that it is possible to obtain quantitative mass and size measurements from the ATOFMS but in order to demonstrate the applicability to other instruments laboratory work would have to be carried as well as more field studies with parallel ATOFMS and impactor sampling.

Chapter 6

Characterisation of ambient particles for human exposure studies

Chapter 6 Characterisation of ambient particles for human exposure studies

6.1. Introduction

Epidemiological and toxicological studies have consistently shown that elevated levels of particulate air pollution (quantities of PM_{10} and/or $PM_{2.5}$) are associated with adverse health effects such as asthma and respiratory problems, as well as increased mortality not only from respiratory causes but also from cardiovascular disease (Pope, 1999; WHO, 2003). There is growing evidence that air pollution can precipitate acute cardiac events (Prescott *et al*, 1998). It has been hypothesised that the smallest particles translocate from the lungs into the circulation therefore influencing cardiovascular endpoints more directly (Nemmar *et al*, 2002; Oberdorster *et al*, 2004).

For this reason there has been increasing interest towards ultrafine ($PM_{0.1}$) and fine ($PM_{2.5}$) particles. Toxicological studies involving different types of $PM_{0.1}$ & $PM_{2.5}$ have revealed a wide range of adverse health effects, ranging from very high to mild acute pulmonary inflammatory responses to effects on extra-pulmonary organs such as the cardiovascular system (Donaldson *et al*, 2002). Strong evidence is available suggesting that fine particles settle deep within the respiratory system (Dockery *et al*, 1993) and can undergo translocation from the respiratory tract to other organs including the brain. Oberdorster (2004) monitored the progress of carbon particles, with diameters of 35 nm, which had been inhaled by rats, were monitored and reported that these particles translocated to the brain. Similarly Nemmar *et al.* (2002) showed that ultrafine particles can pass through the lungs and enter blood circulation by taking measurements of the blood from volunteers who had inhaled radioactively labelled ultrafine carbon particles.

The two important challenges for researchers in this field are to establish both the physicochemical properties of the inhaled particles and the consequent biological mechanisms responsible for the different observed associations. Progress on the former requires better size and chemical characterisation of the ambient particles to which populations or cohort members are exposed, whilst progress on the latter requires experiments testing potential causal mechanisms either in vitro or, ideally, in vivo using model or genuine PM. A major criticism of most mechanistic studies is that the exposure route is artificial and the PM dose is very high.

Alternative methods have been developed to determine the effect of particulate pollution on human health. These methods use specially designed exposure units which allow human/animal subjects to be exposed to concentrated ambient (or model) particles. The first unit designed was known as the Versatile Aerosol Concentration Enrichment System (VACES). The VACES was developed for use in experimental exposure studies to concentrate ambient particles by about 30 times without changing their physical properties (Sioutas *et al*, 1995; 1997). Since the initial development of the particle concentrator several new models have been designed such as the Harvard Ambient Particle Concentrator (HAPC) (Lawrence *et al*, 2004) and more recently particle concentrators that allow particles in different size ranges to be concentrated (ultrafine, fine and coarse) (Kim *et al*, 2001a; 2001b). All instruments are based on the same operational principle (Section 6.2) and only differ slightly depending on the intended application. The concentrated ambient particles are known as CAPs.

Devlin *et al.* (2003) exposed elderly humans to CAPs, with diameters less than 2.5 μm, for 2 h with no exercise. They reported changes in heart rate variability (HRV) which was measured immediately before, immediately following and 24 h after exposure. Significant decreases in HRV were reported and these changes occasionally persisted for 24 h. The data from this study were compared to a similar one in which young healthy volunteers were exposed to CAPs but no change in HRV was reported. Other studies have been carried out on rats and mice. Chen *et al.* (Chen & Hwang, 2005; Chen & Nadziejko, 2005) carried out a study which investigated

many of the possible detrimental effects of CAPs on mice. During this study the VACES system was used to examine 32 mice at one time. Some of the results show the damaging effects, induced by the inhalation of CAPs, on cardiac functions and HRV (Chen & Hwang, 2005; Chen & Nadziejko, 2005). Wellenius *et al.* (2003) reported on exposing mongrel canines to CAPs using the HAPC. It was reported that under controlled laboratory conditions CAPs significantly exacerbate myocardial ischemia (reduced blood flow to the heart) during acute coronary artery occlusion.

Particle concentrators provide a direct and controlled method of investigating the link between inhalation of particulate matter and health effects in humans and animals. Results can be obtained over a period of days rather than years and specific criteria are used to determine the health effects in each study.

6.1.1. Evaluation of particle concentrators

Several recent studies have employed the use of single particle mass spectrometers to determine if single particle chemical composition is affected by particle concentrators. Moffet *et al.* (2004) used an ATOFMS in conjunction with particle sizing instrumentation to determine the size, chemical composition and concentration enrichment of the HAPC. During this study the HAPC concentrated particles in the $PM_{2.5-10}$ range. It was reported that no or little change in the composition of particle types were detected in the pre- and post-concentrated air flows.

An AMS was used to investigate the effects of concentrating semi-volatile aerosols using water-condensation technology with the VACES. Slight changes in the size distribution of semi-volatile aerosols were observed. The shape of the size distribution for sulphate particles remained the same between upstream (US) and downstream (DS) sampling, but only remained similar during clean periods for organics, ammonium and nitrate. On polluted days the concentration of these compounds, especially the nitrate, increased (Khlystov *et al*, 2005).

Zhao *et al.* (2005) coupled the VACES with a RSMS-3 to investigate if the VACES induced changes in particle composition with diameters between 40 – 640 nm. Small

differences in chemical composition were observed between samples with and without the VACES particle concentrator. The shift of 8-10% of the particles from one class to another was suggested to be due to changes in the composition of the ambient air rather than changes induced by the VACES particle concentrator.

In this work an ATOFMS instrument was coupled with a Mobile Ambient Particle Concentrator Laboratory (MAPCEL) which contained the VACES, and will be referred to as MAPCEL-VACES. The effect of the particle concentrator on single particle composition with diameters between 0.3 and 3 μm was studied.

6.1.2. Chemical characterisation of ambient aerosol during exposure studies

Determining the size-segregated chemical composition of an aerosol is an important part of any human exposure study in order to correlate certain particle types with deleterious health effects. Ambient particle concentrators concentrate ambient particles which exhibit variability in both particle mass and composition. This variability in particle mass and concentration makes it difficult to characterise them. Characterisation of concentrated particles for both human and animal exposures has been carried out using impactor instruments or by collecting particles onto Teflon filters (Sioutas *et al*, 1995).

The disadvantage with filter techniques, already discussed in Chapter 1, is that only information on the chemical species under investigation is provided and it is not possible to determine if there is internal or external mixing within the particles. Another disadvantage is the time between collection and analysis. Filters are usually stored in a cool place until analysis takes place sometimes up to a month after sampling. The loss of gaseous semi-volatile species is possible as well as chemical reactions taking place on the filter changing the chemical species collected before particle analysis takes place. In addition to the above points exposure studies are normally only conducted for 2 h which makes it difficult to acquire enough particulate mass on filters for analysis.

In this study, an ATOFMS was used to determine the chemical composition of the ambient aerosol during the first UK-based CAPs exposure study (Mills *et al*, 2005a). The data from the ATOFMS were used to determine if certain particle types caused more of an effect than others and also to determine the chemical variability of ambient particles over short periods of time.

The advantage of using the ATOFMS instrument over filter-based techniques is that the ATOFMS can obtain single particle information with high time resolution compared to bulk analysis techniques where particles are collected on a filter and have a wide range of particle size and composition. In some exposure studies (Wellenius *et al*, 2003) particles were characterised by a plethora of instruments such as gravimetric determinations for particle mass, ion chromatography for sulphate, X-ray fluorescence analysis for elemental composition, and thermal and optical reflectance analysis for elemental and organic carbon. The ATOFMS can provide information on a wide range of particle compositions with high time resolution and, with the presence of an adequate scaling function, provide semi-quantitative mass measurements.

6.1.3. Outline of the exposure study

The MAPCEL-VACES particle concentrator was brought to Edinburgh, UK where Mills *et al.* (2005a) designed a study to investigate the effect of particulate matter on human cardiac function. This is the first study undertaken where the health effects induced by the inhalation of CAPs on patients with ischemic heart disease has been assessed.

Twelve male patients with stable ischemic heart disease and 12 age-matched non-smoking volunteers were recruited. These individuals were exposed to CAPs in Edinburgh or filtered air during 2 hours of intermittent exercise using a randomised double-blinded cross-over study design (meaning that neither the patient or the doctor knew whether the patient was being exposed to filtered air or concentrated ambient particles and the exposures were randomnly assigned to filtered air or concentrated ambient exposure). A series of tests were carried out by Mills *et al.*

(2005a) to determine any adverse cardiac health effects. These tests were carried out immediately before, immediately following and 24 h after exposure. The hypothesis of this study was that exposure to CAPs causes systemic inflammation and detrimental vascular effects. Exposures were carried out over two fortnight sessions. The first was carried out on healthy age-matched individuals and the second was carried out on age-matched individuals who suffered from heart disease.

Sampling was conducted outside the Royal Infirmary Hospital, an urban background site, outside of central Edinburgh (3.22° W 55.95° N) for two weeks during February 2004. The ATOFMS and MAPCEL-VACES were situated in a public car park directly in front of Accident and Emergency (Figure 6.1). There was a bus route passing directly in front of the sampling area as well as an arterial route (A7) a few hundred metres away.

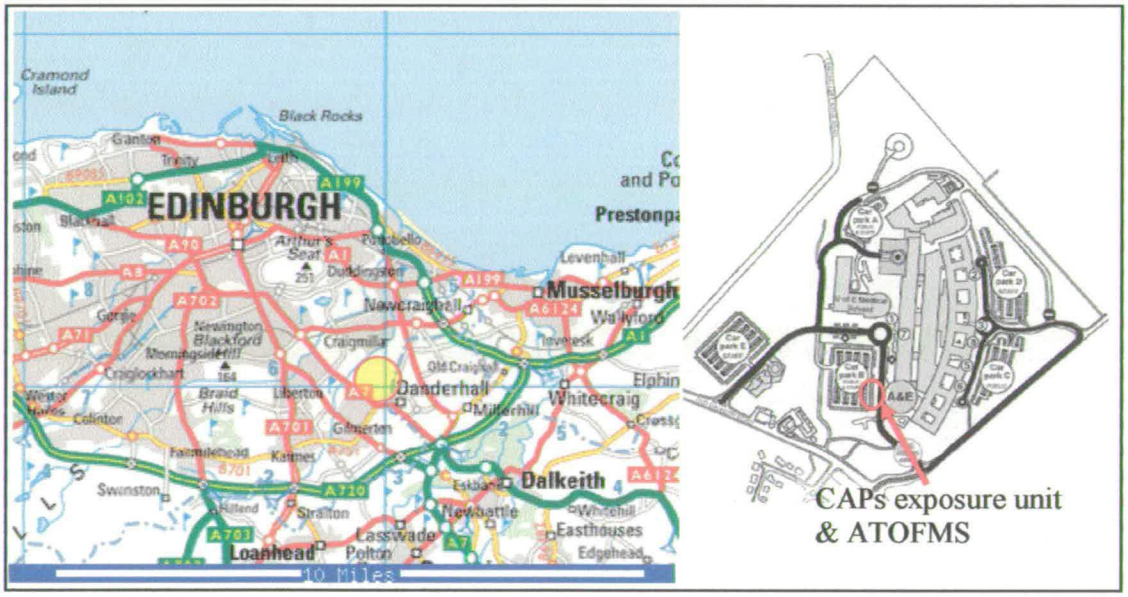

Figure 6.1. Location of CAPs exposure unit and ATOFMS during exposure and characterisation studies

The primary reason for the sampling location was for safety as this was the first time a study had been carried out in the UK and the first time ever that a study had been carried out on human subjects with heart disease. If a major response occurred in the human subject it was possible to get appropriate help in a short time. Also as several

health tests had to be carried out immediately before and after exposure it was necessary to have access to relevant equipment (Mills *et al*, 2005a).

6.2. Experimental

The particle concentrator is designed to concentrate ambient particulate matter, with particle diameters < 2.5 μm and deliver them to the exposure chamber at a flow rate of 50 LPM in order to fulfil human breathing requirements. A schematic diagram outlining the operation of the particle concentrator is shown in Figure 6.2.

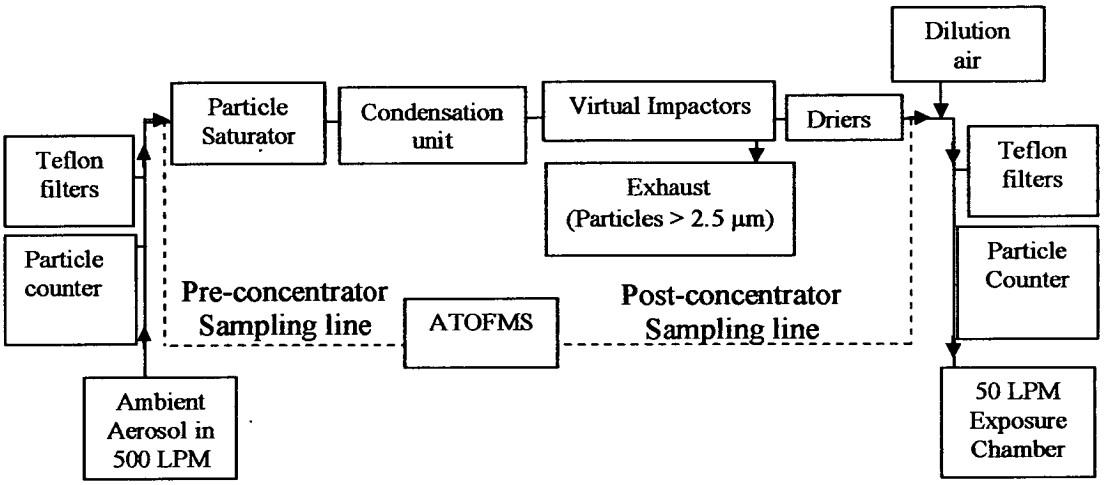

Figure 6.2. Schematic diagram depicting the operation of the ambient particle concentrator used in this study. The dotted lines illustrate the sampling lines to the ATOFMS. The ATOFMS was switched between sampling lines for 40 minutes each.

The MAPCEL-VACES (Figure 6.2) operates at an intake flow rate of 500 LPM. Ambient particles are passed through a particle saturator which consists of deionised water and a heating bath. The heated vapour of the deionised water is mixed with the particulate matter, resulting in a saturated aerosol. The saturated aerosol enters into a condensation unit where the aerosol is cooled causing water to condense onto each particle. The size that a particle grows to depends on its original diameter. The outward flow from the condensation unit was 110 LPM.

There was no size selection inlet to remove coarser particles but this made little difference as particles >2.5 μm are largely deposited in the concentrator. The number concentration of particles with diameters < 2.5 μm is increased using virtual impactors. The minor flow of the virtual impactor contains the concentrated aerosol. The outward flow was 25 LPM from the virtual impactors. The concentrated fine particles were then passed through a number of silica gel dryers. These dryers removed the water condensed on the particles with the expectation that the particles returned to their original size (and composition). After flowing out of the drying stages, the concentrated particles were diluted with particle-free conditioning air (at a flow rate of 25 LPM) which was introduced around the concentrated airflow. This air was added to provide enough airflow for human subjects' breathing requirements. The outward airflow into the exposure unit was 50 LPM. The overall concentration factor of the aerosol, after dilution with the conditioning air, was in the range of 6-11.

The ATOFMS was housed inside a transit van; stainless steel tubing was attached to the inlet of the ATOFMS and exited through the rear door of the van. Portable heaters were operated inside the van in order to maintain optimum working temperatures for the ATOFMS instrument (20-30°C). The ATOFMS monitored the ambient air outside the concentrator van during the first part of the experiment where data on the chemical composition of the ambient air at the time of the human exposure were required.

During the second part of the experiment the effect of the particle concentrator on the particle ensemble was investigated. The ATOFMS inlet was connected to the upstream and down-stream flows of the particle concentrator via copper tubing (1 cm i.d.), as shown in Figure 6.2. The connections to the upstream and downstream airflows alternated every 40 minutes of sampling. This allowed for a statistically-relevant sample size to be collected for analysis. Figure 6.3 shows a photograph of the ATOFMS instrument housed inside the transit van with the copper tubing connected into the MAPCEL-VACES unit.

Figure 6.3. A photograph of the ATOFMS instrument sampling from the upstream/downstream air flows of the MAPCEL-VACES unit.

The analysis of the individual particle mass spectra was carried out using a statistical package (MINITAB® Release 14.13.) employing a K-means algorithm which is a non-hierarchical clustering procedure. This algorithm has already been explained in detail in Chapter 4. Microsoft Access®2002 and Excel®2002 were also employed to examine trends in these data based on the results from the K-means algorithm.

Twenty clusters were chosen initially to classify the dataset using the K-means clustering. Although this resulted in a large number of the particle classes contributing <1% each of the total number of particles in the whole dataset, it allowed a sufficient amount of clusters to be created in order to describe the sampled aerosol. If any clusters appeared to be similar in mass spectral pattern, size distribution and temporal trend, the clusters were combined. All data were prepared in the same manner as in Chapter 4.

6.3. Results and Discussion

Analysis of ambient particulate matter during exposure studies was carried out for eight days. The aim of the experiment was to characterise the chemical composition of atmospheric particulate matter during subject exposure and to use these data to correlate particle composition with detrimental effects, if any, in the subject as well as observing the temporal variation of particulate matter during short periods of time. Each exposure study was carried out for approximately two hours. The ATOFMS sampling was often carried out for 3 h depending on the weather conditions and how well the instrument was working on that particular day. The exposure days and times, together with mean weather conditions**, are listed in Table 6.1.

Date	*Sampling Time*	*Temp /°C*	*Wind direction* / degrees	*Wind speed m/s*	*RH /%*
02/02/04	7:51:28 – 12:00:32	7.6	228	4.5	81
03/02/04	*Problem with ATOFMS*	13	207	10.5	82
04/02/04	7:39:54 – 10:31:07	9.1	230	6.3	78
05/02/04	7:57:09 – 10:31:09	10.6	234	8.5	70
09/02/04	8:59:42 – 11:04:09	1.5	255	2.8	72
10/02/04	7:46:12 – 10:53:01	8.7	250	9.7	85
11/02/04	9:55:03 – 12:11:06	8.9	230	2.4	83
12/02/04	7:44:37 – 10:56:50	4.2	242	0.8	97
17/02/04	10:53:37 – 12:54:57	5.5	280	1.5	75
18/02/04	11:02:12 – 12:40:46	5.4	223	0.7	71

Table 6.1. Dates, times and weather conditions of human exposure to CAPS when the ATOFMS was sampling**

6.3.1. Air mass back trajectories

Air mass back plots were used in order to understand the source of the ambient aerosol detected. In this study, 5-day back plots with an Edinburgh arrival point of 3.2°W, 55.9°N were computed for the sampling period and are shown in Figure 6.4.

** Weather information was supplied by the Edinburgh meteorological office situated at Edinburgh Gogarbank, Lat/Long: 55°56'N, 3°21'W, Altitude 57 m. Weather conditions were recorded only for the sampling times shown.

NAME back maps[††] were plotted for all air arriving within the boundary layer depth at the receptor between time intervals of 0700-1100 h on each day of sampling. The NAME model is explained in detail in Chapter 4 Section 4.3.1. The criteria used to classify each of the NAME back trajectories are explained in Table 6.1.

From the back trajectories it can be assumed that the particles detected by the ATOFMS instrument are going to be dominated by particles from a marine air source and consist mainly of sea-salt and other inorganic type particles. Any carbonaceous particles detected are more likely to originate from local sources.

[††] NAME back plots were supplied by Mark Harrison at the Met. Office

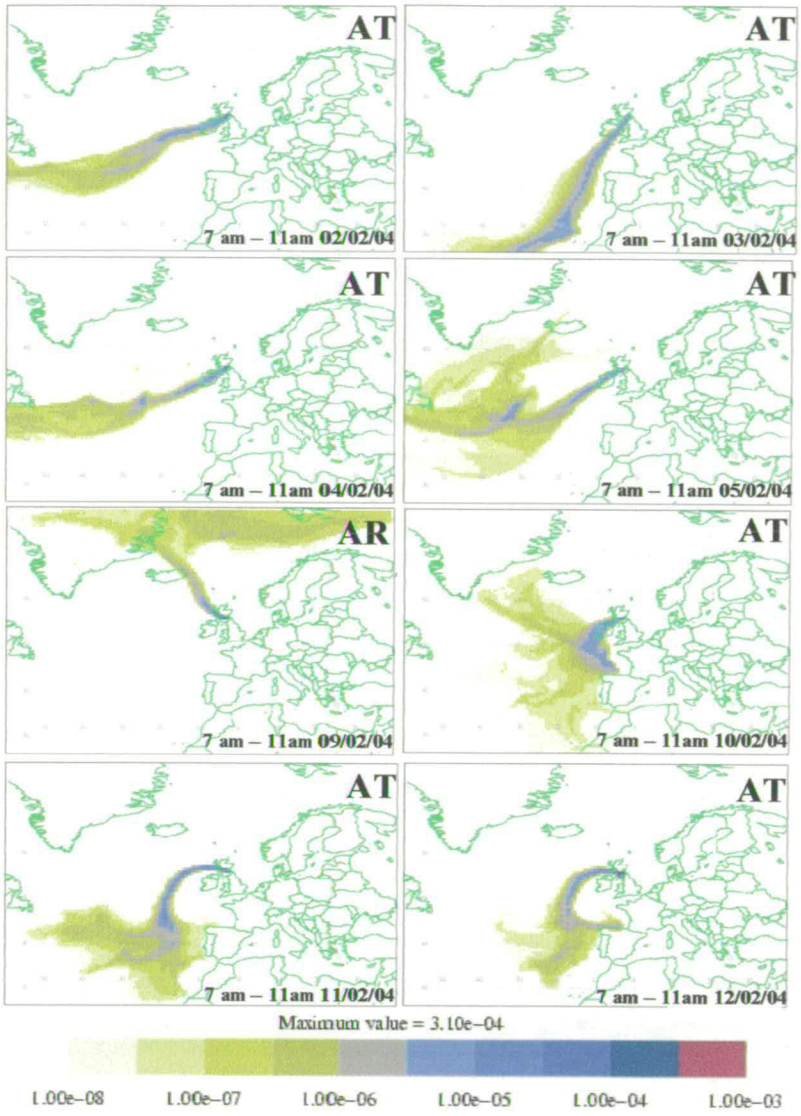

Figure 6.4. Five-day back maps for air arriving in Edinburgh in the boundary layer for week 1 (2^{nd} -5^{th} Feb 2004) and week 2 (9^{th} – 12^{th} Feb 2004) of sampling. The scale is a relative measure of the contribution of source regions. Back trajectories were classified according to the criteria in Table 6.2.

Category	*Description of trajectory categories*
AT	Trajectory spending most of 5-day period crossing the Atlantic Ocean
AR	Trajectory spending most of 5-day period in the region 60-70°N and 10°N-10°E, including those originating over or near Greenland

Table 6.2. Criteria used to classify predominant source regions.

6.3.2. Chemical characterisation of ambient air during human CAPS exposures

All of the particles detected by the ATOFMS were included in the same work sheet and a K-means analysis was carried out on all of the single particle mass spectra (18,732 particles). This allowed for the whole dataset to be considered for the same particle types and also allowed the change in the chemical composition to be viewed as a function of time.

As mentioned in Section 6.2, 20 clusters were chosen for the analysis. It was possible to group these clusters into six large particle groupings containing sea-salt (mixed, pure and reacted), carbonaceous (elemental (EC) and secondary elemental) and dust (Al/Fe/Ca) particles. A full description of each of the particle classes is shown in Table 4.3. A full description will be provided of any new particle classes that were identified in this study that were not previously explained in Chapter 4.

Temporal trends of the proportion contribution of each particle class, grouped in 1 hour time intervals, are shown in Figure 6.5. It can be seen that salt particles dominate the total number of particles detected with a total contribution of 90%. Pure, mixed and aged sea-salt particles are present in the coarse size distribution as shown in Figure 6.6. Carbonaceous type particles contribute 4% of the particles sampled to the total particles detected and dominate the finer fraction of the total aerosol size distribution. Dust particles show a broad monomodal distribution and contribute a total of 6% to all particles detected.

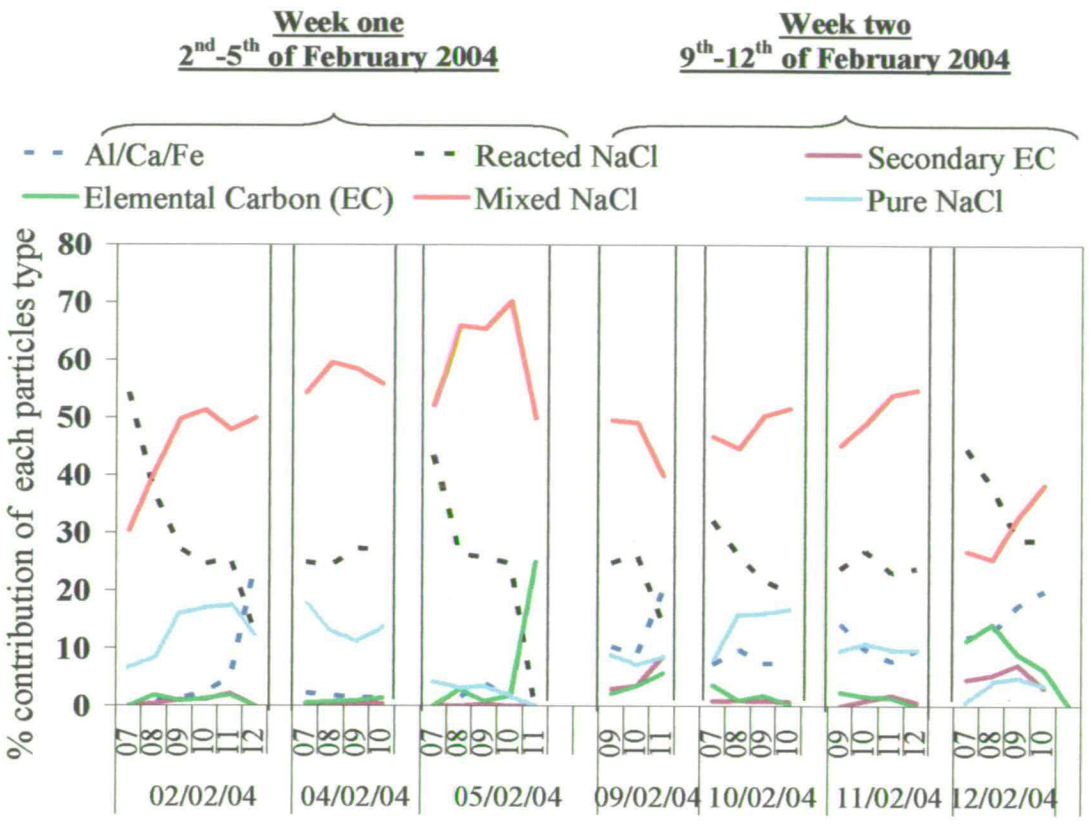

Figure 6.5. Percentage contribution of the six main clusters present over time.

The chemical composition of the particles remained relatively constant throughout the sampling period. Figure 6.5 shows that during the first week of sampling a high number of 'clean' marine particles were detected (except during 1100-1200 h on the 05/02/04) whereas more carbonaceous material was detected during the second week of sampling particularly during 1100-1200 h on the 9/02/04 and all of the 12/02/04.

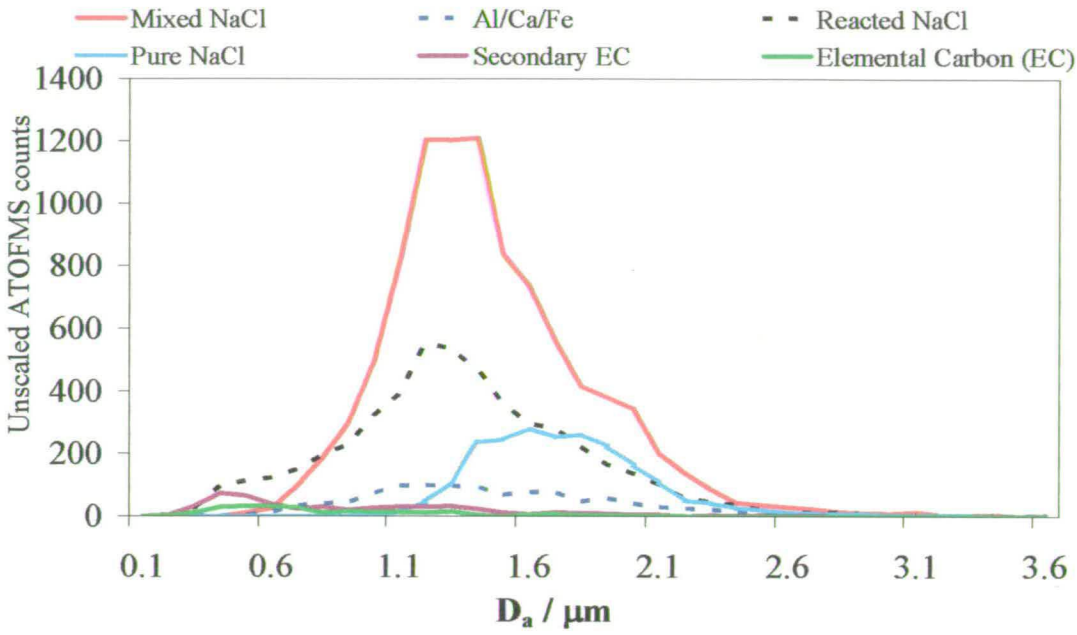

Figure 6.6. Size distributions of the six main particle types detected during CAPs exposures

During the sampling period the aerosol detected in Edinburgh had a strong marine influence (Figure 6.4) explaining the dominance of sea-salt particles in the dataset. Examples of the most common laser desorption/ionisation mass spectra from an individual pure and mixed sea-salt particle are shown in Figure 6.7 and 6.8 respectively. 12% of all particles detected contained pure sodium chloride. It is likely that these particles originated directly from the sea without undergoing any secondary processing. The pure salt particles were mainly distributed in the coarser aerosol fraction with diameters greater than 1.1 µm (Figure 6.6).

Almost all of the peaks observed, in the mass spectra of the pure salt particles, are attributable to sodium chloride clusters. In the positive ion mass spectrum, peaks are present for Na^+ (*m/z* 23), NaO/K^+ (*m/z* 39) and $(NaCl)_nNa^+$ (*m/z* 81, 139, 197). In the negative ion mass spectrum, peaks are present for OH^- (*m/z* 17), Na^- (*m/z* 23), Cl^- (*m/z* 35), $NaCl^-$ (*m/z* 58), $(NaCl)_nCl^-$ (*m/z* 93, 151, 209) and $(NaCl)Cl(H_2O)_n^-$ (*m/z* 111, 129). The presence of peaks for $Na(H_2O)^+$ (*m/z* 41) and $Na(H_2O)_2^+$ (*m/z* 59) were observed in several mass spectra along with some negative sodium chloride cluster peaks for $(NaCl)Cl(H_2O)^-$ (*m/z* -111) and $(NaCl)Cl(H_2O)_2^-$ (*m/z* -129). These

ion signals have also been detected during the NAMBLEX campaign carried out at Mace Head (Chapter 4) and also coincided with peaks at *m/z* O^- (*m/z* -16) and OH^- (*m/z* -17) which suggests that water is strongly associated with these particles. These peaks were detected in both the mixed and pure salt. Additional ion signals for nitrate, NO_2^- (*m/z* -46), NO_3^- (*m/z* -62), $(NaCl)NO_2^-$ (*m/z* -104) and $(NaCl)NO_3^-$ (*m/z* –120) were present in the negative ion mass spectra of those particles classified as mixed salt. Mixed salt particles contributed 51% to the total particle ensemble detected. Sea-salt aerosols can react with HNO_3 to form nitrate and release hydrogen chloride to the gas phase (Harrison *et al*, 1999; Harrison & Pio, 1983; Pakkanen, 1996).

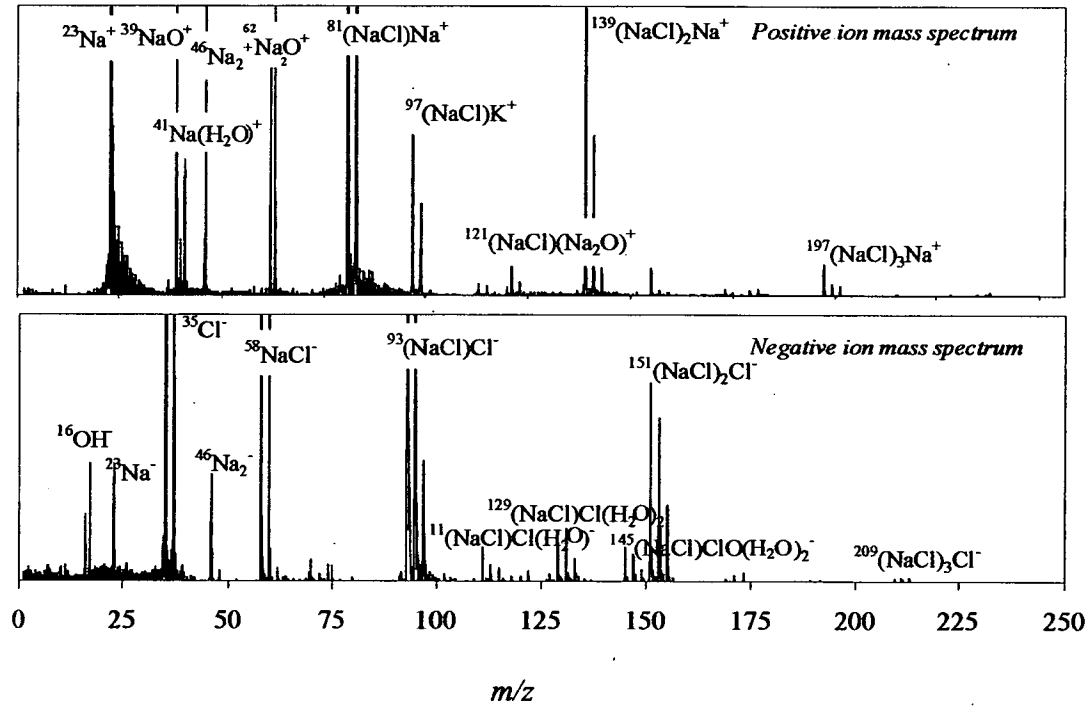

Figure 6.7. Positive and negative ion mass spectra from a 2.18 μm particle classified as pure sea-salt.

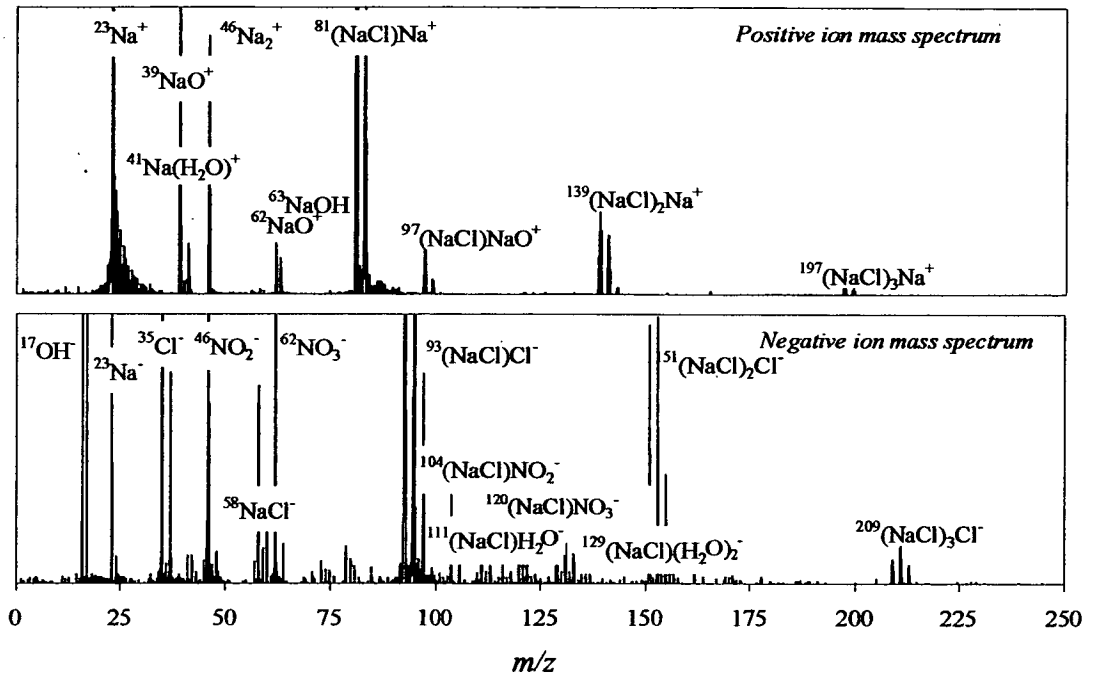

Figure 6.8. Positive and negative ion mass spectra from a 1.70 μm particle classified as mixed sea-salt.

27% of all particles detected were classified as reacted sea-salt. An example of a positive and negative ion mass spectrum resulting from reacted sea-salt particles is shown in Figure 6.9. These particles were identified as having signals for sodium in the positive ion mass spectrum and having no chloride species present in the positive or negative ion mass spectrum. During this study many of the particles that were classified as being reacted sea-salt contained little or no negative ion mass spectrum. When a negative ion mass spectrum was detected peaks for nitrate/sulphate species were detected in the negative ion mass spectra. It was classified as reacted sea-salt as the positive ion mass spectra contained strong signals for Na^+ and NaO^+. It is possible that this lack of negative ion mass spectra could be due to a different particle type although it is more likely that it is a result of instrumental problems rather than a different particle type (Moffet *et al*, 2004). During a TSI workshop at the Leipzig EAC conference 2003 the University of California Riverside group suggested that the lack of negative ion mass spectra was related to high relative humidity. Since the relative humidity during these measurements was always above 70% it is not possible to accurately account for this problem.

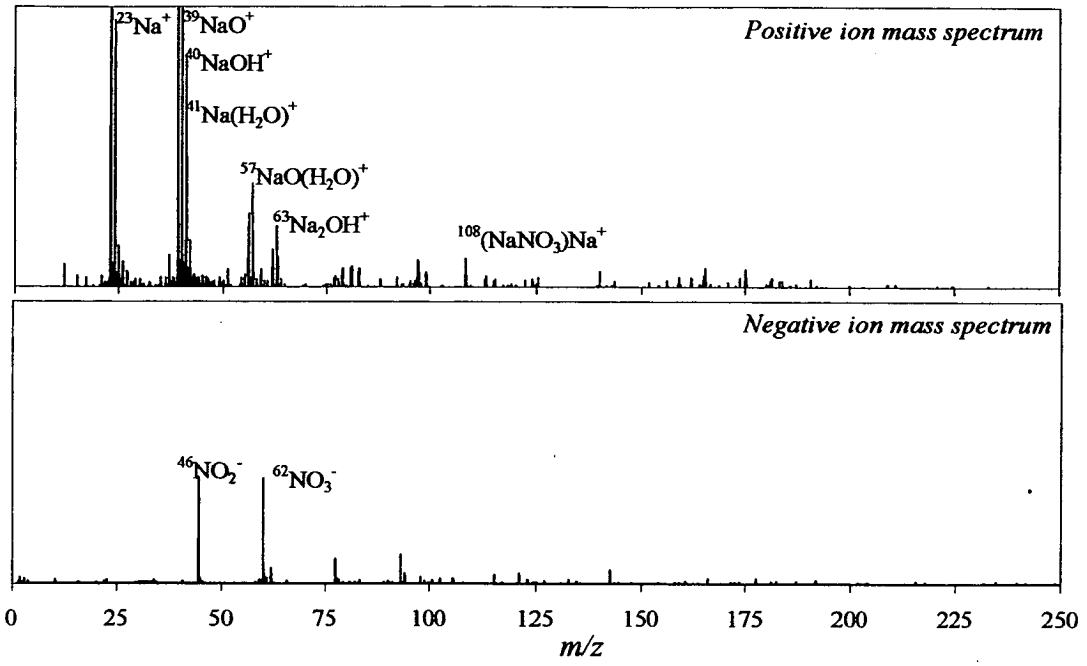

Figure 6.9. Positive and negative ion mass spectra from a 1.12 μm particle classified as reacted sea-salt particle.

The sea-salt aerosols were mainly distributed in the super-micron (>1 μm) size distribution. This is expected as airborne sea-salt particles are released to the atmosphere from spray formed by wave action in the surface layer of seawater (Odowd *et al*, 1997).

The mixed or reacted sodium chloride particles can originate from two possible sources. Air masses were arriving from a westerly direction throughout the sampling period. Sea-salt particles travelling from the sea will have crossed over Glasgow and the centre belt of Scotland before reaching Edinburgh. It is possible for these particles to become mixed with secondary species such as SO_4^- (*m/z* -96) and NO_3^- (*m/z* -62). The second possibility is road salt. As the sampling was carried out in early February there was transient snow and ice present and the roads were salted at least daily. The mixed salt particles detected could have resulted from the re-suspension of gritting salt on the roads. A sample of road salt was taken into the laboratory and dissolved in deionised water and nebulised into the ATOFMS instrument. The data were analysed using the K-means clustering algorithm and

almost 70% of the particles had ion signals for mixed sodium chloride particles, 20% of the particles were classified as dust, and the remaining 10% were pure sea-salt. The particles classified from the road salt mixture did not contain any ion signals specific to that mixture.

6% of the total particles were classified as dust-containing particles. As mentioned previously, in Chapters 1 and 4, dust is a significant contributor to tropospheric particulate matter throughout the world and is the second largest primary particle source after sea-salt. There have been several records of the transport of soil dust over long distances (Silva *et al*, 2000; Dall'Osto *et al*, 2004). These clusters contained positive ion signals for lithium, aluminium and calcium along with negative ion signals for sulphate and nitrate. An example of a positive and negative ion mass spectrum of a dust particle is shown in Figure 6.10. The size distribution of dust particles, shown in Figure 6.6, is broad and monomodal ranging from 0.3 to 3 μm. The dust particles can be divided up into different sub groups of particles originating from different sources. The most common type of dust particle detected contained ion signals for aluminium and calcium and contributed 5.2% to all the particles sampled. Many of the dust particles contained ion signals for Na^+ (*m/z* 23), K^+ (*m/z* 39), Cl^- (*m/z* -35, -37) and OH^- (*m/z* -17) indicating that they were mixed with sea-salt. Similar observations were reported in Chapter 4. The second type of particle is the calcium containing particle contributing 0.66% to the total particles sampled. The least common type of dust particle contained Na^+ (*m/z* 23), Al^+ (*m/z* 27), K^+ (*m/z* 39) and Fe^+ (*m/z* 54, 56) and contributed 0.12% to the total particles detected. Three isotopes of Mg^+, (*m/z* 24, 25 and 26) were often present in this particle mass spectrum. This combination of peaks have been reported to be more indicative of dust from sand sources, rather than soil (Silva *et al*, 2000). It is possible that these particles are originating from a sand source most likely from the beaches along the Edinburgh coastline. In the sand-type and mixed dust particles, peaks for SO_2^- (*m/z* -64) and SO_3^-(*m/z* -80) dominate the mass spectra along with those of NO_2^- (*m/z* -46) and NO_3^- (*m/z* -62). From this analysis it was evident that nitrate peaks occur much more frequently in sand-type dust particles (61%) than the calcium-rich dust particles (39%) which might suggest that these sand-type particles are a result of

long range transport. Li^+ (*m/z* 7) was present in 16% of the particles classified as dust, and is likely to have originated from coal fly ash particles reacting with the dust particles.

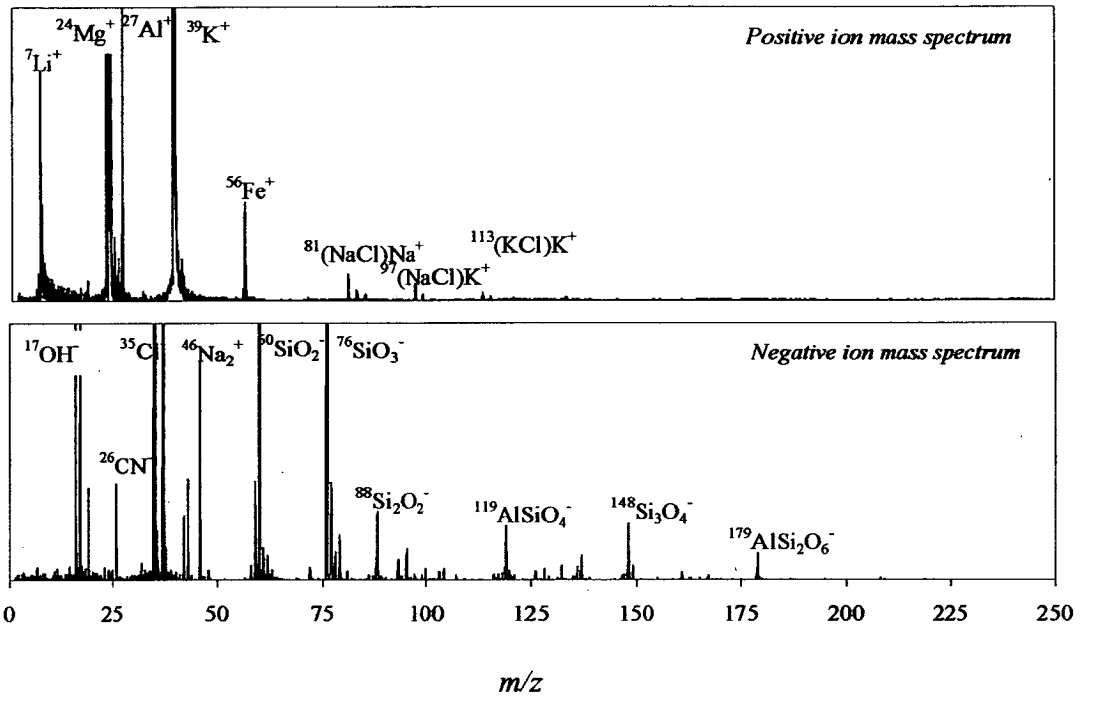

Figure 6.10. Positive and negative ion mass spectra from a 2.22 μm particle classified as dust

PO_2^- and PO_3^- (*m/z* -63 and -79 respectively) were present in both aluminium dust (13%) and calcium containing dusts (5%). Chloride signals were identified in 58% of the particles classified as dust. Both types of dust particles contained low amounts of carbonaceous material; 3% of the aluminium iron (sand particles) particles and 6.6% of the calcium type particles contained ion signals for carbonaceous material. As only small percentages of the total dust class was made up of only aluminium or only calcium they are shown as one dust grouping in Figures 6.5 and 6.6.

Only 4% of the total particles detected contained carbonaceous ion signals, $C^{+/-}$, $C_3^{+/-}$ (*m/z* 12, 36 respectively). Carbonaceous aerosol is usually classified into two large categories of black or elemental carbon (Castro *et al*, 1999) and organic carbon. These particles were mainly detected during the second week of sampling from the

09/02/04-12/02/04. From Figure 6.4 it is observed that the source of all air masses was comparable and originated from the AT or AR regions. This information suggests that carbon particles sampled by the ATOFMS during these periods are from a local source rather than from long-range transport of air masses. Heal *et al.* (2005) reported that Black Smoke (BS) measurements taken in Edinburgh showed much less variation with air-mass source than PM_{10} or $PM_{2.5}$, implying that urban BS is more dominated by local sources and less impacted by the air-mass origin than other components of PM_{10}.

The highest proportions of carbonaceous particles were on the 12/02/04. On this day wind speeds and temperature were low at 0.8 m s^{-1} and 4.2 °C, respectively. This implies a wintertime stagnation or inversion event and that local emissions are the most likely source of these carbonaceous particles.

Elemental carbon is a primary pollutant emitted directly during the incomplete combustion of fossil and contemporary biomass carbonaceous fuels; 1.5 % of the total particles detected were classified as elemental carbon. Figure 6.11 shows an example of a positive and negative ion mass spectrum containing ion signals for elemental carbon.

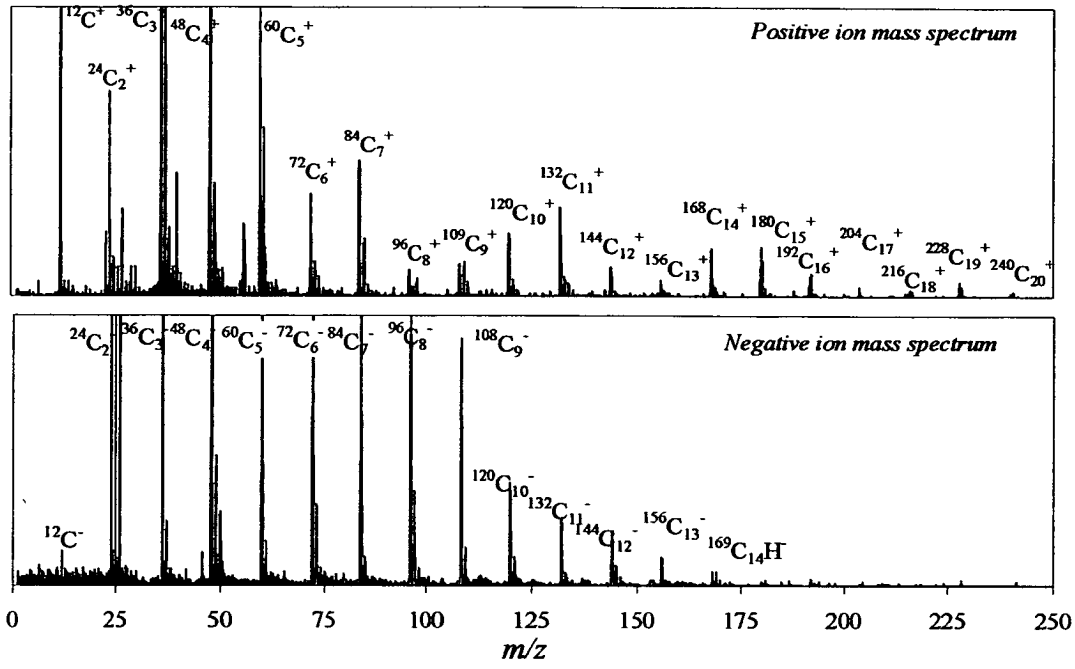

Figure 6.11. Positive and negative ion mass spectra from a 1.31 μm particle classified as elemental carbon.

Secondary EC was identified as having a strong negative ion mass spectrum dominated by sulphate ions and a positive ion mass spectrum containing signals for carbon. Secondary EC particles contributed 2.5 % to the total particles identified by the ATOFMS. From Figure 6.6 it is observed that the majority of the carbonaceous particles detected were in the sub-micrometer mode with very few of these particles having diameters greater than 1.3 μm.

An example of a positive and negative ion mass spectrum resulting from a secondary EC particle is shown in Figure 6.12. There are a lot of secondary species present on this type of particle and the negative ion mass spectrum is dominated by sulphate signals. This particle has an aerodynamic diameter of 0.59 μm and contains ion signals for lead at *m/z* 208. Lead is often used in metallurgical processes and could occur as impurities or additives in fuels used in industrial products. Diesel emissions, known to have high sulphur content, from the transit van (where the ATOFMS was operating) were measured for a short period during sampling. Similarities are seen between these diesel particles and the carbonaceous particles detected during the

ambient particle measurements. This suggests that some of the carbonaceous aerosol could be apportioned to diesel particles from the buses passing outside the hospital.

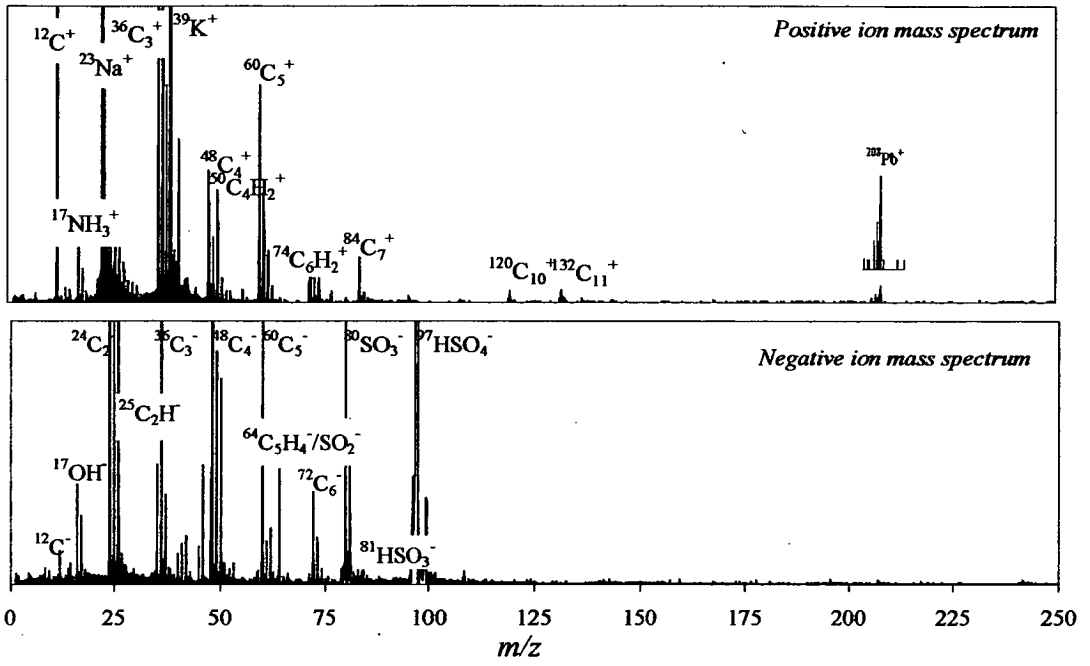

Figure 6.12. Positive and negative ion mass spectra from a 0.59 μm secondary EC-type particle.

6.3.3. Effect of CAPS on human health.

The volunteers were unaffected by exposure to the Edinburgh CAPs or filtered air in either group. Another study was carried out by Mills *et al.* (2005b) in Sweden in April 2004, where volunteers were exposed to filtered diesel exhaust that was generated from an idling Volvo diesel engine (Volvo TD45, 4.5 L, 4 cylinders, 680 rpm). Over 90% of the exhaust was shunted away and the remaining 10% was diluted with air and fed into the exposure chamber. The results showed that at levels encountered in an urban environment, inhalation of dilute diesel exhaust impairs vascular function in human subjects. However, as shown in this study using the ATOFMS, the equivalent mass of ambient particulate, low in combustion component, does not affect vascular function. It was suggested that the vascular effects are a result of the oxidative stress induced by diesel exhaust particles (Mills *et al*, 2005b). These findings provide a potential mechanism that links combustion-

derived air pollution to the pathogenesis of atherothrombosis and acute myocardial infarction. The data have also demonstrated the importance of sampling particulate composition as well as particle size.

6.3.4. Characterisation of concentrated ambient particles using the ATOFMS

As the MAPCEL-VACES is designed to concentrate PM, vapour-phase semi-volatile species will not be concentrated along with the PM. It is possible that the particle chemical composition equilibrium will be disturbed during the concentration process leading to a chemical change in the aerosol. If particles are concentrated then the total particle surface area per unit volume of air has been increased which may give rise to different semi volatile gas-phase partitioning post-concentration compared to pre-concentration. In order to investigate if a change in particle composition is induced by the particle concentrator, single particle composition needs to be analysed.

A study is described here in which particles in the upstream (non-concentrated ambient particles) and downstream (concentrated ambient particles) flows were analysed with the ATOFMS to determine if any chemical differences were induced by the concentration process. Since the particles are under vacuum for less than 1 ms in the ATOFMS, loss of semi volatile compounds is minimal, making the analysis of these species possible (Tobias *et al*, 2000).

The ATOFMS was connected to both the upstream and downstream air flows using copper tubing (i.d. 1 cm). The copper tubing attached to the inlet of the ATOFMS was passed through the floor of the CAPs unit. Inside the CAPs unit the copper tubing was switched between the upstream and downstream airflows (as illustrated in Figure 6.2). The characterisation sampling periods, used to determine whether or not the concentrator chemically altered the particles, were carried out on the 17/03/04 11:02 → 12:40 GMT and 18/03/04 10:53 → 12:54 GMT. The copper tubing was

changed from the upstream to the downstream flows every 40 minutes to ensure a statistically-relevant sample size was collected for analysis.

Important factors that need to be considered when sampling from the concentrator are the temperature and RH of the ambient air being introduced. In a similar study carried out at Chapel Hill, North Carolina, Moffet *et al.* (2004) observed that condensation events affected the results obtained and showed that there were consistent changes in size distributions for all particle classes examined.

When a relatively warm and humid aerosol containing an ambient air sample is transferred into the concentrator at room temperature, there is a possibility for condensation to occur. The temperature at which condensation can occur is called the dew point temperature (T_d). For all the exposures carried out in Edinburgh during February and March 2004 the temperature of the ambient air was below that of the temperature inside the exposure unit (Table 6.1). Therefore it is unlikely that any condensation events occurred during this study.

Table 6.3 lists the concentrator efficiency factors (EF) in this study as a function of particle diameter between 0.2 and 3.2 μm. The EF was essentially constant across the size range 0.2-2.6 μm, with a decline for the largest particle sizes measured (although note that extremely few particles >2.5 μm passed through the apparatus), consistent with the data presented by Kim *et al.*, (2001b). The MAPCEL-VACES is designed to concentrate particles with diameters < 2.5 μm, but a few particles > 2.5 μm were detected.

Study A		Study B	
D_a (μm)	EF	D_a (μm)	EF
0.20 – 0.79	6	0.20 – 0.79	5
0.80 – 1.39	5	0.80 – 1.39	5
1.40 – 1.99	5	1.40 – 1.99	4
2.00 – 2.59	4	2.00 – 2.59	5
2.60 – 3.39	*2*	*2.60 – 3.39*	*2*

Table 6.3. Efficiency factors (EF) during first characterisation study A on the 17/3/04 and for the second characterisation study B on the 18/3/04.

Using the number distributions determined by the un-scaled ATOFMS raw counts it was possible to determine the fraction of particles that had sub- and super- micron diameters. The fractions of sub- and super-micron particles in the total particle number both before and after concentration are shown in Table 6.4. It is observed that the fraction of particles present in both sub and super-micron size fractions did not change due to the concentration process. Figure 6.13 shows the size distribution for both concentrated and non-concentrated particles. Those particles with diameters < 1.5 μm experienced EF far greater than those particles with diameters >1.5 μm. Particles with diameters > 2.5 μm were not detected in high numbers by the ATOFMS although it is only common to detect high numbers of coarser particles (>2.5 μm) when the number concentration is high. It is known that the ATOFMS exhibits size detection biases due to the design of the inlet and a more detailed discussion of this is covered in Chapter 5 of this thesis. This bias means that although the numbers of sub-micron particles present in the atmosphere are far greater than the number of super-micron particles present they will not be efficiently focused by the ATOFMS inlet. No scaling of the ATOFMS-derived number concentration was attempted in this study, but this is not an issue since the concentration factor at a given particle size is as equally derived from a proportional measure of total particle number pre- and post-concentration. Recent advances of ATOFMS instrumentation now mean that there is an aerodynamic inlet available for use in the ATOFMS to improve the sizing efficiency. This aerodynamic inlet system is designed to allow the detection of particles with diameters from 30 nm to 1000 nm (Su *et al*, 2004).

1st Characterisation study	***Sub-micron particles %***	***Super-micron particles %***
Outlet	33	67
Inlet	32	68
2nd Characterisation study	***Sub-micron particles %***	***Super-micron particles %***
Outlet	14	86
Inlet	11	89

Table 6.4. Percentage of sub-micron and super-micron particles detected during the 1st & 2nd characterisation study

The different modes of 1.2 μm and 1.5 μm in the particle size distributions during the first and second characterization studies, respectively (Figure 6.13), reflects a

difference in the chemical composition of the particles detected. Mixed and pure salt dominated the particle composition during the two sampling periods, but considerably more particles classified as dust and coarse carbonaceous aerosol were detected during the second characterisation study. This is also reflected in the number of particles that were detected on each consecutive day (Figure 6.13). As explained in Chapter 3 and Chapter 5 the ATOFMS does not detect sea-salt species with as high efficiency as carbonaceous material.

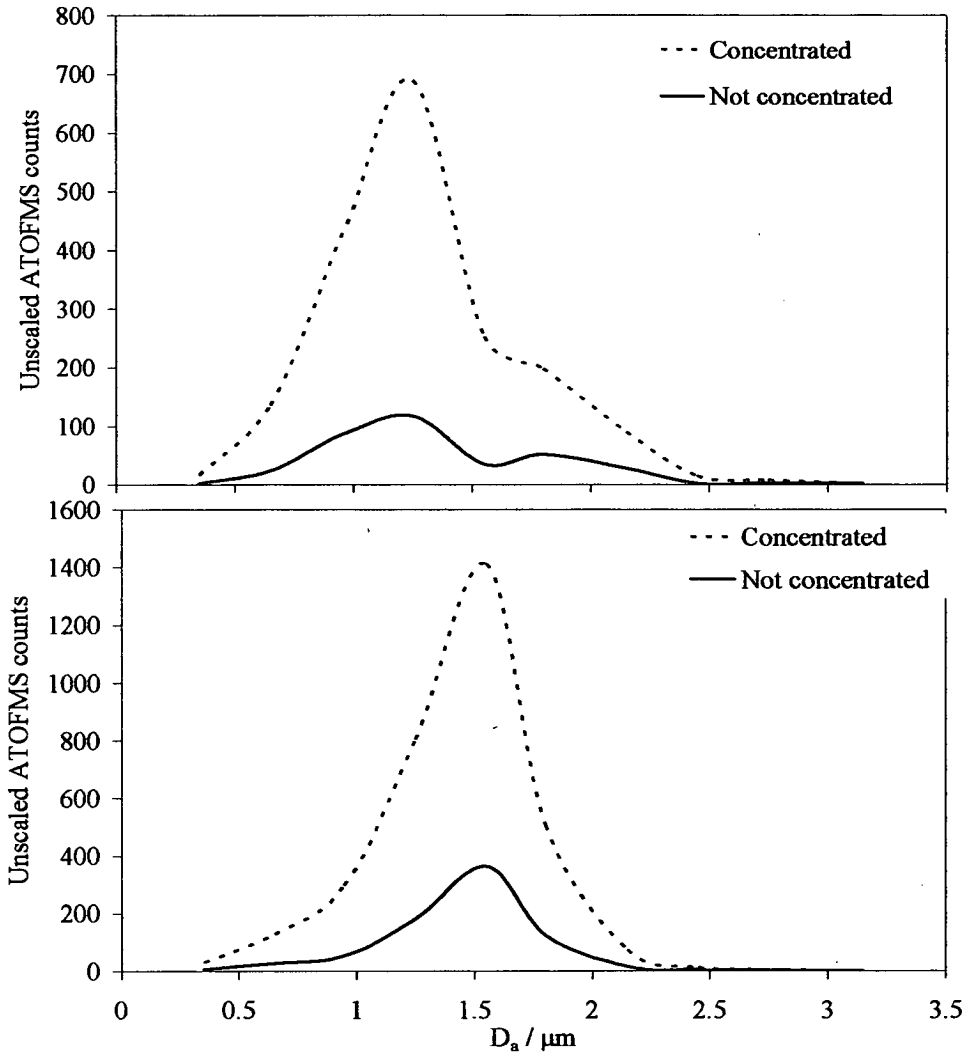

Figure 6.13. Unscaled size distribution produced by the ATOFMS instrument. Average of the two post concentrated data and total of the pre concentrated for the 17th(a) and 18th(b) of March 2004.

The chemical composition during the characterisation studies differed from the first day of sampling (17/03/04) to the second day (18/03/04). In the super-micron size fraction sampled on the 18/03/04 a significant difference to the CAPs exposure study was demonstrated where organic carbon particles and dust made up a larger fraction of the particles sampled.

Effect on composition

Particles from all time intervals were classified together into 20 clusters using the K-means algorithm. After examination of the individual mass spectra, size distribution and temporal trends, a number of particle classes were further combined, yielding a total of four categories of particle composition, which were subsequently subdivided into eight particle types: Sea-salt (Pure, Mixed and Reacted), Carbonaceous (EC and mixed OC/EC), Dust ($CaSO_4$ and $Al^+/Fe^+/Li^+$), and mixed KCl. The evolution of sea-salt particles from pure through mixed to reacted is a consequence of the progressive replacement of chloride with nitrate by reaction with HNO_3, this reaction has been discussed in Chapter 4. The ions signals present in the sea-salt and carbonaceous mass spectra have already been discussed in Section 6.3.2.

The $CaSO_4$ dust class had ion signals for Ca^+ (m/z 40), CaO^+ (m/z 56) and SO_4^- (m/z -96) and HSO_4^- (m/z -97). $CaSO_4$ (Gypsum/Anhydrite) is a major constituent of sedimentary rock salts and this particle class is readily identified as arising from a construction-type source *(heavy construction was underway at the hospital during sampling)*. $CaSO_4$ is also a common fertilizer used as a source of Ca. Similarly $CaCO_3$ (Dolomite) is used as a liming agent in soils. The formation of $CaSO_4$ may have occurred through chemical reactions of $CaCO_3$ in mineral particles with sulphuric acid in the atmosphere (Okada *et al*, 2005). The $Al^+/Fe^+/Li^+$ group is similar to those detected during the first period of the experiment and are due to a crustal/sand source (nearby roads were having rock-salt applied to them daily). The strong phosphate and silicate signals indicates that this particle is more aged than those detected during the exposure studies discussed in section 6.3.2 and could possibly be from longer range transport. This particle type also bears similarities to those detected during two distinct episodes in NAMBLEX described in Chapter 4 suggesting similar sources. Mixed KCl contained ion signals for K^+ (m/z 39), $(KCl)K^+$ (m/z 113/115) and peaks for nitrate and sulphate in the negative ion spectrum indicating presence of secondary inorganic aerosol.

A comparison of the overall particle composition during the upstream (pre-concentrator) and downstream (post-concentrator) airflows was carried out and the

results are shown in Table 6.5. Particle numbers are divided up into sub- and super-micron modes in order to illustrate with more detail that no significant changes in overall particle composition were observed during the upstream and downstream periods in the large particle grouping.

(A)

Particle type	*Down stream*		*Upstream*	
17/03/04	<1	>1	<1	>1
EC	1	0	0	0
Mixed OC/EC	3	1	1	0
$CaSO_4$	0	0	0	0
Al/Fe/Li	2	1	1	1
KCl	0	0	0	0
Reacted NaCl	65	45	72	46
Mixed NaCl	3	7	10	13
Pure NaCl	26	47	15	40

(B)

Particle type	*Down stream*		*Upstream*	
18/03/04	<1	>1	<1	>1
EC	2	0	0	0
Mixed OC/EC	3	5	8	1
$CaSO_4$	1	0	0	0
Al/Fe/Li	2	2	3	3
KCl	31	9	0	1
Reacted NaCl	28	25	78	37
Mixed NaCl	10	19	5	23
Pure NaCl	23	39	5	35

Table 6.5. Percentage contribution of different particle types for the upstream (US) and downstream (DS) particles for the first (A) and the second (B) characterisation studies, divided into particles of diameter < 1 and > 1 μm.

In general, the majority of particles were classified as pure, mixed or reacted sea-salt. This is not surprising given Edinburgh's maritime climate. Nevertheless it should be noted that the particle chemical composition did differ somewhat on the two days so the pre- and post-concentrator particle compositions must be compared on each day separately. For example, during the first characterization study the particle composition was completely dominated by sea-salt, whereas carbonaceous and dust particles constitute a greater fraction of the particles in the second characterisation study (Table 6.5).

The total particle (upstream and downstream sampling) size distributions of the main particle classes averaged for both characterisation days in Figure 6.14. The distribution shows that for most of the particle classes the relative number of particles remained the same between the upstream and downstream sampling. However, an increase in the number of pure sea-salt particles is observed.

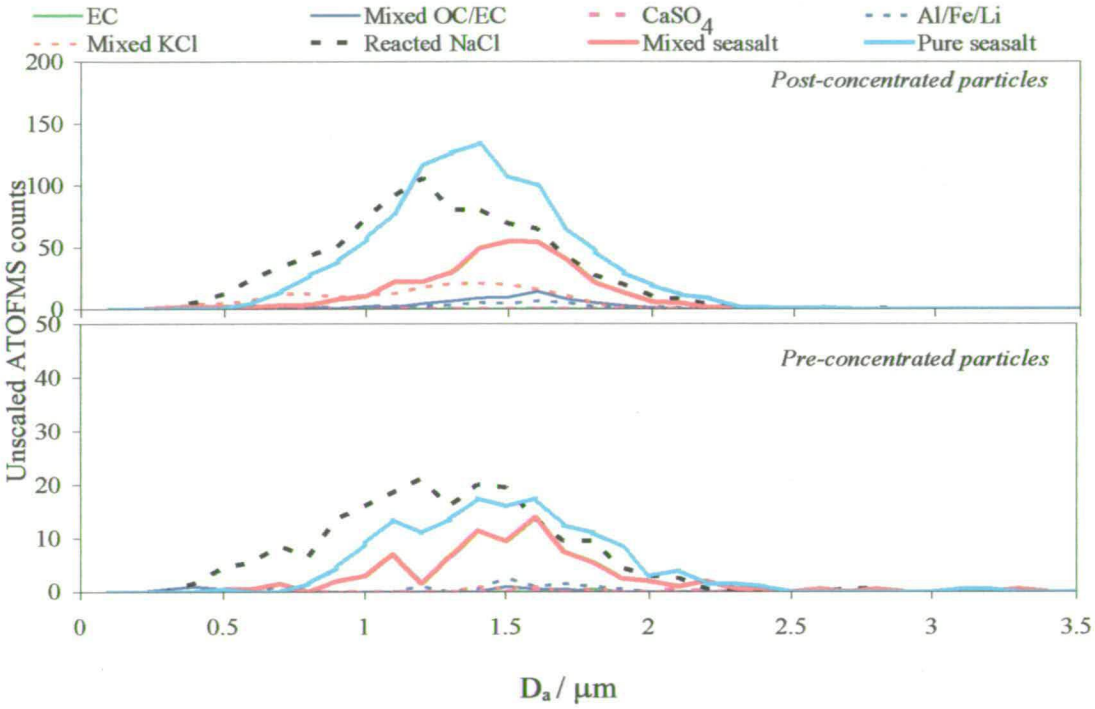

Figure 6.14. Size distributions calculated for the eight main classified particle types sampled in both the upstream and (average of two) downstream sampling averaged for the 17-03-04 and 18-03-04.

Close examination of the dataset revealed that the particle type classified as mixed-KCl, which did appear to show a change in abundance between pre- and post-concentration, was in fact only detected during the first session of downstream sampling in the second characterisation study (illustrated by the shaded region on the time line in Figure 6.15. Since this particle type only appeared during one short period of time, it is concluded that this particle type reflects a genuine difference in ambient particle composition at this time rather than a compositional change induced by the particle concentrator. Particles in this class were within the size range 0.4 –

1.9 µm. These are likely to have originated from burning of biomass, for which potassium is a known marker (Guazzotti *et al*, 2003).

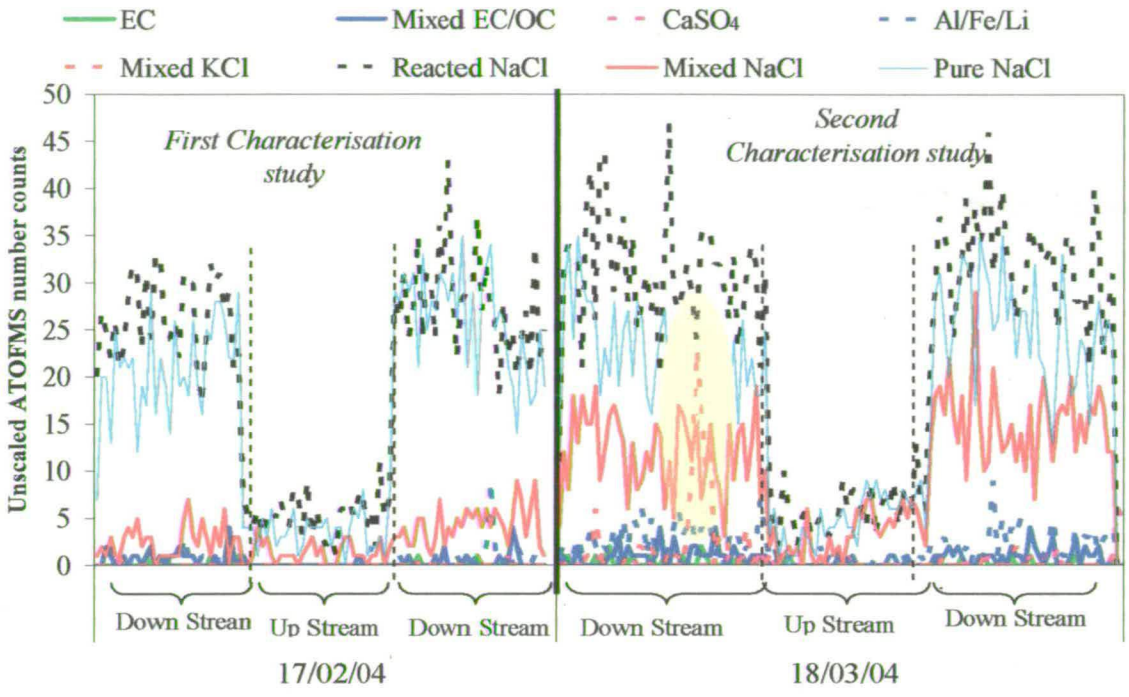

Figure 6.15. Time-line of the eight particle clusters identified during the two characterisation studies.

When investigating each cluster individually, one of the clusters was observed to be present only during the downstream sampling. This was consistent during both characterisation studies. This cluster grouping contained ion signals for aluminium, iron and lithium in the positive ion mass spectra and ion signals for silicates and phosphates in the negative ion mass spectra that were identical to other particles subsequently classed as $Al^+/Fe^+/Li^+$ dust. This smaller cluster grouping contained higher mass negative ion signals for phosphate/silicates and aluminium oxides (e.g. $AlSiO_4^-$ (m/z -119), $AlPO_4^-$ (m/z -122), $(SiO_2)(HPO_3)^-$ (m/z -140)) than the spectra containing similar positive ions and was only present when sampling the post-concentration air flow. As this cluster represented <2.4% of the total particles sampled and as there is no change in particle composition, only in the number of ions detected in the negative ion mass spectra, it was concluded that the concentrator had not caused changes to these particles so they were also assigned to the $Al^+/Fe^+/Li^+$. Although ion intensities in LDI analyses are known to be matrix-dependent (Reilly *et*

al, 2000) the consistent mass spectra overall indicate that there was no different matrices in this instance. A more likely explanation is a straightforward cluster-boundary artefact introduced by the clustering algorithm as has been noted previously by Zhao *et al.* (2005) who observed that the ART-2a neural network algorithm split an ensemble of mixed carbonaceous-ammonium nitrate particles into two depending on the intensity of the nitrate signals.

6.4 Conclusion

The particle concentrator used for human exposure studies did not cause significant size or chemical changes to particles between the upstream and downstream sampling of the concentrator.

Additional measurements run alongside the ATOFMS would greatly complement the semi-quantitative data from the ATOFMS. Measurements using a MOUDI have been used to produce quantitative results with the ATOFMS data (Chapter 5). Having this additional information to scale the single particle ATOFMS data to quantitative numbers would be important from a toxicological perspective, allowing the comparison of species concentrations and particle size with human response.

This study showed the variability of particle composition during 2 h exposures. So far, relating the chemical classes to sources have shown that the concentrated ambient particles in Edinburgh did not result in any significant health effects, as published elsewhere (Mills *et al*, 2005a). Further experiments have been carried out where concentrated diesel particles were used for exposure studies. Results from these studies have shown an effect on human health (Mills *et al*, 2005b). This concludes that clean marine particles generally do not have a strong toxic effect but that particle composition is as important to human health as particle size.

This study and many other exposure studies have helped establish the causal relationship between fine particle exposure and adverse health effects in the lung and cardiovascular system. Many, if not all, of the regulations on particulate pollution focus on the need to reduce the numbers of particles with diameters <10 μm or < 2.5

μm. This study has demonstrated the need to reduce the number of diesel or carbonaceous material as these appear to demonstrate a more toxic effect on human health than ambient marine or dust type particles.

Chapter 7

Characterisation of inhaler drugs using single particle mass spectrometry

Chapter 7 Characterisation of inhaler drugs using single particle mass spectrometry

7.1. Introduction

Asthma, a chronic inflammatory disease of the airways, is characterised by recurrent episodes of wheezing, breathlessness, chest tightness and coughing. Worldwide, asthma is among the most common chronic diseases and, in the USA; approximately 17 million people are estimated to have the disease. The number of people being treated for asthma in the UK reached 5.1 million in 2004. A 20 year growth in the incidence of asthma diagnosed by GPs peaked in the early 1990's and is now 3 to 4 times higher in adults and 6 times higher in children than it was 25 years ago.

There are a number of epidemiological and toxicological studies that correlate increased respiratory illness and aggravation, including asthma attacks, with increased atmospheric pollution and specifically with fine particulate matter. As outlined in Chapters 1 and 6, it is fine particles that are most efficient in causing detrimental health effects; these are particles with diameters less than 2.5 μm. These particles can penetrate and deposit deeply in the respiratory tract resulting in the constriction of the bronchiole tubes.

As particles in this size range are efficient at entering and depositing in the respiratory system many medical companies have employed the use of respiratory devices to deliver drugs, in the form of small particles, to combat a number of illnesses. It is also known that particles can work most efficiently through the use of respiratory drug delivery devices as they can reach the target area in a very short period of time compared to other means of drug delivery.

There have been several devices designed for the delivery of respiratory drug particles. These include metered dose inhalers (MDIs) and powdered dose inhalers

(PDIs). MDIs atomise a drug suspension, creating a spray of fine aerosol particles that may be inhaled to treat asthmatic conditions (Hallworth, 1987; Moren, 1993; Newman, 1984). PDIs come in a number of forms; one is a capsule containing the drug formulation in the presence of lactose. The PDI device is designed so that for each dose delivered only one capsule, containing the active pharmaceutical ingredient (API) and lactose (Carrier) will be used. Other forms of PDI device are designed so that when the device is operated a specific quantity of the drug is dropped into a holding area. The drug is then inhaled from this holding area. Upon inhalation, particles deposit at various locations in the respiratory tract dependent upon the particle velocity and aerodynamic diameter (D_a).

Many of these therapeutic aerosols are local rather than systemic and therefore exhibit a local effect. Common drugs for the treatment of asthma are primarily in one of two categories: (1) bronchodilators, which are intended to stop asthma episodes, and (2) anti-inflammatories, which are more preventative in purpose. Because these drugs mainly affect a local region around the deposition site in the respiratory tract, inhaled doses are commonly more fast-acting than oral doses. Also, MDI and PDI aerosols are effective at much lower doses than oral doses and therefore are less inclined to produce undesirable side effects.

As the doses used in MDI and PDI devices are so small, of the order of 200 μg or less, it is difficult to carry out sample characterisation. The standard method used to characterise MDI and PDI inhalers for size distribution is through the use of a cascade impactor; normally an Anderson impactor is used. The Anderson impactor is designed to reflect the different stages of the human respiratory tract. Using an impactor for aerosol analysis involves collecting the MDI/PDI sample on size segregated filters prior to chemical or mass analysis of the bulk aerosol. Recently optical detection methods have been developed to allow the size distribution of MDI inhalers to be determined in real-time (Mitchell & Nagel, 1996).

In order to chemically characterise the drug samples it is necessary to use HPLC linked with mass spectrometry. Chemical analysis is generally not as important as

size analysis, as the major components of the drug product are already known. However, some chemical analyses have been performed on MDI aerosols, for example, to determine trace level impurities in the dosage (Norwood *et al*, 1995). The chemical characterisation methods generally used are applied to the bulk aerosol sample and do not give any information of the individual drug particles. All of these methods require considerable time and are expensive. Also, as the drug quantities are very low the techniques must be very sensitive and multiple actuations of the drug dispenser are required in order to collect enough sample for analysis.

Recently Noble and Prather (1998) demonstrated the use of the ATOFMS instrument as an analytical method for characterising MDIs in real-time. The ATOFMS can perform both size and chemical composition analysis on each individual particle and the drug product can be delivered directly with no sample pre-treatment required. The time that each particle spends inside the ATOFMS instrument is less than 1 ms which ensures that loss of semi-volatile material and reactions between sampled compounds are kept to a minimum (Tobias *et al*, 2000). Noble and Prather (1998) demonstrated that the ATOFMS instrument can give useful size distribution analysis as well as determining the presence of a drug, through the use of both positive and negative ion mass spectrometry. The great advantage of the ATOFMS instrument is that one can determine the specific size range in which the drug particle appears which can then help to improve drug development.

Karlsson *et al.* (2000) also carried out work for Boehringer Ingelheim Pharmaceuticals using the ATOFMS. They were able to identify individual compounds, such as the APIs in single MDI actuations. The drug product investigated was the Combivent® MDI and the two active ingredients were ipratropium bromide and albuterol sulphate. The ATOFMS instrument was used together with an APS and a SMPS. The latter two instruments are designed for particle sizing in a broad size range but are unable to provide compositional information. Karlsson *et al.* (2000) used specific ion signals to identify the active ingredients in the formulation, such as the presence of bromine isotopes for the ipratropium bromide and sulphate peaks for the albuterol sulphate. It was reported

that the ipratropium bromide was always associated with albuterol sulphate. As ipratropium bromide was not detected on its own it was proposed that these particles homogeneously nucleate during actuation to form particles smaller than 0.3 μm, which were not detected by the ATOFMS. It is also possible that the ipratropium bromide did not absorb at the laser frequency employed during the analysis and that it was only seen when associated with albuterol sulphate due to a matrix effect. This matrix effect is demonstrated later on in this chapter.

Different drug formulations for the treatment and prevention of asthma are commercially available. Some of these formulations show higher efficiency in treating asthma than others. The most widely published drug formulation exhibiting increased efficiency over other drug formulations is Seretide®, marketed by GlaxoSmithKline (GSK). This drug formulation contains salmeterol xinafoate and fluticasone propionate, as well as Lactose. Several clinical trials (Dal Negro *et al*, 2003; Cazzola *et al*, 2004) have shown the increased efficiency of the combined formulation, salmeterol xinafoate and fluticasone propionate, compared to either drug delivered on its own, or sequentially one after the other. These finding suggested that the drugs must be associated with each other on the same particle. Other reviews (Lyseng-Williamson & Plosker, 2003), compared the GSK drug formulation to budesonide plus formoterol which is a similar drug mixture manufactured by Astra Zeneca (Turbuhaler® PDI Astra Zeneca) and reported a much higher efficiency with the GSK formulation. The salmeterol/fluticasone propionate mixture was also shown to be more effective in improving lung function and reducing asthma symptoms than oral leukotriene modifier (Singulair ® Montelukast).

These finding inspired a number of research experiments on the drug formulation produced by GSK. Michael *et al.* (2000) showed that the analysis of a mixture of the two drug solutions (salmeterol xinafoate and fluticasone propionate) using mass spectrometry showed evidence of salmeterol-fluticasone propionate interaction and dimer formation. These studies were carried out using ultraviolet-visible spectroscopy, fluorescence spectroscopy and electro-spray ionisation mass

spectroscopy. Another study examined the average flocculation size of the drug particles individually and in combination as a function of stirrer rate (Michael *et al*, 2001). It was reported that the interaction between the two drugs was such that they did not separate despite having different densities. It was concluded that within an aerosol propellant system, there was an interaction between the drug particles.

Nelson *et al.* (2003) recently published a paper demonstrating the effectiveness of the combined salmeterol/fluticasone propionate formulation through the use of clinical trials. In this paper laser Raman spectroscopy was used to investigate the nature of this agglomeration between salmeterol and fluticasone propionate. Laser Raman spectroscopy is a technique capable of analysing individual drug particles and presenting an image in which individual drugs can be identified. The technique was used to analyse the fluticasone plus salmeterol combination sample taken from stage 4 of an Anderson cascade impactor (the stage considered to represent the dose delivered to central airways). The results showed that the fluticasone plus salmeterol particle agglomerate persist after delivery from either the PDI or the MDI. This method, although useful, is both time and cost intensive and as it requires the use of a cascade impactor it does not analyse the particles in real-time.

In the work presented here, the ATOFMS instrument was used to analyse, in near real-time, the size and chemical composition of two commercially available inhalers, one produced by Astra Zeneca, (Symbicort Turbuhaler® PDI) and the second produced by GSK, (Seretide® PDI). The main objective of this work was to investigate the composition of the single particles produced from the inhalers and attempt to determine whether the APIs co-exist on the same drug particle.

7.2. Experiment

Two commercially available drug products were purchased. The APIs were analysed separately and in the commercial products. By analysing each of the components individually, mass spectral fingerprints could be determined which were later used to identify the APIs within the drug mixture.

Figure 7.1 shows the apparatus set up for the delivery of the drug components to the ATOFMS instrument. This set up consisted of a 2 L chamber, a rectangular box for the inhaler device, a 3 L syringe and a high efficiency particle air filter (HEPA). The 2 L chamber acted as a holding area for the drug particles and also ensured that only the particles of interest were analysed. This chamber had two inlets and one outlet. The outlet was attached to the sampling inlet of the ATOFMS. To one of the inlets a HEPA filter was attached in order to draw filtered air into the 2 L chamber. The second inlet was attached to the drug delivery device. This device consisted of a rectangular box in which the drug product was placed. This box had one inlet and one outlet; the outlet was used to deliver the aerosol drug into the holding chamber while the inlet was attached to plastic tubing. On the end of this plastic tubing was a 3 L syringe. This 3 L syringe was used to deliver a sufficient amount of air to the rectangular box, containing the drug product, to propel the drug products into the 2 L sampling chamber.

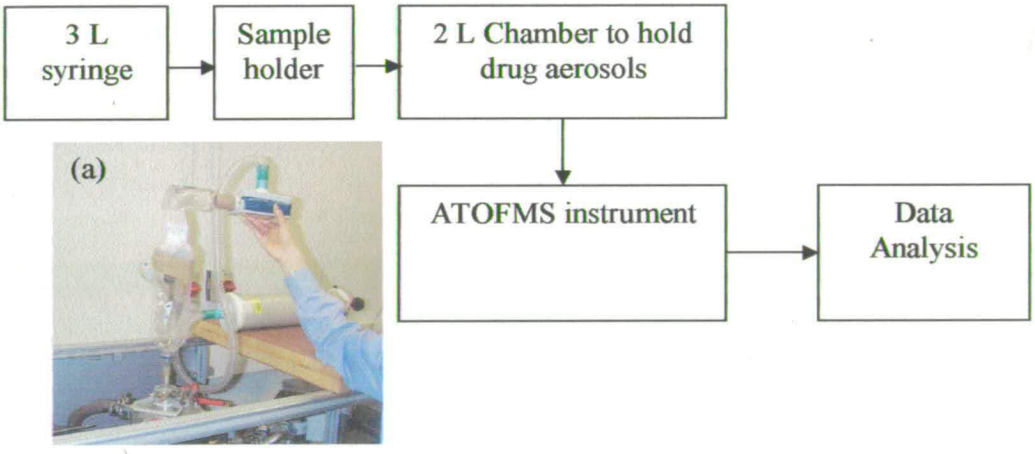

Figure 7.1. Schematic diagram of ATOFMS set up for drug delivery during sampling and (a) photograph of syringe, sample holder and 2L chamber.

All data were collected using the *MassSpec* operational software provided by TSI with the ATOFMS instrument and analysed using *MS-Analyze* software (TSI). Data were also exported into Excel 2000® for analysis. Due to large shot-to-shot variations in the mass spectra obtained using laser ablation and ionisation, a large number of particles (>100) had to be analysed. Mass spectra were then co-added and averaged. In the analysis of mass spectra, a peak threshold value can be set, in *MS-*

Analyze, below which a given peak in the mass spectrum is rejected. For this work, relatively high threshold values were set in order to ensure a high level of confidence in the final results. It should be emphasised that these data obtained with the ATOFMS instrument provides information on whether or not a given molecule (drug) is present in any individual particle but it does not yield information on the quantity of that molecular species present in the particle.

Each of the individual drug components were analysed using a range of laser energies, from 1 mJ to 0.2 mJ, in order to determine the optimum conditions and obtain the maximum amount of information from each of the samples. After examination of both the positive and negative ion mass spectra from each of the drug components it was concluded that the most useful information would be obtained at laser energies in the range of 0.7 to 0.4 mJ.

7.3. AstraZeneca Symbicort Turbuhaler® PDI

In order to fully characterise the sample obtained from an AstraZeneca, Symbicort ® 100/6 Turbuhaler® PDI, it was necessary to obtain mass spectra for each of the individual components present (i.e. formoterol fumarate and budesonide). The product packaging states that each inhalation contains budesonide (equivalent to 200 μg per metered dose) and formoterol fumarate (equivalent to 6 μg per metered dose). This product also contains lactose. As there is only a very small amount of formoterol fumarate present in the mixture it is likely that it will be difficult to detect in the mixed drug formulation. The individual components were sampled at a number of different laser energies in order to determine optimum conditions for analysis. Lower laser energies between 0.7 mJ and 0.5 mJ provided the best conditions for analysis. Data were therefore collected at these laser energies and are used for the analysis presented in this chapter.

7.3.1. Formoterol Fumarate

Positive and negative ion mass spectra of particles containing pure formoterol fumarate were collected using the ATOFMS. Figure 7.2 shows the structure of formoterol and its corresponding salt fumarate. Formoterol fumarate has a molecular weight of 460 g mol^{-1}. Formoterol itself has a molecular weight of 344 g mol^{-1} (C_{19} H_{24} N_2 O_4). As there is a large shot-to-shot variability with the ATOFMS, all of the mass spectra collected under optimum conditions were averaged in order to obtain a reliable analysis of the particles collected. Figure 7.3 shows the average of the 198 positive and negative ion mass spectra sampled under optimum laser conditions. Formoterol fumarate had an overall hit rate of 18% meaning that it was detected with reasonable efficiency.

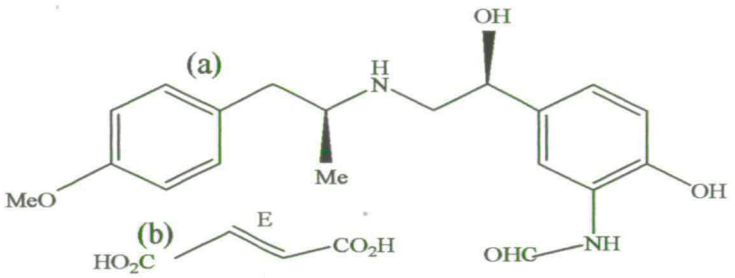

Figure 7.2. (a) Structure of formoterol ($C_{19}H_{24}N_2O_4$) and (b) fumarate ($C_4H_4O_4$).

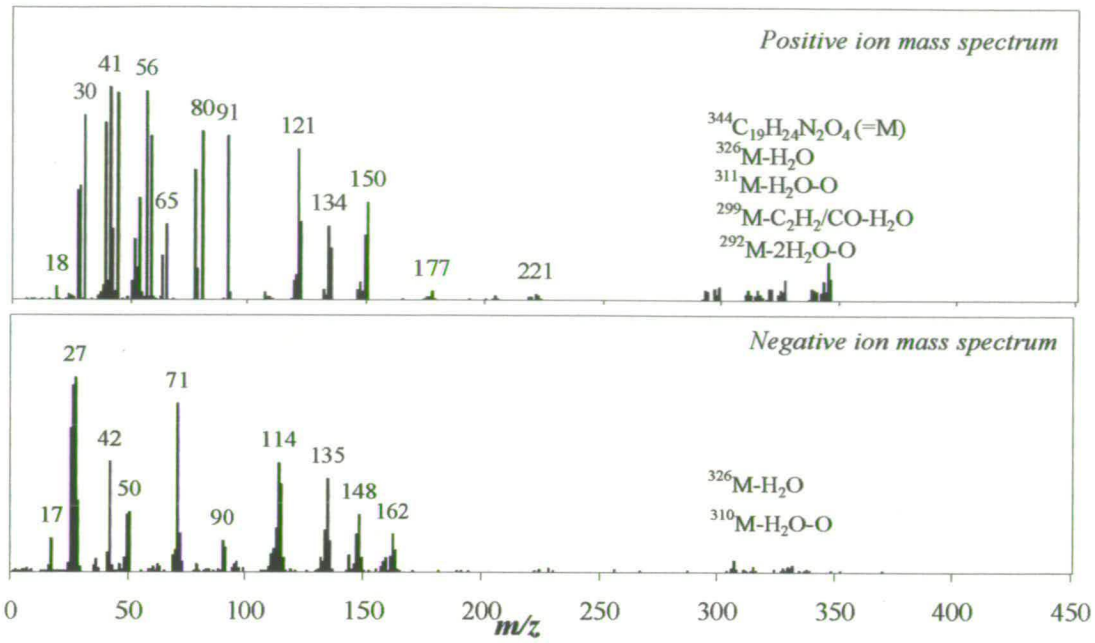

Figure 7.3. Average threshold[‡‡] positive and negative ion mass spectra of 198 formoterol fumarate particles. These average mass spectra were obtained at optimum laser energy (0.7 mJ and 0.5 mJ). The peak thresholds used to obtain these average mass spectra were 5 units above the baseline, 5 square units of area and a fraction of total peak area of 0 (i.e. ≥ 2% of full scale)

Each of the particles detected by the ATOFMS instrument was examined individually for the presence of ion signals that could be used to identify this compound in a mixture. The ions which appeared most often, with the greatest intensity, in the mass spectra of formoterol fumarate are listed in Table 7.1. From Figure 7.3 it is observed that the parent ion is detected in positive ion mass spectra (*m/z* 344). Table 7.1 shows that almost 50% of the particles sampled show ion signals for the parent ion. Having the parent ion present at high *m/z* values increases the likelihood that it will be detected in the drug mixture.

[‡‡] The average threshold graph shows the number of times each of the peaks occurred over a threshold value (2%).

Positive ion mass spectra		
Observed *m/z*	**Number of particles containing this peak**	**Average intensity of this peak in the mass spectra**
90 to 92[§§]	147	65.1
121*	171	121.2
135*	148	63.1
149*	152	102.6
280*	48(*parent ion with loss of* CO/C_2H_2 *and* $2H_2O$ *from parent)*	52.0
298*	45(*with loss of* CO/C_2H_2 *and* H_2O *from parent)*	56.1
326*	75 (*parent ion* – H_20)	51.3
344*	97 *(parent ion)*	88.5
Negative ion mass spectra		
Observed *m/z*	**Number of particles containing this peak**	**Average intensity of this peak in the mass spectra**
-336*	61	43.3
-312*	77	50.5
-162*	158	83.7
-147*	156	59.2
-134*	175	91.8
-114*	186	116.8
-90[1]	148	69.5

Table 7.1. The most common positive and negative ions present in the 198 formoterol fumarate mass spectra sampled using optimum laser energy. The peak thresholds used to obtain these average mass spectra were 5 units above the baseline, 5 square units of area and a fraction of total peak area of 0.

***Ion signals present at higher *m/z* values are subject to *m/z* shifting and the signals are often seen at *m/z* values ± 1 of the listed value. A full list of observed *m/z* values and intensities can be found in appendix 1.1, Table A 1.1 and A1.2.**

The parent ion signal for formoterol (molecular weight of 344 g mol^{-1}) appears at m/z = 344, with two adjacent ion signals, in the positive ion mass spectrum. These adjacent peaks are due to fragmentation with loss of water molecule and a –CO (or C_2H_2) fragments. Figure 7.4 and 7.5 are examples of individual mass spectra of formoterol fumarate sampled at different laser energies, both showing strong signals for the parent ion.

[§§] *m/z* values less than 90 have not been included Table 5.1. For a full list of *m/z* values and their intensities see appendix A1, Table 1A, page 51.

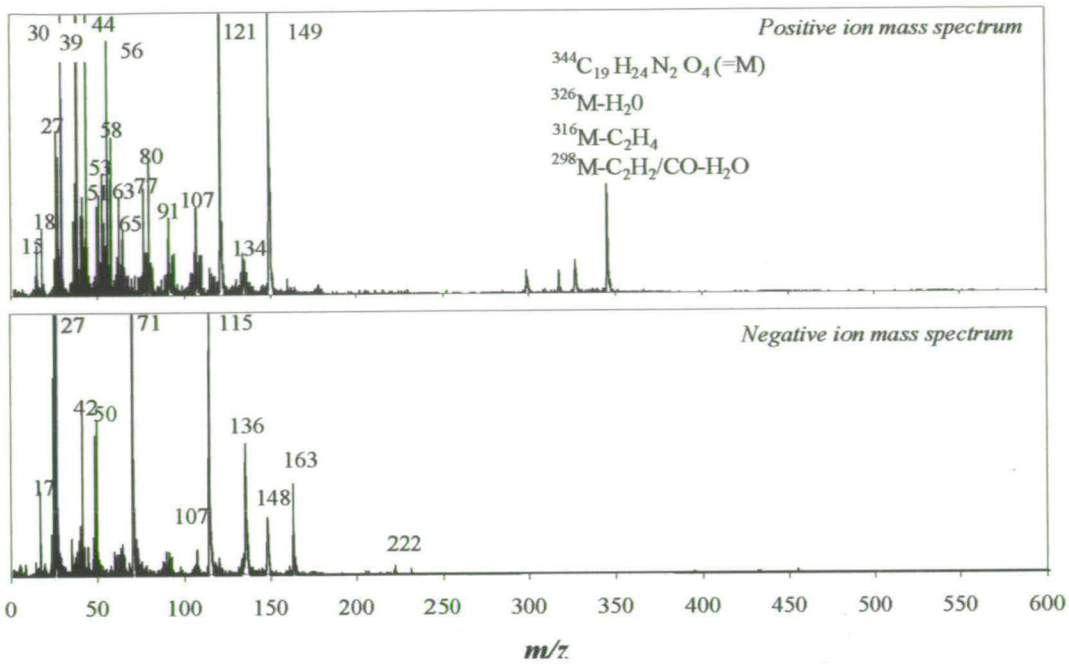

Figure 7.4. Positive and negative ion mass spectra of pure formoterol fumarate sampled with high laser energy (0.7mJ)

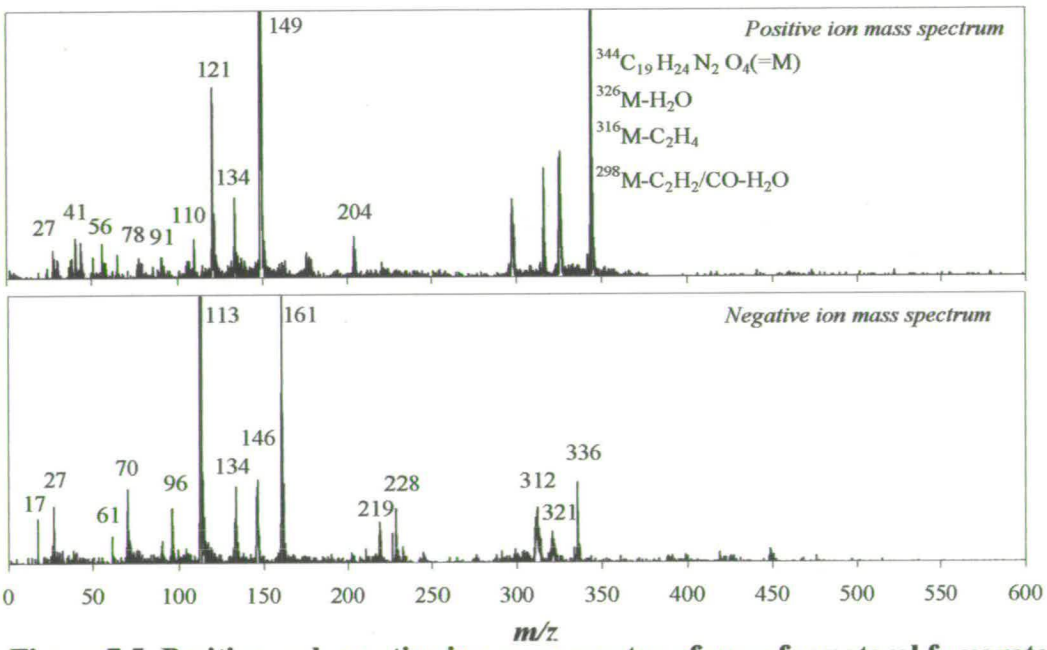

Figure 7.5. Positive and negative ion mass spectra of pure formoterol fumarate sampled at lower laser energy (0.5 mJ)

The laser power was varied from high energy (~0.7 mJ) to low energy (~0.5 mJ). This variation in laser power provided control over the fragmentation processes. This variation in fragmentation is clearly illustrated in Figure 7.4 and 7.5.

The ion signals identified in the single and average mass spectra were then used to search for the presence of formoterol fumarate in commercial products. The fragments, outlined in Table 7.1, are those which are the most useful in the identification of formoterol fumarate. A full list of *m/z* values and the number of spectra that contain them can be found in Appendix 1.1 Table A1.1.

7.3.2. Budesonide

Budesonide is the other API present in the Symbicort® Turbuhaler mixture and is present in much higher quantities (100 μg) than formoterol fumarate (6 μg). The structure of budesonide is shown in Figure 7.6, it has a molecular weight of 430.5 g mol^{-1} ($C_{25}H_{34}O_6$) this larger molecular weight makes it more difficult to detect although there are several other markers that may be used. Under the optimum laser conditions 267 mass spectra were collected. An average of these mass spectra is shown in Figure 7.7. The hit rate for budesonide was 24% indicating that budesonide adsorbed more strongly at 266 nm, the wavelength of the ATOFMS DI laser, than formotorol.

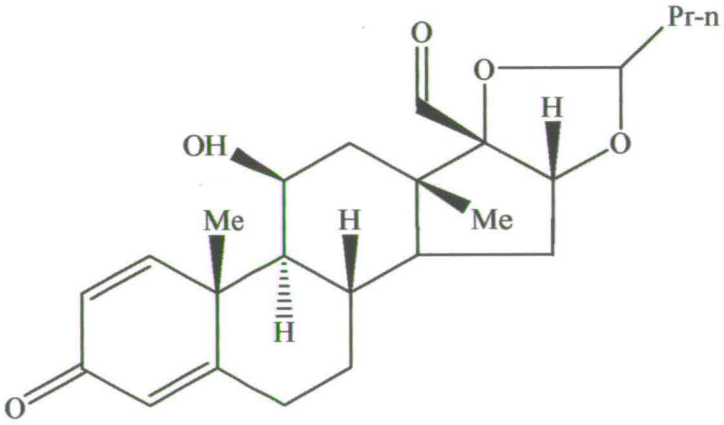

Figure 7.6. Structure of budesonide.

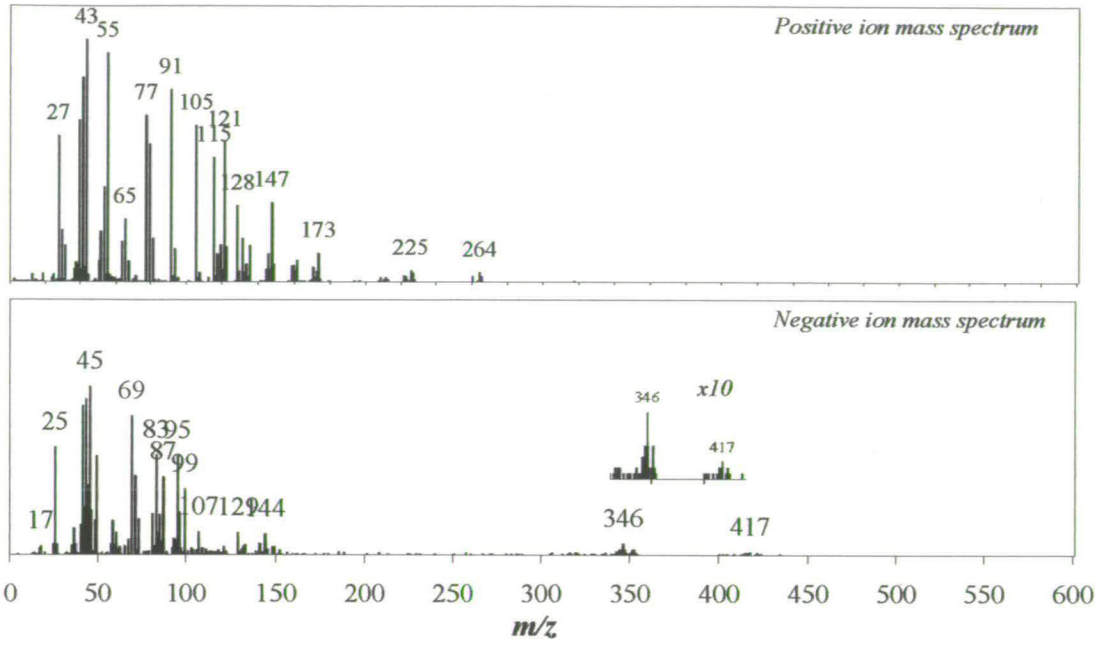

Figure 7.7. Averaged positive and negative ion mass spectra of 267 budesonide particles sampling under optimum laser conditions (between 0.5-0.7 mJ). Peak thresholds were the same as Figure 7.3.

As with formoterol fumarate, each individual mass spectra was analysed for common mass spectral signatures that could be used to identify this compound in a mixture. Table 7.2 shows the number of spectra containing the most common ion signals that will be used later to identify budesonide in the Symbicort® mixture.

Positive ion mass spectra		
Observed *m/z*	**Number of particles containing this peak**	**Average intensity of this peak in the spectra**
91 to 95***	212	68.0
105 to 107	199	55.2
113 to 117	186	61.9
118 to 122	216	68.0
128 to 135	214	51.2
144 to 148	185	50.2
164 to 166	90	34.8
169 to 170	110	40.6
221*	27	33.6
261*	23	31.8

Negative ion mass spectra		
Observed *m/z*	**Number of particles containing this peak**	**Average intensity of this peak in the spectra**
-417	0	***Intensity too weak to be detected at current threshold values***
-346*	35	46.5
-141 to -144	164	50.4
-129 to -132	171	55.9
-106 to -108	132	58.9
-92 to -96	204	50.8

Table 7.2. The most common positive and negative ions present in the budesonide sample. Thresholds as for Table 7.1. A full list of all *m/z* values and intensities can be found in appendix 1.1, Table A1. 3 & A1.4. * Ions at higher *m/z* values are subject to mass shifting and are often found at *m/z* values ± 1 of the listed value.

Budesonide has a parent ion at *m/z* 430.5 (molecular weight 430.5 g mol^{-1}). The parent ion is occasionally seen in the individual mass spectra but has a very low intensity that is below the defined peak thresholds outlined in Figure 7.1 and Table 7.1 and is therefore not reliable. Similar to formoterol, a combination of ions can be used to identify budesonide in a mixture. Figure 7.8 and 7.9 show two examples of individual positive

*** *m/z* values less than 90 were not included in Table 5.1. For a full list of m/z values and their intensities see appendix A1, Table A1.3 & A1.4

and negative ion mass spectra from budesonide sampled at both high and low laser intensities respectively.

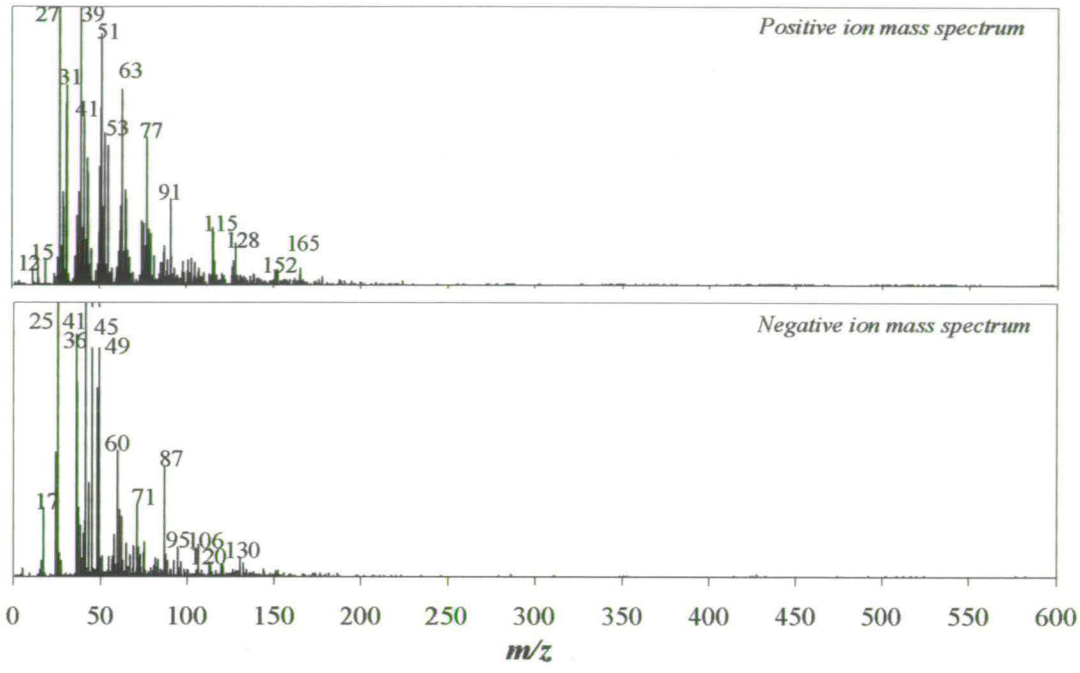

Figure 7.8. Positive and negative ion mass spectra of pure budesonide sampled with high laser energy (0.7mJ)

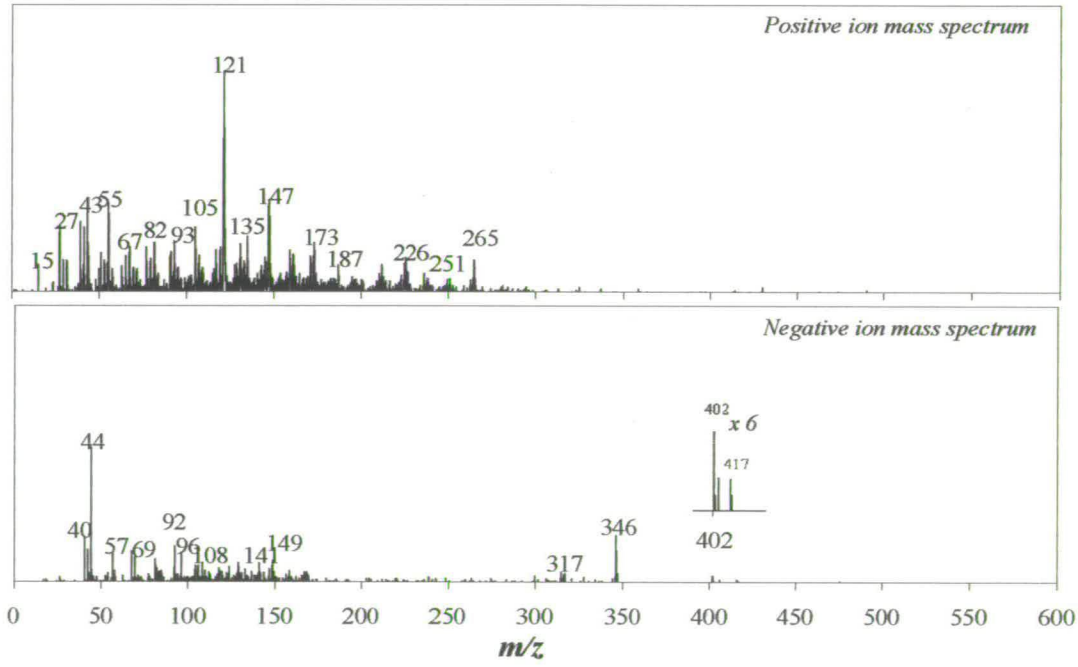

Figure 7.9. Positive and negative ion mass spectra of pure budesonide using low laser energy (0.5 mJ)

The ion signals identified in the budesonide sample were recorded and used to identify budesonide in the Symbicort® mixture.

7.3.3. Lactose

As lactose is present in the Symbicort® mixture, as a carrier for the drug sample, it is necessary to characterise it. It is also useful to be able to characterise the lactose in order to determine if the APIs in the mixture are associated with lactose particles. Pure lactose particles were sampled using the ATOFMS at a range of laser energies from 1 mJ to 0.2 mJ. Only data measured between 0.6 and 0.4 mJ were used for the data analysis as it was within these energies that the most information on lactose was acquired. The hit rate for lactose when sampled at optimum laser conditions was relatively low at 8.3%. Figure 7.10, shows the structure of lactose (molecular weight of 342.3g mol^{-1}). Figure 7.11 shows the averaged positive and negative ion mass spectra of 124 particles obtained from a sample of pure lactose sampling using optimum laser conditions.

Figure 7.12 shows a mass spectrum of Lactose obtained using an electron impact source with ionisation energy of 70 eV. The electron impact spectrum is clearly very different to the spectra obtained using the ATOFMS instrument and is thus of limited value for the present work.

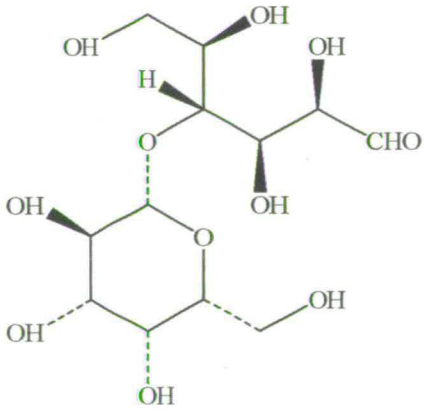

Figure 7.10. Structure of Lactose.

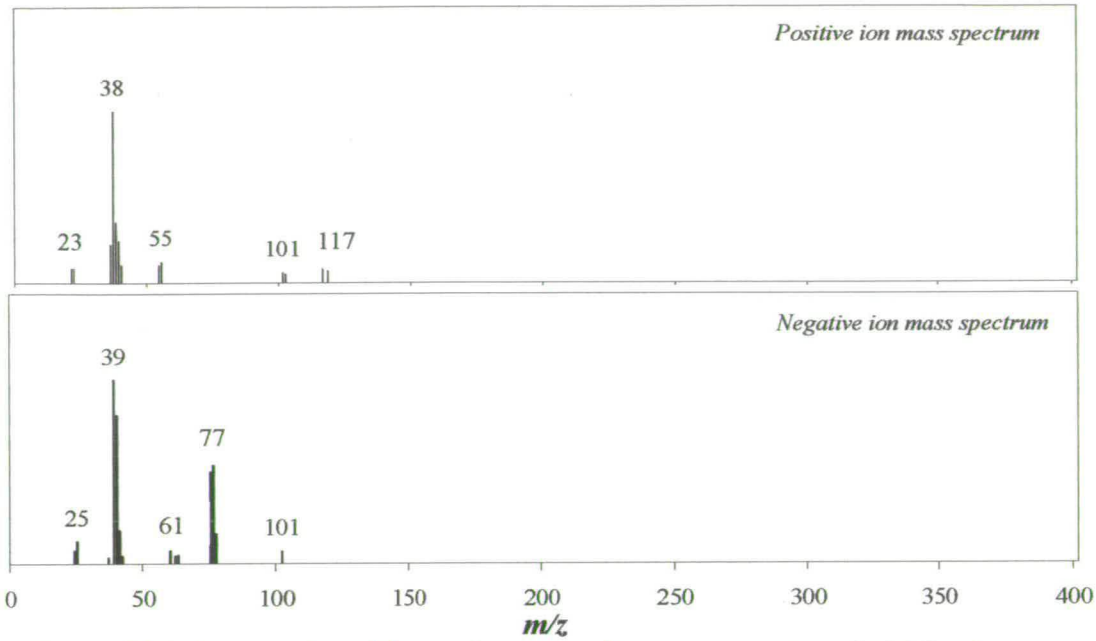

Figure 7.11. Averaged positive and negative ion mass spectra of 124 Lactose particles sampled at optimum laser energies (between 0.4 and 0.6 mJ). Peak thresholds were the same as Figure 7.3. A full list of all positive and negative ions is shown in appendix 1.1 Table A1.5.

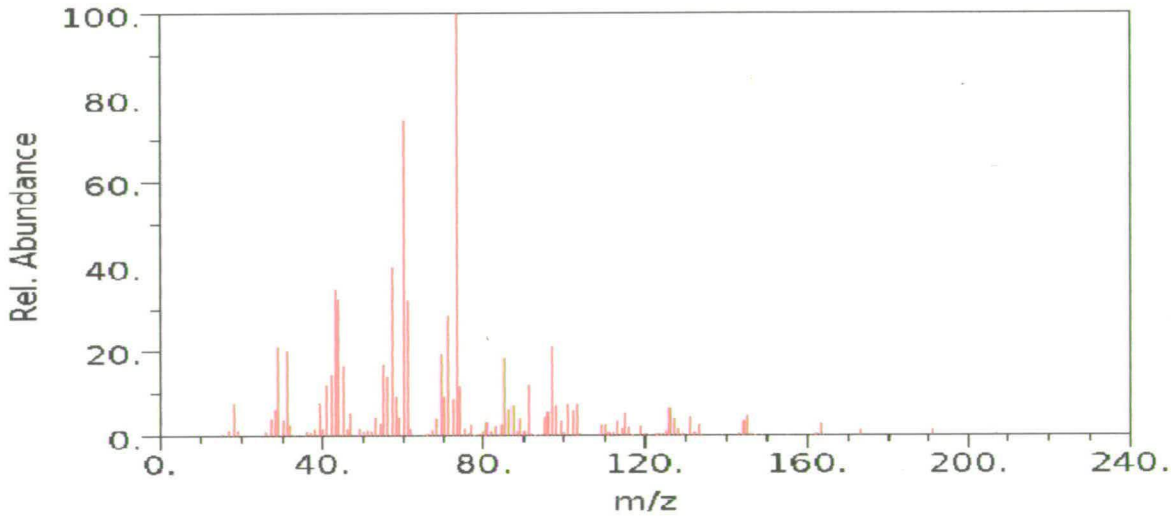

Figure 7.12. Spectrum of Lactose reprinted from NIST chemistry Webbook(NIST, 2005)

The ions which occurred most often and gave the highest intensity, in the ATOFMS mass spectra, are listed in Table 7.3.

Positive ion signals		
Observed *m/z*	**Number of particles containing this peak**	**Average intensity of this peak in spectra**
23	16	188.9
(38 to 41)	122	309.2
55	16	161.7
77	2	106.5
103	18	176.6
117	22	162
(120 to 121)	11	283.8
Negative ion signals		
Observed *m/z*	**Number of particles containing this peak**	**Average intensity of this peak in spectra**
-77 to -79	2	335.5
-61	15	84.5
(-39 to -42)	70	157.4
-25	17	116.5

Table 7.3. The most common ions present in the Lactose sample. Peak thresholds are the same as in Table 7.1.

Lactose does not yield a parent ion but could be monitored using a characteristic set of ion signals. Figure 7.13 and 7.14 show two examples of single shot mass spectra resulting from lactose particles analysed using laser energies of 0.6 and 0.4 mJ respectively.

In the next section, a combination of peaks, given in Table 7.3, were used to try and identify lactose in a mixture. Before the mixture was analysed the predominant ion signals present in each of the individual drug components were investigated to see if overlap occurred.

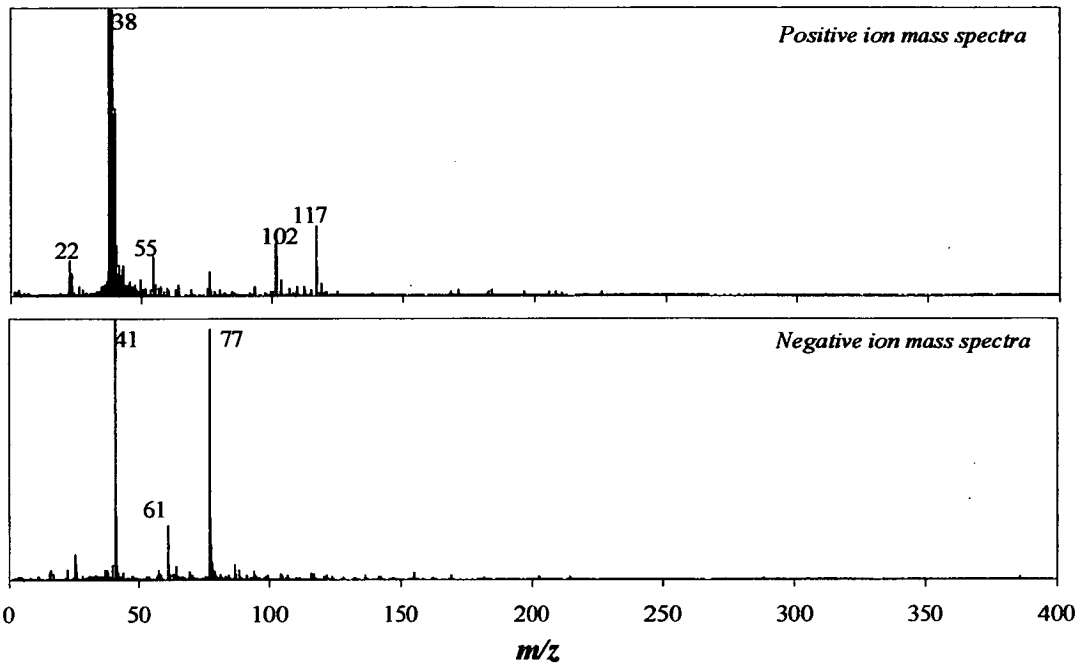

Figure 7.13. Positive and negative ion mass spectra of a lactose particle using high laser energy (0.6 mJ)

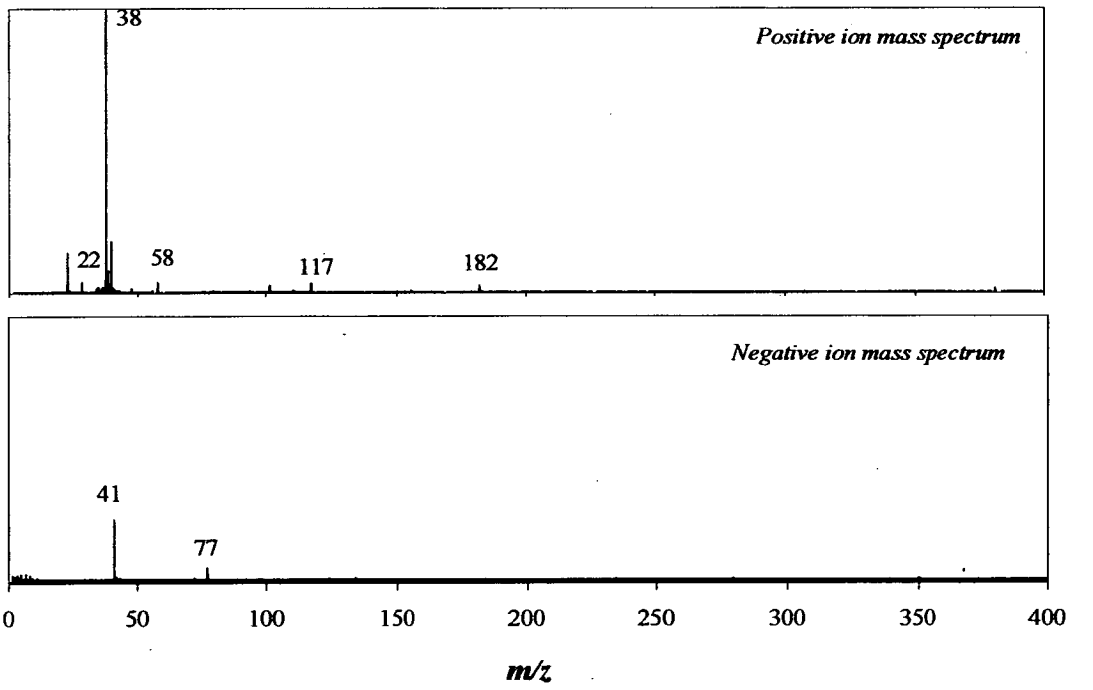

Figure 7.14. Positive and negative ion mass spectra of a lactose particle sampled with a low laser energy (0.4 mJ)

7.3.4. Selection of *m/z* values for drug identification in a mixture.

The ion signals which best identified each of the individual drugs were examined to see where overlap occurred. This was done by carrying out a search through the entire dataset of each of the individual drug components using Microsoft access 2000®. Table 7.4 and 7.5 show the degree of overlap, between the positive and negative ion signals, for the two drugs and lactose.

Positive ion mass spectra			
	338 budesonide mass spectra	*266 formoterol mass spectra*	*124 lactose mass spectra*
Observed *m/z* value	**No. of mass spectra containing this *m/z* value**	**No. of mass spectra containing this *m/z* value**	**No. of mass spectra containing this *m/z* value**
91 to 92	263	140	1
103 to 105	251	90	21
114 to 117	249	94	19
119	196	48	22
120	69	86	9
121	175	139	2
127 to 131	259	20	
134 to 135	91	127	
142 to 147	220	38	
149-150		128	
170 to 172	51		
221*	26	1	
261*	2		
280*		48	
298*		45	
326*		75	
344*		97	

Table 7.4. Positive ion signals corresponding to each individual drug component. For a full list of *m/z* values go to appendix 1.1: Table A1.6. The figures in red refere to ion signals which are unique to that particular drug.* Ions at higher *m/z* values are subject to mass shifting and are often found at *m/z* values ± 1 of the listed value.

Negative ion mass spectra			
	267 budesonide mass spectra	*266 formoterol mass spectra*	*124 lactose mass spectra*
Observed *m/z* value	**No. of mass spectra containing this *m/z* value**	**No. of mass spectra containing this *m/z* value**	**No. of mass spectra containing this *m/z* value**
-355*	69		
-346*	21		
-337*	1	72	
-313*		84	
-309*		9	
-308	1	9	
-307		8	
-306		1	
-224		4	
-162	4	151	
-153	75		
(-148 to -150)	12	152	
-144	173	14	
(-132 to -137)	206	221	
(-113 to -117)	104	238	1
-106	148	99	
-104	12	6	11
(-98 to -94)	246	90	
-90	21	102	8

Table 7. 5. Negative ion signals corresponding to each individual drug component. For a full list of *m/z* values see appendix 1.1: Table A1.7. * Ions at higher *m/z* values are subject to mass shifting and are often found at *m/z* values ± 1 of the listed value.

From Table 7.4 and 7.5 it is possible to conclude that ion signals greater than $m/z = 290$ and ion signals in the range of $m/z = -344$ to -309 can be used for the identification of formoterol in a mixture, together with the ion signals at $m/z = 149$ and 150. For budesonide, ion signals at $m/z = 170$ to 172 along with those at $m/z = 221$ and $m/z = -153$ can be used. Also ion signals at $m/z = -355$ and -346 are unique to the budesonide spectra.

As tables 7.4 and 7.5 show, the peaks which can be used to characterise lactose in a sample are not unique. Unfortunately therefore, lactose containing particles cannot be identified due to interferences from other ions.

7.4. ATOFMS data for AstraZeneca's combination products.

7.4.1. Turbuinhaler budesonide/ formoterol 200/6

AstraZeneca's Symbicort® Turbuhaler was sampled by the ATOFMS to produce a dataset of 430 particles. Figure 7.15 shows the size distribution for the 430 particles sampled. The hit rate for the mixture was 18%.

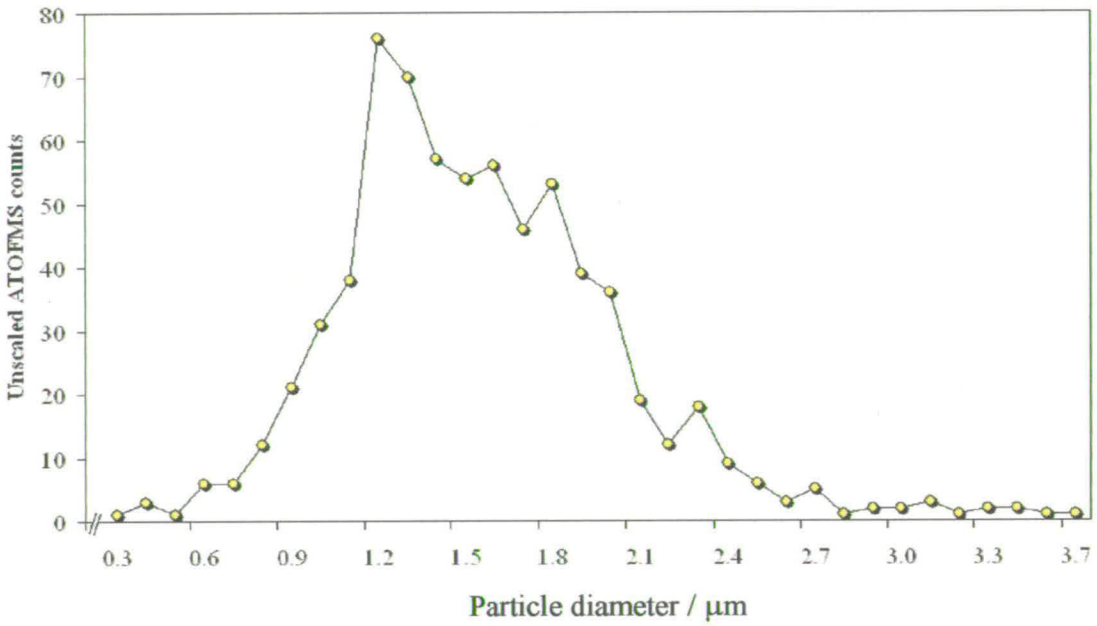

Figure 7.15. Size distribution for Turbuhaler® 200/6 budesonide/formoterol aerosol.

The averaged positive and negative ion mass spectra of all the particles sampled are shown in Figure 7.16. The database obtained for the Turbuhaler® aerosol was examined using MS-Analyze, Microsoft Excel 2000® and Microsoft Access 2000®, for each of the drug components, using the previously defined parameters (section 7.3).

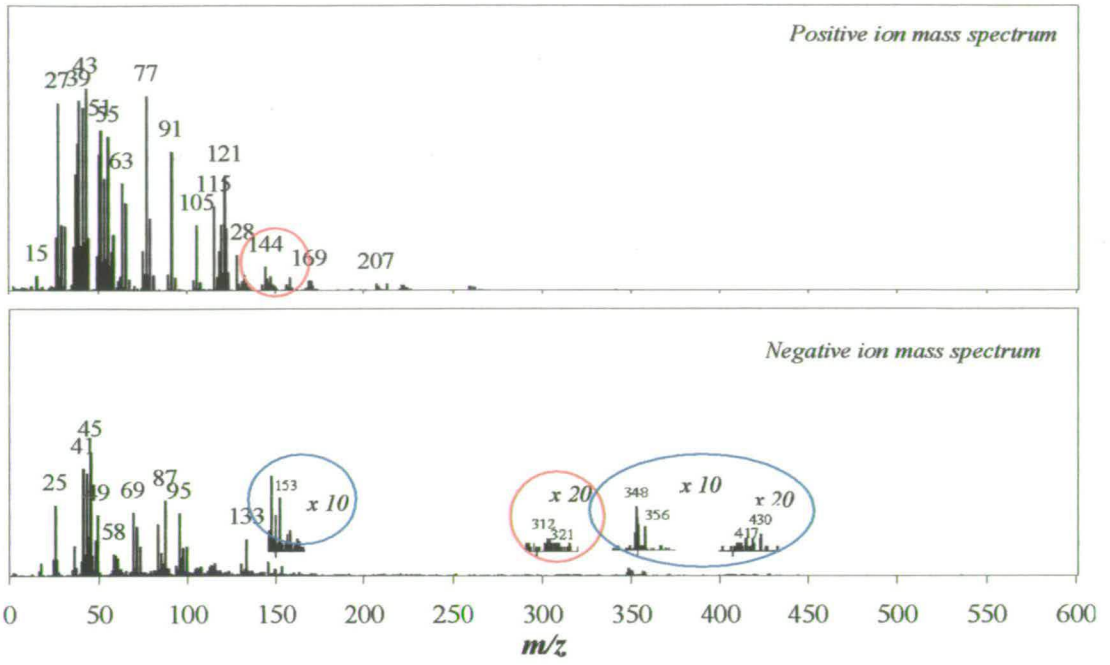

Figure 7.16. Averaged positive and negative ion mass spectra of Turbuhaler® particles sampled by the ATOFMS. Peak thresholds as for Figure 7.3.

From the positive and negative ion mass spectra shown in Figure 7.16 it is possible to see both formoterol fumarate (circled in red *m/z* = 150, -312 & -321) and budesonide (circled in blue *m/z* = -153, -348, -356 & -430) are present in the mixture, although all ion signals have very low intensity and require that the mass spectra be magnified 10/20 times in order to see them more clearly. The database was queried for ion signals representing each of the drug components. Figure 7.17 shows the mass spectrum of a representative particle resulting from the Turbuhaler® mixture which contains ion signals for both formoterol (circled in red *m/z* 150, 306) and budesonide (circled in blue *m/z* = 172, -153 & -358). As with the average mass spectrum the ion signals which were used to identify each of the APIs show very low intensities.

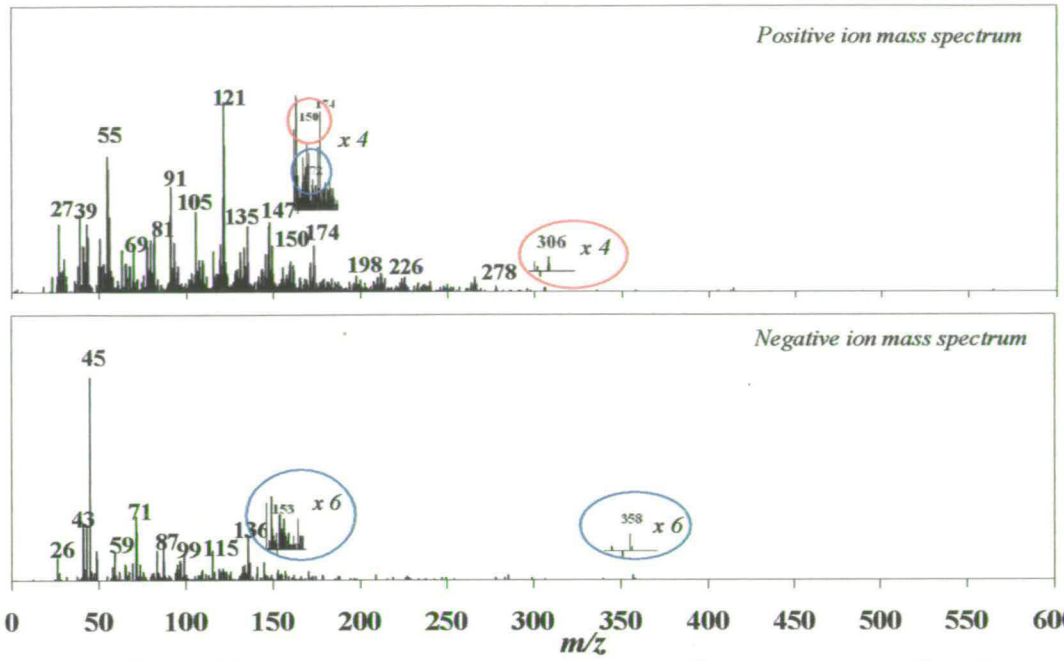

Figure 7.17. Positive and negative ion mass spectra from a single particle from the Turbuhaler® mixture containing ion signals for both drugs.

Table 7.6 summarises the data analysis carried out on the Turbuhaler® mixture. It shows the total number of particles that contain formoterol fumarate and the total number that contain budesonide. Also shown are the number of particles in which formoterol fumarate and budesonide are co-associated. Finally the number of particles that contain only formoterol fumarate and only budesonide are shown. 1% of the dataset contains both drugs in an individual particle. These data are more clearly shown in Figure 7.18 as a function of particle size.

Formoterol fumarate					All	Or
m/z = (-344 to -310)	m/z = (149 to 150)	m/z = (290 to 345)			8	16
Budesonide					**All**	**Or**
m/z = (-353 to -358)	m/z = (-349 to -346)	m/z = (170 to 172)	m/z = (-153)	m/z = (221)	0	75
Formoterol fumarate and Budesonide co - associated					**All**	**Or**
m/z = (-344 to -310)	m/z = (149 to 150)	m/z = (290 to 345)				
m/z = (-353 to -358)	m/z = (-349 to -346)	m/z = (170 to 172)	m/z = (-153)	m/z = (221)	0	5
Formoterol fumarate only					**Total no.**	
m/z = (-344 to -310)	m/z = (149 to 150)	m/z = (290 to 345)			11	
Budesonide only					**Total no.**	
m/z = (-353 to -358)	m/z = (-349 to -346)	m/z = (170 to 172)	m/z = (-153)	m/z = (221)	70	

Table 7.6. Summary of analysis of the Turbuhaler® mixture. 'All' is used to define particles which contained every one of the ion signals being used to identify the drug component in a mixture and 'Or' is used if one or more of the ion signals is present to identify it in a mixture.

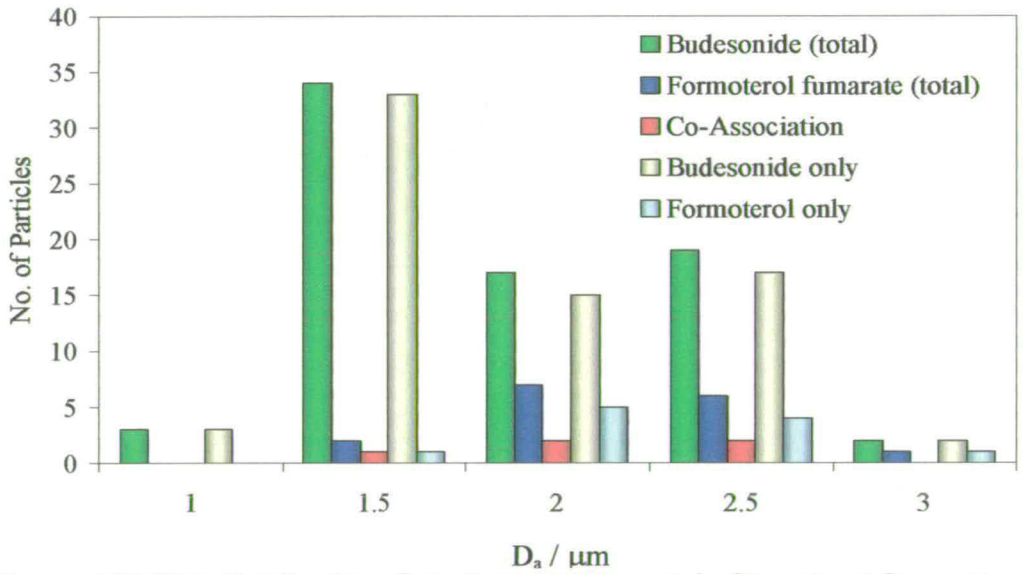

Figure 7.18. Size distribution of particles which contain formoterol fumarate and budesonide, the two drugs in co-association.

In summary, it can be concluded that at least 1% of the total spectra (5.5% of classified particles) contained both drugs together and 19% of the spectra contained only a single

drug component. Only 20% of the spectra have been classified, the remaining spectra did not contain the peaks used to classify the drugs. From the mass spectra shown it can be seen that although ion signals for both components have been identified in individual particles the ion signals have very low intensities. This mixture proven to be very difficult to analyse and the results were not conclusive.

The hit rates of formoterol, budesonide and the Symbicort Turbuhaler were 18%, 24% and 18% respectiviely. Adequate scaling of these data, to correct for differences in hit rate, is required in order to show representative results. After scaling the number of formoterol particles and Symbicort Turbuhaler® particles the overall co-association dropped to 0.8%. At higher laser energies the apparent co-association, scaled for differences in hit rate, dropped to 0.15%.

A second dataset was acquired, from Symbicort ®Turbuhaler 100/6 budesonide/formoterol, the co-association (scaled for hit rate) was 0.3% in this dataset. The ion signals used to identify budesonide and formoterol in the mixture were very weak. Thus, it was difficult to identify both APIs in the mixture.

7.5. GlaxoSmithKline, Seretide ® PDI

The second product analysed was Seretide® PDI commercially available from GSK. The product packaging states that each inhalation contains 50 μg of salmeterol xinafoate and 100 μg of fluticasone propionate. This mixture also contains lactose. As each of the API's are present in similar quantities it should make them easier to detect in the mixture.

7.5.1. Salmeterol Xinafoate

Positive and negative ion mass spectra of particles containing pure salmeterol xinafoate were collected using the ATOFMS at two different laser energies. Figure 7.19 shows the structure of salmeterol, which has a molecular weight of 415g mol^{-1}, and xinafoate, which has a molecular weight of 188g mol^{-1}. Figure 7.20 shows the average of the 152 positive and negative ion mass spectra obtained at optimum laser energies between 0.65

mJ and 0.45 mJ. The hit rate for the salmeterol xinafoate was 12% when sampling at optimum laser conditions.

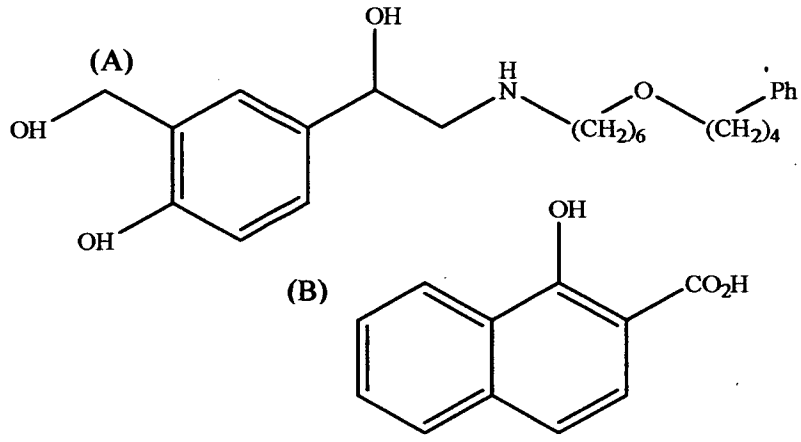

Figure 7.19. Structure of (A) salmeterol and (B) xinafoate

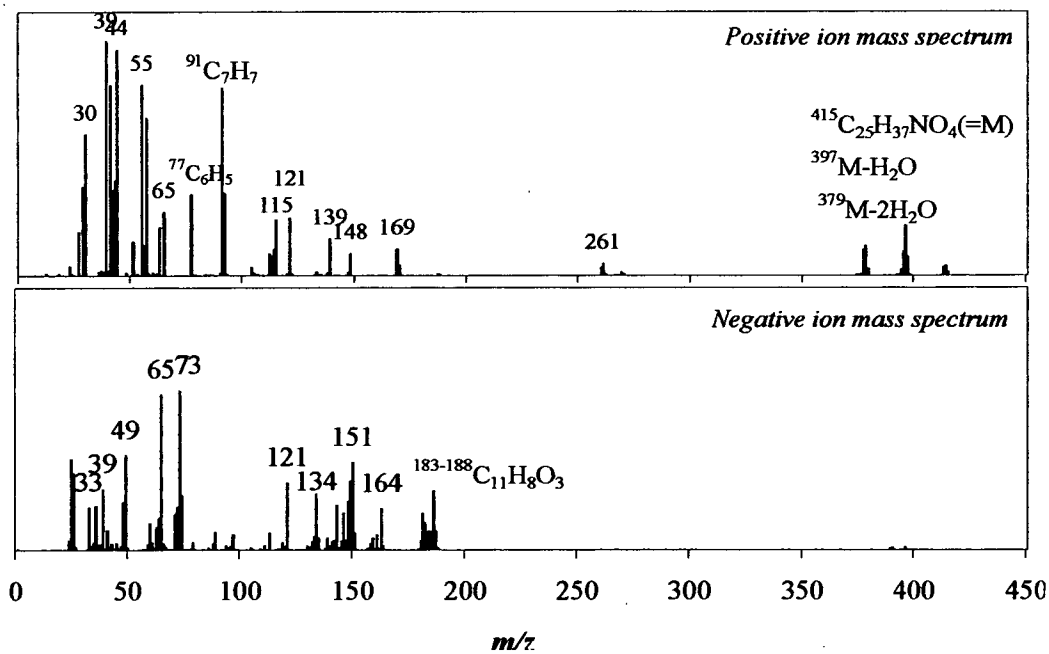

Figure 7.20. Averaged threshold positive and negative ion mass spectra of 152 salmeterol xinafoate particles sampled at optimum conditions. Peak thresholds are the same as those outlined in Figure 7.3.

Each of the individual positive and negative ion mass spectra were analysed for the ions that occurred most often with the greatest intensity. More attention was focused on those ion signals present at higher *m/z* values as these masses are easier to identify

in a mixture. From the averaged positive and negative ion mass spectra it is possible to identify two key ion signals. The first is the parent ion for salmeterol at *m/z* 415 and the second is the ion fragment for xinafoate at *m/z* 188, which is only detected in the negative ion mass spectra. The ions which appeared most often, with the greatest intensity, in the mass spectra of salmeterol xinafoate are listed in Table 7.7.

Positive ion mass spectra		
Observed *m/z*	**Number of particles containing this peak**	**Average intensity of this peak in spectra**[†††]
39 to 44	107	276.6
50 to 55	115	292.7
61 to 65	51	212.5
76 to 79	50	191.4
90 to 92	132	235.5
114 to 115	55	201.8
379 to 415	17	184.9
Negative ion mass spectra		
Observed *m/z*	**Number of particles containing this peak**	**Average intensity of this peak in spectra**
-188 to -180	127	166.8
-158 to -162	104	136.8
-149 to -144	127	163.4
-138 to -142	116	169.7
-130 to -134	100	181.5
-118 to -121	90	187.4
-111 to -112	83	167.1
-103 to -104	52	148.3
-72 to -73	73	113.5
-59 to -61	88	116.3
-47 to -49	106	172.2
-42 to -38	91	111.8
-23 to -27	106	189.8

Table 7.7. The most common ions present in the salmeterol xinafoate mass spectra. The peak thresholds are the same as those outlined in Table 7.1.

[†††] These values are taken from the average intensity mass spectra.

In addition to the ion signals at *m/z* = 91, ions often appear at *m/z* 92 and *m/z* 90: this could be the result of protonation of the *m/z* = 91 fragment or the loss of a hydrogen atom, respectively. The *m/z* = 91 peak frequently appears as a broad peak and is then assigned two *m/z* values by the software. A similar problem arises for the xinafoate fragment: negative ions often appear in the range of *m/z* = -182 to -188. This is most likely due to different fragmentation processes.

The parent ion signal for salmeterol at m/z = 415, appears together with two other ion signals, one at *m/z* = 379 and the other at *m/z* = 397. The three ion signals appear in the ratio of 1:3:1. The two adjacent ions (397 and 379) are a result of the loss of one and two water molecules, respectively. Figure 7.21 and 7.22 show examples of individual spectra resulting from the sampling of salmeterol xinafoate at different laser energies.

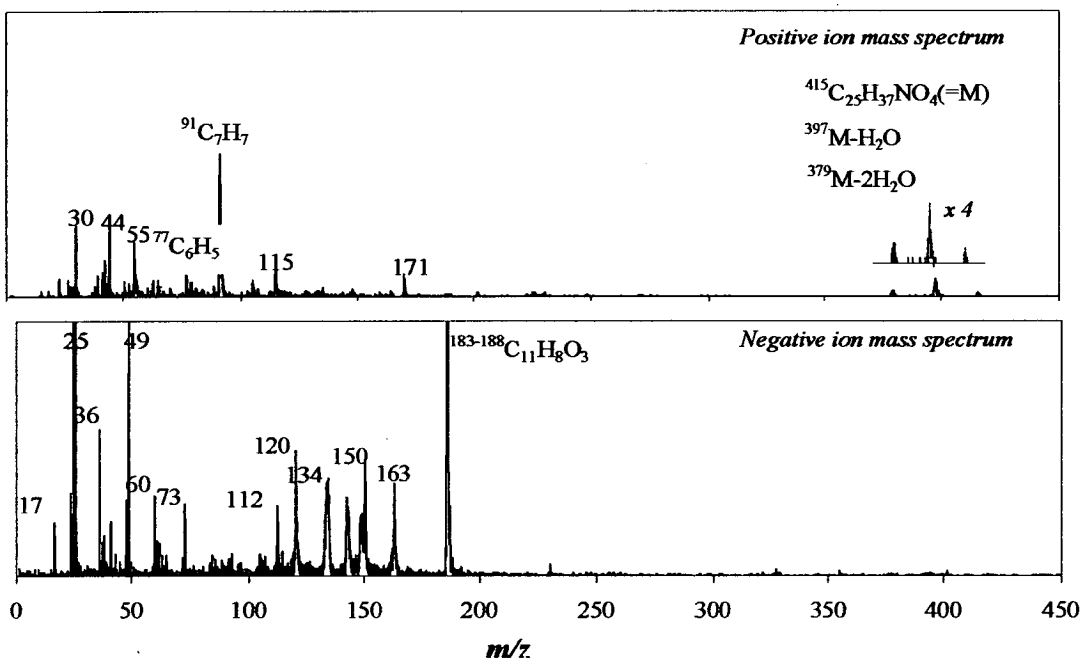

Figure 7.21. Positive and negative ion mass spectra of pure salmeterol xinafoate sampled with high laser energy (0.6 mJ)

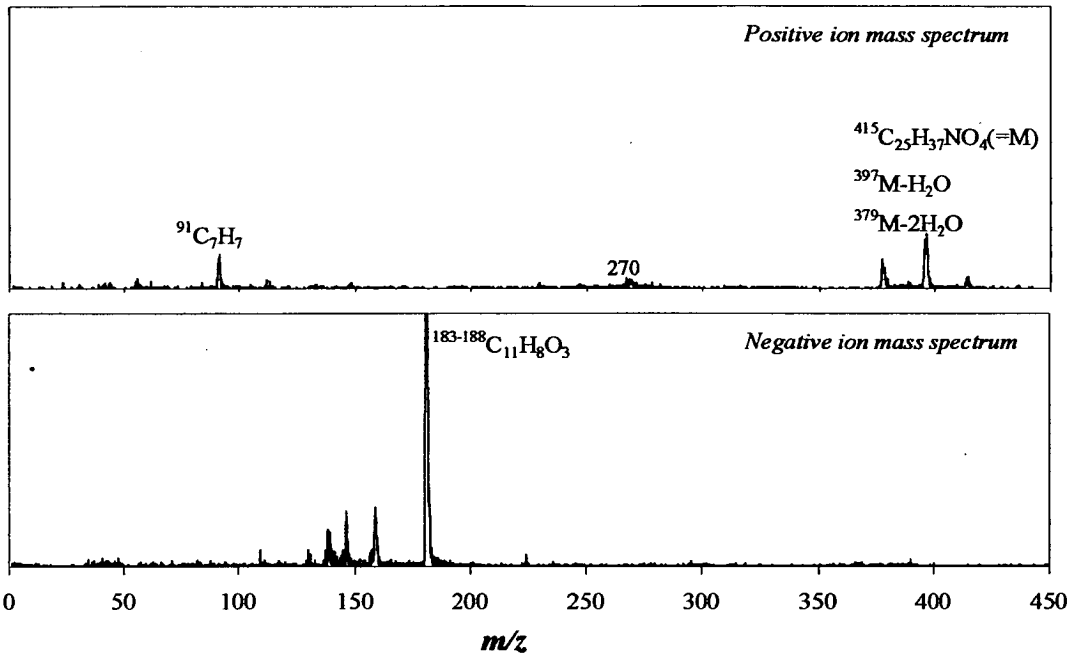

Figure 7.22. Positive and negative ion mass spectra of pure Salmeterol Xinafoate sampled at lower laser energy (0.4 mJ)

The variation in laser power provided control over the amount of fragmentation present in the positive and negative ion mass spectra. This variation in fragmentation is clearly illustrated in Figures 7.21 and 7.22. The optimum conditions for sampling were between 0.4 and 0.6 mJ. The ion signals identified in Table 7.7 will be used to develop a fingerprint for the analysis of salmeterol xinafoate in the mixture.

7.5.2. Fluticasone propionate

Fluticasone has a molecular weight of 500.6 g mol^{-1}, this high molecular weight suggests that it will be difficult to see a parent ion with the ATOFMS and it may be necessary to rely on characteristic fragment ion signals. It does however have some distinctive elements (F & S), shown in Figure 7.23, which may allow its identification. Positive and negative ion mass spectra of pure fluticasone propionate particles were collected using the ATOFMS. The hit rate for the fluticasone propionate was 9% only when sampling at optimum laser energy, indicating that fluticasone is not readily detected at 266 nm. Figure 7.24 shows the average of 121 positive and negative ion mass spectra obtained at optimum laser conditions.

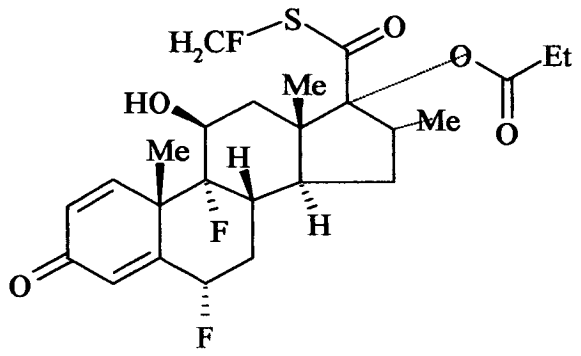

$C_{25}H_{31}F_3O_5S$

Figure 7.23. Structure of fluticasone propionate

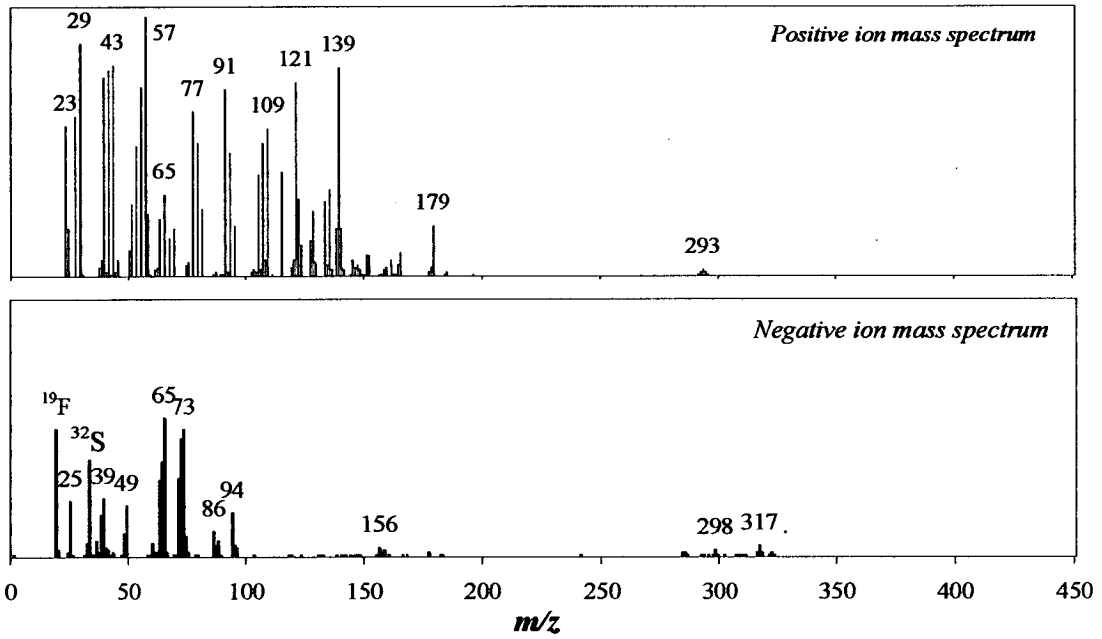

Figure 7.24. Averaged positive and negative ion mass spectra of 121 fluticasone propionate particles. Peak thresholds were the same as Figure 3.1.

The ions which appeared most often with the strongest intensity in the mass spectra of fluticasone propionate are listed in Table 7.8.

Positive ion mass spectra		
Observed *m/z*	**Number of peaks containing this instrument**	**Average intensity of this peak in spectra**
26 to 29	66	41.2
41 to 43	36	34.8
55 to 57	76	49.7
62 to 65	16	24.5
76 to 77	20	38.3
119 to 121	47	32.8
138 to 139	68	42.9
Negative ion mass spectra		
Observed *m/z*	**Number of peaks containing this instrument**	**Average intensity of this peak in spectra**
-155 to -158	71	49.8
-94 to -96	90	55.7
-88 to -86	87	46.7
-70 to -73	119	148.5
-62 to -65	115	90.2
-48 to -49	50	99.9
-37 to -39	101	64.7
-32 to -33	74 *(S/SH)*	86.9
-25 to -24	58	89.2
-19	79 *(F)*	131.4

Table 7.8. The most common positive and negative ions present in the fluticasone propionate sample. Thresholds as for Table 7.1. A full list of all the positive and negative ions detected can be found in appendix 1.2 Table A1.8 and A2.9.

Fluticasone propionate did not yield a parent ion but distinctive positive and negative ion fragments can be used for identification. Figure 7.25 and 7.26 show two examples of individual mass spectra from fluticasone propionate sampled at both high and low laser intensities respectively. The optimum conditions for sampling were between 0.4 and 0.6 mJ, the data have been analysed under these conditions.

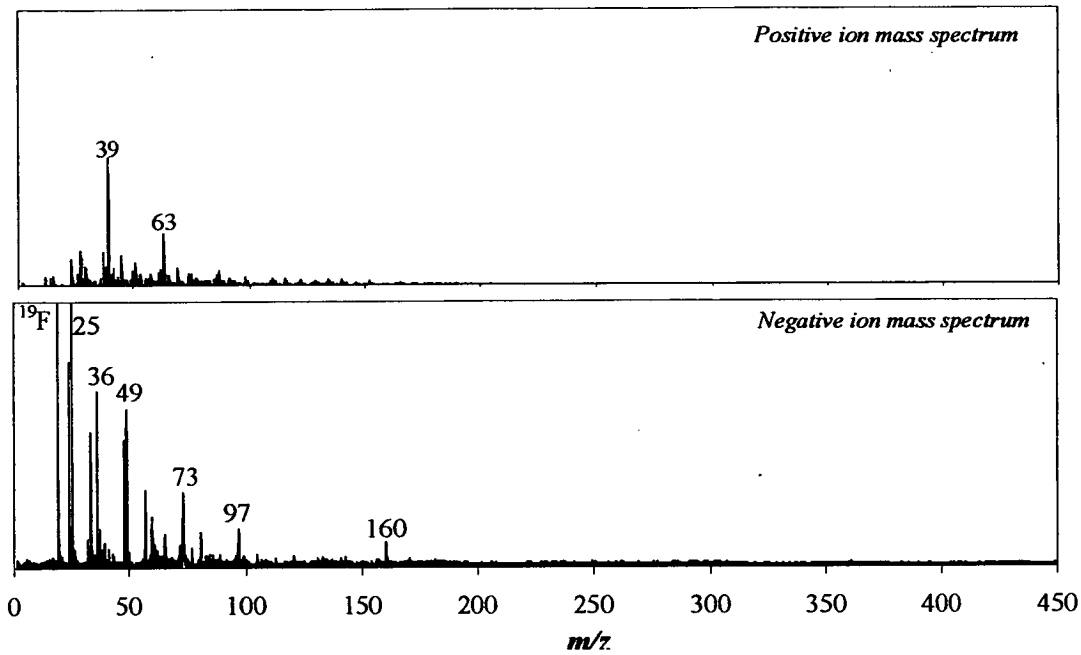

Figure 7.25. Positive and negative ion mass spectra of pure fluticasone propionate sampled with high laser energy (0.6 mJ)

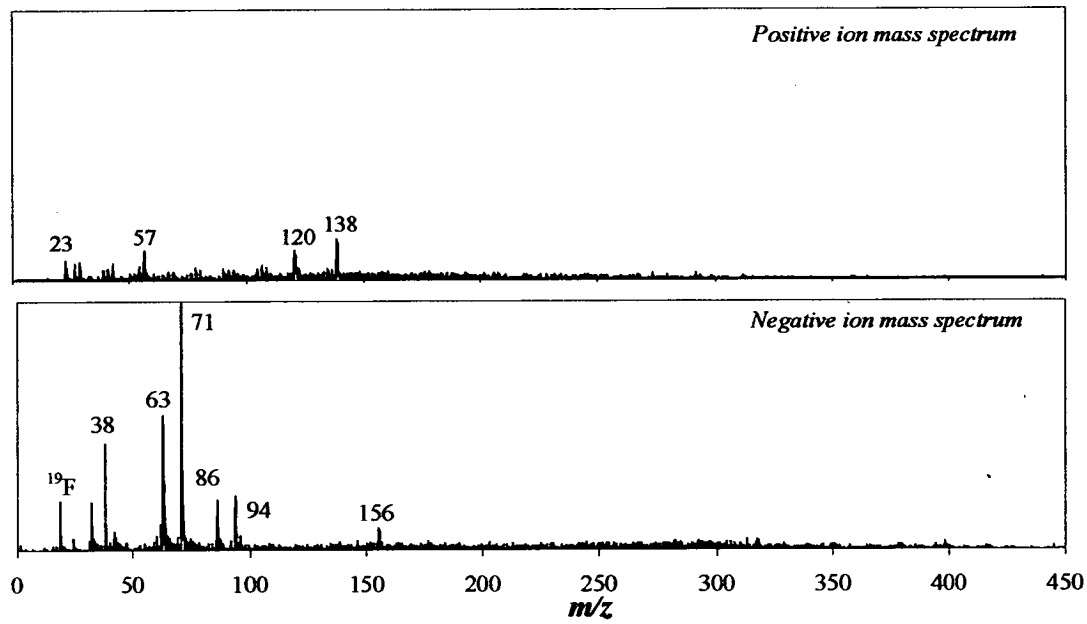

Figure 7.26. Positive and negative ion mass spectra of pure fluticasone propionate using low laser energy (0.4 mJ)

Using a combination of all of these peaks at optimum sampling conditions, 100% of the spectra can be classified. This combination of peaks could therefore be used for the identification of fluticasone propionate in a mixture.

7.5.3. Selection of *m/z* values for drug identification in a mixture.

The ion signals which best identified each of the individual drugs were examined to see where overlap occurred. This was done by carrying out a search through the entire dataset of each of the individual drug components using MS-Analyze, Microsoft excel 2000® and Microsoft access 2000®. Table 7.9 and 7.10 show the degree of overlap between different positive and negative ion signals for the two drugs and lactose.

Positive ion mass spectra						
	121 Fluticasone propionate mass spectra		*150 Salmeterol Xinafoate mass spectra*		*124 Lactose mass spectra*	
Observed *m/z*	**Number of particles containing this peak**	**Average intensity of this peak in spectra**	**Number of particles containing this peak**	**Average intensity of this peak in spectra**	**Number of particles containing this peak**	**Average intensity of this peak in spectra**
26 to 29	66	41.2	7	272.0	2	245
39 to 44	57	44.5	107	276.6	171	344.5
50 to 55	19	40.7	115	292.7	10	257.7
55 to 57	76	49.7	6	103.8	11	165.5
62 to 65	16	24.5	51	212.5	2	188.0
76 to 79	20	38.3	50	191.4	0	0.0
90 to 91	17	44.0	132	235.5	1	103.0
103	0	0	0	0	**19**	**201.1**
109	**4**	**30.3**	0	0.0	0	0.0
114 to 115	8	27.5	55	201.8	0	0.0
119 to 121	47	32.8	0	0.0	35	258.0
138 to 139	**68**	**42.9**	0	0.0	0	0.0
379 to 415	0	0	**17**	**184.9**	0	0.0

Table 7.9. Positive ion signals corresponding to each individual drug component.

Negative ion spectra						
	121 Fluticasone propionate mass spectra		*150 Salmeterol Xinafoate mass spectra*		*124 Lactose mass spectra*	
Observed *m/z*	**Number of particles containing this peak**	**Average intensity of this peak in spectra**	**Number of particles containing this peak**	**Average intensity of this peak in spectra**	**Number of particles containing this peak**	**Average intensity of this peak in spectra**
-188 to -180	0	0	127	166.8	0	0.0
-158 to -162	30	59.7	104	136.8	0	0.0
-155 to -158	71	49.8	13	209.4	0	0.0
-149 to -144	4	55.2	127	163.4	0	0.0
-138 to -142	3	57.3	116	169.7	0	0.0
-130 to -134	6	119	100	181.5	0	0.0
-118 to -121	2	35	90	187.4	3	80.0
-111 to -112	5	23.7	83	167.1	0	0.0
-103 to -104	3	24.6	52	148.3	3	72.5
-94 to -96	90	55.7	20	97.3	1	76.0
-88 to -86	87	46.7	22	87.5	0	0.0
-70 to -73	119	148.5	73	113.5	2	77.0
-59 to -61	31	47.1	88	116.3	2	81.5
-62 to -65	115	90.2	33	100.0	17	87.7
-48 to -49	50	99.9	106	172.2	2	123
-37 to -42	101	64.7	91	111.8	70	157.4
-32 to -33	74	86.9	0	0.0	0	0.0
-27 to -23	58	89.2	106	189.8	17	161.9
-18 to -19	79	131.4	0	0.0	0	0.0

Table 7.10. Negative ion signals corresponding to each individual drug component.

From Table 7.9 and 7.10 it can be concluded that for salmeterol xinafoate it is possible to use the parent ion peaks at the *m/z* 379 to 415 to identify the drug in a mixture, together with the ion signals at *m/z* = -182 to -188 and -148. For fluticasone, ion signals at *m/z* -19, -32, -33 and (138 to 139) are unique to the fluticasone spectra. All other ion signals which represent fluticasone unfortunately overlap with lactose and salmeterol xinafoate. As tables 7.9 and 7.10 show, it is not possible to identify lactose in the mixture with any certainty.

7.6. ATOFMS data for combination products.

7.6.2. Seretide® 50/100 Salmeterol xinafoate/fluticasone propionate (SX/FP)

Three doses of Seretide® 50/100 SX/FP were sampled by the ATOFMS, from a discus, to produce this dataset. 647 mass spectra were collected and analysed under optimum laser energies. Figure 7.27 shows the size distribution for the 647 particles sampled. The hit rate for the Seretide® device was 19%.

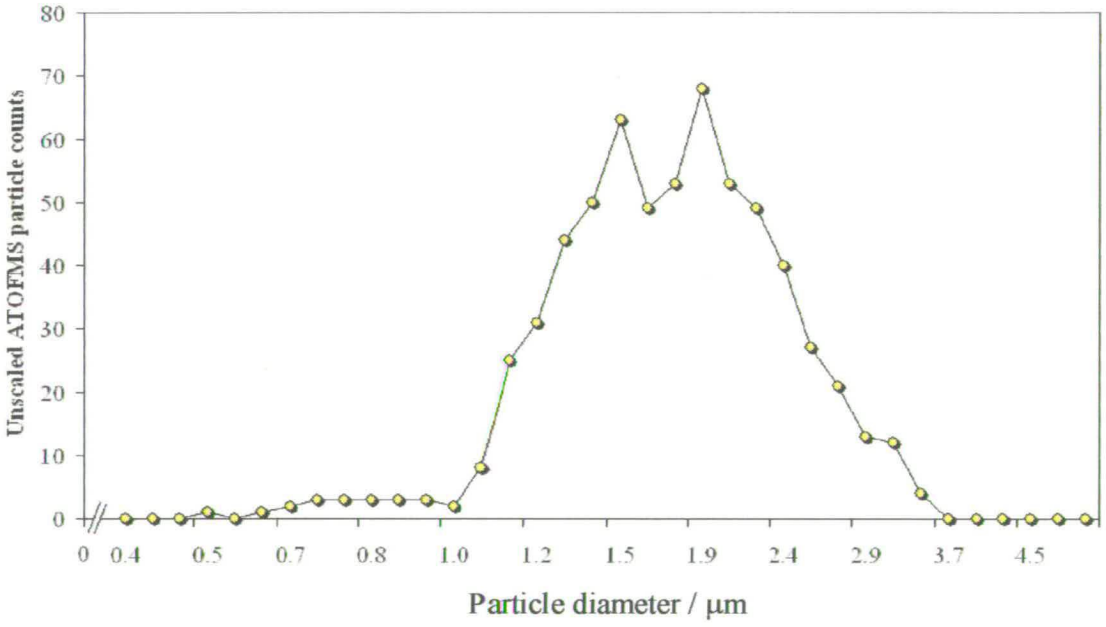

Figure 7.27. Size distribution for Seretide® 50/100 SX/FP aerosol.

Average positive and negative ion mass spectra of all the particles are shown in Figure 7.28. The database obtained for the Seretide® aerosol was examined using MS-Analyze,

Microsoft excel 2000® and Microsoft access 2000® for each of the drug components using the previously defined parameters (section 7.5).

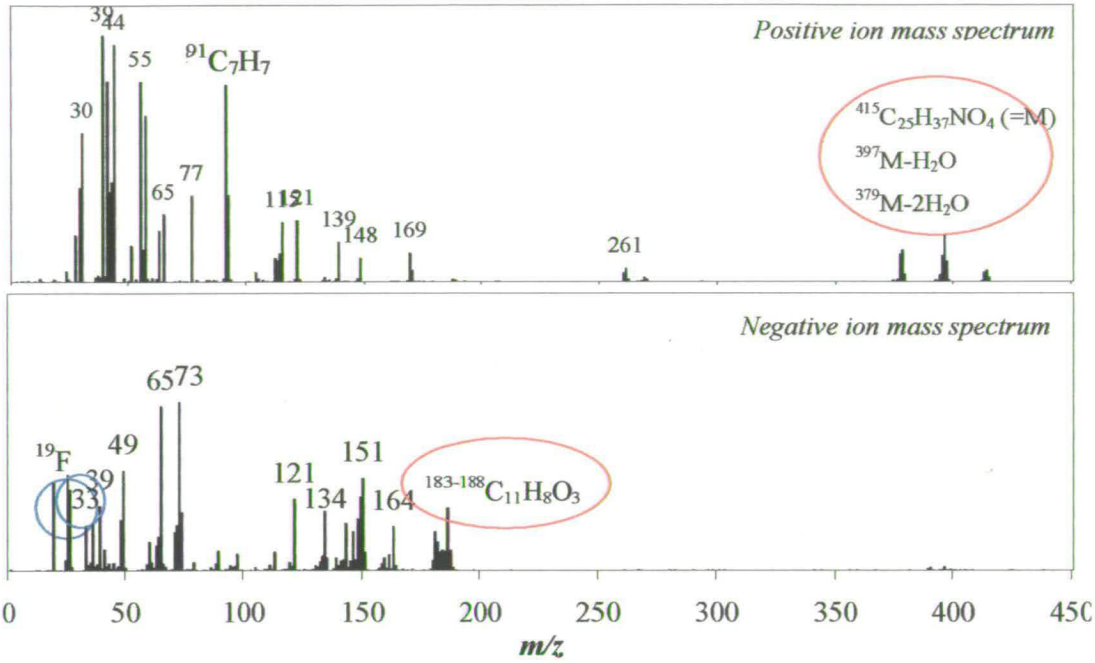

Figure 7.28. Averages positive and negative ion mass spectra from Seretide® particles sampled by the ATOFMS. Peak thresholds as for Figure 3.1.

From the averaged positive and negative ion mass spectra in Figure 7.28 it is possible to see that ions from both salmeterol xinafoate (circled in red) and fluticasone propionate (circled in blue) are present in the mixture with reasonable intensities. The database was queried for ion signals representing each of the drug components.

Figure 7.29 shows a positive and negative ion mass spectrum of an individual particle resulting from the Seretide® mixture. Ion signals for both salmeterol xinafoate (circled in red) and fluticasone propionate (circled in blue) are observed.

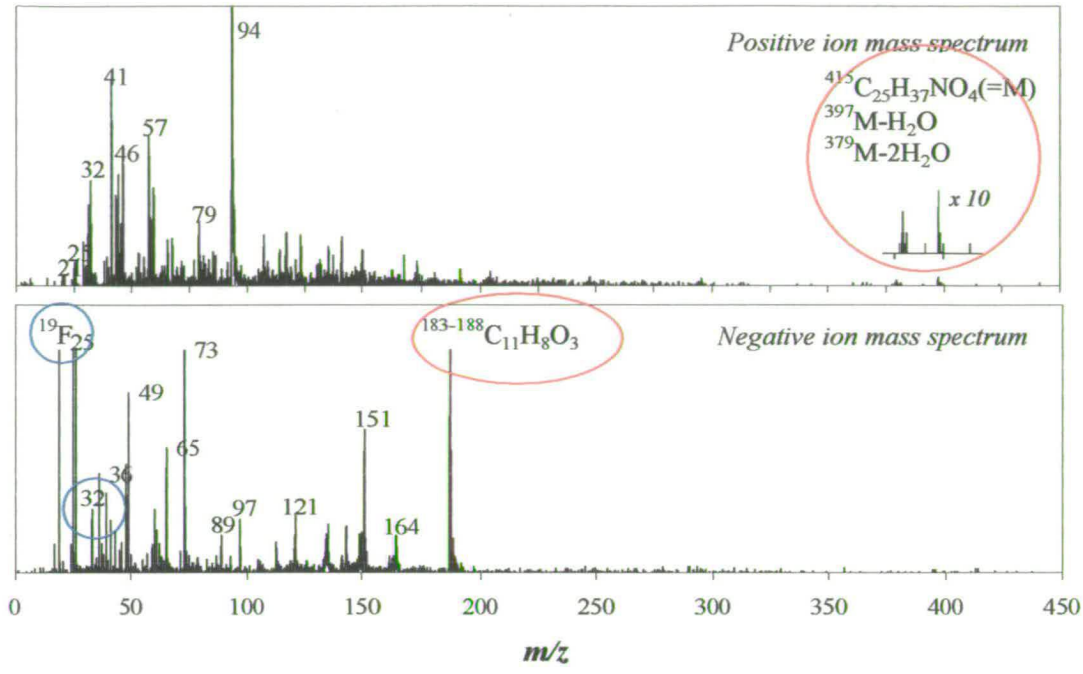

Figure 7.29. Positive and negative ion mass spectra of a single particle from the Seretide® mixture containing ion signals for both drugs.

Table 7.11 summarises the data analysis carried out on the Seretide® mixture. It shows the total number of particles that contain fluticasone propionate and the total number that contain salmeterol xinafoate. Also shown are the number of particles in which fluticasone propionate and salmeterol xinafoate are co-associated. Finally, the number of particles that contain only fluticasone propionate and only salmeterol xinafoate are shown. 58% of the dataset contains both drugs in an individual particle. These data are more clearly shown in Figure 7.30 as a function of particle size.

Fluticasone propionate				All	Or
m/z = -19	m/z = -32	m/z = -33	m/z = 138 to 139	8	397
Salmeterol xinafoate				**All**	**Or**
m/z = 376 to 415	m/z = -182 to -187			96	595
Fluticasone propionate and Salmeterol xinafoate co - associated				**All**	**Or**
m/z = -19	m/z = -32	m/z = -33	m/z = 138 to 139		
m/z = 376 to 415	m/z = -182 to -187	m/z = -148		1	376
Fluticasone propionate only				**Total no.**	
m/z = -19	m/z = -32	m/z = -33	m/z = 138-139	21	
Salmeterol xinafoate only				**Total no.**	
m/z = 376 to 415	m/z = -182 to -187	m/z = -148		219	

Table 7. 11. Summary of analysis of the Seretide® mixture. 'All' is used to define particles which contained every one of the ion signals being used to identify the drug component in a mixture and 'Or' is used if one or more of the ion signals is present to identify it in a mixture.

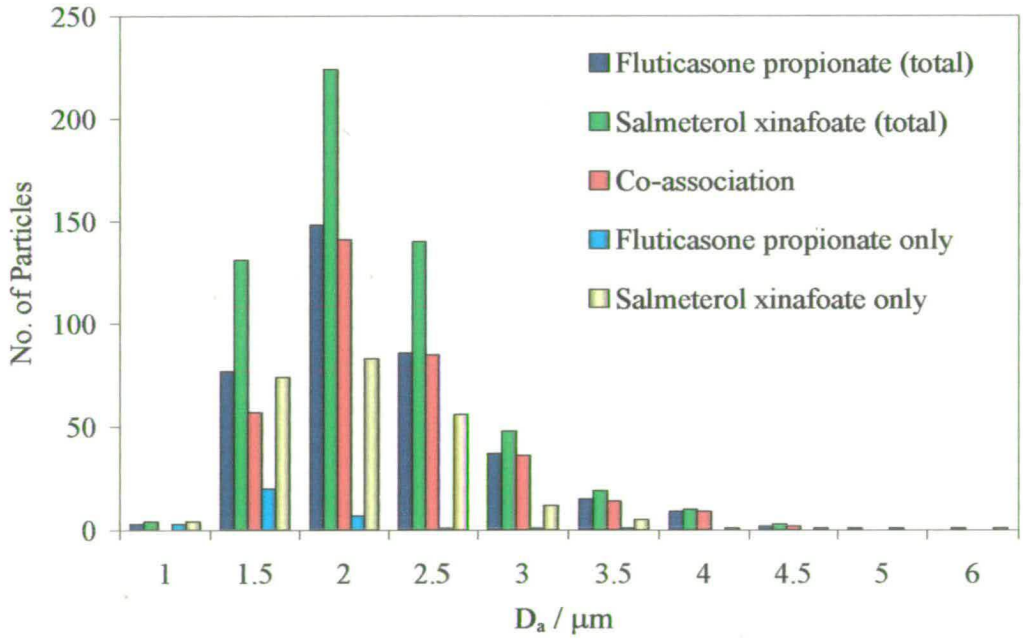

Figure 7.30. Size distribution of particles that contain fluticasone propionate, salmeterol xinafoate, the two drugs in co-association and particles that contain only one drug.

In summary, at least 58 % of the hit particles contained both drugs and 37% of the hit particles probably contain only a single drug component (usually salmeterol). 95% of the spectra have been classified; the remaining spectra did not contain peaks used to classify the drugs.

From Figure 7.30 and Table 7.11 it is apparent that fluticasone is mainly detected when associated with salmeterol xinafoate. A similar finding was reported by Karlsson *et al.* (2000) when analysing the ipratropium bromide from the Combivent® MDI. It was suggested that this was due to the ipratropium bromide particles homogeneously nucleating, during actuation, to form particles smaller than 0.3 μm. Here it is possible that a similar phenomenon is happening with the fluticasone propionate but as previously noted the low hit rate for fluticasone propionate makes it more likely that these particles are not detected with as high efficiency as the pure salmeterol xinafoate particles, or the agglomerate particle of salmeterol xinafoate and fluticasone propionate. This is a frequently observed effect with the ATOFMS instrument and is commonly referred to as the matrix effect where the presence of certain chemical species can enhance ion formation from species that would not normally absorb sufficient energy to cause the formation of ions. It works in a similar manner to MALDI where the non-absorbing sample is mixed with a strongly absorbing matrix. The energy absorbed by the matrix is transferred to the non-absorbing sample causing it to fragment into positive and negative ions.

At higher laser energies the apparent co-association present in the sample dropped to 45% due to the loss of the parent ion signal (i.e. fragmentation of the parent ion). Using a throat cast, to sample the aerosol, the percentage of co-association dropped to 28%, due to the loss of the coarser particles. A brief experiment was done with an MDI mixture of the two drugs (25/250 salmeterol xinafoate/fluticasone propionate), with the throat cast, and it was reported that co-association was 45%. Graphs and tables showing the results from these experiments can be found in appendix 1.3.

As the hit rate (HR) for the fluticasone propionate (HR = 9%), salmeterol xinafoate (HR=12%) and the Seretide® (HR=19%) are different, it is necessary to scale up the

number of particles for each of the pure drugs to make them comparable to the Seretide® mixture, so that each of samples can be compared with each other. The hit rate for fluticasone propionate at optimum laser conditions was 9%, and the observed number of particles containing only fluticasone propionate was 21. When corrected for hit rate this number increases to 44. For salmeterol xinafoate the number of particles increased from 219 to 347 after the hit rate correction is made.

This increases the effective number of particles sampled from 647 to 798 and therefore results in a drop in the overall co-association to 47%.

7.7. Conclusion

After looking at two of the commercially available drug formulations it is possible to see that there is a big difference between the two drug formulations. In the first drug analysed (Symbicort Turbuhaler®), the results were not conclusive as it was difficult to get a large enough ion signals. For this reason it is difficult to say with any certainty that the drugs were or were not associated with each other. Further work experimenting with different threshold values need to be carried out in order to improve the ATOFMS signal output from these drug products. This drug is compared with the second drug formulation (Seretide® PDI) where a clear association between the two drug formulations is seen after actuation.

These studies have demonstrated the effectiveness of the ATOFMS in analysing single drug components. If developed further these technique could replace the time and cost intensive sampling methods currently used.

Chapter 8

Final discussion and future work

Chapter 8 Conclusions and future work

The work presented in this thesis has allowed improvements of the quantitative output of the ATOFMS instrument and has addressed the mechanisms of reactions occuring in laser ablation of single particles. These fundamental improvements will allow a better understanding of the mass spectra generated from the ATOFMS as well as providing improved single particle data. In addition, the ATOFMS has been used to characterise aerosol particles for medicinal purposes and has demonstrated its effectiveness in investigating the impact of ambient particles on air pollution and health. This thesis has demonstrated the wide range of applications for the ATOFMS.

Results obtained from the studies of aerosol particles and laser radiation have improved the understanding of laser interactions with single particles as well as the ion-molecule reactions occurring within the ATOFMS. Further experiments using different particle types, such as those that absorb strongly at the laser wavelength used, as well as mixtures of absorbing and non-absorbing compounds will provide useful information.

Moreover, molecular dynamic models of absorbing compounds and mixtures of absorbing and non-absorbing compounds have been studied extensively by Garrison & co-workers, (Schoolcraft *et al*, 2001; 2000; Zhigilei & Garrison, 1998). Using this information in combination with experimental data will help to fully establish the mechanisms occurring in laser ablation of single aerosol particles.

The Nd:YAG laser used in the ATOFMS instrument has a Gaussian profile. If particles always intercept the laser at the same place, it is likely that they will absorb similar amounts of energy. As this can not be guaranteed, it is likely that each particle hit by the ablation laser absorbs variable quantities of incident energy which affects the ions being formed. Improving the output of the laser so that a flat top profile is achieved will improve the reproducibility of the mass spectral pattern. This improvement will also ensure that successive particles will absorb similar quantities of energy allowing variations from shot-to-shot laser pulses to be reduced. Wenzel &

Prather (2004) and more recently Steele *et al,*(2005) have demonstrated that flat top laser profiles can be achieved through the use of either optic fibres or extracavity optics. Using better laser profiles allows the mass spectral differences to be related to particle morphology or ion-molecule reactions in the plume rather than to differences in the energy absorbed by the particle.

Ion-molecule reactions occurring in the ATOFMS can only be explained through their resulting mass spectral signatures. Delaying the extraction of ions from the source region would allow reactions to be studied in more detail. By varying the extraction time, reactions can proceed for longer and will result in different mass spectral signatures.

Furthermore, delaying the extraction of ions from the source region has been shown to improve the resolution of ions having higher *m/z* values (Czerwieniec *et al*, 2005). Currently, the mass spectral resolution, in the ATOFMS, of higher *m/z* ions is poor and their calibration is difficult. Czerwieniec *et al,* (2005) showed that using a linear TOF, implementing delayed extraction, gating of lower *m/z* ions, and ion guide, significantly improved the TOF resolution for higher *m/z* ions. It is possible that further research into this area could lead to improvements in mass spectral signatures and resolution.

Moffet *et al,* (2004) demonstrated that ATOFMS hit rate was substantially affected by the relative humidity (RH). Neubauer *et al,* (1997) used a similar instrument to look at the effects of RH on mass spectral ion signals. Investigating mass spectral patterns as a function of RH is an area that needs specific attention. Depending on the RH, particles can be wet (and have a spherical shape) or dry (with an irregular shape). As all inlets are designed to focus spherical particles, this affects how efficiently dry particles are focused into the particle beam.

Heterogeneous atmospheric reactions have been detected and monitored by the ATOFMS in both rural and urban environments. More laboratory studies using the ATOFMS to investigate heterogeneous reactions in controlled environments will

provide a greater understanding of the mass spectral patterns observed from aerosols in the ambient atmosphere.

Investigations into the reactions of amines (Angelino *et al*, 2001) and markers for aqueous chemistry (Whiteaker & Prather, 2003) have proven invaluable when analysing ambient atmospheres. Only recently, work has been published demonstrating the ability of the ATOFMS to investigate heterogeneous chemistry in laboratory environments through the use of flow tube reactors (Sullivan *et al*, 2005).

Operating the ATOFMS instrument alongside conventional samplers for longer periods of time as well as in a variety of atmospheric conditions will allow more robust scaling functions for both particle number and, more importantly, particle mass to be developed. Comparison studies with different aerosol mass spectrometers located in the same or different areas can be used to provide complementary information on aerosol particles as well as providing a means of following air mass trajectories.

Dall'Osto *et al*, (2005) compared the ATOFMS and AMS instruments. A marine biogenic class was detected by the ATOFMS and correlated with increased organic measurements from the AMS. More comparative research with these aerosol mass spectrometers will be useful for understanding aerosol formation and for the improvement of climate models. Recent improvements of the AMS instrument have replaced the quadrupole mass spectrometer with a TOF mass spectrometer, permitting the comparison of single particle mass spectrometers. It is possible that a comparison between these two TOF instruments, either through laboratory or field experiments, would allow a high resolution, single particle, quantitative scaling factor to be determined for the ATOFMS instrument.

The use of single particle aerosol mass spectrometers to monitor the ambient aerosol during exposure studies allows the toxicity of certain chemical components to be investigated. Conventionally, these experiments employed bulk filter analysis techniques. As exposure studies are only run for two hour periods at a time it is

difficult to obtain a sufficient particle mass for analysis, especially if the ambient number concentration is low. The ATOFMS, however, can detect particles with high time resolution even in low particle number concentration. Further studies using the ATOFMS in parallel with exposure studies for longer periods of time and in a number of different atmospheric conditions (.i.e. polluted & clean airmasses) will help to establish the relationship between particle toxicity, size and detrimental health effects. Improving the ATOFMS quantitative mass output will provide significant information for these studies.

The current inlet used by the ATOFMS instrument is a converging nozzle. This set-up means that a high percentage of particles entering the inlet system are lost to the inlet walls. Su *et al,* (2004) has described a new aerodynamic inlet that focuses a wider range of particles. Employing the aerodynamic inlet will enable a larger percentage of particles to travel down the centre line of the instrument and intersect the focal point of the laser beam. This will result in more reproducible mass spectra. Using the aerodynamic inlet will also permit the study of the finer particle size fraction.

Finally, the ATOFMS was used to examine how single drug particles interact as they are delivered to the lung. At present, pharmaceutical methods for determining the effects of drug particles involve the use of bulk analysis techniques which are time and cost intensive. The ATOFMS instrument can be used both to size and chemically characterise individual particles and could possibly be developed to incorporate real-time processing of the data. It will be necessary to develop strong fingerprints of each drug component as was shown in Chapter 7. It is possible that by incorporating these mass spectral fingerprints into software, such as the ART-2a neural network, will identify when these particles are present in real-time.

It may be that research using the ATOFMS instrument will lead to the design of a new generation of aerosol mass spectrometers aimed solely at the pharmaceutical industry. It is likely that the Aerodyne AMS will be more suited to development in the pharmaceutical industry as it is designed to provide quantitative information on

non-refractory organic compounds. The new AMS with the TOF mass spectrometer would be ideal for pharmaceutical applications, allowing quantitative single particle data to be acquired. Although as the method of ionization used in the AMS is electron impact there is still a large amount of fragmentation present in the mass spectra making it difficult to acquire molecular information. There are a number of research groups investigating the use of softer ionization techniques in the AMS instrument (Nash *et al*, 2005).

Chapter 9.0

References

Chapter 9.0 References

Adams,M.J. (1995) *Chemometrics in analytical spectroscopy,* RSC Analytical Spectroscopy Monographs.

Aitken,J. (1888) On the number of deust particles in the atmophere. *Nature*, **1**, 428-430.

Alfarra,M.R., Coe,H., Allan,J.D., Bower,K.N., Boudries,H., Canagaratna,M.R., Jimenez,J.L., Jayne,J.T., Garforth,A.A., Li,S.M., & Worsnop,D.R. (2004) Characterization of urban and rural organic particulate in the lower Fraser valley using two aerodyne aerosol mass spectrometers. *Atmospheric Environment*, **38**, 5745-5758.

Allen,J.O., Fergenson,D.P., Gard,E.E., Hughes,L.S., Morrical,B.D., Kleeman,M.J., Gross,D.S., Galli,M.E., Prather,K.A., & Cass,G.R. (2000) Particle detection efficiencies of aerosol time of flight mass spectrometers under ambient sampling conditions. *Environmental Science & Technology*, **34**, 211-217.

Anderson,B.J., Musicant,D.R., Ritz,A.M., Ault,A., Gross,D., Yuen,M., & Galli,M. User-friendly clustering for atmospheric data analysis. Technical report. 2005. Carleton College Computer Science.
Ref Type: Report

Anderson,K.R., Avol,E.L., Edwards,S.A., Shamoo,D.A., Peng,R.C., Linn,W.S., & Hackney,J.D. (1992) Controlled exposures of volunteers to respirable carbon and sulfuric-acid aerosols. *Journal of the Air & Waste Management Association*, **42**, 770-776.

Andreae,M.O., Charlson,R.J., Bruynseels,F., Storms,H., Vangrieken,R., & Maenhaut,W. (1986) Internal Mixture of Sea Salt, Silicates, and Excess Sulfate in Marine Aerosols. *Science*, **232**, 1620-1623.

Angelino,S., Suess,D.T., & Prather,K.A. (2001) Formation of aerosol particles from reactions of secondary and tertiary alkylamines: Characterization by aerosol time-of- flight mass spectrometry. *Environmental Science & Technology*, **35**, 3130-3138.

AQEG. Air quality expert group report on particulate matter in the United Kingdom. 2005.
Ref Type: Report

Arimoto,R., Duce,R.A., Ray,B.J., Ellis,W.G., Cullen,J.D., & Merrill,J.T. (1995) Trace-elements in the atmosphere over the north-Atlantic. *Journal of Geophysical Research*, **100**, 1199-1213.

Armendariz,A., Leith,D., Boundy,M., Goodman,R., Smith,L., & Carlton,G. (2003) Sampling and analysis of aircraft engine cold start particles and

demonstration of an electrostatic personal particle sampler. *AIHA Journal*, **64**, 777-784.

Bahreini,R., Jimenez,J.L., Wang,J., Flagan,R.C., Seinfeld,J.H., Jayne,J.T., & Worsnop,D.R. (2003) Aircraft-based aerosol size and composition measurements during ACE-Asia using an Aerodyne aerosol mass spectrometer. *Journal of Geophysical Research*, **108**.

Baltensperger,U., Kalberer,M., Dommen,J., Paulsen,D., Alfarra,M.R., Coe,H., Fisseha,R., Gascho,A., Gysel,M., Nyeki,S., Sax,M., Steinbacher,M., Prevot,A.S.H., Sjoren,S., Weingartner,E., & Zenobi,R. (2005) Secondary organic aerosols from anthropogenic and biogenic precursors. *Faraday Discussions*, **130**, 265-278.

Baron,P.A. & Willeke,K. (2001) Aerosol fundamentals. Aerosol measurement; Principals, techniques and applications (ed. by P. A. Baron & K. Willeke), pp. 45-61. Wiley-interscience.

Bauerle,D. (2000) *Laser processing and chemistry*, Springer-Verlag, Berlin Heidelberg 2000.

Beddows,D.C.S., Donovan,R.J., Harrison,R.M., Heal,M.R., Kinnersley,R.P., King,M.D., Nicholson,D.H., & Thompson,K.C. (2004) Correlations in the chemical composition of rural background atmospheric aerosol in the UK determined in real time using time-of-flight mass spectrometry. *Journal of Environmental Monitoring*, **6**, 124-133.

Bhave,P.V., Allen,J.O., Morrical,B.D., Fergenson,D.P., Cass,G.R., & Prather,K.A. (2002) A field-based approach for determining ATOFMS instrument sensitivities to ammonium and nitrate. *Environmental Science & Technology*, **36**, 4868-4879.

Bhave,P.V., Fergenson,D.P., Prather,K.A., & Cass,G.R. (2001) Source apportionment of fine particulate matter by clustering single-particle data: Tests of receptor model accuracy. *Environmental Science & Technology*, **35**, 2060-2072.

Blando,J.D. & Turpin,B.J. (2000) Secondary organic aerosol formation in cloud and fog droplets: a literature evaluation of plausibility. *Atmospheric Environment*, **34**, 1623-1632.

Carson,P.G., Johnston,M.V., & Wexler,A.S. (1997) Laser desorption/ionization of ultrafine aerosol particles. *Rapid Communications in Mass Spectrometry*, **11**, 993-996.

Carson,P.G., Neubauer,K.R., Johnston,M.V., & Wexler,A.S. (1995) Online chemical-analysis of aerosols by rapid single-particle mass-spectrometry. *Journal of Aerosol Science*, **26**, 535-545.

Castro,L.M., Pio,C.A., Harrison,R.M., & Smith,D.J.T. (1999) Carbonaceous aerosol in urban and rural European atmospheres: estimation of secondary organic carbon concentrations. *Atmospheric Environment*, **33**, 2771-2781.

Cavalli,F., Facchini,M.C., Decesari,S., Mircea,M., Emblico,L., Fuzzi,S., Ceburnis,D., Yoon,Y.J., O'Dowd,C.D., Putaud,J.P., & Dell'Acqua,A. (2004) Advances in characterization of size-resolved organic matter in marine aerosol over the North Atlantic. *Journal of Geophysical Research*, **109**.

Cazzola,M., Noschese,P., Centanni,S., Santus,P., Di Marco,F., Spicuzza,L., & Ugo Di Maria,G. (2004) Salmeterol/Fluticasone propionate in a single inhaler device versus theophylline + fluticasone propionate in patients with COPD. *Pulmonary Pharmacology and Therapeutics*, **17**, 141-145.

Ceburnis,D., Jennings,S.G., O'Dowd,C.D., & Aalto,P. Sub/super micron particle measurements with emphasis on physical properties of atmospheric aerosol. 2004a.
Ref Type: Personal Communication

Ceburnis,D., Jennings,S.G., O'Dowd,C.D., & Aalto,P. Sub/super micron particle measurements with emphasis on physical properties of atmospheric aerosol. 2004b.
Ref Type: Personal Communication

Chatfield,R.B. (1994) Anomalous HNO3 / NOx ratio of remote tropospheric air Conversion of nitric acid to formic acid and NOx. *Geophysical Research Letters*, **21**, 2705-2708.

Chen,L.C. & Hwang,J.S. (2005) Effects of subchronic exposures to concentrated ambient particles (CAPs) in mice: IV. Characterization of acute and chronic effects of ambient air fine particulate matter exposures on heart-rate variability. *Inhalation Toxicology*, **17**, 209-216.

Chen,L.C. & Nadziejko,C. (2005) Effects of subchronic exposures to concentrated ambient particles (CAPs) in mice: V. CAPs exacerbate aortic plaque development in hyperlipidemic mice. *Inhalation Toxicology*, **17**, 217-224.

Christie,W.H., Eby,R.E., Warmack,R.J., & Landau,L. (1981) Determination of boron and lithium in nuclear-materials by secondary ion mass-spectrometry. *Analytical Chemistry*, **53**, 13-17.

Coe,H., Allan,J.A., Alfarra,M.R., Bower,K.N., Flynn,M.J., McFiggans,G.B., Topping,D.O., Williams,P.I., O'Dowd,C.D., Dall'Osto,M., Beddows,D.C.S., & Harrison,R.M. (2005) Chemical and physical characteristics of aerosol particles at a remote coastal location, Mace Head, Ireland, during NAMBLEX. *Atmospheric Chemistry and Physics Discussions*, 11643-11678.

Cohen,M.D., Flagan,R.C., & Seinfeld,J.H. (1987) Studies of concentrated electrolyte solutions using the electrodynamic balance. 2. water activities for mixed-electrolyte Solutions. *Journal of Physical Chemistry*, **91**, 4575-4582.

COMEAP. Commitee on the medical effects of air pollutants. 1998.
Ref Type: Report

Covert,D.S., Kapustin,V.N., Quinn,P.K., & Bates,T.S. (1992) New particle formation in the marine boundary-layer. *Journal of Geophysical Research*, **97**, 20581-20589.

Cramer,L.P., Langford,S.C., Hess,W.P., & Dickinson,J.T. (2002) Wavelength dependence of UV-laser induced emission of neutral and ionic species from single crystal $NaNO^3$. *Applied Surface Science*, **197**, 35-40.

Czerwieniec,G.A., Russell,S.C., Lebrilla,C.B., Coffee,K.R., Riot,V., Steele,P.T., Frank,M., & Gard,E.E. (2005) Improved sensitivity and mass range in time-of-flight bioaerosol mass spectrometry using an electrostatic ion guide. *Journal of the American Society for Mass Spectrometry*, **16**, 1866-1875.

Dahneke,B.E. & Cheng,Y.S. (1979) Properties of continuum source particle beams .1. calculation methods and results. *Journal of Aerosol Science*, **10**, 257-274.

Dal Negro,R.W., Pomari,C., Tognella,S., & Micheletto,C. (2003) Salmeterol and Fluticasone 50μg/250μg bid in combination provides a better long-term control than salmeterol 50μg bid alone and placebo in COPD patients already treated with theophylline. *Pulmonary Pharmacology and Therapeutics*, **16**, 241-246.

Dall'Osto,M., Beddows,D.C.S., Kinnersley,R.P., Harrison,R.M., Donovan,R.J., & Heal,M.R. (2004) Characterization of individual airborne particles by using aerosol time-of-flight mass spectrometry at Mace Head, Ireland. *Journal of Geophysical Research*, **109**, D21302.

Dall'Osto,M., Harrison,R.M., Furutani,H., Prather,K.A., Coe,H., & Allan,J.D. (2005) Studies of aerosol at a coastal site using two aerosol mass spectrometry instruments and identification of biogenic particles types. *Atmospheric Chemical and Physics Discussions*, 1680-7375.

Davis,W.D. (1973) Surface ionization mass spectroscopy of airborne particulates. *Journal of Vacuum Science & Technology*, **10**, 278-&.

DeCarlo,P.F., Aiken,A., Kimmel,J., Northway,M., Trimborn,A., Gross,E., Gonin,M., Furher,K., Horvath,T., Drewnick,F., Hings,S., Jayne,J., Canagaratna,M., Onasch,T., Williams,L.R., Boudries,H., Worsnop,D.R., & Jimenex,J.L. (2005) Development of a high mass resolution time of flight aerosol mass spectrometer. p.206. European aerosol conference 2005, European aerosol conference 2005.

Derwent,R.G., Ryall,D.B., Manning,A., Simmonds,P.G., O'Doherty,S., Biraud,S., Ciais,P., Ramonet,M., & Jennings,S.G. (2002) Continuous observations of carbon dioxide at Mace Head, Ireland from 1995 to 1999 and its net European ecosystem exchange. *Atmospheric Environment*, **36**, 2799-2807.

Derwent,R.G., Simmonds,P.G., O'Doherty,S., & Ryall,D.B. (1998) The impact of the Montreal Protocol on halocarbon concentrations in northern hemisphere baseline and European air masses at Mace Head, Ireland over a ten year period from 1987-1996. *Atmospheric Environment*, **32**, 3689-3702.

Devlin,R.B., Ghio,A.J., Kehrl,H., Sanders,G., & Cascio,W. (2003) Elderly humans exposed to concentrated air pollution particles have decreased heart rate variability. *European Respiratory Journal*, **21**, 76S-80S.

Dockery,D.W., Pope,C.A., Xu,X.P., Spengler,J.D., Ware,J.H., Fay,M.E., Ferris,B.G., & Speizer,F.E. (1993) An association between air-pollution and mortality in 6 United-States cities. *New England Journal of Medicine*, **329**, 1753-1759.

Donaldson,K., Jimenez,A., Rahman,I., Faux,S., MacNee,W., Gilmour,P., Borm,P., Schins,R., Shi,T., & Stone,V. (2004) Respiratory health effects of ambient air pollution particles: Role of reactive species. *Lung Biology in Health and Disease*, **187**, 257-288.

Donaldson,K., Brown,D., Clouter,A., Duffin,R., Macnee,W., Renwick,L., Tran,L., & Stone,V. (2002) The pulmonary toxicology of ultrafine particles. *Journal of Aerosol Medicine-Deposition Clearance and Effects in the Lung*, **15**, 213-220.

Drewnick,F., Hings,S.S., Decarlo,P., Jayne,J.T., Gonin,M., Fuhrer,K., Weimer,S., Jimenez,J.L., Demerjian,K.L., Borrmann,S., & Worsnop,D.R. (2005) A new time-of-flight aerosol mass spectrometer (TOF-AMS) - Instrument description and first field deployment. *Aerosol Science and Technology*, **39**, 637-658.

Erdmann,N., Dell'Acqua,A., Cavalli,P., Gruning,C., Omenetto,N., Putaud,J.P., Raes,F., & Van Dingenen,R. (2005) Instrument characterization and first application of the single particle analysis and sizing system (SPASS) for atmospheric aerosols. *Aerosol Science and Technology*, **39**, 377-393.

Fan,X.B., Okada,K., Niimura,N., Kai,K., Arao,K., Shi,G.Y., Qin,Y., & Mitsuta,Y. (1996) Mineral particles collected in China and Japan during the same Asian dust-storm event. *Atmospheric Environment*, **30**, 347-351.

Fergenson,D.P., Song,X.H., Ramadan,Z., Allen,J.O., Hughes,L.S., Cass,G.R., Hopke,P.K., & Prather,K.A. (2001) Quantification of ATOFMS data by multivariate methods. *Analytical Chemistry*, **73**, 3535-3541.

Finlayson-Pitts,B.J. & Hemminger,J.C. (2000) Physical chemistry of airborne sea salt particles and their components. *Journal Physical Chemistry A*, **104**, 11463-11477.

Finlayson-Pitts,B.J. & Pitts,J.N. (1999a) Analytical methods and typical atmospheric concentrations for gases and particles. Chemistry of the upper and lower atmosphere; Theory, experiment and applications., pp. 548-656. Acedemic press.

Finlayson-Pitts,B.J. & Pitts,J.N. (1999b) *The chemistry of the upper and lower atmosphere; Theory, experiments and applications,* Acedemic press.

Gard,E., Mayer,J.E., Morrical,B.D., Dienes,T., Fergenson,D.P., & Prather,K.A. (1997) Real-time analysis of individual atmospheric aerosol particles: Design and performance of a portable ATOFMS. *Analytical Chemistry*, **69**, 4083-4091.

Gard,E.E., Coffee,K.R., Matthias,F., Tobias,H.J., Fergenson,D.P., Madden,N., Riot,V.J., Steele,P.T., & Woods,B.W. Real-time detection method and system for identifying individual aerosol particles. 2004-916737[2005073683]. 2005.
Ref Type: Patent

Gard,E.E., Kleeman,M.J., Gross,D.S., Hughes,L.S., Allen,J.O., Morrical,B.D., Fergenson,D.P., Dienes,T., Galli,M.E., Johnson,R.J., Cass,G.R., & Prather,K.A. (1998) Direct observation of heterogeneous chemistry in the atmosphere. *Science*, **279**, 1184-1187.

Gaudichet,A., Echalar,F., Chatenet,B., Quisefit,J.P., Malingre,G., Cachier,H., Buatmenard,P., Artaxo,P., & Maenhaut,W. (1995) Trace-Elements in tropical African savanna biomass burning aerosols. *Journal of Atmospheric Chemistry*, **22**, 19-39.

Ge,Z.Z., Wexler,A.S., & Johnston,M.V. (1998) Laser desorption/ionization of single ultrafine multicomponent aerosols. *Environmental Science & Technology*, **32**, 3218-3223.

Gieray,R.A., Reilly,P.T.A., Yang,M., Whitten,W.B., & Ramsey,J.M. (1997) Real-time detection of individual airborne bacteria. *Journal of Microbiological Methods*, **29**, 191-199.

Greenaway,R., Dalley,J., Ulanowki,J., & Kaye,P.H. (2005) Single-Particle Raman Spectrometer (SPaRS) for the non-destructive physio-chemical characterisation of aerosol particles. European Aerosol Conference 2005.

Gross,D.S., Barron,A.R., Sukovich,E.M., Warren,B.S., Jarvis,J.C., Suess,D.T., & Prather,K.A. (2005) Stability of single particle tracers for differentiating between heavy- and light-duty vehicle emissions. *Atmospheric Environment*, **39**, 2889-2901.

Gross,D.S., Galli,M.E., Silva,P.J., & Prather,K.A. (2000a) Relative sensitivity factors for alkali metal and ammonium cations in single particle aerosol time-of-flight mass spectra. *Analytical Chemistry*, **72**, 416-422.

Gross,D.S., Galli,M.E., Silva,P.J., Wood,S.H., Liu,D.Y., & Prather,K.A. (2000b) Single particle characterization of automobile and diesel truck emissions in the Caldecott Tunnel. *Aerosol Science and Technology*, **32**, 152-163.

Guazzotti,S.A., Suess,D.T., Coffee,K.R., Quinn,P.K., Bates,T.S., Wisthaler,A., Hansel,A., Ball,W.P., Dickerson,R.R., Neususs,C., Crutzen,P.J., & Prather,K.A. (2003) Characterization of carbonaceous aerosols outflow from India and Arabia: Biomass/biofuel burning and fossil fuel combustion. *Journal of Geophysical Research*, **108**.

Hallworth,G.W. (1987) The formulation and evaluation of pressurised metered-dose inhalers. Drug Delivery to the Respiratory Tract (ed. by D. Ganderton & T. M. Jones) Ellis Horwood, Chichester.

Harrison,R.M. & Pio,C. (1983) Major ion composition and chemical association of inorganic atmospheric aerosols. *Environmental science and technology*, **17**, 169-174.

Harrison,R.M. (2001) *Pollution : causes, effects and control*, 4th edn, pp. xxiv, 579. Royal Society of Chemistry, Cambridge.

Harrison,R.M., Grenfell,J.L., Yamulki,S., Clemitshaw,K.C., Penkett,S.A., Cape,J.N., & McFadyen,G.G. (1999) Budget of NOy species measured at a coastal site. *Atmospheric Environment*, **33**, 4255-4272.

Harrison,R.M. & Yin,J.X. (2000) Particulate matter in the atmosphere: which particle properties are important for its effects on health? *Science of the Total Environment*, **249**, 85-101.

Heal,M.R., Hibbs,L.R., Agius,R.M., & Beverland,I.J. (2005) Interpretation of variations in fine, coarse and black smoke particulate matter concentrations in a northern European city. *Atmospheric Environment*, **39**, 3711-3718.

Heard,D.E., Read,K.A., Al-Haider,S., Bloss,W.J., Johnson,G.P., Pilling,M.J., Rickard,A., Seakins,P.W., Smith,S.C., & Sommariva,R.A. (2005) The North Atlantic Marine Boundary Layer Experiment (NAMBLEX). Overview of the campaign held at Mace Head, Ireland, in summer 2002. *Atmospheric Chemical and Physics (Discussions)*.

Hering,S.V. & McMurry,P.H. (1991) Optical counter response to monodisperse atmospheric aerosols. *Atmospheric Environment*, **25**, 463-468.

Hinds,W.C. (1999) Atmospheric Aerosols. Aerosol Technology, pp. 304-315. Wiley-interscience publication.

Hinz,K.P., Erdmann,N., Gruning,C., & Spengler,B. (2005) Results of data analysis of aerosol particle spectra detected with two mass spectrometers LAMPAS 2 and SPASS.

Hinz,K.P., Kaufmann,R., & Spengler,B. (1994) Laser-induced mass analysis of single particles in the airborne state. *Analytical Chemistry*, **66**, 2071-2076.

Hoffman,R.C., Laskin,A., & Finlayson-Pitts,B.J. (2004) Sodium nitrate particles: physical and chemical properties during hydration and dehydration, and implications for aged sea salt aerosols. *Aerosol science*, **35**, 869-887.

Huang,S., Arimoto,R., & Rahn,K.A. (2001) Sources and source variations for aerosol at Mace Head, Ireland. *Atmospheric Environment*, **35**, 1421-1437.

IPCC. Climate Change 2001: Impacts, Adaptation and Vulnerability. 2001.
Ref Type: Report

Jacobson,M.Z. (2000) A physically-based treatment of elemental carbon optics: Implications for global direct forcing of aerosols. *Geophysical Research Letters*, **27**, 217-220.

Jayne,J.T., Leard,D.C., Zhang,X.F., Davidovits,P., Smith,K.A., Kolb,C.E., & Worsnop,D.R. (2000) Development of an aerosol mass spectrometer for size and composition analysis of submicron particles. *Aerosol Science and Technology*, **33**, 49-70.

Jennings,S.G., Geever,M., McGovern,F.M., Francis,J., Spain,T.G., & Donaghy,T. (1997) Microphysical and physico-chemical characterization of atmospheric marine and continental aerosol at Mace Head. *Atmospheric Environment*, **31**, 2795-2808.

Jennings,S.G., McGovern,F.M., & Cooke,W.F. (1993) Carbon mass concentration measurements at Mace Head, on the west-coast of Ireland. *Atmospheric Environment*, **27**, 1229-1239.

Johnston,M.V. & Wexler,A.S. (1995) On the Cover - Ms of individual aerosol-particles. *Analytical Chemistry*, **67**, A721-A726.

Kafalas,P. & Ferdinand,J.A.P. (1973) Fog droplet vaporization and fragmentation by a 10.6 μm laser pulse. *Applied Optics*, **12**, 29-33.

Kane,D.B. & Johnston,M.V. (2001) Enhancing the detection of sulfate particles for laser ablation aerosol mass spectrometry. *Analytical Chemistry*, **73**, 5365-5369.

Kane,D.B., Wang,J.J., Frost,K., & Johnston,M.V. (2002) Detection of negative ions from individual ultrafine particles. *Analytical Chemistry*, **74**, 2092-2096.

Karlsson,R., Galli,M., & Etzler,F. Identification of APIs by ATOFMS in individual particles actuated from Combivent ® MDI. 2000.

Ref Type: Personal Communication

Kaye,P.H., Barton,J.E., Hirst,E., & Clark,J.M. (2000) Simultaneous light scattering and intrinsic fluorescence measurement for the classification of airborne particles. *Applied Optics*, **39**, 3738-3745.

Kerminen,V.M., Teinila,K., Hillamo,R., & Pakkanen,T. (1998) Substitution of chloride in sea-salt particles by inorganic and organic anions. *Journal of Aerosol Science*, **29**, 929-942.

Khlystov,A., Zhang,Q., Jimenez,J.L., Stanier,C., Pandis,S.N., Canagaratna,M.R., Fine,P., Misra,C., & Sioutas,C. (2005) In situ concentration of semi-volatile aerosol using water-condensation technology. *Journal of Aerosol Science*, **36**, 866-880.

Kim,S., Jaques,P.A., Chang,M.C., Barone,T., Xiong,C., Friedlander,S.K., & Sioutas,C. (2001a) Versatile aerosol concentration enrichment system (VACES) for simultaneous in vivo and in vitro evaluation of toxic effects of ultrafine, fine and coarse ambient particles - Part II: Field evaluation. *Journal of Aerosol Science*, **32**, 1299-1314.

Kim,S., Jaques,P.A., Chang,M.C., Froines,J.R., & Sioutas,C. (2001b) Versatile aerosol concentration enrichment system (VACES) for simultaneous in vivo and in vitro evaluation of toxic effects of ultrafine, fine and coarse ambient particles - Part I: Development and laboratory characterization. *Journal of Aerosol Science*, **32**, 1281-1297.

Knochenmuss,R. & Zenobi,R. (2003) MALDI ionization: The role of in-plume processes. *Chemical Reviews*, **103**, 441-452.

Kruger,R. & Karas,M. (2003) Ion formation in MALDI: The cluster ionisation mechanism. *Chemical reviews*, **103**, 427-439.

Kulmala,M., Vehkamaki,H., Petajda,T., Dal Maso,M., Lauri,A., Kerminen,V.M., Birmili,W., & Mcmurry,P.H. (2004) Formation and growth rates of ultrafine atmospheric particles: a review of observations. *Journal of Aerosol Science*, **35**, 143-176.

Kurten,A., Curtius,J., & Borrman,S. (2005) Development and characterization of a novel ion trap mass spectrometer for atmospheric aerosol particles. p.207. European Aerosol Conference 2005.

Lake,D.A., Tolocka,M.P., Johnston,M.V., & Wexler,A.S. (2004) The Character of single particle sulfate in Baltimore. *Atmospheric Environment*, **38**, 5311-5320.

Langer,S., Pemberton,R.S., & FinlaysonPitts,B.J. (1997) Diffuse reflectance infrared studies of the reaction of synthetic sea salt mixtures with NO2: A key role for hydrates in the kinetics and mechanism. *Journal of Physical Chemistry A*, **101**, 1277-1286.

Laskin,A., Gaspar,D.J., Iedema,M.J., & Cowin,J.P. (2003) Exploring single-particle heterogeneous chemistry of aerosols using SEM, CCSEM, ESEM and TOF-SIMS analytical techniques. pp. 565-569. Combustion and atmospheric pollution St.Petersburg, Russian Federation.

Lawrence,J., Wolfson,J.M., Ferguson,S., Koutrakis,P., & Godleski,J. (2004) Performance stability of the Harvard ambient particle concentrator. *Aerosol Science and Technology*, **38**, 219-227.

Lee,S.H., Murphy,D.M., Thomson,D.S., & Middlebrook,A.M. (2002) Chemical components of single particles measured with Particle Analysis by Laser Mass Spectrometry (PALMS) during the Atlanta SuperSite Project: Focus on organic/sulfate, lead, soot, and mineral particles. *Journal of Geophysical Research-Atmospheres*, **107**.

Lee,S.H., Murphy,D.M., Thomson,D.S., & Middlebrook,A.M. (2003) Nitrate and oxidized organic ions in single particle mass spectra during the 1999 Atlanta Supersite Project. *Journal of Geophysical Research-Atmospheres*, **108**.

Leung,C., Hanson,I., Xirouchaki,C., Palmer,R.E., & Harrison,R.M. (2005) A novel instrument to measure molecular clusters and newly nucleated particles in the atmosphere. p.305. European Aerosol Conference 2005.

Liu,D.Y., Wenzel,R.J., & Prather,K.A. (2003) Aerosol time-of-flight mass spectrometry during the Atlanta Supersite Experiment: 1. Measurements. *Journal of Geophysical Research*, **108**, 8426.

Liu,D.Y., Prather,K.A., & Hering,S.V. (2000) Variations in the size and chemical composition of nitrate- containing particles in Riverside, CA. *Aerosol Science and Technology*, **33**, 71-86.

Liu,P., Ziemann,P.J., Kittelson,D.B., & Mcmurry,P.H. (1995a) Generating particle beams of controlled dimensions and divergence .1. Theory of particle motion in aerodynamic lenses and nozzle expansions. *Aerosol Science and Technology*, **22**, 293-313.

Liu,P., Ziemann,P.J., Kittelson,D.B., & Mcmurry,P.H. (1995b) Generating particle beams of controlled dimensions and divergence .2. Experimental evaluation of particle motion in aerodynamic lenses and nozzle expansions. *Aerosol Science and Technology*, **22**, 314-324.

Longley,I.D., Gallagher,M.W., Dorsey,J.R., Flynn,M., Allan,J.D., Alfarra,M.R., & Inglis,D. (2003) A case study of aerosol (4.6 nm < D-p < 10 mu m) number and mass size distribution measurements in a busy street canyon in Manchester, UK. *Atmospheric Environment*, **37**, 1563-1571.

Lyseng-Williamson,K.A. & Plosker,G.L. (2003) Inhaled salmeterol/fluticasone propionate combination; A pharmacoeconomic review of its use in the

management of asthma. *ADIS pharmacoeconomic drug evaluation*, **13**, 951-989.

Mallina,R.V., Wexler,A.S., & Johnston,M.V. (1997) Particle growth in high-speed particle beam inlets. *Journal of Aerosol Science*, **28**, 223-238.

Mallina,R.V., Wexler,A.S., Rhoads,K.P., & Johnston,M.V. (2000) High speed particle beam generation: A dynamic focusing mechanism for selecting ultrafine particles. *Aerosol Science and Technology*, **33**, 87-104.

Mansoori,B.A., Johnston,M.V., & Wexler,A.S. (1994) Quantitation of ionic species in single microdroplets by online laser desorption/ionization. *Analytical Chemistry*, **66**, 3681-3687.

Marple,V.A., Rubow,K.L., & Behm,S.M. (1991) A Microorifice Uniform Deposit Impactor (Moudi) - Description, Calibration, and Use. *Aerosol Science and Technology*, **14**, 434-446.

McFiggans,G., Coe,H., Burgess,R., Allan,J., Cubison,M., Alfarra,M.R., Saunders,R., Saiz-Lopez,A., Plane,J.M.C., Wevill,D.J., Carpenter,L.J., Rickard,A.R., & Monks,P.S. (2004) Direct evidence for coastal iodine particles from Laminaria macroalgae - linkage to emissions of molecular iodine. *Atmospheric Chemistry and Physics*, **4**, 701-713.

Mckeown,P.J., Johnston,M.V., & Murphy,D.M. (1991) Online single-particle analysis by laser desorption mass-spectrometry. *Analytical Chemistry*, **63**, 2069-2073.

McKetta,J.J. (1997) *Encyclopedia of chemical processing and design*, Marcel Dekker.

McMurry,P.H. (2000) A review of atmospheric aerosol measurements. *Atmospheric Environment*, **34**, 1959-1999.

Mendes,M. (2002) UV Excimer laser micromachining, laser ablation and surface micro texturing / roughening. PhD.

Michael,Y., Chowdhry,B.Z., Ashurst,I.C., Snowden,M.J., Davis-Cutting,C., & Gray,S. (2000) The physico-chemical properties of salmeterol and fluticasone propionate in different solvent environments. *International Journal of Pharmaceutics*, **200**, 279-288.

Michael,Y., Snowden,M.J., Chowdhry,B.Z., Ashurst,I.C., Davis-Cutting,C.J., & Riley,T. (2001) Characterisation of the aggregation behaviour in a salmeterol and fluticasone propionate inhalation aerosol system. *International Journal of Pharmaceutics*, **221**, 165-174.

Mills,N.L., Robinson,S.D., Anderson D, Freney,E.J., Boon N.A, MacNee,W., Donovan,R.J., Cassee,F.R., Newby,D.E., & Donaldson,K. (2005a) Exposure to concentrated ambient particles does not affect endothelial vasomotor

function in patients with ischaemic heart disease (abstract). Proceedings of the American Thoracic Society 2005.

Mills,N.L., Tornqvist,H., Robinson,S.D., Darnley,K., Gonzales,M., Boon,N.A., MacNee,W., Donaldson,K., Blomberg,A., Sandstrom,T., & Newby,D.E. (2005b) Diesel exhaust inhalation causes vascular dysfunction and impaired endogenous fibrinolysis: An explanation for the increased cardiovascular mortality associated with air pollution. *Journal of the American College of Cardiology*, **45**, 390A.

Mitchell,J.P. & Nagel,M.W. (1996) An assessment of the API Aerososizer® for the real-time measurement of medical inhalers from pressurized metered-dose inhaler (pMDI) systems. *Aerosol Science and Technology*, **25**, 411-423.

Moffet,R.C. & Prather,K.A. (2005) Simultaneous measurements of optical properties, size and chemical composition on single aerosol particles. *Analytical Chemistry*, **77**, 6535-6541.

Moffet,R.C., Shields,L.G., Berntsen,J., Devlin,R.B., & Prather,K.A. (2004) Characterization of an ambient coarse particle concentrator used for human exposure studies: aerosol size distributions, chemical Composition and Concentration Enrichment. *Aerosol Science and Technology*, **38**, 1123-1137.

Moren,F. (1993) Aerosol dosage forms and formulations. Aerosols in Medicine: Principles, Diagnosis and Therapy (ed. by F. Moren, M. B. Dolovich, M. T. Newhouse, & S. P. Newman) Elsevier, Amsterdam.

Morrical,B.D. (1999) Ph.D. Dissertation., University of California.

Morrical,B.D., Fergenson,D.P., & Prather,K.A. (1998) Coupling two-step laser desorption/ionization with aerosol time-of-flight mass spectrometry for the analysis of individual organic particles. *Journal of the American Society for Mass Spectrometry*, **9**, 1068-1073.

Murphy,D.M. & Thomson,D.S. (1995) Laser ionization mass-spectroscopy of single aerosol-particles. *Aerosol Science and Technology*, **22**, 237-249.

Nash,D.G., Liu,X.F., Mysak,E.R., & Baer,T. (2005) Aerosol particle mass spectrometry with low photon energy laser ionization. *International Journal of Mass Spectrometry*, **241**, 89-97.

Nelson,H.S., Chapman,K.R., Pyke,S.D., Johnson,M., & Pritchard,J.N. (2003) Enhanced synergy between fluticasone propionate and salmeterol inhaled from a single inhaler versus separate inhalers. *Journal of Allergy Clinical Immunology*, **112**, 29-36.

Nemmar,A., Hoet,P.H.M., Vanquickenborne,B., Dinsdale,D., Thomeer,M., Hoylaerts,M.F., Vanbilloen,H., Mortelmans,L., & Nemery,B. (2002) Passage of inhaled particles into the blood circulation in humans. *Circulation*, **105**, 411-414.

Neubauer,K.R., Johnston,M.V., & Wexler,A.S. (1997) On-line analysis of aqueous aerosols by laser desorption ionization. *International Journal of Mass Spectrometry and Ion Processes*, **163**, 29-37.

Newman,S.P. (1984) Terapeutic aerosols. Aerosols and the lung: Clinical and Experimental Aspects (ed. by S. W. Clarke & D. Pavia) Butterworths, London.

NIST. NIST Chemistry Webbook. http://webbook.nist.gov/chemistry . 2005.
Ref Type: Electronic Citation

Noble,C.A. & Prather,K.A. (1998) Single particle characterization of albuterol metered dose inhaler aerosol in near real-time. *Aerosol Science and Technology*, **29**, 294-306.

Nordmeyer,T. & Prather,K.A. (1994) Real-time measurement capabilities using aerosol time-of-flight mass-spectrometry. *Analytical Chemistry*, **66**, 3540-3542.

Northway,M., Trimborn,A., Jayne,J., Onasch,T., Canagaratna,M., Worsnop,D.R., Toohey,D., & Jimenez,J. (2005) Development of soft ionization methods for the speciation of organic compounds in aerosol mass spectrometry. European Aerosol Conference 2005.

Norton,E.G., Vaughan,G., Methven,J., Coe,H., Brooks,B., Gallagher,M., & Longley,I. (2005) Boundary layer structure adn decoupling from synoptic scale flow during NAMBLEX. *Atmospheric Chemical Physics Discussions*, **5**, 3223.

Norwood,D.L., Prime,D., Downey,B.P., Creasey,J., Sethi,S.K., & Haywood,P. (1995) Analysis of polycyclic aromatic hydrocarbons in metered dose inhaler drug formulations by isotope dilution gas Chromatrography Mass Spectrometry. *Journal of Pharmaceutical Biomedical Analysis*, **13**, 293-304.

O'Dowd,C.D. (2002) On the spatial extent and evolution of coastal aerosol plumes. *Journal of Geophysical Research*, **107**.

O'Dowd,C.D., Facchini,M.C., Cavalli,F., Ceburnis,D., Mircea,M., Decesari,S., Fuzzi,S., Yoon,Y.J., & Putaud,J.P. (2004) Biogenically driven organic contribution to marine aerosol. *Nature*, **431**, 676-680.

Oberdorster,G., Sharp,Z., Atudorei,V., Elder,A., Gelein,R., Kreyling,W., & Cox,C. (2004) Translocation of inhaled ultrafine particles to the brain. *Inhal.Toxicol.*, **16**, 437-445.

O'Dowd,C.D., Smith,M.H., Consterdine,I.E., & Lowe,J.A. (1997) Marine aerosol, sea-salt, and the marine sulphur cycle: A short review. *Atmospheric Environment*, **31**, 73-80.

O'Dowd,C.D., Smith,M.H., & Jennings,S.G. (1993) Submicron particle, radon, and soot carbon characteristics over the northeast atlantic. *Journal of Geophysical Research*, **98**, 1123-1135.

Okada,K., Qin,Y., & Kai,K. (2005) Elemental composition and mixing properties of atmospheric mineral particles collected in Hohhot, China. *Atmospheric Research*, **73**, 45-67.

Pakkanen,T.A. (1996) Study of formation of coarse particle nitrate aerosol. *Atmospheric Environment*, **30**, 2475-2482.

Pandis,S.N., Harley,R.A., Cass,G.R., & Seinfeld,J.H. (1992) Secondary organic aerosol formation and transport. *Atmospheric Environment*, **26**, 2269-2282.

Pedraza,A.J. (1998) Interaction of UV laser light with wide band gap materials, mechanisms and effects. *Nuclear Instruments and Methods in Physics Research B*, **141**, 709-718.

Penner,J.E., Hegg,D., & Leaitch,R. (2001) Unraveling the role of aerosols in climate change. *Environmental Science & Technology*, **35**, 332A-340A.

Pope,A.C. (1999) Epidemiology of Particle Effects. (ed. by J. T. Holgate, S. M. Samet, H. S. Koren, & R. L. Maryland) Acedemic Press, London.

Prescott,G.J., Cohen,G.R., Elton,R.A., Fowkes,G.R., & Agius,R.M. (1998) Urban air pollution and cardiopulmonary ill health: a 14.5 year time series study. *Occupational Environmental Medicine*, **55**, 697-5704.

Quinn,P.K. & Bates,T.S. (2005) Regional aerosol properties: Comparisons of boundary layer measurements from ACE 1, ACE 2, aerosols99, INDOEX, ACE asia, TARFOX, and NEAQS. *Journal of Geophysical Research*, **110**.

Raes,F., Van Dingenen,R., Vignati,E., Wilson,J., Putaud,J.P., Seinfeld,J.H., & Adams,P. (2000) Formation and cycling of aerosols in the global troposphere. *Atmospheric Environment*, **34**, 4215-4240.

Reents,W.D., Downey,S.W., Emerson,A.B., Mujsce,A.M., Muller,A.J., Siconolfi,D.J., Sinclair,J.D., & Swanson,A.G. (1995) Single-particle characterization by time-of-flight mass-spectrometry. *Aerosol Science and Technology*, **23**, 263-270.

Reilly,P.T.A., Lazar,A.C., Gieray,R.A., Whitten,W.B., & Ramsey,J.M. (2000) The elucidation of charge-transfer-induced matrix effects in environmental aerosols via real-time aerosol mass spectral analysis of individual airborne particles. *Aerosol Science and Technology*, **33**, 135-152.

Ruellan,S., Cachier,H., Gaudichet,A., Masclet,P., & Lacaux,J.P. (1999a) Airborne aerosols over central Africa during the experiment for regional sources and sinks of oxidants (EXPRESSO). *Journal of Geophysical Research*, **104**, 30673-30690.

Ruellan,S., Cachier,H., Gaudichet,A., Masclet,P., & Lacaux,J.P. (1999b) Airborne aerosols over central Africa during the experiment for regional sources and sinks of oxidants (EXPRESSO). *J.Geophys.Res.*, **104**, 30673-30690.

Ryall,D.B. & Maryon,R.H. (1998) Validation of the UK Met. Office's name model against the ETEX dataset. *Atmospheric Environment*, **32**, 4265-4276.

Salt,K., Noble,C.A., & Prather,K.A. (1996) Aerodynamic particle sizing versus light scattering intensity measurement as methods for real time particle sizing coupled with time-of-flight mass spectrometry. *Analytical Chemistry*, **68**, 230-234.

Schofield,M.J. (2003) Sources and properties of airborne particulate matter., School of Geography, Earth and Environmental Sciences, Univeristy of Birmingham.

Schoolcraft,T.A., Constable,G.S., Jackson,B., Zhigilei,L.V., & Garrison,B.J. (2001) Molecular dynamics simulations of laser disintegration of amorphous aerosol particles with spatially nonuniform absorption. *Nuclear instruments and methods in physical research, Section B: Beam interactions with Materials and Atoms*, **180**, 245-250.

Schoolcraft,T.A., Constable,G.S., Zhigilei,L.V., & Garrison,B.J. (2000) Molecular dynamic simulation of the laser disintegration of aerosol particles. *Analytical Chemistry*, **72**, 5143-5150.

Schwartz,S.E. (1988) Mass-transport limitation to the rate of in-cloud oxidation of SO2 - Re-examination in the light of new data. *Atmospheric Environment*, **22**, 2491-2499.

Seaton,A., Macnee,W., Donaldson,K., & Godden,D. (1995) Particulate air-pollution and acute health-effects. *Lancet*, **345**, 176-178.

Silva,P.J., Carlin,R.A., & Prather,K.A. (2000) Single particle analysis of suspended soil dust from Southern California. *Atmospheric Environment*, **34**, 1811-1820.

Silva,P.J., Liu,D.Y., Noble,C.A., & Prather,K.A. (1999) Size and chemical characterization of individual particles resulting from biomass burning of local Southern California species. *Environmental Science & Technology*, **33**, 3068-3076.

Silva,P.J. & Prather,K.A. (2000) Interpretation of mass spectra from organic compounds in aerosol time-of-flight mass spectrometry. *Analytical Chemistry*, **72**, 3553-3562.

Simmonds,P.G., Derwent,R.G., Manning,A.L., & Spain,G. (2004) Significant growth in surface ozone at Mace Head, Ireland, 1987-2003. *Atmospheric Environment*, **38**, 4769-4778.

Simmonds,P.G., Manning,A.J., Derwent,R.G., Ciais,P., Ramonet,M., Kazan,V., & Ryall,D. (2005) A burning question. Can recent growth rate anomalies in the greenhouse gases be attributed to large-scale biomass burning events? *Atmospheric Environment*, **39**, 2513-2517.

Sinha,M.P. (1984) Laser-induced volatilization and ionization of microparticles. *Review of Scientific Instruments*, **55**, 886-891.

Sioutas,C., Koutrakis,P., Ferguson,S.T., & Burton,R.M. (1995) Development and evaluation of a prototype ambient particle concentrator for inhalation exposure studies. *Inhalation Toxicology*, **7**, 633-644.

Sioutas,C., Petros,K., Godleski,J.J., Ferguson,S.T., Chong,K., & Burton,R.M. (1997) Fine particle concentrators for inhalation exposures - effect of particle size and composition. *Journal of Aerosol Science*, **28**, 1057-1071.

Smith,J.N., Moore,K.F., Mcmurry,P.H., & Eisele,F.L. (2004) Atmospheric measurements of sub-20 nm diameter particle chemical composition by thermal desorption chemical ionization mass spectrometry. *Aerosol Science and Technology*, **38**, 100-110.

Sodeman,D.A., Toner,S.M., & Prather,K.A. (2005) Determination of single particle mass spectral signatures from light-duty vehicle emissions. *Environmental Science & Technology*, **39**, 4569-4580.

Song,X.H., Hopke,P.K., Fergenson,D.P., & Prather,K.A. (1999) Classification of single particles analyzed by ATOFMS using an artificial neural network, ART-2A. *Analytical Chemistry*, **71**, 860-865.

Steele,P.T., Srivastava,A., Pitesky,M.E., Fergenson,D.P., Tobias,H.J., Gard,E.E., & Frank,M. (2005) Desorption/ionisation fluence thresholds and improved mass spectral consistency measured using a flattop laser profile in the mass spectrometry of single bacillus endospores. *Analytical Chemistry*, **77**, 7448-7454.

Stein,S.W., Gabrio,B.J., Oberreit,D., Hairston,P., Myrdal,P.B., & Beck,T.J. (2002) An evaluation of mass-weighted size distribution measurements with the Model 3320 aerodynamic particle sizer. *Aerosol Sci.Tech.*, **36**, 845-854.

Su,Y., Sipin M.F, Furutani,H., & Prather,K.A. (2004) Development and characterization of an aerosol time-of-flight mass spectrometer with increased detection efficiency. *Analytical Chemistry*, **76**, 712-719.

Suess,D.T. & Prather,K.A. (1999) Mass spectrometry of aerosols. *Chemical reviews*, **99**, 3007-+.

Sullivan,R.C., Guazzotti,S., & Prather,K.A. (2005) Kinetics of the simultaneous uptake of nitric acid on mineral dust and sea salt aerosols measured by ATOFMS. *Abstracts of Papers of the American Chemical Society*, **229**, U127.

Sullivan,R.C. & Prather,K.A. (2005) Recent advances in our understanding of atmospheric chemistry and climate made possible by on-line aerosol analysis instrumentation. *Analytical Chemistry*, **77**, 3861-3885.

Szymonski,M., Kolodziej,J., Such,B., Pisykowski,P., Struski,P., Czuba,P., & Krok,F. (2001) Nano-scale modification of ionic surfaces induced by electronic transitions. *Progress in Surface Science*, **67**, 123-138.

Tobias,H.J., Kooiman,P.M., Docherty,K.S., & Ziemann,P.J. (2000) Real-time chemical analysis of organic aerosols using a thermal desorption particle beam mass spectrometer. *Aerosol Science and Technology*, **33**, 170-190.

Tolocka,M.P., Lake,D.A., Johnston,M.V., & Wexler,A.S. (2004) Ultrafine nitrate particle events in Baltimore observed by real-time single particle mass spectrometry. *Atmospheric Environment*, **38**, 3215-3223.

Topping,D., Coe,H., McFiggans,G., Burgess,R., Allan,J., Alfarra,M.R., Bower,K., Choularton,T.W., Decesari,S., & Facchini,M.C. (2004) Aerosol chemical characteristics from sampling conducted on the Island of Jeju, Korea during ACE Asia. *Atmospheric Environment*, **38**, 2111-2123.

Twomey,S. (1991) Aerosols, Clouds and Radiation. *Atmospheric Environment*, **25**, 2435-2442.

Twomey,S.A., Piepgrass,M., & Wolfe,T.L. (1984) An assessment of the impact of pollution on global cloud albedo. *Tellus Series B-Chemical and Physical Meteorology*, **36**, 356-366.

Van Dingenen,R., Raes,F., & Jensen,N.R. (1995) Evidence for anthropogenic impact on number concentration and sulfate content of cloud-processed aerosol-particles over the north-Atlantic. *Journal of Geophysical Research*, **100**, 21057-21067.

Van Neste,A., Duce,R.A., & Lee,C. (1987) Methylamines in the Marine Atmosphere. *Geophysical Research Letters*, **14**, 711-714.

van Wuijckhuijse,A.L., Stowers,M.A., Kleefsman,W.A., van Baar,B.L.M., Kientz,C.E., & Marijnissen,J.C.M. (2005) Matrix-assisted laser desorption/ionisation aerosol time-of-flight mass spectrometry for the analysis of bioaerosols: development of a fast detector for airborne biological pathogens. *Journal of Aerosol Science*, **36**, 677-687.

Von-Issendorff,B. & Palmer,R.E. (1999) A new high transmission infinite range mass selector for cluster and nanoparticle beams. *Review of Scientific Instruments*, **70**, 4497-4501.

Wayne,R.P. (2000) Evolution and change in atmospheres and climate. Chemistry of Atmospheres, pp. 651-737.

Wellenius,G.A., Coull,B.A., Godleski,J.J., Koutrakis,P., Okabe,K., Savage,S.T., Lawrence,J.E., Murthy,K.G.G., & Verrier,R.L. (2003) Inhalation of concentrated ambient air particles exacerbates myocardial ischemia in conscious dogs. *Environmental Health Perspectives*, **111**, 402-408.

Wenzel,R.J., Liu,D.Y., Edgerton,E.S., & Prather,K.A. (2003) Aerosol time-of-flight mass spectrometry during the Atlanta Supersite Experiment: 2. Scaling procedures. *Journal of Geophysical Research*, **108**, 8427.

Wenzel,R.J. & Prather,K.A. (2004) Improvements in ion signal reproducibility obtained using a homogeneous laser beam for on-line laser desorption/ionization of single particles. *Rapid Communications in Mass Spectrometry*, **18**, 1525-1533.

Wexler,A.S. & Seinfeld,J.H. (1990) The distribution of ammonium-salts among a size and composition dispersed aerosol. *Atmospheric Environment*, **24**, 1231-1246.

Whiteaker,J.R. & Prather,K.A. (2003) Hydroxymethanesulfonate as a tracer for fog processing of individual aerosol particles. *Atmospheric Environment*, **37**, 1033-1043.

WHO. Health aspects of air pollution with particulate matter, ozone and nitrogen dioxide. Report on a WHO working group. EUR/03/5042688, 1-98. 2003. World Health Organisation.
Ref Type: Report

Wittmaack,K. (1995) Small-area depth profiling in a quadrupole based SIMS instrument. *International Journal of Mass Spectrometry and Ion Processes*, **143**, 19-27.

Woods,E., Smith,G.D., Dessiaterik,Y., Baer,T., & Miller,R.E. (2001) Quantitative detection of aromatic compounds in single aerosol particle mass spectrometry. *Analytical Chemistry*, **73**, 2317-2322.

Yang,M., Reilly,P.T.A., Boraas,K.B., Whitten,W.B., & Ramsey,J.M. (1996) Real-time chemical analysis of aerosol particles using an ion trap mass spectrometer. *Rapid Communications in Mass Spectrometry*, **10**, 347-351.

Yeatman,S.G., Spokes,L.J., & Jickells,T.D. (2001) Comparisons of coarse-mode aerosol nitrate and ammonium at two polluted coastal sites. *Atmospheric Environment*, **35**, 1321-1335.

Zelenyuk,A. & Imre,D. (2005) Single particle laser ablation time-of-flight mass spectrometer: An introduction to SPLAT. *Aerosol Science and Technology*, **39**, 554-568.

Zhao,Y.J., Bein,K.J., Wexler,A.S., Misra,C., Fine,P.M., & Sioutas,C. (2005) Field evaluation of the versatile aerosol concentration enrichment system (VACES)

particle concentrator coupled to the rapid single-particle mass spectrometer (RSMS-3). *Journal of Geophysical Research*, **110**, D07S02.

Zhigilei,L.V. & Garrison,B.J. (1998) Computer simulation study of damage and ablation of submicron particles from short-pulse laser irradiation. *Applied Surface Science*, **127-129**, 142-150.

Zhuang,H., Chan,C.K., Fang,M., & Wexler,A.S. (1999) Size distributions of particulate sulfate, nitrate, and ammonium at a coastal site in Hong Kong. *Atmospheric Environment*, **33**, 843-853.

Appendix

Appendix 1

A1.1 Summary of analysis carried out on Tubuhaler ®

Observed *m/z*	Number of particles containing this peak	Average intensity of this peak in spectra
Positive ions		
14	77	46.1
15	73	40.8
17	112	68.6
18	118	55.0
23	12	176.4
25 to 30	207	112.9
36 to 44	228	120.3
50 to 55	212	109.9
56	181	177.4
57	160	78.2
62 to 67	188	69.2
74 to 80	197	82.1
90 to 92	188	81.2
103 to 105	104	33.7
114 to 117	112	34.1
119	55	51.4
120	92	74.8
121	185	195.7
127 to 131	21	61.3
134 to 135	151	75.5
145 to 147	46	111.7
149-150	159	122.1
> 290	119	57.4

Table A1.1. A full list of all the positive ions resulting from the formoterol mixture

Observed *m/z*	Number of particles containing this peak	Average intensity of this peak in spectra
Negative ions		
(-344 to -320)	72	40.7
(-319 to -310)	84	51.1
-309	9	61.6
-308	9	58.3
-307	8	64.6
-306	1	22.0
-224	4	42.5
(162 to -165)	151	78.8
(-148 to -150)	152	68.8
-144	14	60.3
(-132 to -137)	221	83.6
(-113 to -117)	238	137.7
-106	99.5	34.1
(-98 to -94)	90	50.8
-90	102	42.2
(-73 to -68)	232	98.7
-64	123	46.8
-61	71	33.7
-60	67	39.5
-50	101	112.5
-48	139	86.1
(-39 to -45)	207	67.0
(-25 to -27)	230	263.9
-24	73.5	60.5
-17	206	122.7
-16	47	61.2

Table A1.2. A full list of all the negative ions resulting from the negative ion mass spectra from the formoterol fumarate sample

Observed *m/z*	Number of particles containing this peak	Average intensity of this peak in spectra
Positive ions		
14	68	34.2
15	17	32.3
17	10	43.9
18	21	28.0
23	12	154.5
25 to 30	298	72.9
36 to 44	325	82.8
50 to 55	300	85.3
56	40	49.1
57	30	37.5
62 to 67	265	66.1
74 to 80	277	63.6
90 to 92	263	79.0
103 to 105	251	54.4
114 to 117	249	66.9
119	196	56.0
120	69	52.3
121	175	102.3
127 to 131	259	54.0
134 to 135	91	36.8
142 to 147	220	45.9
170 to 172	51	30.3
221	26	34.8

Table A1.3. A full list of all *m/z* values and intensities for the positive ions from the budesonide sample

Observed *m/z*	Number of particles containing this peak	Average intensity of this peak in spectra
Negative ions		
(-353 to -358)	69	39.1
(-349 to -346)	21	45.4
-153	75	34.3
(-148 to -150)	12	33.6
-144	173	45.9
(-132 to -137)	206	32.5
(-113 to -117)	104	31.1
-106	148	39.0
-104	12	25.5
(-98 to -94)	246	43.0
-97	56	32.4
-90	21	24.3
-86	218.5	49.5
(-83 to -82)	214	54.4
-79	84	34.9
(-73 to -68)	239	54.0
-64	114	41.0
-61	109	44.9
-60	108	54.4
-50	53	38.6
-48	128	99.1
(-39 to -45)	297	119.1
(-25 to -27)	203	92.1
-24	107	82.0
-17	149	55.8
-16	9	147.0

Table A1.4. A full list of all *m/z* values and intensities for the negative ions from the budesonide sample

Observed *m/z*	Number of particles containing this peak	Average intensity of this peak in spectra
Positive ions		
23	16	188.9
25 to 30	7	142.0
36 to 44	122	119.2
50 to 55	20	99.8
56	10	238.9
57	4	169.3
62 to 67	2	170.5
74 to 80	6	169.3
103 to 105	21	110.7
117	19	143.2
119	22	162.0
120	9	174.3
Observed *m/z*	**Number of particles containing this peak**	**Average intensity of this peak in spectra**
Negative ions		
-115	1	85.0
-104	11	84.1
-90	8	138.0
-79	2	335.5
-71	3	176.0
-64	17	87.8
-61	15	84.5
-50	1	73.0
-48	2	123.0
(-39 to -45)	69	143.1
(-27 to -25)	237	66.0
-17	7	109.4
-16	5	89.4

Table A1.5. A full list of all the positive and negative ions resulting from the Lactose sample

Observed *m/z* value	Budesonide	Formoterol	Lactose
Positive ions			
12	1	1	
14	68	77	
15	17	73	
17	10	112	
18	21	118	
23	12	12	16
25 to 30	298	207	7
36 to 44	325	228	122
50 to 55	300	212	20
56	40	181	10
57	30	160	4
62 to 67	265	188	2
74 to 80	277	197	6
91 to 92	263	188	1
103 to 105	251	104	21
114 to 117	249	112	19
119	196	55	22
120	69	92	9
121	175	185	2
127 to 131	259	21	
134 to 135	91	151	
138			1
142 to 147	220	46	
149-150		159	
170 to 172	51		
221	26	1	
265	2		
> 290		119	

Table A1.6. A full list of all the positive ion signals used to examine the overlap occurring between the APIs present in the Turbuhaler® mixture

Observed *m/z* value	Budesonide	Formoterol	Lactose
Negative ions			
(-353 to -358)	69		
(-349 to -346)	21		
(-344 to -320)	1	72	
(-319 to -310)		84	
-309		9	
-308	1	9	
-307		8	
-306		1	
-224		4	
(-162 to -165)	4	151	
-153	75		
(-148 to -150)	12	152	
-144	173	14	
(-132 to -137)	206	221	
(-113 to -117)	104	238	1
-106	148	99	
-104	12	6	11
(-98 to -94)	246	90	
-90	21	102	8
-86	218.5	4	
(-83 to -82)	214	7	
-79	84	6	2
(-73 to -68)	239	232	
-71			3
-64	114	123	17
-61	109.5	71	15
-60	108	67	
-50	53	101	1
-48	128.5	139	2
(-39 to -45)	297	207	69
(-25 to -27)	203	230	23
-24	107	73	
-17	149	206	7
-16	9	47	5

Table A1.7. A full list of all the positive ion signals used to examine the overlap occurring between the APIs present in the Turbuhaler® mixture

A1.2 Summary of Seretide analysis

Positive ion mass spectra		
Observed *m/z*	**Number of particles containing this peak**	**Average intensity of this peak in the mass spectra**
27 to 30	155	121.4
36 to 45	175	109.7
49 to 58	165	103.7
62 to 65	138	82.3
76 to 80	146	96.7
90 to 92	147	65.1
119 to 122	171	121.2
132 to 135	148	63.1
147 to 150	152	102.6
280*	48(*parent ion* – *C0* + $2H_20$)	52.0
298*	45(*parent ion* – *C0*)	56.1
326*	75 (*parent ion* – H_20)	51.3
344*	97 (*parent ion*)	88.5
Negative ion mass spectra		
Observed *m/z*	**Number of particles containing this peak**	**Average intensity of this peak in the mass spectra**
-328 to -340	61	43.3
-305 to -317	77	50.5
-164 to -157	158	83.7
-143 to -149	156	59.2
-130 to -137	175	91.8
-111 to -116	186	116.8
-89 to -91)	148	69.5
-69 to -73	176	111.1
-47 to -50	140	85.8
-39 to -44	158	67.8
-24 to -29	178	168.8
-16 to -17	172	115.1

Table A1.8. The most common positive and negative ions present in the formoterol fumarate mass spectra sampled using optimum laser energy. The peak thresholds used were as in Table 3.1. * Ion signals present in this range are subject to *m/z* shifting and the signals are often seen at other *m/z* values.

A1.3 Summary of Analysis carried out with throat cast and MDI inhaler

Size	Co-association	FP	SX	total particles	FP only	SX only
0.5-1	0	6	5	12	6	5
1-1.5	29	56	121	149	27	92
1.5-2	63	77	151	167	14	88
2-2.5	68	78	131	141	10	63
2.5-3	24	30	46	52	6	22
3-3.5	10	12	16	18	2	6
3.5-4	5	5	12	13	0	7
4-4.5	2	2	2	2	0	0
4.5-5	0	1		1	1	0

Table A1. 9. Raw data from Seretide Diskus sampled using throat cast.

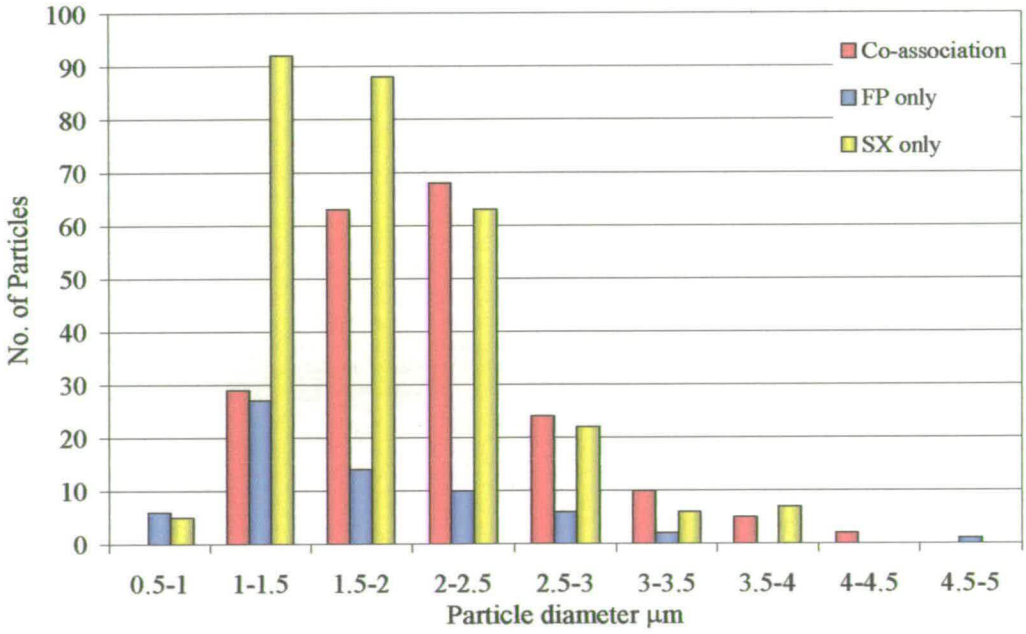

Figure A1.1. Graph of co-association present in the Seretide Diskus using a throat cast.

Size	Co-association	FP	SX	Total particles	FP only	SX only
0.5-1	5	20	7	28	15	2
1-1.5	54	103	76	146	49	22
1.5-2	47	64	66	96	17	19
2-2.5	12	15	16	24	3	4
2.5-3	4	4	5	5	0	1
3-4	0	1		1	1	0

Table A1.10. Raw data from Seretide MDI sampled using throat cast.

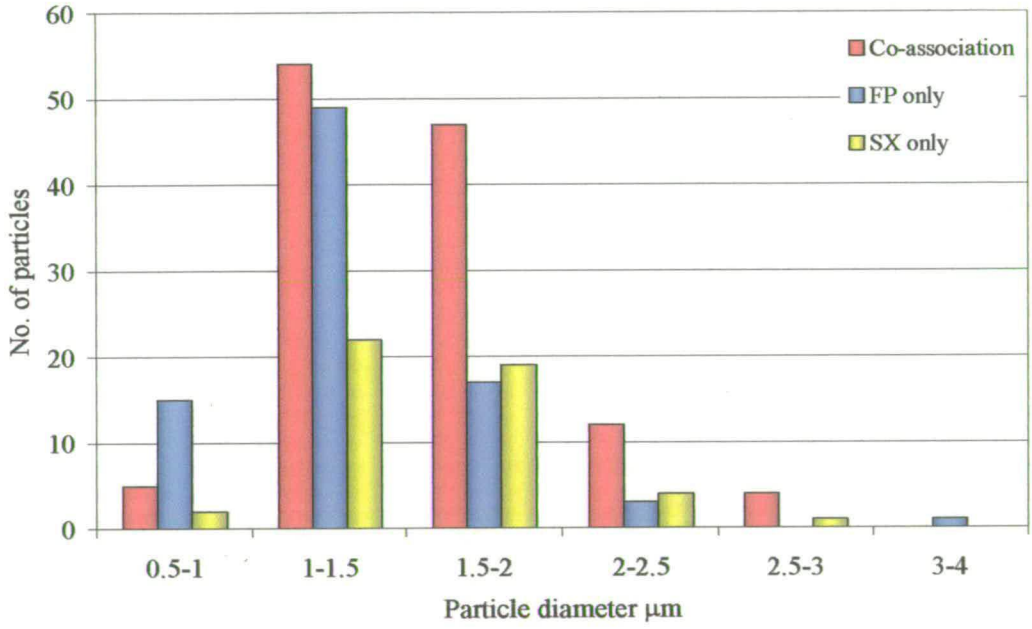

Figure A1. 2. Graph of co-association present in the Seretide Diskus using a throat cast.

Appendix 2

Conferences and courses attended

Firbush
August 2003 (Speaker)

August 2004 (Poster presented)

April 2005 (Speaker)

The Aerosol Society, University of Reading, Reading,

2003 (Delegate)

The Aerosol Society, Manchester

2004 (Poster presented)

Drug Delivery to the Lungs, London

2004 (Delegate)

The European Aerosol Conference, Ghent, Belgium

2005 (Poster presented (2))

Physical Chemistry Section Seminars

School of Chemistry Colloquia

Introduction to Aerosol Science, London

Atmospheric Chemistry, Lecture course	Mat Heal
Lasers in Chemistry, Lecture course:	Robert Donovan, Andy Alexander

Publications

Dall'Osto,M., Harrison,R.M., Beddows,D.C., Freney,E.J., Heal,M.R., & Donovan,R.J. (2006) Single Particle Scaling Efficiencys of Aerosol Time-Of-Flight Mass Spectrometry during NAMBLEX. *Environ. Sci.Technol*, **Submitted**.

Freney, E.J, Harland, P.W, Heal, M.R, Donovan, R.J (2005) Negative ion formation processes in the laser desorption and ionisation of single particles studied using aerosol time-of-flight mass spectrometry, **In preparation.**

E.J. Freney, M.R. Heal, R.J. Donovan, N.L. Mills, K. Donaldson, D.E. Newby, P.H.B. Fokkens, F.R. Cassee (2006) Single particle characterisation of a Mobile Versatile Aerosol Concentration Enrichment System for Exposure Studies, *Particle Fibre and Toxicology*, **Submitted.**